Two-dimensional ice-structure interaction for offshore wind turbines

Dion R.T. Koreman

Two-dimensional ice-structure interaction for offshore wind turbines

by

Dion R.T. Koreman

Graduation thesis

at the Norwegian University of Science and Technology (NTNU) and the Delft University of Technology (TU Delft),

Student number:	517535 (NTNU), 4372328 (TU Delft)	
Project duration:	January 1, 2020 – September 31, 2020	
Gradudadion committee:	Prof. A. Metrikine	TU Delft, supervisor
	Prof. E. Bachynski	NTNU
	Prof. Z. Gao	NTNU
	Dr. H. Hendriks	TU Delft
	Ir. T. Willems	SGRE
	Ir. T. Hammer	TU Delft

This thesis is confidential and connot be made public until 29th of September 2020

EWEM TU Delft NTNU Norwegian University of Science and Technology SIEMENS Gamesa RENEWABLE ENERGY

Contents

1

Introduction

With the Paris climate accords signed in 2016, most countries have committed themselves to ambitious climate targets during the next decades. One of the key focuses of these ambitions is a dramatic increase in the market share of renewable energies in the overall energy portfolio. According to The International Energy Agency (2019), this increase in renewable market share will, for a large part consist of newly built offshore wind farms. This rise in offshore wind energy projects is expected to be especially dramatic in northern regions, where high and constant wind speeds prevail, making offshore wind energy an attractive low carbon energy solution (Arapogianni et al., 2011). However, as offshore wind farm projects move further north, additional challenges need to be faced. One of these is the technical challenge to design offshore wind farms for possible encounters with drifting sea ice. In order to tackle this challenge, a proper understanding of the mechanics associated with encounters of drifting sea ice with offshore wind turbines is essential.

This thesis is the second stage of a two-stage individual study. In the first stage (Koreman, 2019), such encounters and their associated mechanics were extensively reviewed. Specifically, the occurrence of so-called ice-structure interaction phenomena proved to be critical and consequently was the focus of the first stage. In itself, this is not a groundbreaking finding, as ice-structure interaction phenomena historically have been a notable subject within the field of ice engineering. Indeed, research in ice-structure interaction phenomena has been conducted at a varying intensity from the 1960's onward. These decades of research have sprouted numerous ice models capable of simulating ice structure interactions. In turn, the advancement of these models has been respectable, with the more recent having received certification and being used regularly in the industry. Still, to the author's knowledge, most models are fundamentally one-dimensional. Consequently, they are unable to predict both cross-drift structural loads due to ice-structure interaction and the effect cross-drift structural motion has on ice-structure interactions. Based on Siemens Gamesa Renewable Energy (SGRE) knowledge, this gap is especially bothersome for ice-structure interactions with offshore wind turbines; offshore wind turbines, in contrast to traditional offshore structures, are anticipated to vibrate out of line with the far-field ice direction regularly due to ice-wind misalignment.

Therefore, this work aims to develop a two-dimensional ice-structure interaction model, capable of simulating ice-structure interactions on monopile-founded offshore wind turbines for all combinations of drifting sea ice and wind loads. In doing so, the contact area variation ice-structure interaction model by Hendrikse (2017) is used as a cornerstone. This model is hereafter referred to as the Hendrikse (2017) model. This model has been subjected to an extensive validation campaign (Hendrikse et al., 2018) and subsequent DNV-GL certification for use for offshore wind turbines un-

der the name "Variation of contact Area model for Numerical Ice Load Level Analyses (VANILLA)" (Willems and Hendrikse, 2019). By developing a two-dimensional model, this work additionally aims to understand how ice-structure interactions on offshore wind turbines are affected by the inherent two-dimensionality of ice. Both in comparison to one-dimensional ice and for newly simulable load cases of misaligned ice and wind.

In achieving this dual aim, Chapter 2 first provides a brief introduction to ice-structure interaction phenomena during ice crushing. Also, it reviews the fundamentals of the different ice-structure interaction models, with a further focus on the Hendrikse (2017) model used as a cornerstone in this thesis. For a more detailed review of ice actions in general, ice-structure interactions or the different ice-structure interaction models, one is referred to Koreman (2019) - the first phase of this two-phase individual research. Thereafter, Chapters 3, 4 and 5 jointly tackle the first goal of developing a two-dimensional ice-structure interaction model; the "Zero-friction contact Area variation Model By Omnidirectional Numerical Ice (ZAMBONI); More specifically, Chapter 3 discusses the development and functioning of ZAMBONI itself whereas Chapter 4 and Chapter 5 concern its verification and validation respectively. Next, Chapter 6 and Chapter 7 jointly concern the second research question, which is how simulating ice two-dimensionally affects ice-structure interactions on offshore wind turbines, both for aligned and misaligned ice and wind loads. In order to answer this question for a full-scale state-of-the-art wind turbine, Chapter 6 couples ZAMBONI to a modal representation of the SGRE 14-222 DD turbine in Baltic Sea conditions. This procedure enables coupled dynamic simulations for all (crushing) ice and wind conditions. Ultimately, Chapter 7 discusses the results of these dynamic simulations for various ice and wind conditions and various load cases. Despite the wide array of simulation possibilities this gives, the focus of this chapter remains to compare one- and two-dimensional ice and comment on the newly simulable load case of misaligned ice and wind. Finally, Chapter 8 provides a conclusion to this work, highlighting the most notable findings and recommending next steps.

2

Ice-structure interaction phenomena

Before any 2D model simulating crushing ice-structure interactions can be developed, it is crucial to understand what these 'ice-structure interactions' are. Therefore, a brief introduction to crushing ice-structure interactions are given in this chapter. Again, for a detailed review, one is referred to Koreman (2019). Also, this chapter describes the fundamental principles of the different ice-structure interaction models. Finally, the Hendrikse (2017) is discussed at more length, as this model will be used as a cornerstone for the development of the 2D ice-structure interaction model described in Chapter 3

2.1. An introduction to ice-structure interaction phenomena

Crushing ice-structure interactions are phenomena where - during an ice crushing event initiated by an ice floe indenting into a structure - the exerted ice loads and the structural position influence each other, often causing heavy vibrations. This term fundamentally differs from the more general ice actions, in that the structural behaviour significantly influences the ice behaviour. As a result, ice-structure interactions are always dependent on both ice- and structure characteristics.

Ice-structure interactions have been observed as early as the 1960s. For an overview of all observations of ice-structure interactions, one is referred to Koreman (2019), which discusses observations by Peyton (1968), Bjork (1981), Blenkarn (1970), Engelbrektson (1983), Jefferies and Wright (1988), Määttänen (1987), Nordlund et al. (1988) and Yue and Li (2003). During these events, structures were observed to behave in classifiable ways. Although the physical mechanisms causing these behaviours is disputed, the behaviour classification is widely agreed upon. Generally, three types of ice-structure interaction are recognised to exist. These are intermittent crushing, frequency lock-in and continuous brittle crushing. They are highly dependent on the ice indentation speed, allowing for an indentation speed regime classification as given in Figure 2.1, where it should be noted that for rigid structures, by definition, no ice-structure interactions occur and the crushing behaviour is thus simply classified as "crushing". These three different phenomena are all associated with their characteristic structural responses and load profiles, as shown in Figure 2.2. Hereafter, each phenomenon will be discussed individually.

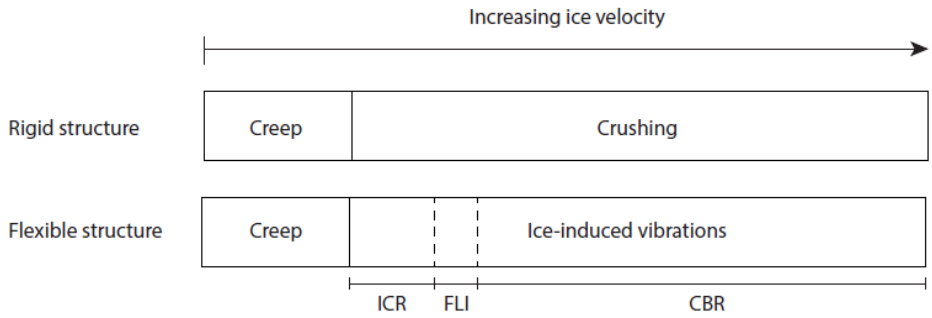

Figure 2.1: Widely recognised regimes of ice action and ice-structure interaction. The ice induced vibrations encompass intermittent crushing (ICR), frequency lock-in (FLI) and continuous brittle crushing (CBR). ICR and FLI do not necessarily develop for all flexible structures and the velocity ranges as shown in this figure are not always representative

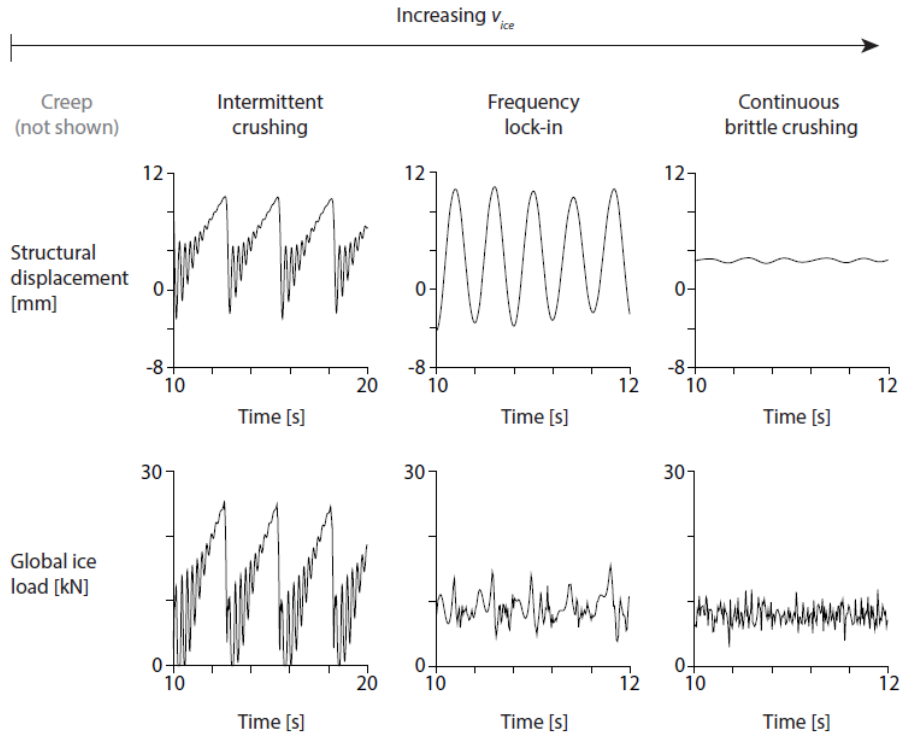

Figure 2.2: Typical structural displacement and global load time series of the three different ice-structure interaction regimes according to Hendrikse and Metrikine (2015). Axes values are not representative

Intermittent Crushing

At low crushing ice indentation speeds, intermittent crushing may develop. This is a well-studied field, as intermittent crushing is the ice-structure interaction phenomenon which is associated with highest global peak loads, relevant for ultimate limit state design. It is characterised by a typical saw-tooth pattern in the structural displacement and ice load time series. This saw-tooth pattern is clearly observable in Figure 2.2. Phenomenologically, each intermittent crushing cycle is recognised to consist of three phases, as best described by Sodhi (1995). These are:

1. The loading phase
2. The extrusion phase

3. The separation phase

During the loading phase, the relative velocity between the interacting ice floe and offshore structure is low, resulting in creep or ductile deformation at the ice-structure interface. The physical mechanisms resulting in this load build-up are disputed. Yet, a consensus is reached on a near-linear load increase as an ice floe indents into a structure. Then, at the point where the pressure at the ice-structure interface exceeds the compressive strength of the ice floe, the ice floe fails in a brittle manner, initiating the extrusion phase. It is at the transition between the loading and extrusion phases that a structure experiences both peak global loads and the largest accelerations due to an aggressive snap back response when the ice fails, causing the structure to release its stored elastic energy. During the subsequent extrusion phase, the structure moves against the ice drift direction at high velocity, extruding the pulverised ice in its way. After the ice rubble has been extruded, the structure vibrates transiently until the gap with the advancing ice floe is closed, upon which the process starts anew. In this final separation phase, a combination of load build-up and structural decay is observable. Furthermore, when an ice floe indents into the structure at a sufficiently large ice floe indentation speed, the separation phase may be non-existent.

Frequency Lock-In

At slightly higher ice indentation speeds, frequency lock-in may develop, which is the most dynamic ice-structure interaction regime. In this interaction regime, the structural displacements show near-harmonic vibrations at a frequency close to one of the structure's natural frequencies. These characteristic near-harmonic vibrations can clearly be observed in Figure 2.2. Because of their relatively high frequency and amplitude, frequency lock-in vibrations can have a severe impact on a structure's fatigue life. Similarly to the intermittent crushing phenomenon, frequency lock-in has an alternating loading and unloading phase, where during the loading phase, creep or ductile deformation occurs, whilst during the unloading phase, the ice floe fails in a brittle manner. However, conversely to the intermittent crushing regime, frequency lock-in hardly has a transient separation phase where no global ice load is present.

Based on field measurements and observations, ISO 19906 (2019) provides a mode-dependent dynamic stability condition predicting the vulnerability of a structure to frequency lock-in during dynamic ice-structure interaction. This condition is given in Equation 2.1. When this condition is satisfied for all modes, said structure will transition directly from intermittent crushing into continuous brittle crushing (Huang et al., 2007).

$$\xi_n \geq \frac{\phi_{nc}^2}{4\pi f_n M_n} h\theta \tag{2.1}$$

Where:

- ξ_n is the structural damping of the natural mode, n, as a fraction of critical damping
- ϕ_{nc} is the modal amplitude at the ice action point in natural mode, n
- M_n is the true modal mass in natural mode, n
- f_n is the natural frequency of natural mode, n
- h is the level ice thickness
- θ is an empirical coefficient with a suggested value of $40 \cdot 10^6$ [kg/ms] (which is derived from ice strength to stress rate dependence in Cook Inlet, Alaska and should be adjusted marginally according to local ice conditions and specific structures)

From Equation 2.1 one can conclude that structures become increasingly vulnerable to the frequency lock-in phenomenon with less structural damping, lower natural frequencies, smaller modal masses, larger modal amplitudes at the waterline and thicker ice floes. Since modal masses and natural frequencies both increase for higher modes, typically, lower modes are most susceptible to the frequency lock-in phenomenon. On the other hand, the modal displacement at the waterline can differ significantly and is known to often be highest in the 2nd bending mode for offshore wind turbines, making that bending mode susceptible to frequency lock-in despite its higher modal mass and frequency.

Still, Equation 2.1 only gives an empirical condition predicting whether frequency lock-in is likely to occur to a certain ice-structure interaction. It does not give a prediction at what ice indentation speeds the ice-structure interaction will transition to and away from frequency lock-in and neither gives an approximation of what the structural response will be during the frequency lock-in event. On the latter, the frequency lock-in relation as found by Toyama et al. (1983) provides some guidance. This relation relates the maximum structural velocity linearly to the ice indentation velocity as in Equation 2.2, where β lies between 1.0 and 1.5 [-]. This relation has been confirmed by subsequent experimental campaigns ranging from small to full scale by Toyama et al. (1983), Timco et al. (1992), Izumiyama et al. (1994), Izumiyama and Uto (1997) and Huang et al. (2007). The resulting relation between maximum structural velocity and ice indentation speed as found by these test campaigns are given in Figure 2.3.

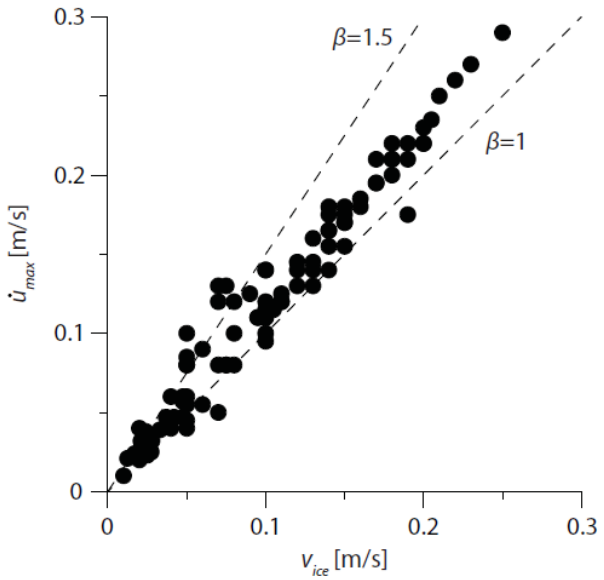

Figure 2.3: Maximum structural velocity in relation to the ice indentation speed during frequency lock-in events as observed by Toyama et al. (1983), Timco et al. (1992), Izumiyama et al. (1994), Izumiyama and Uto (1997) and Huang et al. (2007)

$$\dot{u}_{max} = \beta v_{ice} \tag{2.2}$$

Continuous brittle crushing

Finally, for even higher ice indentation speeds, continuous brittle crushing will develop. In contrast to intermittent crushing and frequency lock-in, phenomenologically, continuous brittle crushing does not include a creep or ductile loading phase. Instead, during continuous brittle crushing, an

ice floe fails directly in brittle crushing at the ice-structure interface. This is the most common interaction regime. However, it is associated with a relatively low and quasi-static structural response. Therefore, it is somewhat less interesting from a structural design point of view. As continuous brittle crushing is a quasi-static ice-structure interaction, its associated loads are rather similar to those loads simulated when ice action instead of dynamic ice-structure interaction was to be assumed for a flexible structure.

Defining the transition between interaction regimes

In most cases of ice-structure interaction, the observed behaviour can be categorised as one of these three phenomena. However, ambiguous cases around the transition from one regime to the next do occur. These ambiguous cases are especially occurring at the transition from intermittent crushing to frequency lock-in. In order to provide consistency for such ambiguous cases throughout the remainder of this report, the frequency lock-in relation of Equation 2.2 is used. That is, for β-ratios higher than 1.5 [-], an interaction is considered intermittent crushing. For β-ratios between 1.5 [-] and 1.0 [-], an interaction is considered frequency lock-in. For β-ratios lower than 1.0 [-], an interaction is considered continuous brittle crushing.

2.2. The Hendrikse (2017) contact area variation ice-structure interaction model

The descriptions of the different ice-structure interaction phenomena of Section 2.1 are widely accepted. Conversely, the fundamental physical mechanisms causing these phenomena are a disputed scientific topic. Historically, two explanations prevail:

1. Ice-structure interaction is caused by a negative damping term due to the dependence of relative ice indentation speed on the structural velocity
2. ice-structure interaction is caused by proximity in the ice crushing frequency and natural frequency of a structure creating resonance

Sodhi (1995) describes these different physical explanations as a dispute on whether ice-structure interactions are driven by relative velocity (explanation 1) or relative displacement (explanation 2). Nearly all models until the late 1990s were based on either of those physical explanations or of a combination of both in the case of Tsuchiya et al. (1985) and Huang and Liu (2009). Nevertheless, many researchers have reported that these models are both inaccurate due to a lack of physical understanding (Muhonen, 1996) and (Dempsey, 2000) - the former of which whilst further highlighting the inherent disagreement of the two physical explanations. Dempsey (2000) additionally concludes that further developing either of these models is essentially useless, proposing that more physical understanding of ice-structure interactions must be gained first. Indeed, in the decade thereafter, mostly phenomenological studies have been performed such as Jordaan (2001), Sodhi (2001) and Kärnä and Jochmann (2003), all without the explicit intention to immediately further develop an ice-structure interaction model. As a new attempt to physically explain the driving mechanism causing ice-structure interaction, Hendrikse (2017) proposes a third physical explanation based on a phenomenological model of contact area variation. These three physical explanations and subsequent models are extensively discussed in Koreman (2019). However, for the purpose of this report, only the contact area variation model of Hendrikse (2017) will be further discussed as it serves as a cornerstone to the newly developed 2D ice-structure interaction model presented in Chapter 3.

Hendrikse (2017) argues in his dissertation that neither the negative damping explanation nor the characteristic failure length explanation provides a consistent theory for level ice action on offshore

structures. The arguments for rejecting both approaches are the same as those provided by Muhonen (1996) and Dempsey (2000). Therefore, Hendrikse (2017) provides a third phenomenological explanation based on ice-structure contact area variation observations during ice-structure interaction by Sodhi (2001) and Sodhi and Haehnel (2003). According to Hendrikse (2017), a proper phenomenological model for ice-structure interaction should at least include:

1. Local contact between ice and structure
2. Elastic deformation of ice
3. Crushing failure
4. Global creep
5. Visco-elastic or visco-plastic deformation resulting in an increase of contact at low loading rates

The resulting mechanical model as first proposed by Hendrikse (2017) and later improved to Hendrikse and Nord (2019) is given in Figure 2.4.

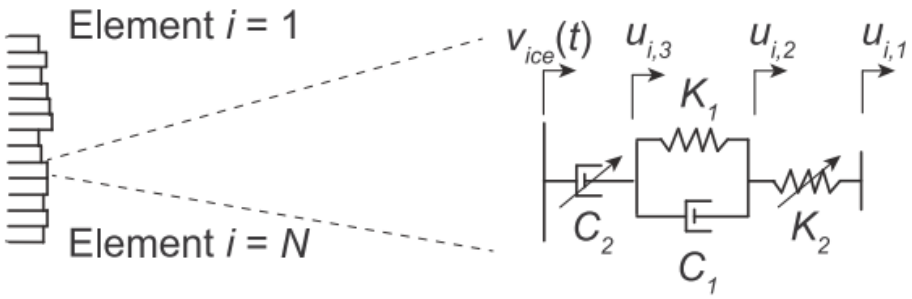

Figure 2.4: Mechanical ice-structure interaction model as first proposed by Hendrikse (2017) and thereafter minorly adapted by Hendrikse and Nord (2019) Left: Top view of modeled ice edge divided into N individual elements. Right: Representation of a single ice element in the contact zone

The left figure in Figure 2.4 fulfils the local contact requirement by modelling the ice floe as N finite elements. The mechanical model in the right figure fulfils requirements 2 to 5. Specifically, the front spring element with coefficient K_2 represents the linearised elastic stiffness of the ice floe, with δ_f the critical local deformation, thereby fulfilling requirements 2 and 3. The rear non-linear dashpot element with coefficient C_2 represents the power-law creep, thereby fulfilling requirement 3. The middle parallel spring-dashpot element with coefficients K_1 and C_1 is a Kelvin unit often used to represent visco-elastic behaviour of ice (Løset et al., 2006), thus fulfilling requirement 5.

The determination of the ice parameters K_2, C_2, K_1, C_1, δ_f, N and r_{max} is an extensive process best described in Hendrikse and Nord (2019) and briefly summarised here. The ice parameters can be found from the dependence of measured global ice load in relation to the ice indentation speed on a rigid structure. An example of such a typical dependence is given in Figure 2.5. From this graph, several characteristic points can be extracted, which in turn lead to the ice parameters according to Equation 2.3a to Equation 2.3e. Finally, parameters K_1 and C_1 can be found by an iterative process according to Equation 2.4a and Equation 2.4b.

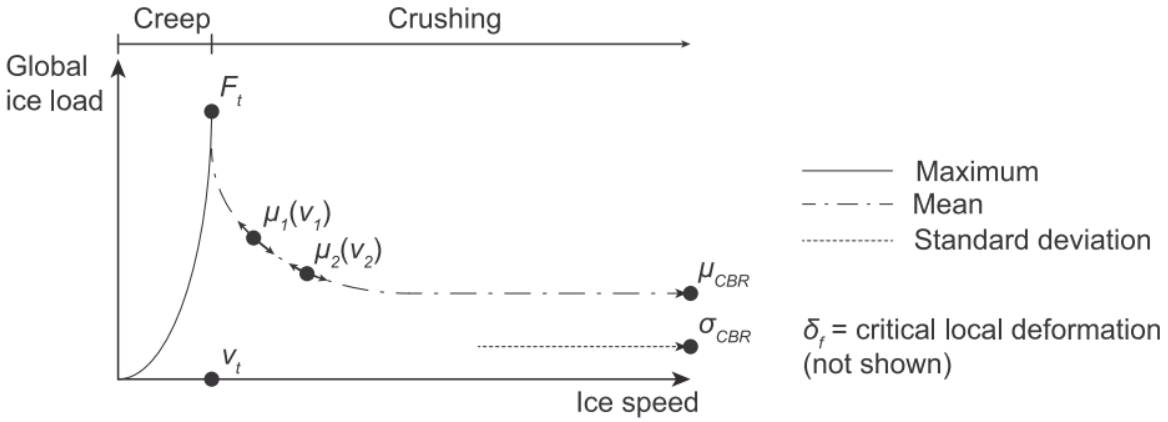

Figure 2.5: Typical trend of global ice load on a rigid structure. F_t is the peak global load, v_t is the ice indentation speed at which this peak global load is reached, μ_{CBR} and σ_{CBR} are the mean global load and standard deviation of the global load during continuous brittle crushing, $\mu_1(v_1)$ and $\mu_2(v_2)$ are two additional points defining the dependence of the mean ice load on the ice drift speed and δ_f is the critical local deformation (not shown)

$$\delta_f = \delta_f \tag{2.3a}$$

$$r_{\max} = \delta_f \left(\frac{F_t}{\mu_{cbr}} - 2 \right) \tag{2.3b}$$

$$N = \frac{\left(\frac{2F_t}{3\mu_{cbr}} - 1 \right)}{\left(\frac{\sigma_{cbr}}{\mu_{cbr}} \right)^2} \tag{2.3c}$$

$$K_2 = \frac{F_t}{\delta_f N} \tag{2.3d}$$

$$C_2 = \frac{F_l^3}{N^3 v_{ice}} \tag{2.3e}$$

$$\mu_1(v_1) = \frac{F_t}{\delta_f} \frac{\int_0^{t_f(v_1)} u_{i,2}(t)\mathrm{d}t}{\frac{0.5 r_{\max}}{v_1} + t_f(v_1)} \tag{2.4a}$$

$$\mu_2(v_2) = \frac{F_t}{\delta_f} \frac{\int_0^{t_f(v_2)} u_{i,2}(t)\mathrm{d}t}{v_2} + t_f(v_2) \tag{2.4b}$$

Finally, the dynamic spring dashpot configuration of Figure 2.4 results in equations of motion governing the dynamics of the distinct positions in a single element, they are given in Equation 2.5a to Equation 2.5c. Note that in these equations, u_s represents the structural position.

$$u_{i,1} = \begin{cases} u_{i,2} & u_{i,1} < u_s \\ u_s & u_{i,1} \geq u_s \end{cases} \tag{2.5a}$$

$$\dot{u}_{i,2} = \frac{K_2}{C_1}\left(u_{i,1} - u_{i,2}\right) + \frac{K_1}{C_1}\left(u_{i,3} - u_{i,2}\right) + v_{ice} - \frac{1}{C_2}\left(K_2\left(u_{i,2} - u_{i,1}\right)\right)^3 \tag{2.5b}$$

$$\dot{u}_{i,3} = v_{ice} - \frac{1}{C_2}\left(K_2\left(u_{i,2} - u_{i,1}\right)\right)^3 \tag{2.5c}$$

3

The Zero-friction contact Area variation Model By Omnidirectional Numerical Ice (ZAMBONI)

With the need for 2D ice models established, this chapter describes the development of such an ice model. In doing so, it uses the contact area variation ice-structure interaction model of Section 2.2 as a cornerstone, keeping its mechanisms unchanged to the largest extent practical. This choice minimises the amount of newly required concepts and principles, which all introduce uncertainties and challenges of their own. Naturally, the downside of making this choice in an early stage is that a sub-optimal solution might be pursued. However, as the model presented here constitutes a first attempt to grasp two-dimensional ice-structure interactions, the risk of arriving at a sub-optimal solution is accepted. As objectives, the to-be-developed two-dimensional extension of the Hendrikse (2017) model should:

1. Be able to simulate ice-structure interactions for all combinations of ice indentation and structural vibration direction
2. Be able to estimate cross-drift forces
3. Be able to simulate with an arbitrary structure and associated waterline shape

These objectives lead to the "Zero-friction contact Area variation Model By Omnidirectional Numerical Ice" (ZAMBONI). It is presented in this chapter in two ways. First, in Section 3.1, its approach is discussed qualitatively through the fundamental principles that differentiate ZAMBONI from the Section 2.2 model. After that, the ice solver of ZAMBONI is shown systematically as a model flow chart in Section 3.2, including its fundamental equations. Finally, Section 3.3 gives recommendations for further model development.

3.1. Fundamental Principles

Thus, a modelling approach is taken, which extends the well established Hendrikse (2017) model to a two-dimensional space. Therefore, the newly developed ZAMBONI can be explained by discussing the differences of ZAMBONI with respect to the Hendrikse (2017) model. Here, these differences are

discussed through the following five fundamental principles that distinguish ZAMBONI from the Hendrikse (2017) model.

1. The location of each ice point is given by its 2D Cartesian coordinates, which jointly represent the frontal edge of the indenting ice floe in a finite area surrounding the structure
2. The ice-structure interface is assumed to be frictionless
3. The ice parameter N, representing a constant number of elements, is replaced with an average ice element resolution R
4. Ice elements are added and deleted when required
5. In global force computations, the frontal spring of each ice element K_2, representing the linear elastic stiffness of the ice floe, acts as one distributed spring $\bar{K}_2$ rather than an integer number of individual springs

In these principles, the concepts of ice points and ice elements are both used frequently. Note that ice elements refer to the ice elements as introduced by Hendrikse (2017), whereas ice points refer to the four distinct positions within a single element ($u_{i,1}$, $u_{i,2}$, $u_{i,3}$, $u_{i,4}$). Furthermore, in understanding these principles, it should be noted that not all principles are independent starting points but instead are often interrelated, such that introducing one principle necessitates the introduction of a second or even third principle. The causal relations between these different principles are given in Figure 3.1, whereafter each principle will be discussed individually.

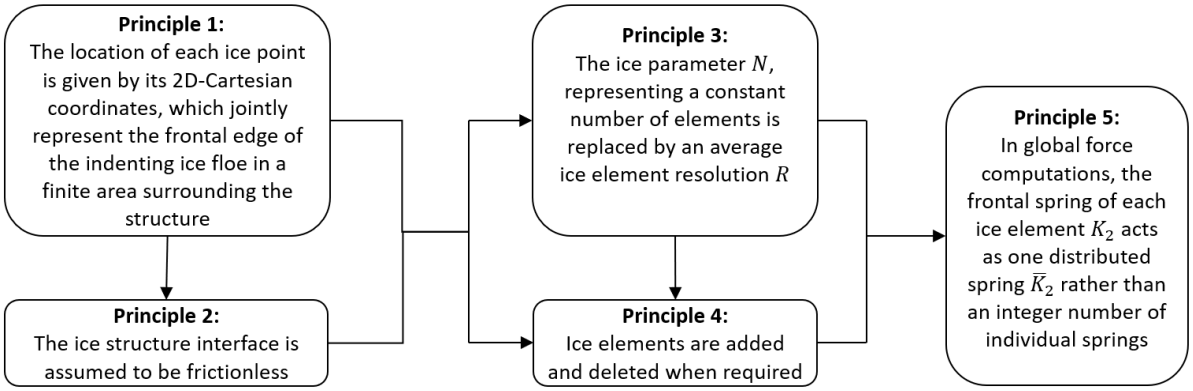

Figure 3.1: Causal relation of the 5 fundamental principles, arrows indicate direct causal relations

3.1.1. Principle 1: The location of each ice point is given by its 2D Cartesian coordinates, which jointly represent the frontal edge of the indenting ice floe in a finite area surrounding the structure

The first fundamental aspect in which ZAMBONI differs from the Hendrikse (2017) model is the 2D Cartesian coordinate representation of its ice points. In the Hendrikse (2017) model, the ice points only hold in-line positions and velocities with respect to the neutral line of the ice-structure interface. On the contrary, in ZAMBONI, each ice point is located at a distinctive 2D Cartesian coordinate. This difference is graphically illustrated in Figure 3.2, where top view representations are given of the ice elements, on the left-hand side for the Hendrikse (2017) model and on the right-hand side for ZAMBONI.

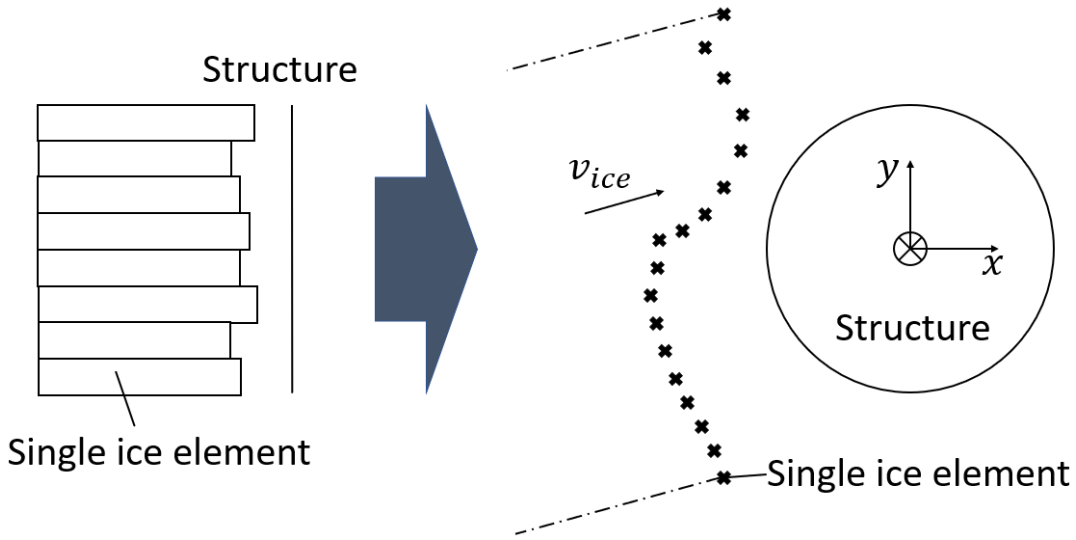

Figure 3.2: Graphical representation of the effect of the 1st principle of ice points existing in a two dimensional space from the 1D Hendrikse (2017) model (left) to the 2D ZAMBONI (right)

Ice points existing in a two-dimensional space is a requirement in any 2D model. Most importantly, it allows for directionality in the movement of individual ice elements, which is unachievable with a 1D ice representation as in the Hendrikse (2017) model. It simultaneously allows for cross-drift structural vibrations to deform the ice edge, which is one of the objectives listed in this chapter's introduction. These new functionalities of ZAMBONI, are shown in Figure 3.3, where cases are shown of an irregularly shaped ice edge indenting into a cylindrical structure at an angle for cases of both in-line and (exaggerated) cross-drift vibrations. Since ice elements now represent the ice edge, an impractically large number of elements would be required to describe an entire ice floe. Therefore, only ice points that might engage in ice-structure interaction are stored by defining an appropriate enclosed area around the structure. In Figure 3.3, the area encircled by the dashed line represents this enclosed area.

Finally, ice points existing in a two-dimensional space is also a necessary step towards incorporating the structure's waterline shape in the ice-structure interaction model. Previously, in the Hendrikse (2017) model, ice parameters had to be altered for the structure's waterline shape, which is not the case for ZAMBONI. In ZAMBONI, ice points - and thus also the ice elements they jointly make up - will locally encounter a certain angle of attack with respect to the structure's interface, influencing the local behaviour of the ice points. For the mechanics of such local behaviour, the second principle of assumed zero-friction comes into effect.

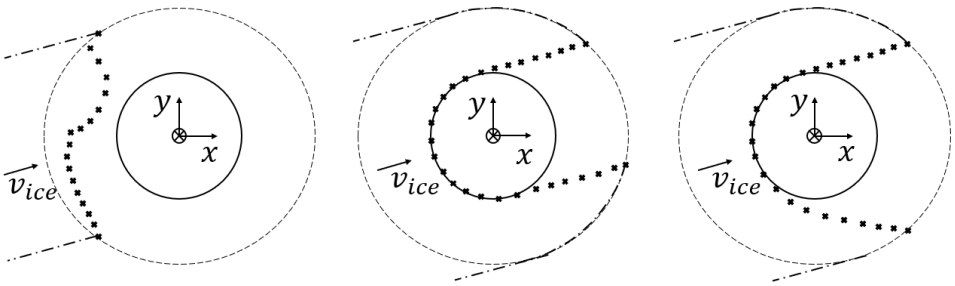

Figure 3.3: Graphical representation of ice elements during an indentation event. Left: irregularly shaped ice edge prior to indentation. Middle: ice edge encompassed structure during in-line structural vibrations. Right: ice edge encompassed structure during cross-drift structural vibrations causing the ice edge to detach from the structure (dimension are exaggerated)

3.1.2. Principle 2: The ice-structure interface is assumed to be frictionless

Principle 1 allows for ice elements and their ice points to freely move in a two-dimensional space, thereby satisfying several of the objectives outlined in this chapter's introduction. However, the two-dimensional implications of local ice-structure interaction have not been discussed. For that discussion, the principle of assuming no friction at the ice-structure interface is fundamental.

According to Timco and Weeks (2010), ice friction forces along a sloped ice-structure interface are about 2% to 10% of the normal force for ice-steel interfaces. These small shear forces lead to a simplification possibility through assuming shear forces to be entirely non-existent. Then, when reasoning from single ice elements, ice points must remain aligned when no internal shear forces are present. More precisely, these ice points must remain orthogonal to the local ice-structure interface. Therefore, the mechanical Burgers model of Hendrikse (2017), which is displayed on the right-hand side of Figure 2.4, can be applied one-dimensionally for each local element.

However, in order to apply this one-dimensional Burgers model, the aligned positions must still be found. After all, if ice point i_1 remains fixed to its first indentation position along the structure's edge and ice point i_4 is indeed undisturbed, ice points i_1 and i_4 will most likely not remain aligned orthogonally to the structure's surface. The only way to ensure alignment orthogonally to the structure's surface whilst keeping ice point i_4 undisturbed is to let ice points i_1, i_2 and i_3 slip to the unique orthogonal line passing through ice point i_4, which constitutes the approach in ZAMBONI. Note that this entails a shift from the Hendrikse (2017) model as in ZAMBONI, the positions of the i_4 ice points hold meaning, whereas in the Hendrikse (2017) model, only the velocity of the undisturbed ice affects the ice dynamics. In fact, in the Hendrikse (2017) model, ice point i_4 was not described specifically as its velocity equals the far-field ice velocity for all elements. From here, the mechanical Burgers model of Figure 2.4 and Equation 2.5 can be applied, where u_i represents the positions along the aforementioned orthogonal line and the ice points velocities $\dot{u}_i$ are relative to the orthogonal line. In summary, when introducing the zero-friction principle, the local mechanics within an ice element follow the following four-step process each time step:

1. The undisturbed ice element moves to its new position
2. The structure moves to its new position
3. Ice elements i_1 to i_3 slip freely to the line orthogonal to the structure's edge and passing through i_4 whilst remaining equally distant from the structure's edge
4. The mechanical ice equations of Equation 2.5 are applied to determine the new positions of ice points i_2 and i_3

Section 3.2 discusses this four-step process in more detail. Graphically, this process is shown in Figure 3.4. Note that the ice elements appear to move along the structure's edge. Indeed, when applying the zero-friction principle, ice elements will slip along the structure's edge. Partly, this is convenient, as it results in the ice elements encompassing a structure automatically. However, it also introduces some new challenges, one of which is remaining a constant number of elements in contact with the structure at all time whilst also ensuring equidistant elements. After all, from Section 2.2, the number of ice elements N is an ice parameter relating to the numerical properties of the ice floe, and varying it during a simulation can therefore result in false ice properties. In order to tackle these issues, principles 3 and 4 are introduced.

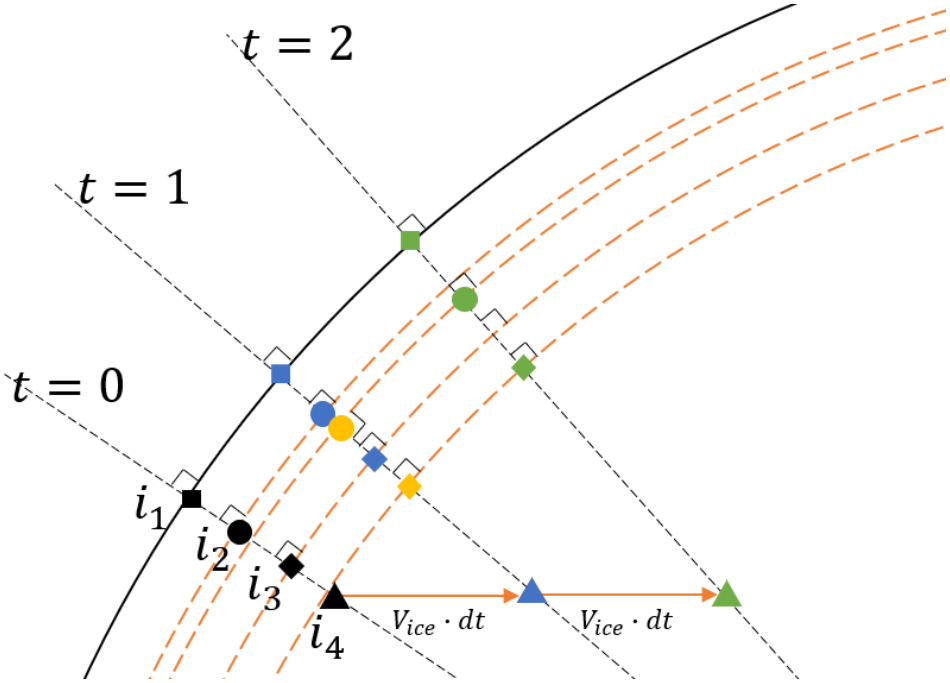

Figure 3.4: Graphical representation of the zero-friction concept. Ice points i_1 to i_4 are represented by squares, circles, diamonds and triangles respectively. Black markers represent the original position of ice points, blue markers represent the position of the same ice points after application of the zero-friction principle, yellow markers represent ice point i_2 and i_3 after application of the dynamic ice equations of motion of Equation 2.5 and the green markers represent the position of the ice points after a second application of the zero-friction principle

As the correctness of ZAMBONI hinges on the extent to which these simplifications have an influence on the simulated ice-structure interactions, they must be discussed. According to ice friction tests summarised by Timco and Weeks (2010), the kinetic friction coefficient of saline ice on steel varies from 0.02 [-] to 0.1 [-], depending on the ice indentation speed and smoothness of the steel surface. Although such friction coefficients may be considered small, they are not insignificant. To assess the effect of including frictional forces, two areas are explored; the effect on the structural response and the effect on ice-element behaviour. Note that during ice-structure interaction, these effects in turn affect each other, which is neglected for this analysis.

The effect of frictional forces on the structural response is expected to be most influential in the cross-drift direction, because frictional loads are orthogonal to normal loads, and normal loads are dominant in the in-line direction. However, as with normal loads, the loads of these cross-drift frictional forces should cancel each other out for symmetric structures. On the contrary, frictional loads will increase the global in-line ice loads, as on regular symmetric structures, all in-line frictional loads will be superposed. However, this increase is expected to be in the order of a few per-

centages, due to the orthogonal orientation of friction forces with respect to the in-line dominant normal loads, and due to the small friction coefficient.

The effect of frictional forces on the behaviour of ice-points within individual ice elements can be qualitatively assessed by considering the hypothetical case of full traction at the ice-structure interface. In that case, all ice points will be aligned parallel to the ice drift direction at all times. Therefore, essentially, this case corresponds to the one-dimensional Hendrikse (2017). This leads to the hypothesis that the true orientation of ice points must lie between the ice drift direction and the local orthogonal lines. The ultimate response expected can therefore also be described as a combination of ZAMBONI and the Hendrikse (2017). However, due to the low friction values, the ultimate response is expected to lie much closer to ZAMBONI. As ZAMBONI serves as a first attempt to develop a two-dimensional ice-structure interaction model, it is deemed acceptable to make a simplification as significant as the zero-friction principle.

3.1.3. Principle 3: The ice parameter N, representing a constant number of elements is replaced with an average ice element resolution R

One of the challenges introduced by allowing ice elements to move freely in a two-dimensional space concerns the ice parameter N. As shown in Figure 3.3, according to the 1st fundamental principle of ZAMBONI, ice elements represent the ice edge in a finite area around the structure. Therefore, generally, several ice elements will be interacting with the structure, whereas others will not. These non-interacting elements already entail a shift from the Hendrikse (2017) model, where all ice elements are interacting with the structure. This leads to an issue as the number of elements in contact with the structure partly determines the statistical properties of the ice. Furthermore, with the introduction of the 2nd principle, specific ice elements will not continue interacting with the structure indefinitely, as ice elements slip along the structure's edge. Therefore, fixing a set of elements to remain in contact with the structure contradicts principle 2.

Therefore, the 3rd fundamental principle is introduced, which replaces the fixed number of elements N with an average distance between two ice elements, or resolution R. This is an elegant solution as it allows for any number of elements to exist, thus describing any possible ice-edge of any required size, albeit with a fixed resolution. Furthermore, defining the desired resolution R can be used to evaluate whether any two adjacent ice points are at an unacceptable distance from each other, which will prove useful when introducing principle 4. Mathematically, the element resolution R relates to the characteristic number of elements N through a structure's cross-sectional width w_c according to Equation 3.1, where $w_c = D$ for a cylindrical structure

$$R = \frac{w_c}{N} = \frac{D}{N} \tag{3.1}$$

3.1.4. Principle 4: Ice elements are added and deleted when required

Although introducing the average resolution R partly resolves the issues raised by fundamental principles 1 and 2 discussed in Subsection 3.1.2, the need to replace ice elements continuously remains eminent. After all, when during an indentation event, ice elements slip from a central position along the edge to a more outward position and eventually away from the structure, over time, ever fewer ice elements will be in contact with the structure. Therefore, ice elements must be added or deleted when locally required. In ZAMBONI, this occurs whenever two adjacent ice elements are positioned too far away from each other or too close to each other, with the strictest possible margins achievable when adding or deleting one element at a time. This strictness is desired to limit the resulting inconsistency in the actual ice element resolution. Equation 3.2a presents a set of conditions to

which d_{min} and d_{max} must adhere. Solving these conditions for the strictest possible margins then results in the d_{max} and d_{min} values used in Equation 3.2b. The process of adding and deleting elements is shown graphically in Figure 3.5.

$$\begin{cases} R - d_{min} & = d_{max} - R \text{ , to ensure mean resolution = } R \\ 2d_{min} & \leq d_{max} \text{ , to ensure newly added points are not too close to eachother} \end{cases} \tag{3.2a}$$

$$\begin{cases} d_{max} & \leq \frac{4}{3}R \longrightarrow d_{max,ZAMBONI} = \frac{4}{3}R \\ d_{min} & \geq \frac{2}{3}R \longrightarrow d_{min,ZAMBONI} = \frac{2}{3}R \end{cases} \tag{3.2b}$$

Despite these strict margins, adding or deleting an ice element engaging in ice-structure interaction will have immediate consequences on the statistical properties of the ice floe these elements resemble. Nonetheless, when acquiring a sense of the severeness of the fluctuations of element resolution, the effect proves to be minimal. First of all, the maximum immediate percentage shift in average ice element resolution on the ice-structure interface caused by adding or deleting a single ice element is related to the original parameter N according to Equation 3.3, indicating that this immediate shift is relatively low for a large number of elements. Furthermore, consistent testing during the simulations performed for the verification and validation of Chapter 4 and Chapter 5 showed that the measured resolution of ice elements at the structure's interface remains within 5% of the intended resolution. Additionally, with the introduction of principle 5, the effects of having a non-constant element resolution at the ice-structure interface will be limited further.

$$\left(\frac{|R_{new} - R_{old}|}{R_{old}} \right)_{single\ element} = \frac{1}{N} \tag{3.3}$$

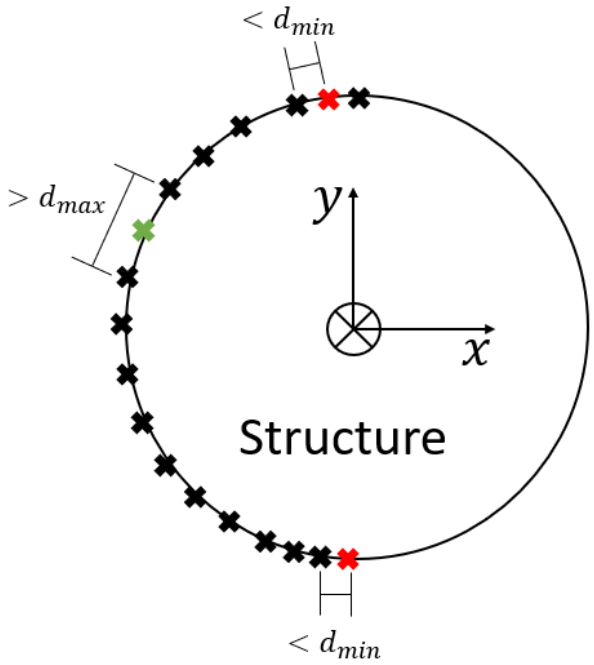

Figure 3.5: Graphical representation of manner in which ice elements are added and deleted continuously. Black markers represent regular ice elements, red markers represent ice elements to be deleted and green markers represent ice elements to be added

3.1.5. Principle 5: In global force computations, the frontal spring of each ice element K_2, representing the linear elastic stiffness of the ice floe, act as one distributed spring $\bar{K}_2$ rather than an integer number of individual springs

With principles 1 to 4 discussed, a two-dimensional model is approached. The primary shortcoming left to discuss is the fact that the ice elements as described up to this point will not be equidistant. By the introduction of the 4th principle, element spacing is allowed up to 33 [%] of the intended spacing, which is not insignificant. A potential problem arising with non-equidistant ice elements is a false interpretation of the global forces caused by an indenting ice sheet. Such a case is illustrated in Figure 3.6, where element spacing on the lower side of the structure is sparser than on the upper side of the structure, causing an unrealistic global ice force.

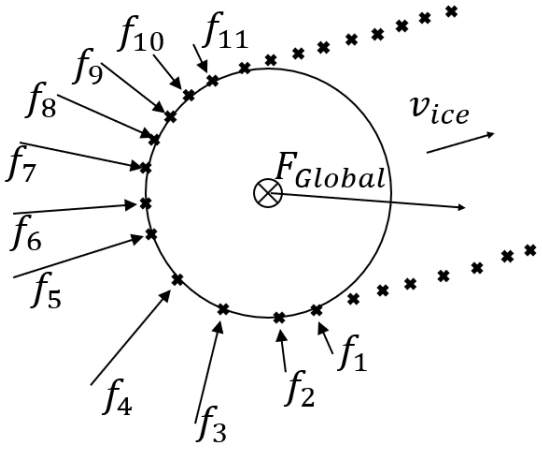

Figure 3.6: Graphical representation of a potentially false computation of global ice load due to non-equidistant ice elements

Therefore, principle 5 is introduced, which attempts to arrange the ice element configuration on Figure 2.4 as distributed springs and dashpots rather than individually acting elements. Such a 'distributed' system can be achieved by either realising equidistant elements or scaling the parameters within an element to the width on which an element has an effect. As determined earlier, the former option opposes principles 1 to 4. Therefore, the latter option of parameter scaling is pursued instead. When scaling the ice parameters K_2, K_1, C_1 and C_2 to achieve a distributed spring-dashpot configuration and account for non-equidistant ice elements, the most intuitive solution is to scale all parameters. Although this is entirely possible, it introduces unnecessary complexity into ZAMBONI. When examining the non-equidistant case of Figure 3.6, the local interaction between the ice points within an ice element is correct, whilst only the force computation of the elements causes issues. Since only parameter K_2 is involved in each elements' force computation, a far more elegant solution is to introduce a separate parameter $\bar{K_2}$ according to Equation 3.4. After that, the force exerted on the structure by each element can be computed by Equation 3.5 and the global force exerted by the ice on the structure is found by summing the force contributions of the single elements according to Equation 3.6. This solution resolves falsely computed global forces when adding or deleting elements, both in terms of non-equidistant element spacing and the effect of adding or deleting elements. However, the standard deviation of those forces might still vary slightly due to adding or deleting elements. This slight inaccuracy is accepted, as it is expected to be minimal because of the minimal deviation in ice element spacing discussed in Subsection 3.1.4. Nevertheless, during the verification phase of ZAMBONI discussed in Chapter 4, special attention will be given to inconsistencies in standard deviation, thereby determining if the effect on the standard deviation is traceable.

$$\bar{K_2} = \frac{K_2}{R} \tag{3.4}$$

$$f_i = \bar{K_2}\left(u_{i,2} - u_{i,1}\right)\frac{|\mathbf{u}_{i+1} - \mathbf{u}_{i-1}|}{2} \tag{3.5}$$

$$F_{ice,global} = \sum_{i=1}^{N_{el}} \mathbf{f}_i \tag{3.6}$$

3.2. ZAMBONI break down in flowchart

Section 3.1 explained ZAMBONI through its fundamental principles. Although this should suffice to understand ZAMBONI, it does not give a step by step overview of ZAMBONI. Therefore, here, the ZAMBONI ice simulation is broken down more extensively in its step by step components. The flowchart of the repetitive ice solver module is given in Figure 3.7. Furthermore, in this case, a cylindrical structure is assumed, such that all orthogonal lines pass through the centre of the structure. Therefore, these orthogonal lines can be fully described by their radial angle θ. An overview of all variables shown in Figure 3.7 is given in Table 3.1. Finally, Figure 3.7 refers to several equations, these are given in Equation 3.7 to Equation 3.13, and concisely explained below:

- Equation 3.7, Equation 3.8 and Equation 3.9 jointly estimate the ice point velocity of ice points i_2 and i_3. $\dot{u}_{i,4,r}$ is the relative velocity of ice point i_4 projected to its orthogonal line, found by evaluating both i_4 and $i_{4,zf}$, the virtual position if i_4 would not have advanced but instead would have slipped similarly to i_1, i_2 and i_3
- Equation 3.10 finds the new positions of all ice points

- Equation 3.11 and Equation 3.12 find the effective interface area and the the global ice loads according to the distributed spring principle as discussed in Subsection 3.1.5.
- Equation 3.13 finds the structural response to the global ice loads according to the structure's equations of motion

$$d\dot{u}_{i,3} = \frac{1}{C_2}\left(K_2\left(u_{i,2} - u_{i,1}\right)\right)^3 \tag{3.7a}$$

$$d\dot{u}_{i,2} = \frac{K_2}{C_1}\left(u_{i,1} - u_{i,2}\right) + \frac{K_1}{C_1}\left(u_{i,3} - u_{i,2}\right) \tag{3.7b}$$

$$\dot{u}_{i,3} = \dot{u}_{i,4,r} - d\dot{u}_{i,3} \tag{3.8a}$$

$$\dot{u}_{i,2} = \dot{u}_{i,3} - d\dot{u}_{i,2} \tag{3.8b}$$

$$\dot{u}_{i,4,r} = \frac{i_4 - i_{4,zf}}{dt} \tag{3.9}$$

$$i_3 = i_3 + \dot{u}_{i,3} \cdot dt \tag{3.10a}$$

$$i_2 = i_2 + \dot{u}_{i,3} \cdot dt \tag{3.10b}$$

$$w_{i,eff} = \frac{|\mathbf{u}_{i+1} - \mathbf{u}_{i-1}|}{2} \tag{3.11}$$

$$f_i = \bar{K}_2\left(\frac{D}{2} - r_{i,2}\right) w_{i,eff} \tag{3.12a}$$

$$F_x = \sum_{i=1}^{N_{el}} f_i \cos\left(dir_i\right) \tag{3.12b}$$

$$F_y = \sum_{i=1}^{N_{el}} -f_i \sin\left(dir_i\right) \tag{3.12c}$$

$$\ddot{u} = F - 2\mathbf{Z_s}\Omega_\mathbf{s}\dot{u}_s - {\Omega_\mathbf{s}}^2 u_s \tag{3.13}$$

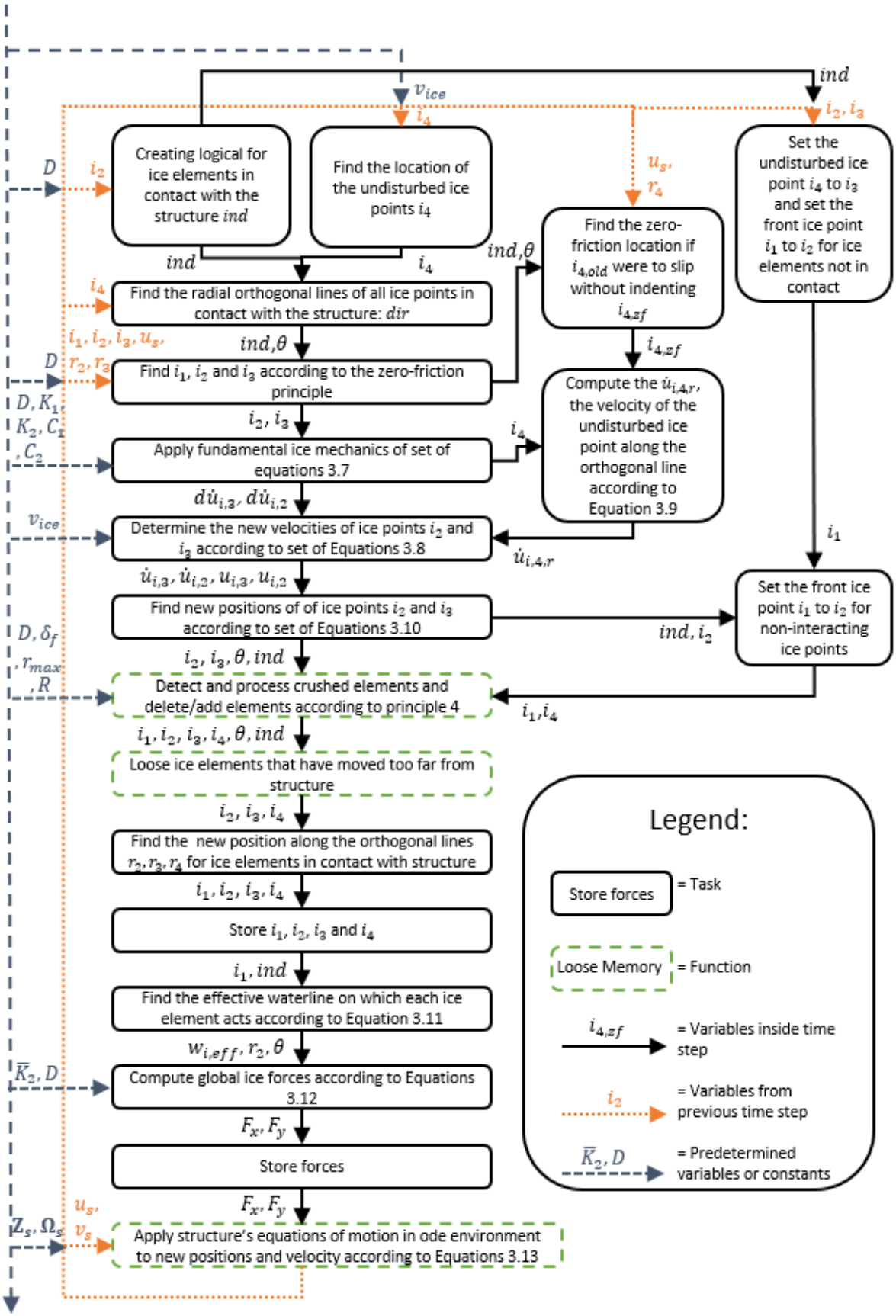

Figure 3.7: Flowchart of the ice solver of ZAMBONI for a cylindrical structure

Type	Symbol	Desciption	[Unit]
Predetermined variables and constants	D	Structural Diameter	[m]
	v_{ice}	Far field ice velocity	[m/s,m/s] (x,y)
	K_1	Ice parameter according to Hendrikse (2017)	[N/m]
	K_2	Ice parameter according to Hendrikse (2017)	[N/m]
	C_1	Ice parameter according to Hendrikse (2017)	[Ns/m]
	C_2	Ice parameter according to Hendrikse (2017)	[Ns/m^3]
	δ_f	Ice parameter according to Hendrikse (2017)	[m]
	r_{max}	Ice parameter according to Hendrikse (2017)	[m]
	R	Ice resolution according to principle 3	[m]
	$\bar{K}_2$	Distributed spring according to principle 5	[m/s^2]
	$\mathbf{Z_s}$	Mass normalised structural damping ratio	[-]
	$\Omega_\mathbf{s}$	Mass normalised structural natural frequency	[rad/s]
Fedback positions of ice points for all ice elements or for structure	i_1	Positions of frontal ice points	[m,m] (x,y)
	i_2	Positions of force determining ice points	[m,m] (x,y)
	i_3	Positions of creep ice points	[m,m] (x,y)
	i_4	Positions of undisturbed ice points	[m,m] (x,y)
	r_2	Radial position of i_2 along orthogonal line	[m]
	r_3	Radial position of i_3 along orthogonal line	[m]
	r_4	Radial position of i_4 along orthogonal line	[m]
	u_s	Structural displacement	[m]
	$\dot{u}_s$	Structural velocity	[m/s]
Variables existing only in the ice solver of Figure 3.7	ind	Logical for ice elements in contact with structure	[m,m] (x,y)
	θ	Radial angles describing orthogonal lines	[m,m] (x,y)
	$i_{4,zf}$	Positions of the virtual ice points	[m,m] (x,y)
	$\dot{u}_{i,4,r}$	Virtual velocity of i_4 along orthogonal lines	[m/s,m/s] (x,y)
	$d\dot{u}_{i,3}$	Velocity deficit of i_3 with respect to $\dot{u}_{i,4,r}$	[m/s,m/s] (x,y)
	$d\dot{u}_{i,2}$	Velocity deficit of i_2 with respect to i_3	[m/s,m/s] (x,y)
	$w_{i,eff}$	Waterline width on which each elements acts	[m]
Global forces	F_x	Global force in the X-direction	[N]
	F_y	Global force in the y-direction	[N]

Table 3.1: Overview of the meaning and units of all variables and constants as shown in Figure 3.7

3.3. Recommendations for further development of ZAMBONI

As stated in this chapter's introduction, ZAMBONI constitutes a first attempt to simulate ice-structure interactions in a two-dimensional environment. Naturally, such a first attempt leaves room for improvement. Therefore, this section serves as a guide to whomever further develops ZAMBONI, as well as to those that attempt to develop other two-dimensional ice-structure interaction models.

Within the realm of currently applied fundamental principles, several improvements can be made. The first is a computational recommendation. The ice solver module of Section 3.2 works on a time step basis, where Figure 3.7 represents the computations during a single time step. Of these computations, only the final structural equations of motion of Equation 3.13 are solved with an ordinary differential equation (ode) solver. Thus, the differential ice equations of Equation 3.7 are solved outside an ode environment. Including these equations in the ode environments will increase the accuracy of the ice mechanics as it solves initial value problems iteratively according to Runge-Kutta

methods.

Secondly, in Subsection 3.1.4, it was shown that achieving a constant ice element resolution on the ice-structure interface is incompatible with the fundamental principles of Section 3.1. Furthermore, when replacing one element at a time, the allowed element spacing deviation must be at least 33 % of the intended resolution according to Equations 3.2a and 3.2b. However, it should be possible to lower this allowed deviation when replacing multiple elements at a time. Naturally, when pursuing this option, a trade-off issue arises where further cutting the allowed spacing deviation results in more frequent adding and deleting of ice elements.

Thirdly, in theory, the principles of Section 3.1 allow for ZAMBONI to be applied to any arbitrary structure. However, in the ice solver of Section 3.2, a circular waterline shape is assumed. The current ZAMBONI is indeed tailored to circular waterline shapes. Although possible within ZAMBONI's principles, deviating from a circular waterline shape introduces additional challenges. Most notably, a cylindrical structure is a special case because all orthogonal lines pass through a single point, the centre of the structure. Therefore, at all times, finding the orthogonal line through i_4 can be achieved by simply finding the unique line that passes through both i_4 and the centre of the structure. For more complex waterline shapes, this shortcut cannot be applied, thereby requiring a new solution that finds the orthogonal lines. Furthermore, for a cylindrical structure, each point i_4 has one unique orthogonal line. However, for other structures, more orthogonal lines may exist. Examples of such waterline shapes are rectangles and parabolic shapes, which have two and three uniquely orthogonal lines for specific i_4 positions respectively, as shown in Figure 3.8. For these cases, additional criteria should be developed to define which orthogonal lines correspond to a single element's one-dimensional Burgers model.

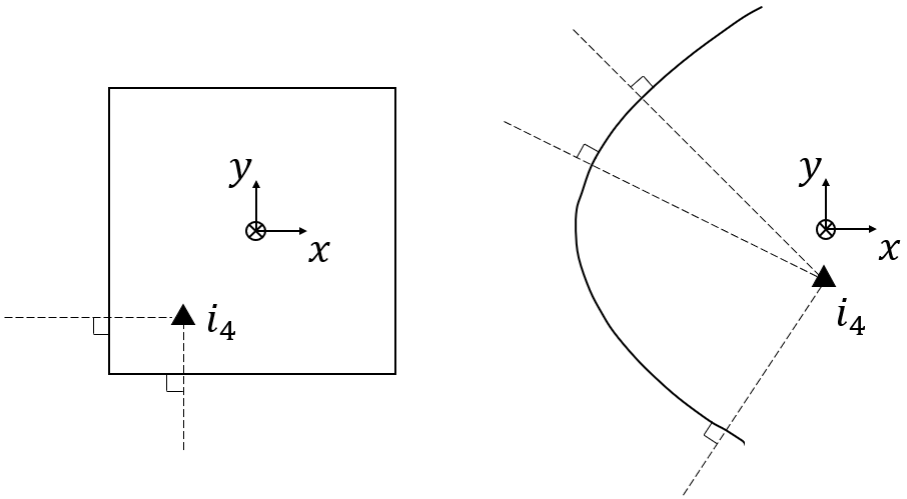

Figure 3.8: Examples of two waterline shapes, square and parabolic, which have two or three orthogonal lines passing through i_4 respectively

The recommendations mentioned above all uphold the 5 fundamental principles of Section 3.1 without adding any new ones. However, by adding some principles, more indentation events can be simulated. In the current ZAMBONI, each ice floe is assumed to be infinitely large. Therefore, the far-field ice velocity is not affected by the ice-structure interaction. In reality, however, the structure will have its effects on the far-field ice velocity. Hendrikse and Nord (2019), have already developed a model in 1D where ice drift equations are applied such that the far-field ice velocity is dependent on the ice-structure interactions. When pursuing this extension, additionally, two-dimensional effects

should be taken into account, such as an ice floe turning due to the forces exerted by the structure on the ice floe.

Finally, when improving on ZAMBONI, the possibility must always be considered to change its fundamental principles and modelling choices. As early as in this chapter's introduction, it has been acknowledged that the design choice to apply the principles of the Hendrikse (2017) model as consistently as practical might lead to a sub-optimal solution. This author indeed hypothesises that more precise two-dimensional ice-structure interaction models are achievable when the 2nd fundamental principle of assumed zero-friction is refrained, as discussed in Subsection 3.1.2. However, when such modelling solutions are pursued, many new challenges will arise. Perhaps the most eminent of those are the computational speeds of said models, as virtually all other modelling solutions will require more computational power. Still, solutions based on the interaction between individual elements or even lattice ice models are a highly interesting and unexplored area, which for that reason solely should be further explored. Hopefully, in doing so, this first attempt at creating a two-dimensional ice-structural interaction model will prove helpful.

4

Verification of ZAMBONI

In order to assert value to ZAMBONI, it is important to prove its correctness and assess its accuracy. To that end, a verification procedure is performed. Ideally, such a verification procedure would consist of comparing ZAMBONI to another well established 2D ice-structure interaction model, which also includes contact area variation. However, as discussed in Chapter 2, no other contact area variation 2D ice-structure interaction models exist. Therefore, full verification of ZAMBONI is not achievable. Instead, ZAMBONI is verified only in the in-line direction, with the contact area variation ice-structure interaction model as presented by Hendrikse (2017). In doing so, this chapter first describes the verification procedure. Next, the verification results are presented. After that, a detailed discussion follows, wherein the deviations between the different models are highlighted. Finally, recommendations are given towards further verifying ZAMBONI.

4.1. Verification method

As thoroughly explained in Chapter 3, the Hendrikse (2017) model has been used as a cornerstone for ZAMBONI. Therefore, the most straightforward way of verifying ZAMBONI is by comparing its simulations with the Hendrikse (2017) model. That way, differences in simulations of the two models must be the effect of ZAMBONI's fundamental principles, discussed in Section 3.1, allowing for an accurate assessment of the effect of these fundamental principles. On the other hand, since the Hendrikse (2017) model is one-dimensional, one cannot definitively conclude from this verification procedure solely what causes deviations between both models; correctly simulated differences between one-dimensional and two-dimensional ice dynamics, or inaccuracies in ZAMBONI. Nevertheless, in Section 4.3, an attempt is made to attribute the observed deviations to either of those reasons.

Aside from deciding on a top-level verification strategy and a model to verify with, in order to perform simulations, one must also decide on a physical ice field and structure to simulate ice indentation events for comparison between both models. Here, it is decided to apply one of the model-scale set-ups originally used to mimic the Toyama et al. (1983) tests. The primary motivation to make use of this particular combination of ice and structure is that these correspond to the default ice and structure settings of the openly available Mendeley version of the MATLAB implemented Hendrikse (2017) model; (Hendrikse, 2018), making this verification easily reproducible. Furthermore, the corresponding structure is a quasi-single degree of freedom (SDOF) structure, which is desirable as it simplifies the interaction, thereby amplifying the differences in the two ice models. Finally, the Toyama et al. (1983) tests were conducted in natural saline ice. As the ultimate aim of this thesis

is to better understand ice-structure interactions on offshore wind turbines in offshore conditions, the coupled simulations of Chapter 7 also apply natural saline ice, making this the preferred ice type for the verification procedure. The corresponding ice and structure characteristics are given in Table 4.1. Here, note that by using similar parameters for both models, this verification procedure compares a rectangular structure in the Hendrikse (2017) model to a cylindrical structure in ZAMBONI, regardless of whether these ice parameters were initially intended for a cylindrical or a rectangular structure.

Table 4.1: Overview of ice- and structure parameters used for ZAMBONI's verification

Ice parameters			Structure Parameters (SDOF)		
Symbol	Value	[Unit]	Symbol	Value	[Unit]
K_1	20126	[N/m]	D	0.2	[m]
K_2	190750	[N/m]	M_s	9803	[kg]
C_1	73772	[Ns/m]	ω_s	7.98	[rad/s]
C_2	$5.55\ 10^{10}$	[Ns/m^3]	ζ_s	0.0023	[-]
δ_f	0.002	[m]			
r_{max}	0.0029	[m]			
N	15	[-]			

As discussed in Chapter 2, the most crucial factor predicting ice-structure interaction phenomena is the ice-indentation speed. Therefore, verification must be performed at different ice indentation speeds. Since this study focuses mostly on intermittent crushing and frequency lock-in, the range of indentation speeds to simulate at is chosen from 0.1 [mm/s] to 500 [mm/s]. In order to visualise these simulations in such a wide range, simulation results are shown logarithmically. Furthermore, the statistical characteristics of each simulation are reported rather than the time series. These statistical characteristics are shown for ice forces, structural displacements and velocities and dominant vibration frequencies for each simulation. Specifically, the mean, maximum, minimum and standard deviation of these time series is presented, thereby vastly reducing the number of data points per simulation.

Only the steady-state regimes of the time series are included in the statistics. Inconveniently, the length of the transient stage differs substantially per indentation speed. Consequently, the setting at which the different simulations are run should be customised to some extent. An overview of the settings for different simulation ranges is given in Table 4.2 for both the Hendrikse (2017) model and ZAMBONI. In Table 4.2, V_{From} and V_{To} represent the boundaries of each simulation range, and dV is the ice indentation speed step between two simulations. Furthermore, dt is the time step for which ice loads are simulated, t_{Sim} is the simulation duration of each simulation, and t_{Trans} is the assumed subsequent transient time, during which no statistical measurements are taken. Finally, t_{In} represents the ice initialisation time, where an ice floe is rapidly indented into a structure such that it fully encompasses the structure. This initialisation phase is only required for ZAMBONI.

Table 4.2: Settings of the different simulation ranges used in the verification procedure, the prescripts of Z or H in $\#_{Sim}$ refer to ZAMBONI and the Hendrikse (2017) model respectively

$\#_{Sim}$	V_{From} [mm/s]	V_{To} [mm/s]	dV [mm/s]	dt [s]	t_{Sim} [s]	t_{In} [s]	t_{Trans} [s]	Notes
Z1	0.1	1.0	0.1	0.005	700	30	470	Creep
Z2	1.1	2.0	0.1	0.01	2000	30	70	Low IC
Z3	2.0	5.0	0.1	0.001	1000	30	70	Medium IC
Z4	5.0	100	1	0.001	500	30	70	High IC and FLI
Z5	100	200	10	0.0002	400	30	320	FLI to CBC
Z6	200	500	50	0.0004	500	30	70	CBC
H1	0.1	1.0	0.1	NA	2000	NA	1300	Creep
H2	1.1	2.0	0.1	NA	1000	NA	100	Low IC
H3	2.0	10	0.1	NA	300	NA	100	Medium IC
H4	10	100	1	NA	500	NA	100	High IC and FLI
H5	100	200	10	NA	400	NA	320	FLI to CBC
H6	200	500	50	NA	1000	NA	200	CBC

4.2. Verification results

With the verification method described in Section 4.1, the verification results are compactly presented here. Since all conclusions are derived from a combination of the different results, it is chosen to first present all verification results compactly in this section and subsequently discuss them in Section 4.3. All figures in this section present data of both ZAMBONI and the Hendrikse (2017) model, with which ZAMBONI is compared. The following results are presented:

- Figure 4.1 to Figure 4.3 show a statistical representation of the time series of all performed simulations
- Figure 4.4 and Figure 4.5 provide additional insight in the forces and displacements of Figure 4.1 and Figure 4.2 respectively by presenting statistical ratios between both models, thus amplifying the deviations between both models
- Figure 4.6 and Figure 4.7 compare the dominant structural frequencies and β-ratios at different ice indentation speeds respectively
- Figure 4.8a and Figure 4.8b show the force and displacement time series for both models of a typical intermittent crushing simulation at an ice indentation speed of 3 [mm/s]
- Figure 4.9a and Figure 4.9b show the force and displacement time series of a typical frequency lock-in simulation at an ice indentation speed of 40 [mm/s]
- Figure 4.10a and Figure 4.10a show intermittent crushing time series for a special case where ZAMBONI is applied with a rectangular structure. This way, ZAMBONI and the Hendrikse (2017) model can be compared for one-dimensional ice

Note that from Figure 4.7, the phenomena distinction between intermittent crushing and frequency lock-in, and between frequency lock-in and continuous brittle crushing are derived. In all figures in this section, these transitions between phenomena are indicated by the dashed vertical lines. The ice indentation speeds at which a phenomenon transition occurs differ slightly between models,

as further discussed in Section 4.3. However, to assure clarity in the already crowded figures, only one transition line is shown for each transition. Further note that the ice indentation speed on the horizontal axes refers to the far-field ice velocity as opposed to the local (relative) ice-indentation speeds.

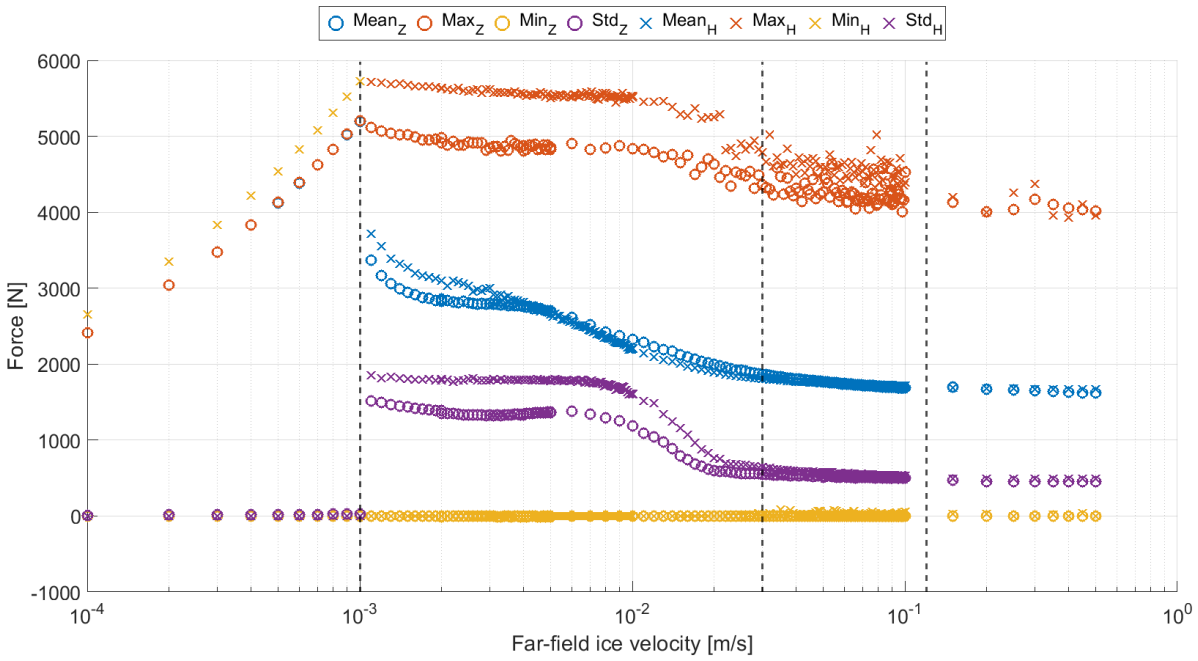

Figure 4.1: Statistical characteristics of the in-line force exerted by an indenting ice floe for varying ice indentation speeds and ice and structure characteristics as listed in Table 4.1. Results are depicted for both the 1D Hendrikse (2017) model (subscript 'H') and ZAMBONI (subscript 'Z'). Note that in the creep regime, the mean, minimum and maximum in-line forces overlap

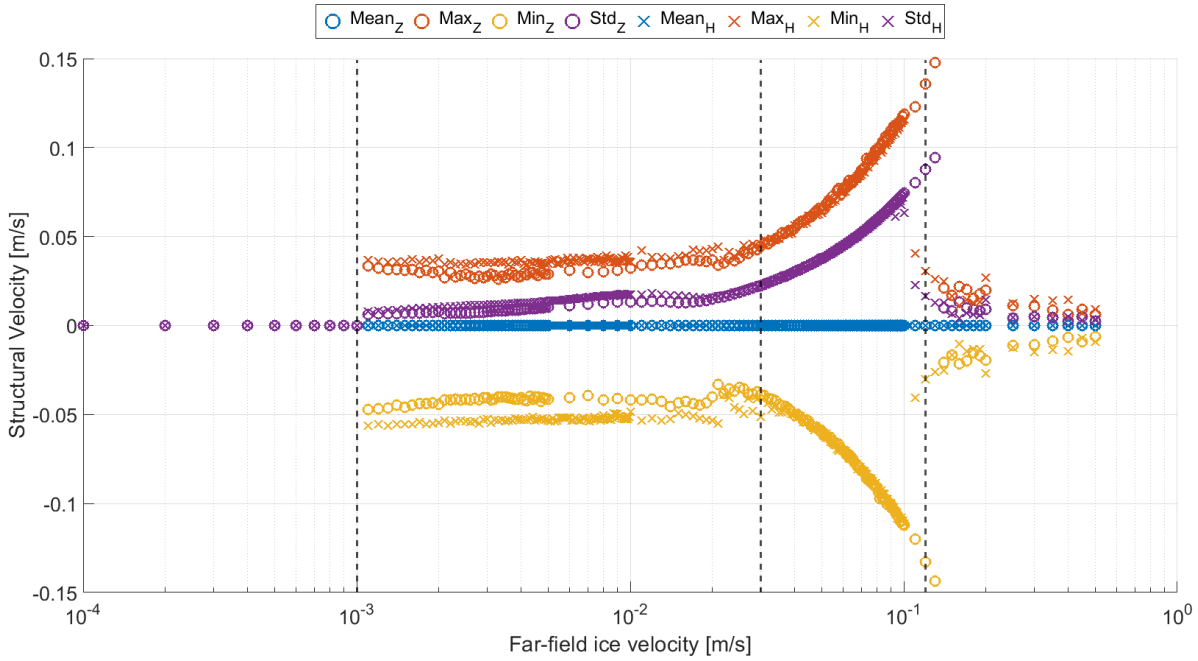

Figure 4.2: Statistical characteristics of the in-line structural displacement for varying ice indentation speeds and ice and structure characteristics as listed in Table 4.1. Results are depicted for both the 1D Hendrikse (2017) model (subscript 'H') and ZAMBONI (subscript 'Z'). Note that in the creep regime, the mean, minimum and maximum in-line forces overlap

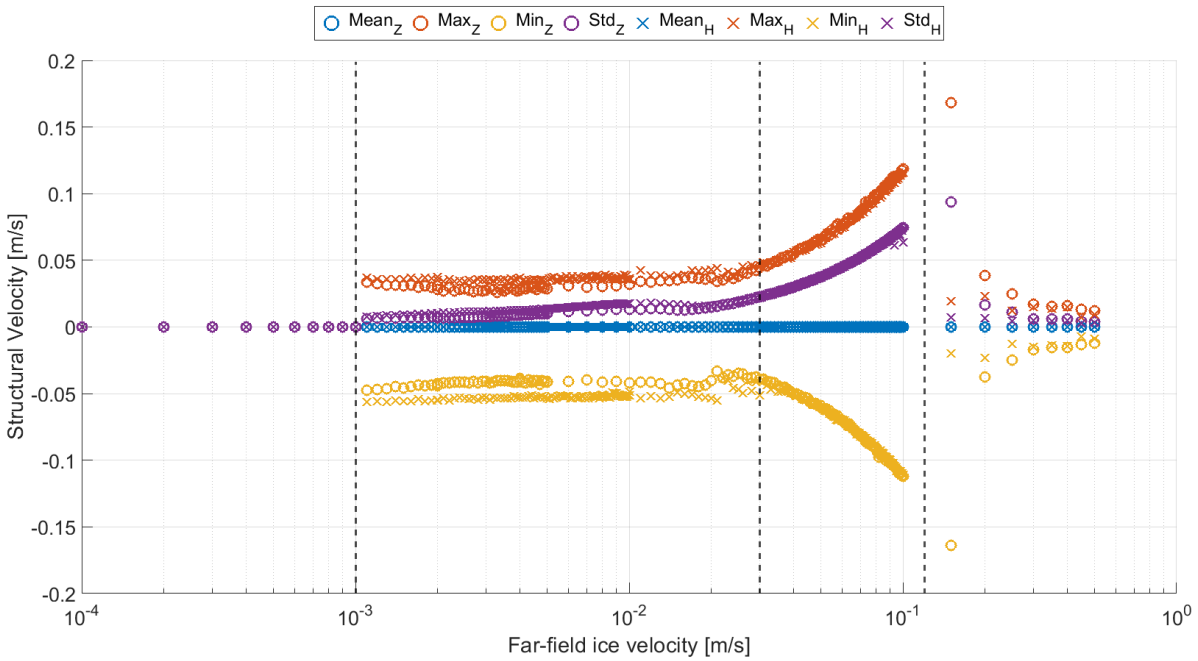

Figure 4.3: Statistical characteristics of the in-line structural velocity for varying ice indentation speeds and ice and structure characteristics as listed in Table 4.1. Results are depicted for both the 1D Hendrikse (2017) model (subscript 'H') and ZAMBONI (subscript 'Z'). Note that in the creep regime, the mean, minimum and maximum in-line structural velocities overlap

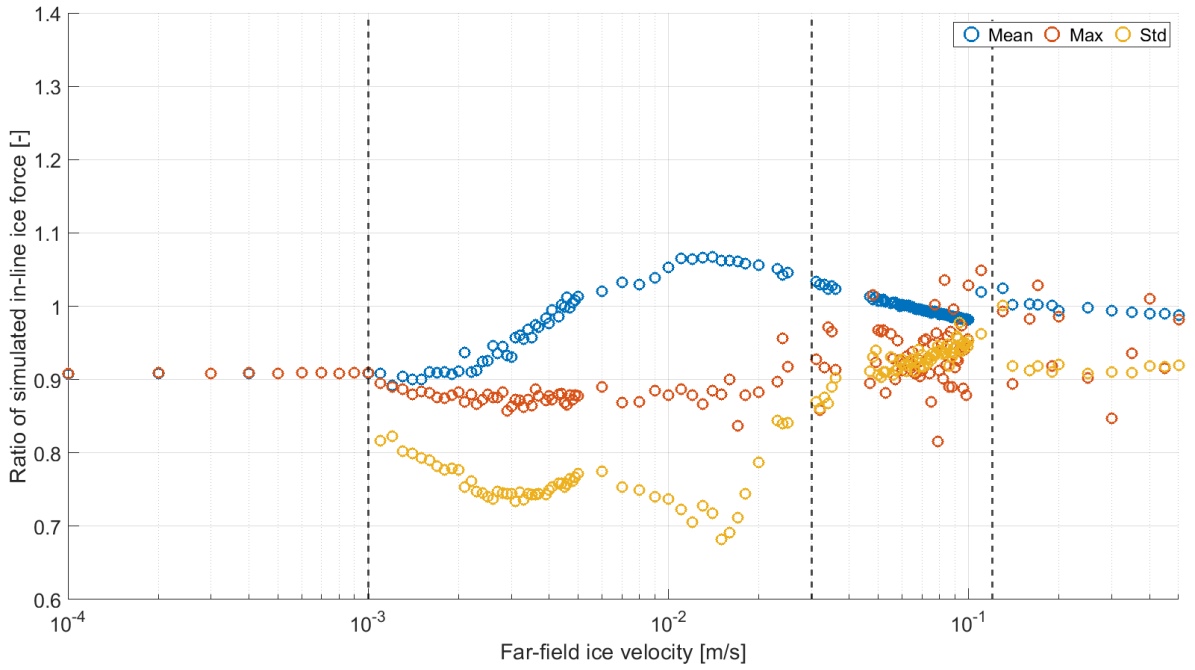

Figure 4.4: Ratios of statistical force characteristics of the Hendrikse (2017) model to ZAMBONI, for varying ice indentation speeds and ice and structure characteristics as listed in Table 4.1

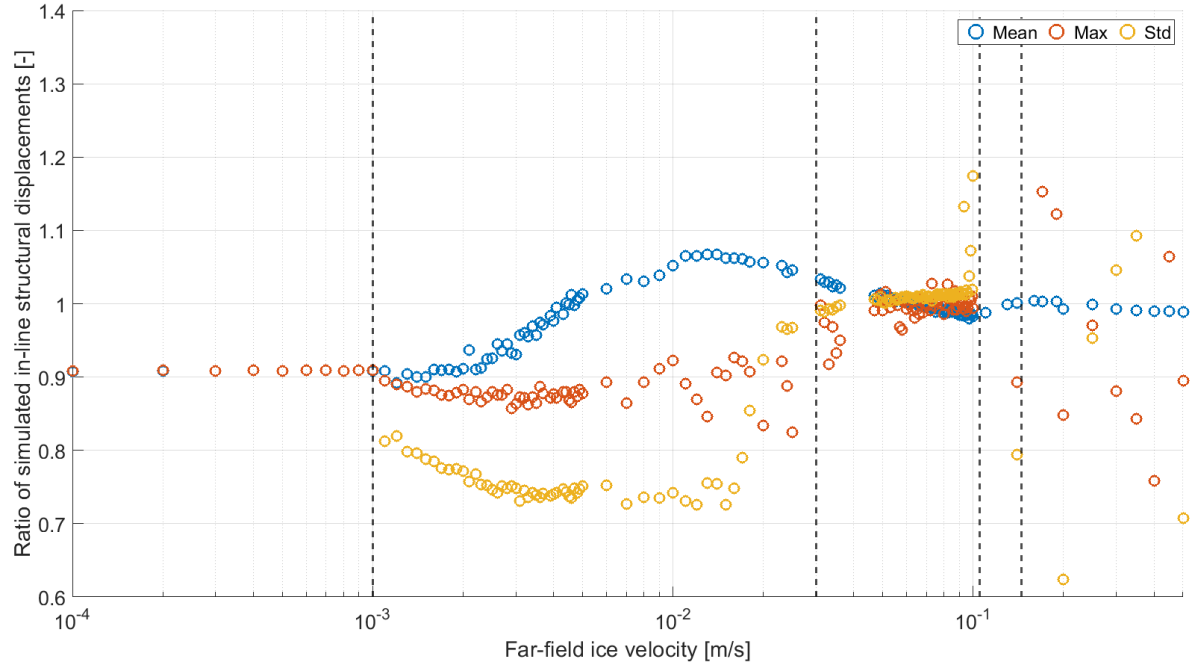

Figure 4.5: Ratios of statistical structural displacement characteristics of the Hendrikse (2017) model to ZAMBONI, for varying ice indentation speeds and ice and structure characteristics as listed in Table 4.1

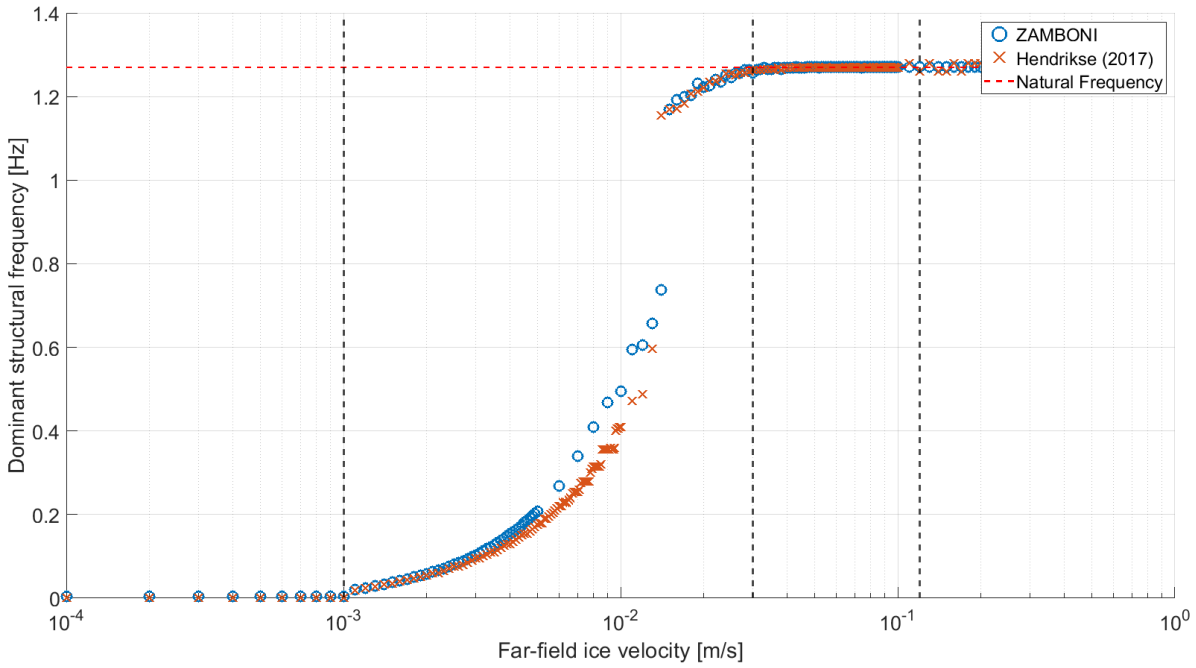

Figure 4.6: Dominant in-line structural frequency for varying ice indentation speeds and ice and structure characteristics as listed in Table 4.1. Results are depicted for both the 1D Hendrikse (2017) model and ZAMBONI

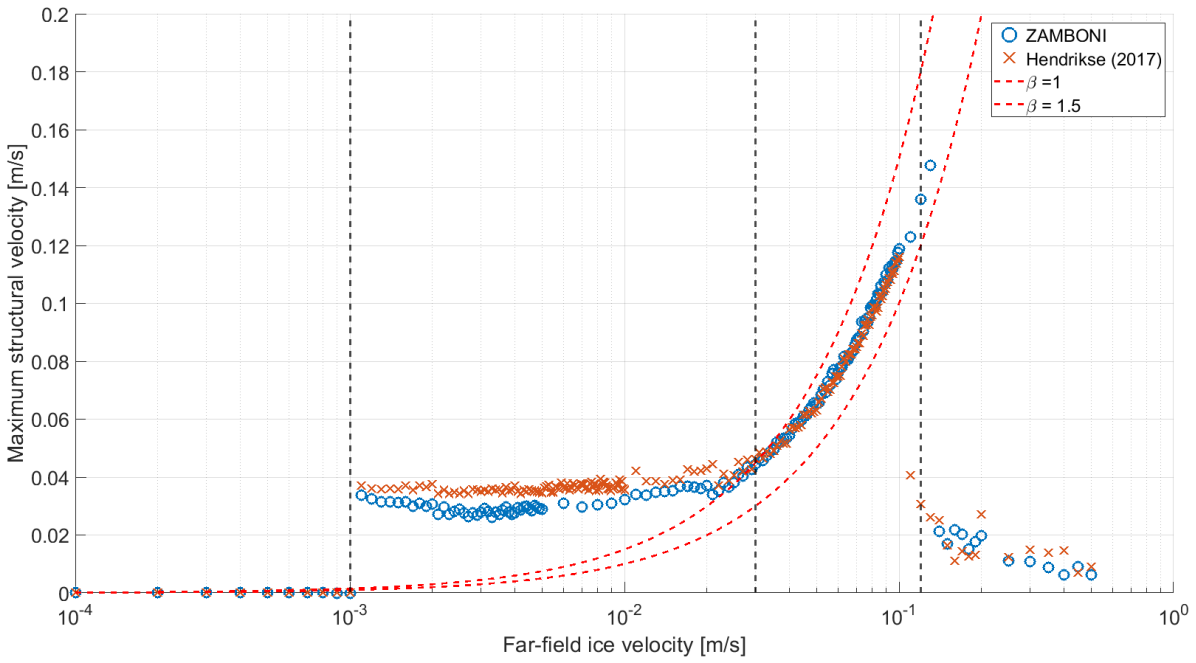

Figure 4.7: Ratio of maximum structural velocity and ice indentation speed - otherwise known as the β-value as introduced by Toyama et al. (1983) - for varying ice indentation speeds and ice and structure characteristics as listed in Table 4.1. Results are depicted for both the 1D Hendrikse (2017) model and ZAMBONI

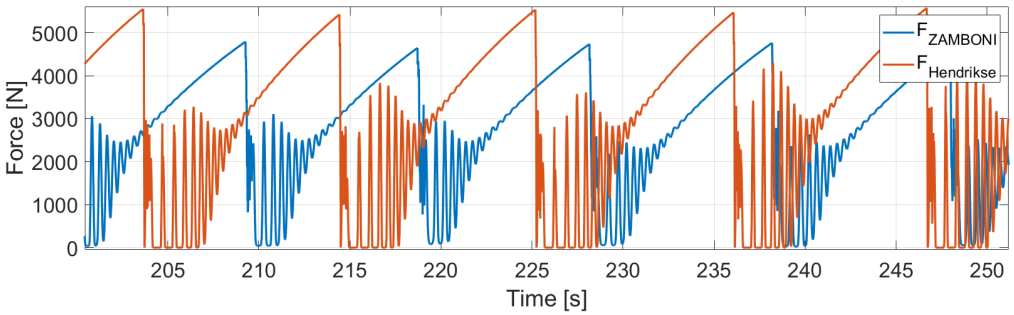

(a) Forces

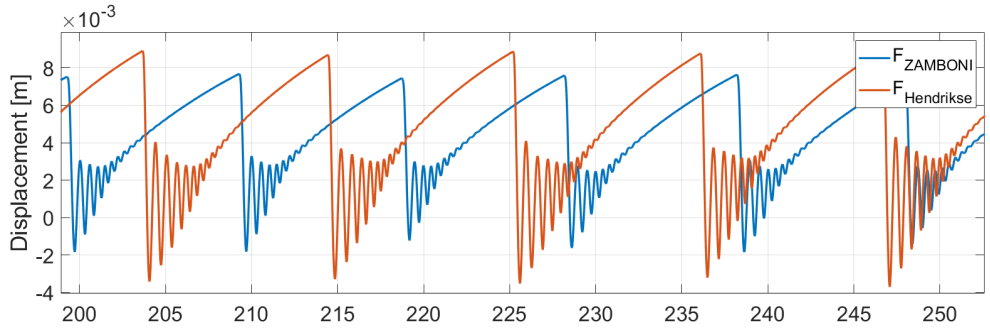

(b) Displacements

Figure 4.8: Time series of an intermittent crushing event at an ice indentation speed of 3 [mm/s] for both the Hendrikse (2017) model and ZAMBONI

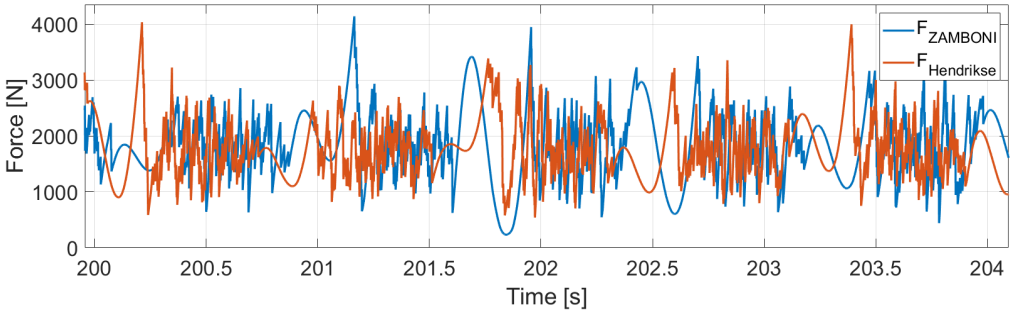

(a) Forces

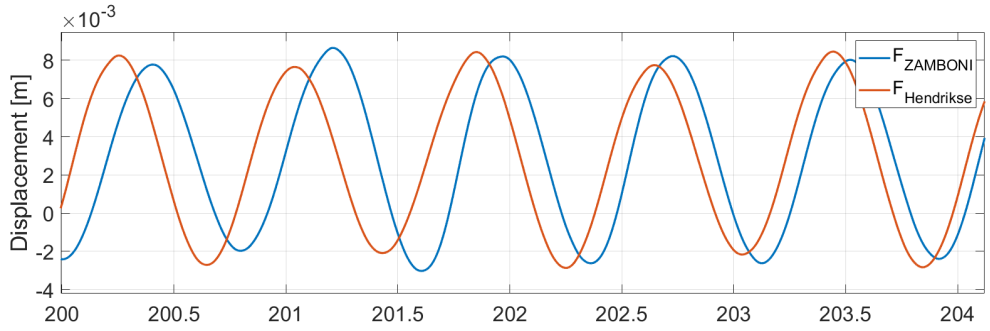

(b) Displacements

Figure 4.9: Time series of a frequency lock-in event at an ice indentation speed of 40 [mm/s] for both the Hendrikse (2017) model and ZAMBONI

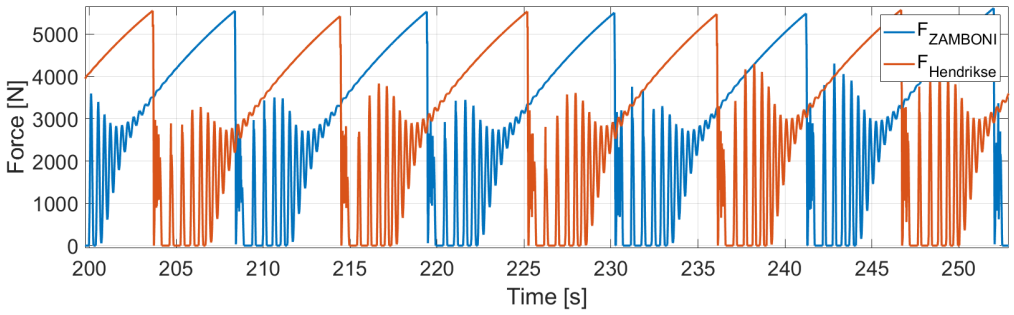

(a) Forces

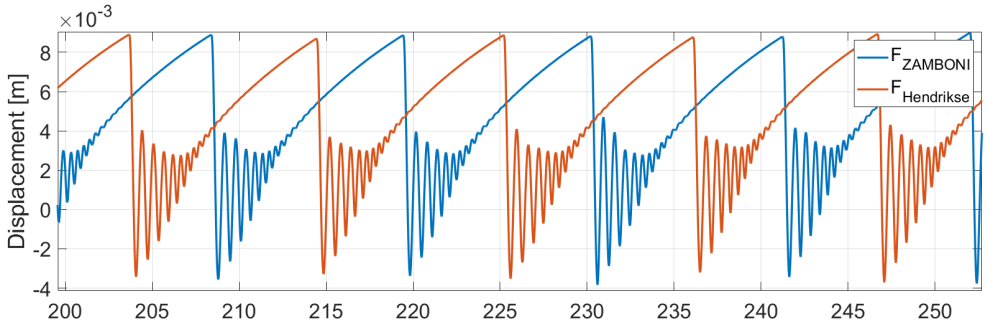

(b) Displacements

Figure 4.10: Time series of an intermittent crushing event at an ice indentation speed of 3 [mm/s] for both the Hendrikse (2017) model and ZAMBONI, in ZAMBONI a rectangular structure is applied rather than a cylindrical structure

4.3. Discussion of verification results

In Figure 4.1 to Figure 4.7, the results of the verification procedure are presented statistically for different ice indentation speeds. In these figures, between ice indentation speeds of 0.1 [mm/s] and 1 [mm/s], creep occurs. Note that creep is not an ice-structure interaction phenomenon but rather is an ice action phenomena. Therefore, the loads during creep are static. Statistically, this results in zero standard deviation and mean, maximum and minimum values that overlap. Then, from indentation speeds of 1 [mm/s] to approximately 20 [mm/s] intermittent crushing occurs. This regime is characterised by high global maximum loads and large negative structural velocities during the aggressive snap back of the structure. Thereafter, from ice indentation speeds of approximately 20 [mm/s] to 100/130 [mm/s], frequency lock-in occurs. Notice that the ice indentation speed termination of the frequency lock-in regime differs for both models, which will be further discussed in Subsection 4.3.3. This regime is recognisable by its high structural displacements and velocities and high standard deviations which are well observable in Figure 4.2 and Figure 4.3. Also, during frequency lock-in, the dominant structural frequency lies in the proximity of the structure's natural frequency, as shown in Figure 4.6. Additionally, the β-value as described in Chapter 2 and shown for this verification procedure in Figure 4.7 lies between 1.0 and 1.5 [-]. Finally, for ice indentation speeds higher than 100/130 [mm/s], continuous brittle crushing starts to occur. This regime is recognisable by low global ice forces, low standard deviations of these ice forces and small structural displacements and velocities, especially compared to the frequency lock-in regime.

As a first general observation, the statistical representations of forces, displacements and structural velocities of both models are similar. Nevertheless, several remarkable deviations and results are observable. Many of these deviations and results are not stand-alone findings but rather are causally related to another top-level finding. Therefore, the remarkable deviations and results are compactly listed below, where causally related observations are listed on a sub-level.

1. Forces in the creep and intermittent crushing regime are larger for the Hendrikse (2017) model than for ZAMBONI
    (a) The resulting structural velocities and displacements during creep and intermittent crushing in the Hendrikse (2017) model are greater than those in ZAMBONI
    (b) The in-line structural frequencies during intermittent crushing are larger for ZAMBONI.
    (c) The β-values during intermittent crushing are larger for the Hendrikse (2017) model.
2. Within the frequency lock-in regime, no significant differences in structural velocities, structural displacements, structural frequencies or β-values are observed, despite the higher maximum forces for the Hendrikse (2017) model
3. The frequency lock-in terminates at higher ice indentation speeds for ZAMBONI than for the Hendrikse (2017) model
    (a) Locally, from ice indentation speeds of 100 [mm/s] to 130 [mm/s] higher structural responses are observed for ZAMBONI than for the Hendrikse (2017)

The causalities listed above are concisely argued here. First of all, the fact that the Hendrikse (2017) model predicts slightly higher global ice loads during creep and intermittent crushing results directly in three secondary observations. When considering the typical saw-tooth pattern of an intermittent crushing load time-series, it stands to reason that a higher global load during the loading phase of intermittent crushing results in larger maximum displacements. This reasoning also holds for creep as a creep load is essentially an infinitely ongoing loading phase of intermittent crushing. Next, the in-line structural frequency is causally related to the maximum global ice force during intermittent crushing through the time taken for a single loading phase. If a during a loading cycle, the structure is displaced further, the relative indentation of ice into the structure becomes smaller. Therefore, for further displaced structure ice can indent further, resulting in a larger in-line structural frequency. The β-values are related to the maximum global load during intermittent crushing as for a higher global load, a higher maximum structural displacement is reached, which in turn results in a more aggressive snap back response of the structure. Since the β-values of a structure are linearly dependent on the maximum structural velocity, these β-values are then also dependent on the maximum structural force during intermittent crushing. Finally, the causal relation of larger local structural responses due to different observed phenomena is also somewhat straightforward. For the particular larger structural responses in ZAMBONI mentioned above, the Hendrikse (2017) model already has fully transitioned into continuous brittle crushing whereas ZAMBONI still simulates frequency lock-in. Still, with the causal relations explained, the top-level observations themselves have not been discussed. Therefore, the three aforementioned top-level observations between simulations conducted with the Hendrikse (2017) model and ZAMBONI are discussed individually hereafter.

4.3.1. The Hendrikse (2017) model simulates larger global maximum forces than ZAMBONI

Perhaps the clearest observable top-level deviation between the Hendrikse (2017) model and ZAMBONI is the higher observed maximum global force in the Hendrikse (2017) model. This difference appears to be caused entirely by the cylindrical shape applied in ZAMBONI. Since the Hendrikse (2017) model is one-dimensional, it cannot integrate different structural waterline shapes in its ice-structure mechanics. Instead, the ice parameters are preferably derived from rigid structure tests on the desired structural waterline shape according to the method presented in Section 2.2. Thus,

although a particular set of parameters correspond to a structural shape, the structural shape is not modelled itself, and the local ice-structure mechanics are thus similar to those of a straight ice-structure interface. On the contrary, in ZAMBONI, the local angle of attack of the indenting ice is of crucial importance, as thoroughly explained in Chapter 3. These local angles of attack inevitably lead to lower global maximum forces than a straight ice-structure interface. This local effect is best explained by evaluating the maximum global load case at the transition from creep to intermittent crushing. This transition is observable at an ice indentation speed of 1 [mm/s] in Figure 4.1. The high global force reached at this transition follows from the sum of high local forces in each ice element. In turn, these individual elements all exert the largest forces on the structure for a particular local ice-indentation speed. For a straight ice-structure interface, these local ice-indentation speeds are all equal to the far-field ice velocity. Therefore, a high peak load is achievable when all ice elements indent at local ice-indentation speeds corresponding to the largest global loads. However, for a cylindrical structure, such a uniform local ice indentation speed is unachievable, where only at the centre of the structure, local ice indentation speeds equal the far-field ice velocity. Towards the side of the structure, the local ice indentation speeds grow lower as the local angles of attack increase. As a result, locally, all ice elements except those located near the centre of the structure will indent at lower ice indentation speeds causing sub-maximum local ice loads in each ice element. Therefore, cylindrical structures always experience a lower maximum global load than rectangular structures when the cylindrical structure's diameter equals the rectangular structure's width.

Interestingly, Korzhavin (1962) already empirically concluded that the maximum global ice load experienced by a cylindrical structure during crushing is roughly 90 % of the maximum global ice load on a rectangular structure where the cylinder's diameter equals the rectangular width, according to the shape factor he introduced. When observing the maximum loads in Figure 4.4, this load ratio indeed appears close to 0.9 [-] for creep and intermediate crushing. Nevertheless, during frequency lock-in and continuous brittle crushing, the Korzhavin (1962) relation does not hold, indicating an ice-indentation speed-dependent load factor. The implications of a speed-dependent load factor are further discussed in Section 4.4.

Thus, the lower global ice loads simulated by ZAMBONI compared to those computed by the Hendrikse (2017) model are both theoretically expected and in line with empirical observations as far back as to the 1960s. However, in order to ascertain whether this deviation is indeed solely due to the cause above, the two models are compared with a rectangular structure as well. As described in Chapter 3, currently, ZAMBONI assumes a cylindrical structure by default. However, a simulation can be performed on a quasi rectangular structure be applying an infinitely large diameter and manually setting the ice field according to the intended rectangular width. That way, locally, a quasi-straight interface will be encountered by each ice element. The resulting forces and displacements for this simulation are plotted jointly with time series of the Hendrikse (2017) model in Figures 4.10a and 4.10b. Indeed, the maximum global loads reached in these simulations are equal. Putting it more strongly, when qualitatively assessing both figures, the simulations appear to be near-identical. On the contrary, in Figures 4.8a and 4.8b, the same simulation is performed but for a cylindrical structure, which clearly illustrates the differences between both shapes.

4.3.2. During frequency lock-in, the structural responses of both models are identical, despite being caused by different global loads

The second remarkable finding of this verification procedure is not a deviation between both models, but instead concerns the near-similar structural response during frequency lock-in. This near-similar structural response is remarkable because the forces governing this structural response are not exactly similar, as observable in Figure 4.1. Perhaps, these similar structural responses can be declared through a review of what exactly constitutes a frequency lock-in ice-structure interaction.

From Section 2.1, during frequency lock-in, a structure vibrates at a frequency close to one of its natural frequencies. Since an SDOF structure is concerned here, during frequency lock-in, the structure must vibrate at one particular frequency. Additionally, during frequency lock-in, the Toyama et al. (1983) relation of Equation 2.2 applies. Therefore, the maximum structural velocity of any structure during a frequency lock-in event must lie between a β-factor of 1 [-] and 1.5 [-] times the ice indentation speed. Thus, both the vibration frequency and peak structural velocity are not governed by loads exerted on the structure as long as that structure is in frequency lock-in. Then, with a fixed frequency and peak structural velocity, the entire velocity time series of a structure can be predicted, which in turn governs the entire structural response. In other words, once in frequency-lock in, the response of an SDOF structure can be entirely described from a structure's natural frequency and the ice indentation speed. Consequently, since both of these are equal for the Hendrikse (2017) model and ZAMBONI, it stands to reason that the structural response simulated by both models must be similar within the frequency lock-in regime, despite the newly introduced fundamental principles of ZAMBONI. This near-similar structural response is underlined in Figure 4.5, where during frequency lock-in, the ratios between structural displacement simulated in the Hendrikse (2017) model and ZAMBONI are equal to 1 [-] in contrast to the global in-line force ratios which range from 0.9 [-] to 1 [-].

4.3.3. The frequency lock-in regime is terminated at higher ice indentation speeds for ZAMBONI than for the Hendrikse (2017) model

Although the response within the frequency lock-in regime is similar for the Hendrikse (2017) model and ZAMBONI, the ice indentation regime during which frequency lock-in occurs does not have the same boundaries. In fact, when examining Figure 4.7, the lock-in regime appears to last to higher ice indentation speeds for ZAMBONI. This is an important finding since especially at the the transition from frequency lock-in to continuous brittle crushing, the most dynamic structural behaviour occurs, as is shown by the high minimums, maximums and standard deviation of the structural displacement and velocity in that range in Figures 4.2 and 4.3. Indeed, from Figure 4.7 the highest ice indentation speed for which frequency lock-in is observed in the Hendrikse (2017) model is 100 [mm/s] whereas for ZAMBONI, frequency lock-in is observed up to indentations speeds of 130 [mm/s]. This deviation leads to differences in the maximum observed structural vibrational amplitude of over 8 [mm], or 30%.

At first glance, the fact that for ZAMBONI, frequency lock-in occurs up to higher ice indentation speeds is somewhat counterintuitive. As implied in Subsection 4.3.2, the higher maximum loads of the Hendrikse (2017) model might not influence the structural response during frequency lock-in but are hypothesised to influence the ice indentation region for which frequency lock-in occurs. Indeed, when referring to the well-established frequency lock-in prediction equation of Equation 2.1, larger global ice loads (which manifest in Equation 2.1 through the ice thickness) make the occurrence of frequency lock-in more likely. Still, one explanation for this counterintuitive result exists, which once again lies in the difference of structural shape between the two models. As thoroughly argued in Subsection 3.1.2 and Subsection 4.3.1, the zero-friction principle causes local ice indentation speeds at all points along the structure's edge to be smaller than the far-field ice velocity, except for the unique point where the orthogonal line lies parallel to the far-field ice velocity. Therefore, locally, a cylindrical structure will encounter lower ice-indentation speeds than a rectangular structure. From that perspective, it is rather sensible that for cylindrical structures, frequency lock-in occurs up to higher far-field ice velocities. Due to the complexity of the frequency lock-in regime, it is more difficult to comment on the observed difference of this transition speed. Still, a crude attempt is made here. The observed difference is an estimated 30 %. Nevertheless, based on the simulation resolution at these indentation speeds, it can differ from 20 % to as much as 40 %. An-

alytically, for any fluid indenting into a cylindrical structure, the mean local indentation speed is $\frac{2}{\pi}$ times the far-field indentation speed, or roughly 64 %. If this ratio would be entirely indicative of the velocity up to which frequency lock-in occurs, the observed difference should be as high as 50 %. However, the ice elements interacting at a locally flatter ice-structure interface are likely to be dominant over those interacting at a locally steeper ice structure interface. Raising the effective mean ice indentation speed and lowering the expected difference in transition speeds. Finally, the possibility has to be considered that the hypothesised effect of larger maximum global loads for the Hendrikse (2017) does occur but is overshadowed by the counteracting effect of lower local ice indentation speeds. Further analysing the exact relation of structural shapes and transitions speeds from lock-in to continuous brittle crushing is a complex topic, and will not be attempted to solve here. Instead, the simulated differences are accepted as possibly explainable by the aforementioned local ice indentation speed theory.

4.4. Recommendations towards further verification

Generally, the verification procedure described in this chapter is considered successful. During all ice-structure interaction regimes as well as during the static creep regime, the in-line ice load and structural response either resemble that of the one-dimensional Hendrikse (2017) model or deviates as should be expected for a two-dimensional model. Still, when pursuing further verification, three areas can potentially be interesting. First of all, the verification procedure described in this chapter concerns one specific structure responding to a specific indenting ice floe. Therefore, a sounder verification can be achieved by adding simulations for different combinations of ice and structure parameters. Second of all, this verification procedure has not attempted to verify the cross-drift ice loads and structural responses, as no suitable model exists to compare simulations. Nevertheless, it might be valuable to evaluate the cross-drift forces and structural response qualitatively. Third of all, this verification procedure compared a rectangular structure in the Hendrikse (2017) model with a cylindrical structure in ZAMBONI. It would be valuable to compare two cylindrical structures. However, in order to do this, one would require two different sets of ice parameters, one from an ice indentation test into a rigid cylindrical structure (for the Hendrikse (2017) model) and the others from an ice indentation test into a rigid rectangular structure (for ZAMBONI). Additionally, these indentation tests must be performed with the same ice floes in order to arrive at compatible ice parameters for both cases.

Although the verification is considered successful, it also triggers some new unanswered questions. First of all, the simulated shape effect on global ice loads appears to be dependent on ice-indentation speed, which can cause significant deviations between one- and two-dimensional ice models. In Subsection 4.3.1, the shape effect has been discussed, since it fully accounts for the maximum global load discrepancy between the Hendrikse (2017) model and ZAMBONI. However, a closer evaluation of the load ratios of Figure 4.4 leads to the observation that the Korzhavin (1962) shape factor of 0.9 [-] indeed applies for the static creep regime, but does not apply for the dynamic intermittent crushing and frequency-lock in regimes. More precisely, during intermittent crushing, the shape factor appears to drop below 0.9 [-] whereas, during frequency lock-in, the shape factor appears to approach 1.0. A possible and preliminary conclusion derived from this non-constant shape factor is that the certified one-dimensional ice-structure interaction models such as the Hendrikse (2017) model underestimate the forces exerted on a cylindrical structure by up to 10 %. Naturally, this conclusion can also be drawn reversely such that possibly ZAMBONI overestimates the forces exerted on a cylindrical structure. It is not attempted here to resolve this unanswered question. However, due to the importance of frequency lock-in within the field of ice engineering, it is recommended to conduct further research in this area. Still, even if this conclusion holds, it is not expected to have a large effect on the structural response, as the global ice loads do not govern the

structural response during frequency lock-in, as argued in Subsection 4.3.2. However, the ice indentation speed range during which frequency lock-in is expected to occur is likely to be affected by underestimated global loads, as suggested in Subsection 4.3.3.

Finally, the second raised question by this verification procedure concerns the shape effect on ice-structure interaction regime transition speeds. An initial hypothesised theory for this shape effect has been suggested in Subsection 4.3.3. In order to further analyse this shape effect and transitions speeds, a recommended first step is to perform additional simulations, for Hendrikse (2017) model between ice indentation speeds of 100 [mm/s] and 110 [mm/s] model and for ZAMBONI between 130 [mm/s] and 140 [mm/s], that way the difference between the regime transition speeds for a rectangular and cylindrical structure can be estimated more precisely

5

Validation of ZAMBONI

The main gap of the verification procedure described in the previous chapter is a discussion of the simulated forces and displacements in the cross-drift direction. Due to the non-existence of 2D ice-structure interaction models in the scientific realm, this gap is inevitable. Yet, achieving confirmation of the correctness of the cross-drift direction results remains vital to a model which eminently concerns the cross-drift direction. Therefore, the goals of this validation procedure are as follows:

- Validate the order-of-magnitude of the simulated cross-drift forces
- Identify and comment on differences between the simulation and test data
- Suggest an approach for further validation where appropriate

In an attempt to satisfy these goals, this chapter first describes the test data available and used for validation. Next, a validation strategy is described corresponding to the (limited) possibilities of said data. After that, the results of the validation study are presented and discussed. Finally, a proposal for a more extensive validation campaign is given.

5.1. Description of the ice test used for validation

Historically, a lack of available data has been one of the factors stalling innovation in the field of ice-structure interaction, as argued in the first phase of this thesis (Koreman, 2019). Inconveniently, this issue is not easily resolved due to the high costs associated with ice testing. Nevertheless, several joint ice test campaigns have been launched to overcome this lack of data. For this validation, the test results of the IVOS test campaign have been used. IVOS comprises 51 test runs, which are concisely documented in the IVOS final report (HSVA, 2020). In order to achieve the validation goals listed in this chapter's introduction, a given data set should fulfil the following requirements:

- The structure tested must be a (quasi-)SDOF structure to compare it to ZAMBONI
- The experiment must be documented in sufficient detail to repeat it when desired
- Ice failure must occur primarily in crushing
- Measurements must be available in both the in-line and cross-drift direction.

First of all, it should be noted that data sets fulfilling all requirements above are scarce, especially regarding the measurements in the cross-drift direction. This cross-drift data scarcity also holds for the IVOS test campaign, where insight in the cross-drift direction was not amongst the considered primary goals (HSVA, 2020). Nevertheless, ice force in the cross-drift direction was measured in several of the test runs. Of these, test run 21010 is considered most suitable for validation purposes because of its extensive documentation (HSVA, 2020), the visually observed crushing and the apparent presence of all three ice structure interaction regimes. The relevant test characteristics of test run 21010 are summarised in Table 5.1. The first critical remark when observing Table 5.1 are the unknown structural damping ratio and uniaxial compressive strength of ice. Although these missing inputs are inconvenient, it is possible to work around them, as is further discussed in Section 5.2. Still, estimating them introduces inaccuracy in the simulations to be performed. An overview of the different measurements taken during test run 21010 and used in this validation are given in Table 5.2, where the $K_{2,ref}$, $C_{1,ref}$ and $C_{2,ref}$ values are in turn based on $K_{1,ref}$.

Test characteristic	Symbol	Unit	Value
Structure shape	-	[-]	Cylindrical
Structure diameter/width	D	[m]	0.2
Structure natural frequency	f_n	[Hz]	3.4
Structural stiffness	k_s	[kN/m]	798
Structural damping ratio	ζ_s	[-]	**?**
Uni-axial ice strength	σ	[kPa]	**?**
Ice thickness	h	[m]	0.023

Table 5.1: Structural and ice characteristics of IVOS test run 21010 according to [TIMO STANGE and IVOS PROJECT REPORT]

Measurement	Symbol	Unit
In-line force	F_x	[N]
Cross-drift force	F_y	[N]
In-line structural deflection	d_x	[mm]
Carriage indentation	d_{ice}	[m]
Carriage indentation speed	v_{ice}	[m/s]
Time	t	[s]

Table 5.2: Measurement taken throughout IVOS test run 21010 and used in this report

Figure 5.1a shows the carriage indentation speed - or ice indentation speed - during the full test run. As one can observe, the ice indentation speed is steadily increased from roughly 6 [mm/s] to 150 [mm/s]. Figure 5.1b is a close up of Figure 5.1a. This close up shows that the ice indentation speed is increased in increments of roughly 10 [s] to 15 [s] each. However, during these intended constant indentation speed increments, the measured carriage indentation speed still fluctuates in a range of 8 [mm/s]. It is unclear whether these fluctuations are caused by inaccurate measurements or by actual fluctuations in the carriage indentation speed. The latter of which seems somewhat more likely as the recording sensitivity is 1 [mm/s]. Either way, these fluctuations introduce additional uncertainty in this validation procedure.

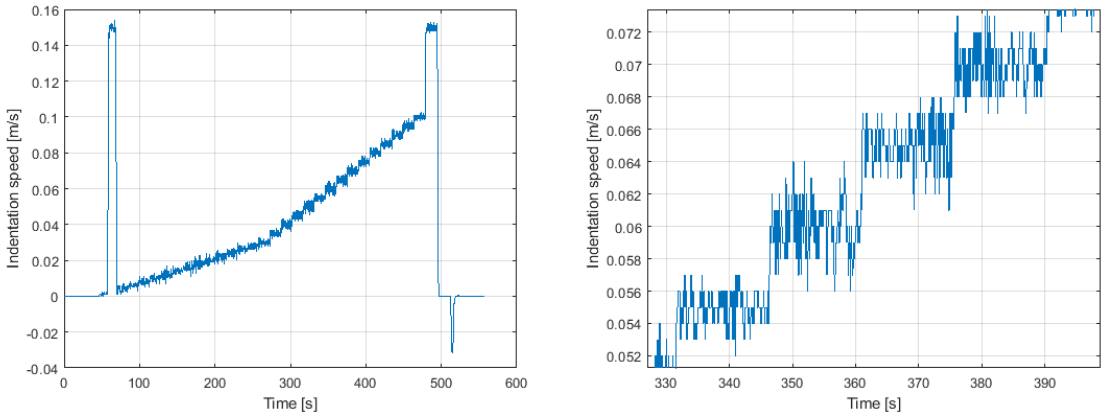

(a) Full test run

(b) Close up

Figure 5.1: Ice velocity profile of test run 21010 of the IVOS phase 1 test cycle

Finally, in discussing test run 21010 of the IVOS tests, it should be noted that all three interaction regimes are claimed to be present by HSVA (2020). As discussed in Section 2.1, the transition between these regimes is best identified by looking at the dominant structural frequency and the ratio of maximum structural velocity and ice indentation speed. Applying these rules of thumb for regime separation here shows that indeed, all three ice-structure interaction regimes appear to be present. To demonstrate that intermittent crushing and frequency lock-in both occur, Figure 5.2 and Figure 5.3 show the typical force and displacement time series during intermittent crushing and frequency lock-in, respectively.

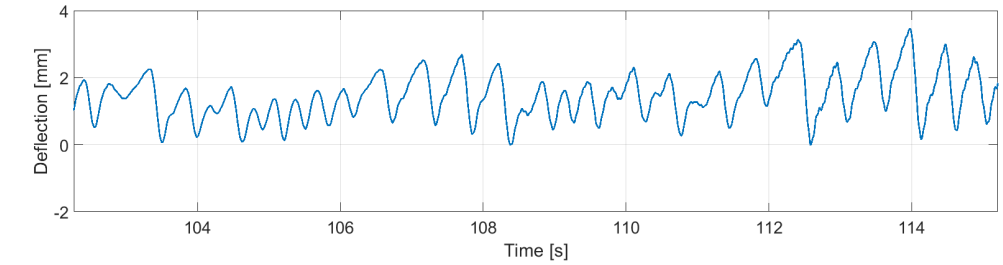

(a) Characteristic saw-tooth profile of the structural deflection during intermittent crushing

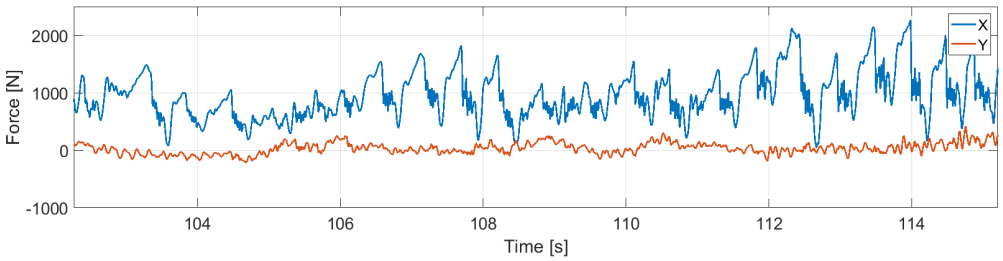

(b) Forces during intermittent crushing

Figure 5.2: Measured structural deflection and forces during IVOS test run 21010 at an ice indentation speed of 8 [mm/s]

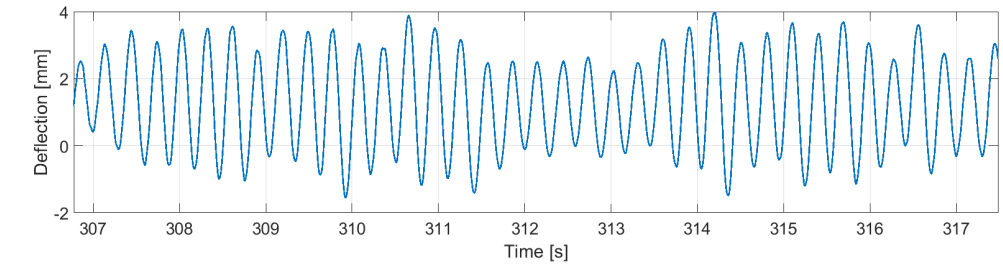

(a) Characteristic heavy harmonic vibrations of structural deflection during frequency lock-in

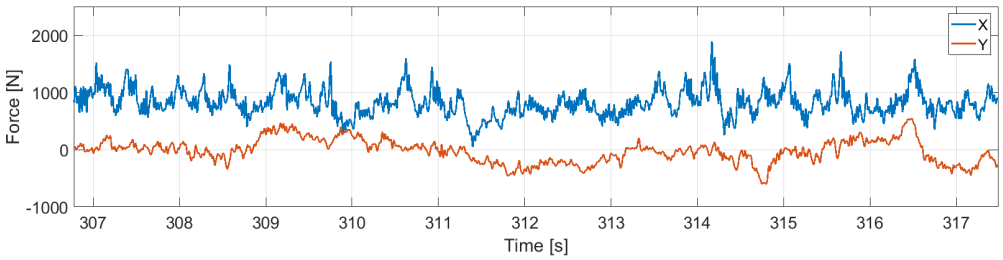

(b) Forces during frequency lock-in

Figure 5.3: Measured structural deflection and forces during IVOS test run 21010 at an ice indentation speed of 45 [mm/s]

5.2. Validation method

With the validation goals outlined and the experimental measurement data of IVOS test run 21010 discussed, the validation method can be discussed. In order to perform even a simple order of magnitude validation, the following steps have to be taken:

1. Recognise the different ice indentation speed increments during test run 21010 such that validation can be performed at different ice indentation speeds, similarly to the model verification of Chapter 4
2. Apply a reasonable value for the unknown structural damping of Table 5.1 as input during simulations
3. Apply a reasonable value for the unknown uni-axial compressive strength of Table 5.1 to use as input for estimating the ice parameters.
4. Estimate ice input parameters (K_1,K_2,C_1,C_2,δ_f,r_{max},N) based on the ice and structure knowledge as summarised in Table 5.1

As mentioned in Section 5.1, the carriage indentation speed appears to be increased in increments of roughly 10 [s] to 15 [s], albeit with significant fluctuations of up to 8 [mm/s] within these individual increments. In order to better identify these indentation speed increments, a 5 [s] trailing moving mean of the carriage indentation speed is evaluated. Then, a constant velocity increment is identified as the period where the 5 [s] trailing moving mean of the carriage indentation speed fluctuates no more than 0.5 [mm/s]. In this way, 28 different ice indentation speed increments are identified. They are shown in Figure 5.4a. Furthermore, Figure 5.4b shows a close up of the 5 [s] trailing moving mean to give additional insight into how the different ice indentation increments are identified.

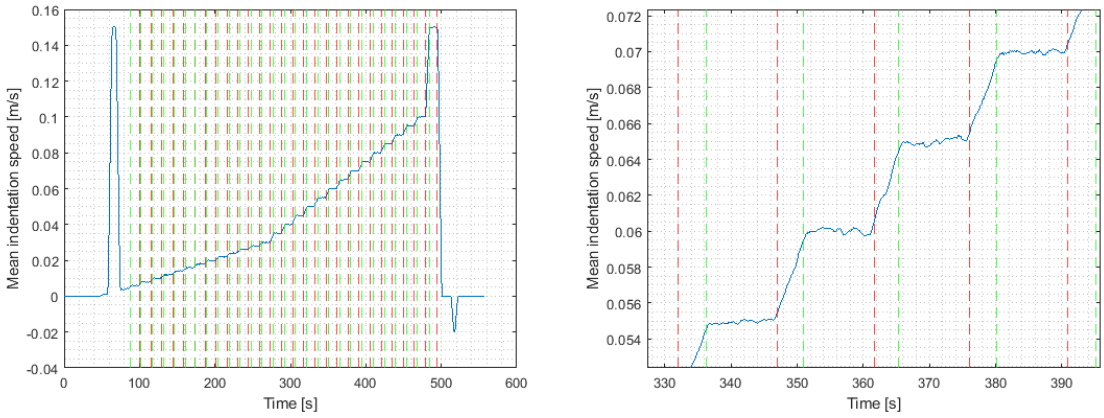

(a) Full test run with all 28 velocity regimes

(b) Close up

Figure 5.4: Trailing moving mean of the ice indentation velocity of test run 21010 of the IVOS phase 1 test cycle - green and red dashed lines represent the start and end of an identified constant velocity regime

Since the structural damping during IVOS test run 21010 is not documented, it has to be estimated. The most straightforward way to determine the damping ratio is through a decay test. Conveniently, at the end of test run 21010, the carriage is stopped whilst structural deflection continues to be measured. These measurements suffice to estimate the damping ratio through the empirical decay test of Equation 5.1. In Equation 5.1, A_{t1} and A_{t2} are the amplitudes of structural deflection at two distinct points in time, τ is the duration between these two points and f_d is the damped frequency of the structure, which is approximately equal to the natural frequency of the structure for small damping ratios. Through Equation 5.1, the damping ratio is found to equal approximately 0.0053 [-].

$$\zeta = \frac{\ln\left(A_{t1}/A_{t2}\right)}{\sqrt{\left(2\pi f_d \tau\right)^2 + \ln\left(A_{t1}/A_{t2}\right)^2}} \approx 5.3 \cdot 10^{-3} \tag{5.1}$$

Determining the uniaxial compressive strength of the ice used during IVOS test run 21010 is somewhat less straightforward. Still, this is a crucial driver when estimating the different ice parameters. Since the uniaxial compressive strength was not measured or documented for test run 21010, the only possibility to estimate the uniaxial compressive strength is by choosing it such that it best fits the in-line force measurements. Therefore, 28 simulations are performed at all 28 ice indentation speed increments with an initially guessed ice uniaxial compressive strength of 75 [kPa]. Then, the simulated in-line ice loads are compared to the measured in-line ice loads through the ratio of their means and maxima, which are shown in Figure 5.5. Since the uniaxial compressive strength of ice statically follows from the global ice force and the ice deformation, it is best scaled with measurements during which the least interaction takes place. In line with the theory summarised in Section 2.1, the least interaction occurs during continuous brittle crushing, which in this case occurs most purely at the highest indentation speed of 0.15 [m/s]. By applying this method, it is found that the uniaxial compressive strength was initially underestimated by a factor of roughly 1.75 [-]. Multiplying this factor with the initially guessed uni-axial compressive strength of 75 [kPa] yields an estimated uni-axial compressive strength of roughly 131 [kPa], as will be applied in this validation procedure. Note that generally, such a method for determining the uniaxial compressive strength is disadvised, as it may lead to a self-fulfilling validation as one of the simulation inputs is derived from the statistical data with which the simulation is supposed to be validated. However, for this validation, this problem should not arise as the uniaxial compressive strength is derived solely from

quasi-static measurements during continuous brittle crushing. In contrast, the validation is aimed at the dynamic ice-structure interaction regimes of intermittent crushing and frequency lock-in. This difference is underlined by the high diversity in the ratio of measured global in-line forces and simulated global in-line forces for the initially assumed uniaxial compressive strength of 75 [kPa] shown in Figure 5.5.

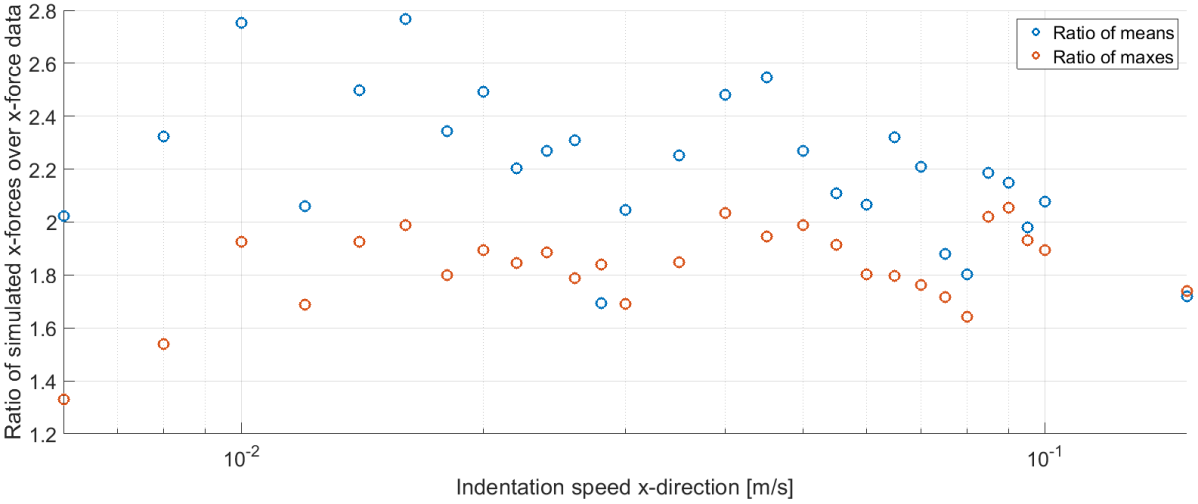

Figure 5.5: Ratios of means and maximums of the in-line force measurement and in-line force simulations with an initially guessed uni-axial compressive strength of ice of 75 [kPa]

With the structural width and shape, the ice thickness and the uniaxial compressive strength of ice known or estimated, the scaling method of Hendrikse et al. (2018) can be applied to find the necessary structural input parameters K_1, K_2, C_1, C_2, δ_f, r_{max} and R for ZAMBONI as described in Chapter 3. Since this scaling method is extensively discussed in Hendrikse (2017) and applied during validation in Hendrikse et al. (2018), it will not be further discussed here. Instead, the method is presented in Equation 5.2a to Equation 5.2g. Note that the shape and scale factor as used in Hendrikse et al. (2018) has been omitted from Equation 5.2a to Equation 5.2g. As argued in Chapter 3, through the very essence of ZAMBONI, the shape does not have to be accounted for. Finally, the reference values and the resulting ice parameters are listed jointly in Table 5.3.

$$K_1 = \frac{\sigma}{\sigma_{ref}} \frac{h}{h_{ref}} K_{1,ref} \tag{5.2a}$$

$$K_2 = \frac{\sigma}{\sigma_{ref}} \frac{h}{h_{ref}} K_{2,ref} \tag{5.2b}$$

$$C_1 = \frac{\sigma}{\sigma_{ref}} \frac{h}{h_{ref}} C_{1,ref} \tag{5.2c}$$

$$C_2 = \frac{\sigma}{\sigma_{ref}} \frac{h}{h_{ref}} C_{2,ref} \tag{5.2d}$$

$$N = N_{ref} \frac{D}{D_{ref}} \tag{5.2e}$$

$$\delta_f = \delta_{f,ref} \tag{5.2f}$$

$$r_{max} = r_{max,ref} \tag{5.2g}$$

Reference Parameter	Value	Resulting ZAMBONI ice parameter	Value	Unit
$K_{1,ref}$	5372	K_1	3113	[N/m]
$K_{2,ref}$	50910	K_2	29498	[N/m]
$C_{1,ref}$	17021	C_1	9862	[Ns/m]
$C_{2,ref}$	$1.05 \cdot 10^9$	C_2	$6.08 \cdot 10^8$	[N^3s/m]
$\delta_{f,ref}$	0.002	δ_f	0.002	[m]
$r_{max,ref}$	0.0029	r_{max}	0.0029	[m]
N_{ref}	39			[-]
D_{ref}	0.2			[m]
σ_{ref}	$100 \cdot 10^3$			[Pa]
h_{ref}	0.052			[m]
		R	0.0051	[m]

Table 5.3: List of reference values applied in Equation 5.2a to Equation 5.2g and their resulting model input parameters

Although the method above allows for a validation to be performed, it is not a sound validation procedure and any conclusions derived from both those results confirming, and those results arguing the validity of ZAMBONI must be taken with caution. Indeed, more reasons exist to distrust this validation procedure than to trust it, especially when it comes to detailed observations. To further underline this, below, a point-by-point summation is given of the different factors introducing uncertainty in this validation procedure.

- The damping ratio of the structure is derived from a decay test with a small offset in the neutral position. Therefore, the small perturbation on the structure might lead to an inaccurate damping ratio estimation
- Scaling of ice parameters is known to be theoretically incorrect and only usable for values close to the reference point (Hendrikse et al., 2018)
- The uniaxial compressive strength of ice is unknown and chosen best to fit in-line load data during continuous brittle crushing, thus erasing any issues with the global ice load simulated by ZAMBONI during that ice-structure interaction regime.
- The duration of each constant ice indentation velocity interval is approximately 10 [s] only, leading to the following uncertainties:
  - The steady-state cannot be identified, nor can it be guaranteed that a steady-state is reached at the end of each measurement
  - At low indentation speeds, only several load cycles will occur within an increment, limiting the accuracy of the statistical representation of time series at those indentation speeds
- Although according to visual observations, ice failed in crushing. It cannot be guaranteed that pure crushing occurred at all times. Additionally, HSVA (2020), states that during these measurements at least once, flexural failure was observed.
- Measurements show that during each increment, carriage indentation speed fluctuates up to as much as 8 [mm/s]

5.3. Validation results

Thus, simulations in ZAMBONI can be performed mimicking the data of IVOS test run 21010. First, the in-line IVOS data are compared to the ZAMBONI simulations. To that end, in Figures 5.6 and 5.7, the statistical in-line ice forces and structural displacements are presented for each ice speed increment respectively. First of all, the mean global in-line ice loads appear to be simulated consistent with the measurements, as in Figure 5.6, the simulated mean global loads are close to the measured mean global loads with outliers both above and below the mean global load simulations. On the contrary, the simulated standard deviation of these global loads appears to be smaller for ZAMBONI than the global loads measured and proportionally, the maximum global loads simulated by ZAMBONI are smaller than those measured. This difference can be caused both by inaccuracies in ZAMBONI and by inaccuracies in the validation method. From this validation alone, it is impossible to conclude whether the underestimated standard deviation of the global load in ZAMBONI is due to a modelling error. However, such an underestimation was not noted in the verification of Chapter 4. In turn, the Hendrikse (2017) model did not note any underestimation of load standard deviations during its validation procedure (Hendrikse et al., 2018). Therefore, it is concluded that most likely, this underestimation is caused by some inaccuracy in the validation method.

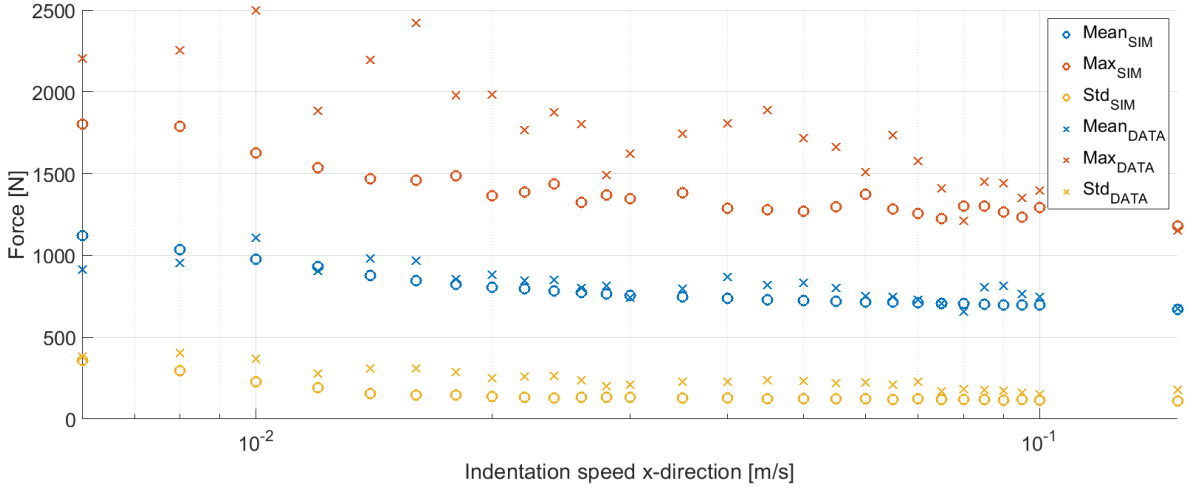

Figure 5.6: In-line force

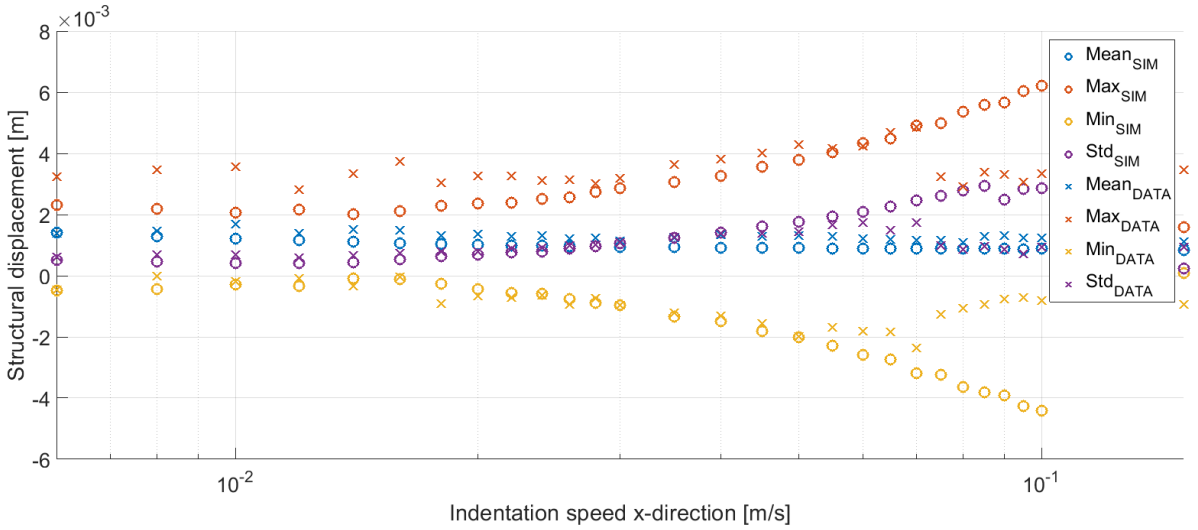

Figure 5.7: In-line displacement

Next, when evaluating the in-line structural displacements of Figure 5.7 again, the simulated displacements appear to be close to the measured displacements. Those differences that do manifest are primarily related to the aforementioned underestimated standard deviation of in-line forces. Still, one observable difference between the simulated in-line displacements and the measured in-line displacements cannot be derived from the underestimated force standard deviation. This difference is the frequency lock-in regime which lasts to much higher indentation speeds for ZAMBONI than for the measurements. In order to assess the importance of this apparent difference, it should be noted that each measurement point is derived from a short 'constant' speed increment lasting no longer than 15 [s]. However, as explained in Chapter 4, frequency lock-in takes some time to develop, especially for higher ice indentation speeds. Therefore, it is likely that the small measured structural displacements at ice indentation speeds that according to ZAMBONI should result in frequency lock-in are small simply because frequency lock-in has not developed yet and the ice-structure interaction is still transient. This explanation is likely since the minimum displacements at these ice-indentation speeds remain negative, whereas, for continuous brittle crushing, the minimum structural displacements are generally positive. Additionally, according to HSVA (2020), one of the observations of this test run is that frequency lock-in was terminated by flexural ice failure. Although it is unclear at what ice indentation speed this termination occurs precisely, it would limit the structural response, which would declare the early observed termination of the lock-in regime in Figure 5.7.

Finally, the cross-drift measurements are compared to ZAMBONI to validate ZAMBONI in the cross-drift direction. In contrast to the in-line direction, no measurements are taken of the cross-drift displacement. Therefore, this part of the validation can only be applied to the measured cross-drift forces. To that end, Figure 5.8 shows the measured and simulated cross-drift forces. The mean, maximum, and minimum measured cross-drift forces all closely resemble those simulated by ZAMBONI. For some simulations, these statistical values are slightly overestimated during a simulation, whereas for others, they are slightly underestimated, indicating limited bias in the simulated cross-drift ice loads. Still, similarly to the in-line loads, the standard deviation of the measured cross-drift ice loads is consistently higher than those of the simulated ice loads. Again, this can be caused by a wide array of causes, similar to those mentioned in Section 5.2. However, with certainty, it can be concluded that at least the order-of-magnitude of the simulated cross-drift ice loads is correct. Since the cross-drift response has not been verified with a validated model, this successful order-of-magnitude cross-drift force simulation is crucial to this report. Still, it remains only an order-of-

magnitude validation, and therefore, properly validating ZAMBONI remains a top-priority.

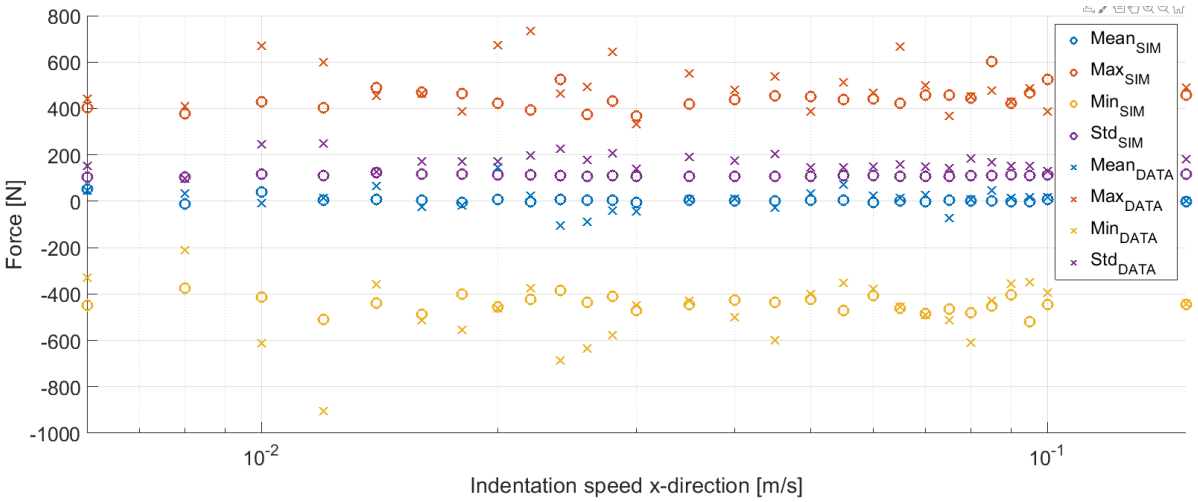

Figure 5.8: Cross-drift force

5.4. Proposition for a more extensive validation procedure

Thus, the order-of-magnitude of cross-drift forces simulated by ZAMBONI appears to be consistent with the measurement. However, no detailed validation can be performed based on these measurements and thus, ZAMBONI cannot be declared valid from these data alone. Furthermore, to the author's knowledge, no test data are readily available that could achieve further validation. Therefore, the logical conclusion is that a new model test must be performed. This section proposes several types of new model tests specifically for validating ZAMBONI. The following three areas are considered.

- Validation of ZAMBONI's fundamental principles, as discussed in Section 3.1
- Structural response validation of ZAMBONI - similar to the validation attempted in this chapter
- Validation of observed ice behaviour through forced structural vibrations

As argued in Chapter 3, ZAMBONI is merely a two-dimensional extension of the certified Hendrikse (2017). Therefore, a sensible starting point is to consider whether test set-ups can be designed that specifically validate one or more of the fundamental principles as discussed in Section 3.1. Of the five fundamental principles, especially the validity of the zero-friction principle is doubtful, as argued in Subsection 3.1.2. More precisely, the zero-friction principle is fundamentally incorrect, but the extent to which this deliberate simplification alters the simulated results is unknown and expected to be small. Therefore, it is desirable to design a test set-up which tests the zero-friction principle explicitly. Such a test set-up could include a simple sloped structure at different angles of attack, as shown in Figure 5.9, where each slope measures global ice loads independently. With this test set-up, the friction on each slope can be estimated, such that the friction errors introduced by the zero-friction principle can be quantified. From a design point of view, the difficulty of this test set-up is that the global ice forces on each of the five slopes have to measured independently. Also, the transition angle between slopes should be sufficiently small, such that no splitting or other undesired ice failure mode is triggered at the slope transitions.

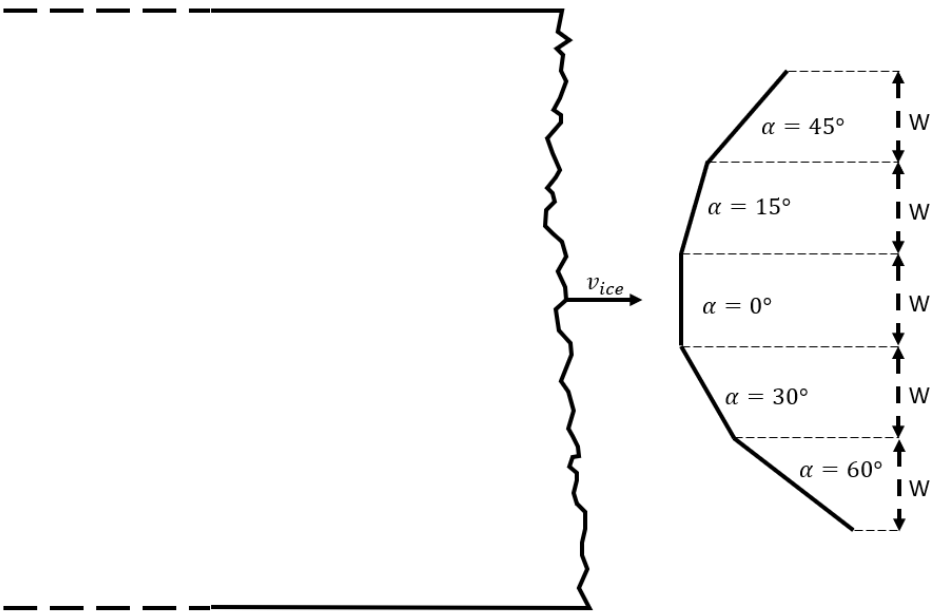

Figure 5.9: Proposal of test set-up to validate the zero-friction principle

Subsequently, a model scale validation campaign has to be performed, where for varying ice indentation speeds, model test data are compared to ZAMBONI's simulation results. This validation set-up is valuable since it allows to determine the ice parameters of an ice floe before testing, which serve as input for ZAMBONI. Ideally, this test campaign would consist of two stages. In the first stage, ice indentation tests should be performed at varying ice-indentation speeds, with an emphasis on ice-indentation speeds corresponding to intermittent crushing and frequency lock-in. Essentially, this stage resembles the validation procedure described in this chapter, with the distinction that during this validation campaign ice and structure parameters do not have to be estimated in hindsight, but can instead be measured prior to testing. Therefore, the deviations found in this proposed validation can be assessed in significantly more detail. In the second stage, test runs are proposed that correspond to the most critical load cases. Several of these critical load cases are discussed in Chapter 7, but they can also originate from design standards or knowledge in the industry. That way, ZAMBONI can be validated in additional detail where its results have to be most accurate. Naturally, some of these critical cases will also involve misaligned wind loads, which can be mimicked with a hardware-in-the-loop system or actuator.

The final advised validation procedure is to qualitatively assess ice behaviour when moving a structure through ice in a predefined manner. This validation procedure opens a wide array of validation possibilities as both the model test and ZAMBONI do not have to adhere by the natural movement of a structure through ice, allowing for explicit testing of simulable phenomena. Anticipatory of the to-be discussed coupled simulation results of Chapter 7, one of these cases is the expected decreased global ice loads during forced cross-drift vibrations due to ice crushing at the sides of the structure.

6

Coupling of a wind turbine to ZAMBONI

In order to perform simulations with ZAMBONI, it should be coupled to a wind turbine. To that end, Siemens Gamesa Renewable Energy has supplied a structural model in the modal domain that represents an offshore wind turbine in conditions like those at Kriegers Flak. Due to confidentiality reasons and since this model is not the creation of the author, the structural model will not be discussed in detail. Instead, Section 6.1 describes the theoretical background of structures in the modal domain, and how they can be coupled to ZAMBONI. After that, Section 6.2 describes the geometry of the turbine, as well as some of its relevant modes. Finally, in Section 6.3, the implementation of wind force and aerodynamic damping are discussed.

6.1. Theoretical background and implication of modal analysis

Applying a structural model in the modal domain is practical, as it ultimately results in a fixed number of linearly independent equations of motion - one for each mode of vibration - that need to be solved. It reaches this useful property by defining each displacement as a summation of numerous modes, which are all displaced to a certain extent in the modal domain according to Equation 6.1. In Equation 6.1, $\mathbf{x}$ are the structure's displacements in all DoFs $\underline{\hat{x}}_i$ is the eigenvector of mode shape i, and u_i is the modal displacement in mode shape i. Then the structural response in any DoF can be retrieved by applying Equation 6.1 with the $\hat{x}_i$ eigenvector value corresponding to the desired DoF. By applying the modal representation of the displacement vector $\mathbf{x}$ of Equation 6.1 in the general equation of motion of Equation 6.2, the linearly independent equations can be derived. Here, that derivation is concisely shown in Equation 6.3. In Equation 6.3, note that the $\mathbf{M}^*$, $\mathbf{C}^*$ and $\mathbf{K}^*$ matrices are diagonal due to the orthogonality property of the undamped eigenmatrix $\mathbf{E}$. In turn, $\mathbf{E}$ consists of eigenvectors for all different modes. Further note that the ultimately derived Equation 6.3h describes the equation of motion as used in ZAMBONI. Since for the coupled simulations performed in Chapter 7 only 4 degrees of freedom are of interest, the modal structure applied here greatly simplifies the dynamic equations. Consequently, the required computational power for coupling a modal structure to ZAMBONI is limited as well.

$$\mathbf{x}(t) = \sum_{i=1}^{N} \underline{\hat{x}}_i u_i(t) = \mathbf{E}\mathbf{u}(t) \tag{6.1}$$

$$\mathbf{M}\ddot{\mathbf{x}} + \mathbf{C}\dot{\mathbf{x}} + \mathbf{K}\mathbf{x} = \mathbf{F} = \mathbf{F}_{\mathbf{ice}} + \mathbf{F}_{\mathbf{wind}} + \mathbf{F}_{\mathbf{current}} \tag{6.2}$$

$$\mathbf{ME\ddot{u}} + \mathbf{CE\dot{x}} + \mathbf{KEu} = \mathbf{F} \tag{6.3a}$$

Pre-multiplying with $\mathbf{E}^T$:

$$\mathbf{E^T ME\ddot{u}} + \mathbf{E^T CE\dot{x}} + \mathbf{E^T KEu} = \mathbf{E^T F} \tag{6.3b}$$

$$\mathbf{M^* \ddot{u}} + \mathbf{C^* \dot{u}} + \mathbf{K^* u} = \mathbf{E^T F} \tag{6.3c}$$

Pre-multiplying with $\left(\mathbf{M}^*\right)^{-1}$:

$$\left(\mathbf{M}^*\right)^{-1}\mathbf{M}^*\ddot{\mathbf{u}} + \left(\mathbf{M}^*\right)^{-1}\mathbf{C}^*\dot{\mathbf{u}} + \left(\mathbf{M}^*\right)^{-1}\mathbf{K}^*\mathbf{u} = \left(\mathbf{M}^*\right)^{-1}\mathbf{E}^\mathbf{T}\mathbf{F} \tag{6.3d}$$

$$\mathbf{I\ddot{u}} + \left(\mathbf{M}^*\right)^{-1}\mathbf{C}^*\dot{\mathbf{u}} + \Omega^2\mathbf{u} = \left(\mathbf{M}^*\right)^{-1}\mathbf{E}^\mathbf{T}\mathbf{F} \tag{6.3e}$$

Introducing the damping ratio ζ :

$$\zeta_i = \frac{c_{ii}}{c_{ii,crit}} = \frac{c_{ii}}{2\sqrt{k_{ii}m_{ii}}} = \frac{c_{ii}}{2m_{ii}\omega_i} \Rightarrow \mathbf{C}^* = 2\mathbf{M}^*\mathbf{Z}\Omega \tag{6.3f}$$

Substituting $\mathbf{C}^*$ into Equation 6.3e:

$$\ddot{\mathbf{u}} + 2\left(\mathbf{M}^*\right)^{-1}\mathbf{M}^*\mathbf{Z}\Omega\dot{\mathbf{u}} + \Omega^2\mathbf{u} = \left(\mathbf{M}^*\right)^{-1}\mathbf{E}^\mathbf{T}\mathbf{F} \tag{6.3g}$$

$$\ddot{\mathbf{u}} + 2\mathbf{Z}\Omega\dot{\mathbf{u}} + \Omega^2\mathbf{u} = \left(\mathbf{M}^*\right)^{-1}\mathbf{E}^\mathbf{T}\mathbf{F} \tag{6.3h}$$

The structural wind turbine model in the modal domain described by Siemens Gamesa is a 564 degree of freedom (DoF) modal model. These 564 DoFs follow from 94 distinct nodes at different turbine locations, with 6 DoFs for each node. However, only four of these degrees of freedom are applied in the coupled simulations of Chapter 7. Those are the fore-aft and side-side DoFs of the nodes at mean sea level (MSL) and hub height. Unfortunately, no particular node could be identified as the node at hub height. Instead, the node at tower top is used. Nevertheless, for the remainder of this thesis, this position will be referred to as hub height. Furthermore, mode frequencies higher than 20 [Hz] are cut off, leaving the first 103 modes of vibration included. Then, when coupling this structure to ZAMBONI, the only additional steps required in ZAMBONI are as follows:

1. Upon determining the loads for a particular time step, the ice load is transferred to the modal domain by pre-multiplying it with the transpose of the eigenmatrix. That is, the ice force is projected to the fore-aft and side-side directions of the wind turbine, and consequently, the fore-aft ice load is multiplied with the fore-aft modal amplitudes at MSL whereas the side-side ice load is multiplied with the side-side modal amplitudes at MSL. Similarly, the wind force, which is assumed to act fully in the fore-aft direction, is multiplied with the fore-aft modal amplitudes at the tower top
2. In the ODE environment, the equation of motion of Equation 6.3h is solved for all modes
3. The displacements in the modal domain are transferred to displacements in the required de-

grees of freedom according to Equation 6.1

In this 3-step process an implementation mistake occurred. In modal analysis, multiplication should take place with the mode shapes rather than the modal amplitudes. When multiplied with the modal amplitude, mistakes occur for those modes where the signs of the mode shapes are both positive and negative in the DoFs at which the loads act. As mentioned in the first step of this 3-step process, these DoFs are fore-aft at MSL, side-side at MSL and fore-aft at hub height. The most dominant modes for ice-structure interaction are the 1st and 2nd bending mode fore-aft and side-side. For these four bending modes, all mode shape values in the three relevant DoFs are positive, which means that no mistake occurs for these dominant modes, albeit accidentally. However, for some of the other minor modes, certainly mistakes will occur. Although these mistakes are small individually, when added in a degree of freedom, they can result in a significant over prediction of the response. All in all, it is expected that the coupled simulations results and discussion of Chapter 7 remain valid, as the general turbine behaviour is not altered drastically by this modal implementation error. Nevertheless, going forward, resolving this issue is adviced.

6.2. Geometry and properties of coupled turbine

Although the properties of the structural model are not discussed at length, it is essential to have a general idea of the physical configuration simulated in order to understand the coupled simulations of Chapter 7. Therefore, Table 6.1 lists the different characteristic levels along the height of the turbine. Furthermore, in Figure 6.1, the modal amplitudes from pile tip to tower top are plotted for the 1st, 2nd and 3rd bending modes in the fore-aft and side-side directions. These bending modes are plotted as they are known to be the susceptible modes at which ice-structure synchronisation occurs.

Table 6.1: Levels of the structural wind turbine model

Level	z-coordinate	[Unit]
Hub height	139	[m]
Tower top	133	[m]
Interface	14	[m]
Monopile top	2	[m]
Mudline	-30	[m]
Pile tip	-62	[m]

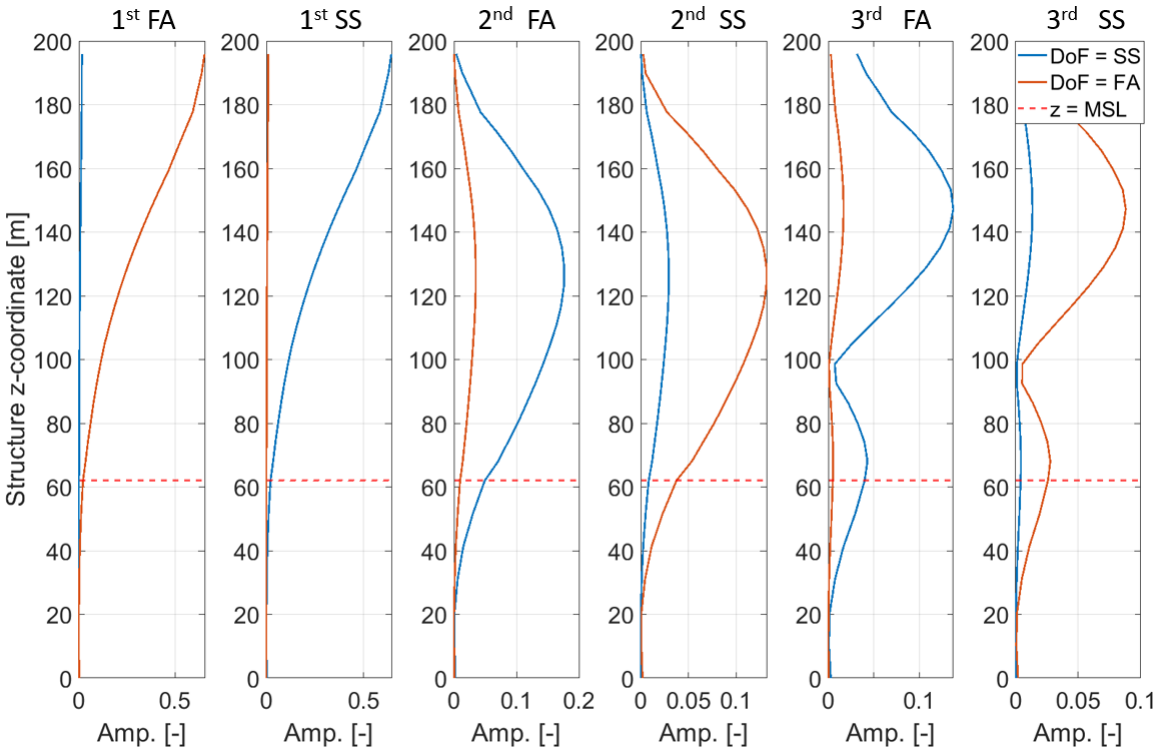

Figure 6.1: Amplitudal representation of the bending mode shapes of the structural model. The 1st bending modes correspond to global modes 1 and 2, the 2nd bending modes correspond to global modes 9 and 10 and the 3rd bending modes correspond to global modes 17 and 18

6.3. Coupling of wind force

With the wind turbine structure described, nearly everything is in place to perform coupled ice and wind simulations. The final step concerns the application of a wind load to the structural model. As in this case, the wind load serves just as a means to simulate the effect of wind disturbance on ice loads, a detailed wind load model is not required. Instead, the simple thrust equation of Equation 6.4 is applied, where c_T and S are turbine specific values and ρ is taken as the average Baltic Sea air density at 100 [m] above sea level. Then, by application of Equation 6.4 and the wind turbine model in the modal domain, a simple dynamic simulation can be performed with solely wind applied to determine whether the observed turbine behaviour is sensible. The resulting displacement at MSL of this simulation is shown in Figure 6.2. At first glance, the structural displacement seems sensible. However, one crucial observation here is that due to fore-aft directed wind loads, the structure also displaces in the side-side direction. This non-symmetric vibration of the wind turbine is a model property that becomes relevant in some of the load cases of Chapter 7.

$$F_{wind} = c_T(v_{wind})\frac{1}{2}\rho v_{wind}^2 S \tag{6.4}$$

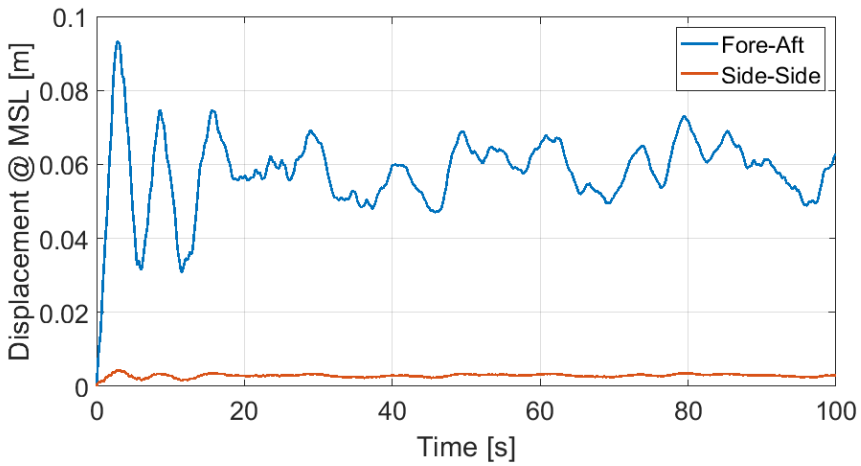

Figure 6.2: Displacement of the wind turbine model in the modal domain due to wind loads according to Equation 6.4

Finally, the application of aerodynamic damping must be discussed. The wind turbine model provided by Siemens Gamesa Renewable Energy contains modal properties for both production and idling load cases, where for the production load cases, the modal properties are dependent on wind speeds. These modal properties for production cases do include aerodynamic damping. However, as they are wind speed specific, they can only be applied for simulations at fixed wind speed. Also, to make the coupled simulations of Chapter 7 better reproducible, it does not suffice to apply a wind speed specific wind turbine model. Finally, applying aerodynamic damping through structural properties does not couple wind to the structure, but rather results in a predescribed wind load being applied to the structure. Therefore, instead, it is decided to use one consistent structural model for all coupled simulation of Chapter 7, namely the structural model corresponding to an idling turbine with no environmental wind speed. On top of that, aerodynamic damping is applied through the wind-thrust equation of Equation 6.4, yielding the relative wind-thrust equation of Equation 6.5. In order to evade self-excited wind vibration, which is a known potential issue with applying aerodynamic damping as in Equation 6.5, C_T remains independent of the structural velocity.

To compare the different methods of aerodynamic damping, in Figure 6.3, the Equation 6.5 method is compared to applying aerodynamic damping through structural characteristics. Specifically, Figure 6.3 shows a decay test for a 100 [s] period of wind around 10 [m/s] followed by a 50 [s] decay period of wind at 5 [m/s]. In Figure 6.3, method 1 has aerodynamic damping applied through the structural properties, method 2 has no aerodynamic damping applied and follows from the structural properties of an idling turbine, and method 3 has aerodynamic damping applied through Equation 6.5, with the structural properties of method 2.

When closely observing the differences between method 1 and method 3 in Figure 6.3, method 3 appears to be slightly over-damped. However, as the difference is insignificant, it is chosen to neglect it. After all, the analyses of Chapter 7 is qualitative, and minor differences in aerodynamic damping are not expected to alter the differences between the discussed load cases in Chapter 7.

$$F_{wind} = c_T\left(v_{wind}\right)\frac{1}{2}\rho\left(v_{wind} - v_{hub}\right)\left|v_{wind} - v_{hub}\right|S \tag{6.5}$$

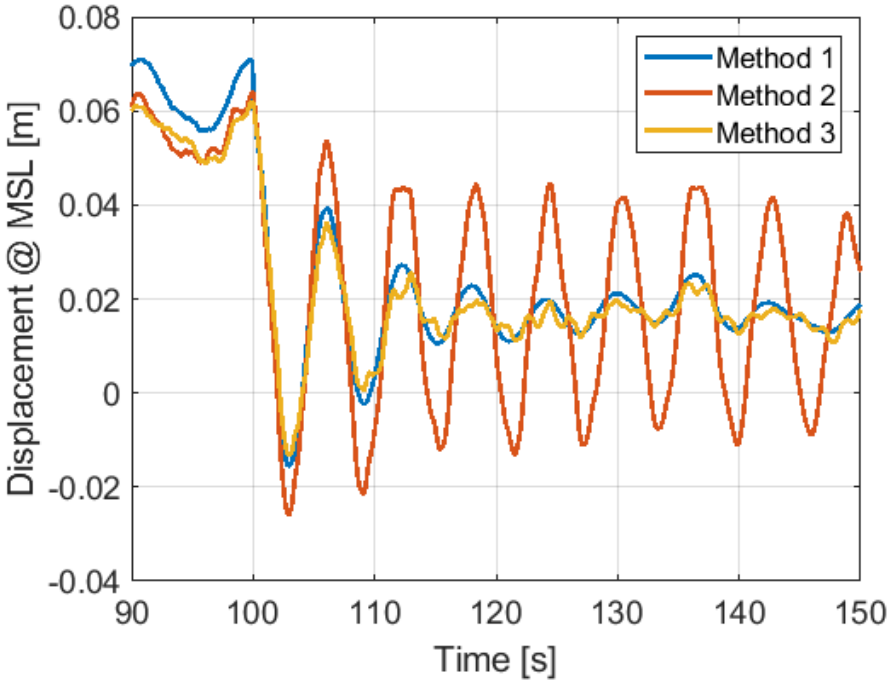

Figure 6.3: Fore-aft displacement at MSL for a decay test when different types of aerodynamic damping are applied. Method 1: structural properties adjusted for wind speed including aerodynamic damping. Method 2: no aerodynamic damping, structural properties for idling turbine. Method 3: Aerodynamic damping through Equation 6.5 with structural properties similar as in method 2

7

Coupled analysis of combined ice- and wind loading on an offshore wind turbine using ZAMBONI

With a turbine coupled to ZAMBONI in Chapter 6, nearly everything is in place to perform fully coupled simulations on an offshore wind turbine on which ice and wind loads are acting simultaneously. In this chapter, these coupled simulations will be performed and analysed. First, Section 7.1 describes the applied environmental conditions, the strategy used for simulations and the different load cases tested. Thereafter, in Section 7.2, the findings across load cases and simulations are discussed, giving a broad overview of the simulation results. Then, in analysing the specific simulations, the most noteworthy findings related to the application of ZAMBONI are discussed. Specifically, the following four areas of analysis are discussed in separate sections.

- In Section 7.3, the effect of two-dimensional ice on the global ice loads is discussed, including its effect on the structural response during intermittent crushing
- In Section 7.4, the effects of two-dimensional ice on a special quasi lock-in ice-structure interaction regime is discussed, which was also identified by Willems and Hendrikse (2019)
- In Section 7.5, the effects of two-dimensional ice on the indentation speed range during which frequency lock-in occurs will be discussed
- In Section 7.6, the effect of slightly misaligned ice and wind loads on ice-structure interactions are discussed.

7.1. Coupled simulation strategy and analysed load cases

Before coupled simulations can be performed, the ice parameters and wind characteristics to perform these simulations with have to be chosen. Similarly as in Chapter 4 and Chapter 5, it is desirable to vary the ice indentation speed. Therefore, to limit the number of simulations to be performed, it is opted to perform simulation for only one particular set of ice parameters and wind speeds, corresponding to the load case that is expected to be most critical.

To that end, the ice parameters are derived from the average annual maximum ice properties occurring in the Danish Belts and Southern Baltic sea proper, which is the primary region for commercial

offshore wind energy projects in icy waters (Koreman, 2019). According to ISO 19906 (2019), the maximum annually occurring ice floe thickness is roughly 40 [cm] in these waters, which is thus used in these simulations. Furthermore, a uniaxial compressive strength of ice of 1 [MPa] was assumed. Then, by making use of the full-scale ice scaling tool of Hendrikse et al. (2018), the ice parameters corresponding to these ice conditions can be derived on a 7.5 [m] diameter structure, similarly to the method described in Section 5.2. Note here that this method of determining ice parameters corresponds to a cylindrical structure. As discussed in Chapter 3, ZAMBONI requires parameters for a straight ice-structure interface. Therefore, the derived ice parameters will not precisely correspond to the intended annual maximum Baltic Sea ice. Nevertheless, these parameters remain realistic for full-scale ice, which is most crucial to the qualitative analysis performed in this chapter. The different environmental inputs and the resulting ice parameters are presented in Table 7.1.

Regarding wind loads, a typical 600 [s] wind speed time series has been used around rated wind speeds. This wind speed time series has inherent turbulence in its time signal. Then, through the simple wind load determination process described in Section 6.3, suitable wind loads can be applied to the structure throughout all simulations.

Table 7.1: List of reference values applied for the computation of Baltic sea ice parameters and the resulting ice parameters

Reference Parameter	Value	Resulting ZAMBONI ice parameter	Value	Unit
$K_{1,norm}$	0.2616	K_1	$6.2287 \cdot 10^6$	[N/m]
$K_{2,norm}$	8.6338	K_2	$2.3811 \cdot 10^7$	[N/m]
$C_{1,norm}$	0.9385	C_1	$2.2346 \cdot 10^7$	[Ns/m]
$C_{2,norm}$	$3.2 \cdot 10^{-5}$	C_2	$4.3199 \cdot 10^{17}$	[N^3s/m]
δ_f	0.004	δ_f	0.004	[m]
r_{max}	0.006	r_{max}	0.006	[m]
N	58			[-]
D	7.5			[m]
σ_{ref}	$1 \cdot 10^6$			[Pa]
h_{ref}	0.4			[m]
		R	0.1293	[m]

Next, the load cases for which simulations are performed need to be discussed. Herein, the final analyses goals are driving, which were stated in this work's introduction as follows:

1. Gain insight into the effect of simulating ice two-dimensionally on ice-structure interactions for conventional (aligned) ice and wind loads
2. Gain insight into the structural response and the development of ice-structure interactions during newly simulable misaligned ice and wind loads

Therefore, at least, load cases must include one-dimensional ice and misaligned ice and wind loads. The former of these is not straightforward, as ZAMBONI is inherently two-dimensional and the Hendrikse (2017) model cannot be applied because when comparing simulations of the Hendrikse (2017) model and ZAMBONI, the differences between ice indentation into a rectangular and cylindrical structure manifest, as argued in detail in Chapter 4. Therefore, a practical solution is pursued where for certain load cases, the wind turbine, as described in Chapter 6, is forced to move only

in the in-line ice direction. That way, the local shape effect of the structure as discussed in Chapter 3 remains intact whilst cross-drift vibrations of the structure are restrained, causing the effect of these cross-drift vibrations on the ice-structure interactions to be analysable. Still, it should be noted that most of the identified differences between one-dimensional and two-dimensional ice as discussed earlier in Chapter 4 consequentially do not manifest in the load cases that are hereafter called 'one-dimensional'.

Regarding the misaligned ice and wind load cases, two particular cases are evaluated. The first one concerns the theoretically interesting case of 90 [°] ice-wind misalignment and the second concerns the most dominantly occurring misalignment case of 20 [°] according to Koreman (2019). The corresponding six load cases on which analysis is performed in this chapter are graphically shown in Figure 7.1.

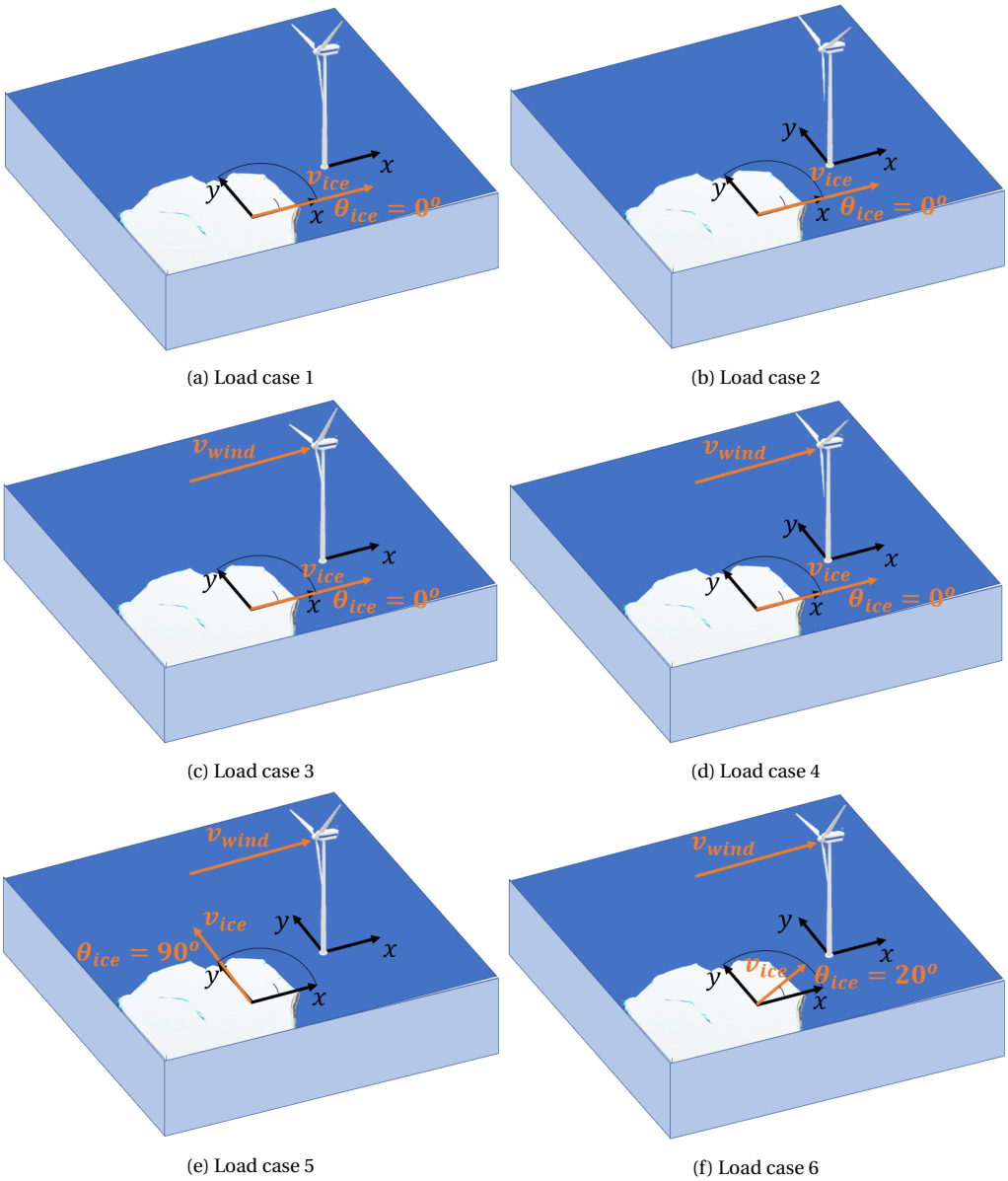

(a) Load case 1

(b) Load case 2

(c) Load case 3

(d) Load case 4

(e) Load case 5

(f) Load case 6

Figure 7.1: Graphic overview of the 6 different load cases. Load case 1: idling with a 1D-restricted turbine. Load case 2: idling. Load case 3: Aligned ice and wind with a 1D-restricted turbine. Load case 4: aligned ice and wind. Load case 5: 90 [°] misaligned ice and wind. Load case 6: 20 [°] misaligned ice and wind

Finally, as argued in Chapter 2 and subsequently executed in Chapter 4 and Chapter 5, it is vital to simulate over a wide range of ice indentation speeds. Therefore, also for all load cases shown in Figure 7.1, simulations are performed at varying ice indentation speeds. Specifically, as the most interesting regimes remain intermittent crushing and frequency lock-in, the ice indentation speed range is chosen around these regimes, from 0.5 [mm/s] to 500 [mm/s].

Additionally, to detect specific findings, load cases have to be compared to each other. These load case combinations are chosen such that specific hypothesised effects can be extracted from the simulations. Below, the different load case combinations are listed, including the reason for comparing these particular load cases.

A. Comparison of load cases 1 and 2 - to deduce the effect of cross-drift vibration on two-dimensional ice as compared to one-dimensional ice for idling wind turbines. It is hypothesised that the cross-vibrations induced by the ice loads themselves cause some ice to crush at the side of the structure, causing slightly smaller global in-line loads. All simulation results for this comparison are given in Appendix A.

B. Comparison of load cases 3 and 4 - to deduce the effect cross-drift vibrations have on two-dimensional ice as compared to one-dimensional ice for wind turbines during production. It is hypothesised that the strong cross-drift vibrations of the turbine induced by wind loads cause ice to break at the side of the structure, causing significantly smaller global in-line loads and displacements. All simulation results for this comparison are given in Appendix B.

C. Comparison of load cases 2 and 4 - to deduce the differences between idling turbines and turbines experiencing aligned wind loads for two-dimensional ice. It is hypothesised that the superposed wind loads cause large global displacements, but at the same time disturb the development of ice-structure interactions, especially at low ice-indentation speeds. All simulation results for this comparison are given in Appendix C.

D. Comparison of load cases 4 and 5 - to deduce the effect of a cross-drift wind load on ice-structure interactions. It is hypothesised that the heavy cross-drift vibrations induced by the cross-drift wind cause significantly smaller global ice loads in the in-line direction. All simulation results for this comparison are given in Appendix D.

E. Comparison of load cases 4 and 6 - to deduce the effect of slightly misaligned wind loads on ice-structure interactions. It is hypothesised that the small cross-drift vibrations induced by the cross-drift wind cause slightly smaller global ice loads in the in-line direction. All simulation results for this comparison are given in Appendix E.

7.2. Overview of general simulation results

As described in this chapter's introduction, the focus of this coupled ice-wind analysis is the specific differences between ZAMBONI and one-dimensional ice and newly simulatable load cases of misaligned ice and wind. Indeed, Sections 7.3 to 7.6 describe these findings. Nevertheless, it remains useful to concisely analyse the general ice-structure interactions that manifest across load cases for this combination of ice and structure. To that end, the statistical representations of all simulations for load cases 2 and 4 are shown in Figures Figure 7.2 to Figure 7.5. More precisely, Figure 7.2 shows the in-line ice loads, Figure 7.3 shows the in-line displacement at waterline, Figure 7.4 show the dominant structural frequencies and Figure 7.5 show the β-ratio's, all for a varying ice indentation speed.

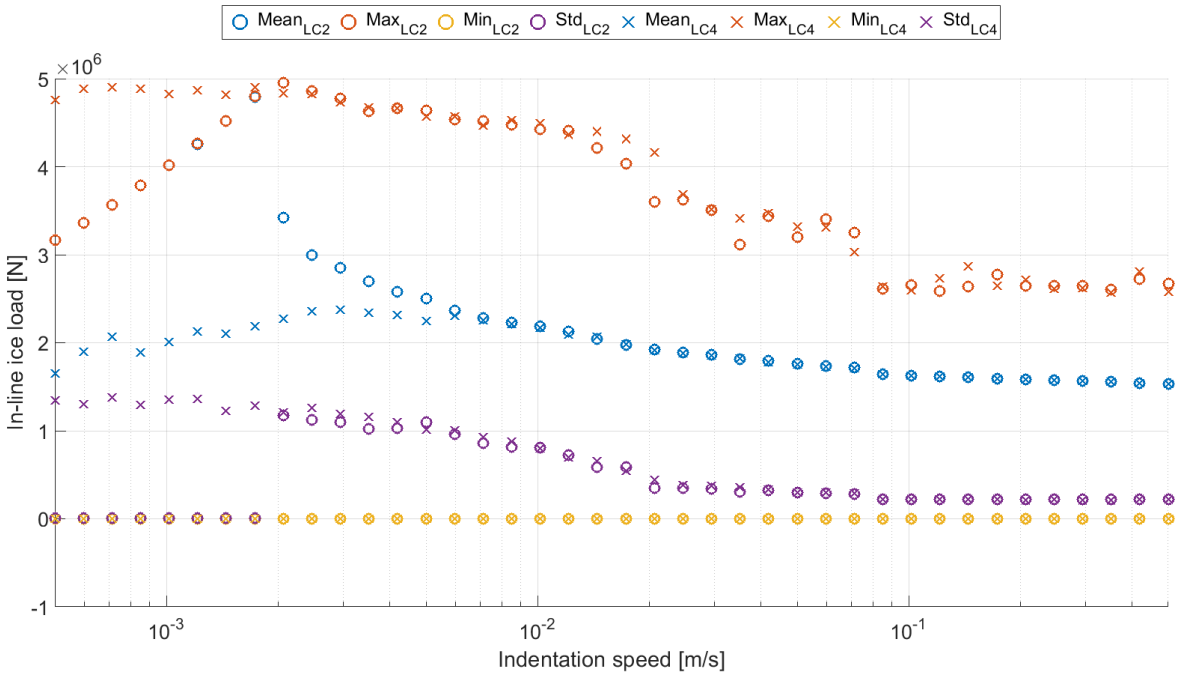

Figure 7.2: Statistical representation of in-line ice loads, both for an idling turbine (LC2) and a turbine experiencing superposed wind loads (LC4)

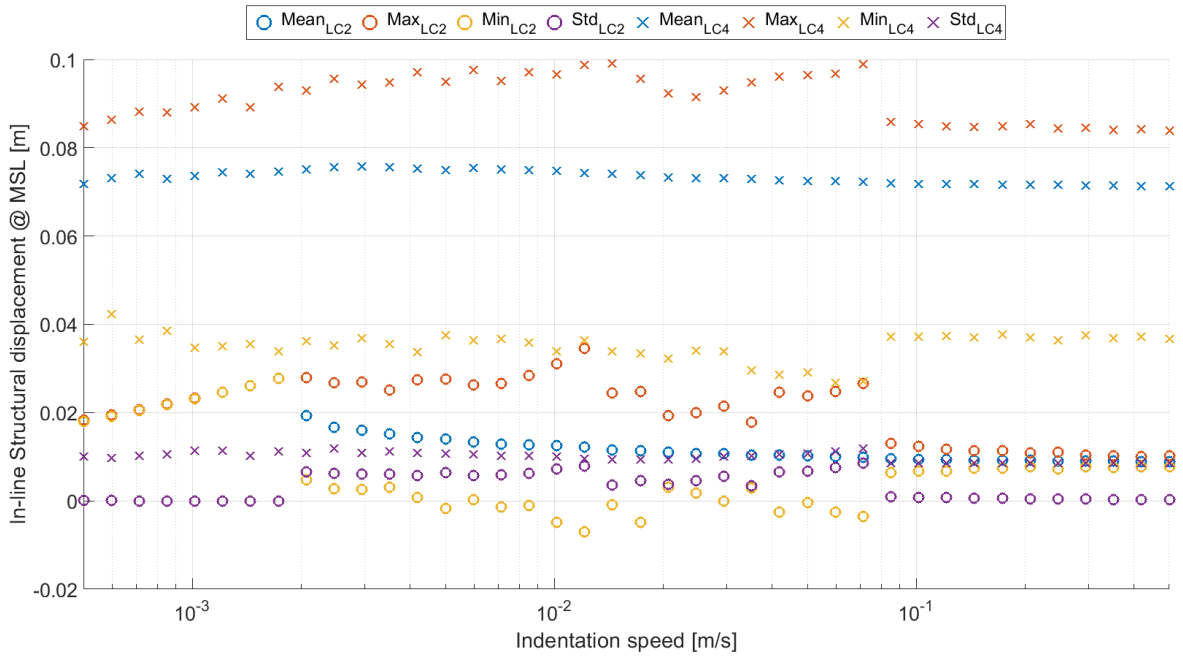

Figure 7.3: Statistical representation of in-line structural displacements at waterline, both for a 2D idling turbine (LC2) and a 2D turbine experiencing superposed wind loads (LC4)

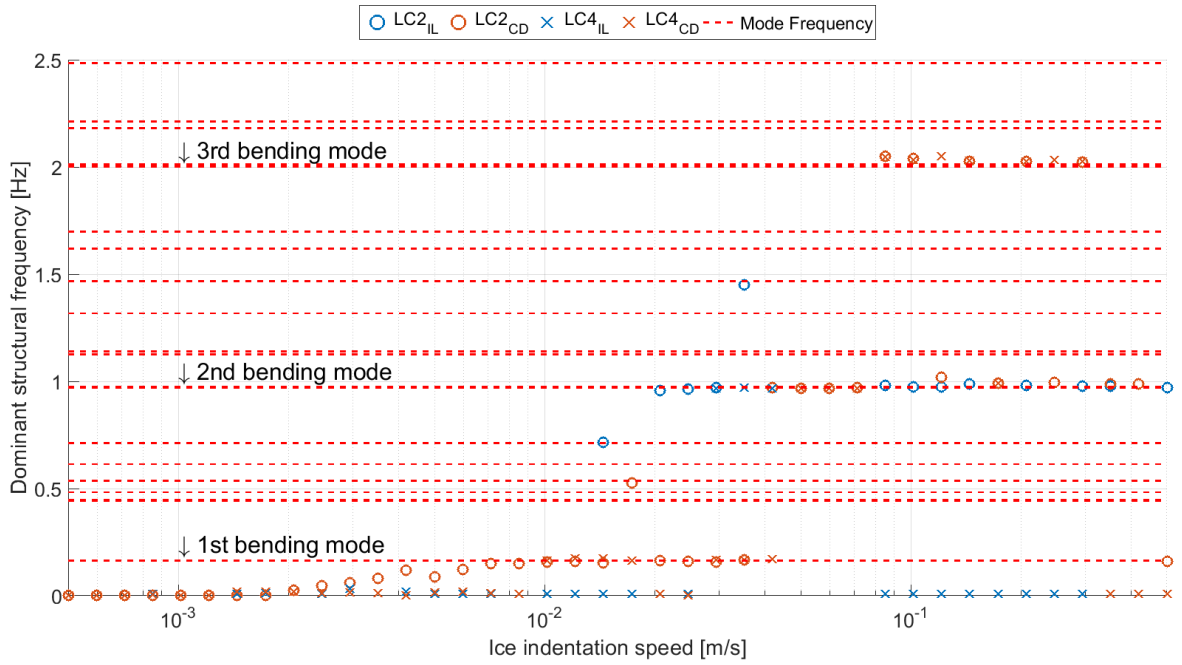

Figure 7.4: Dominant structural response frequencies, both for a 2D idling turbine (LC2) and a 2D turbine experiencing superposed wind loads (LC4)

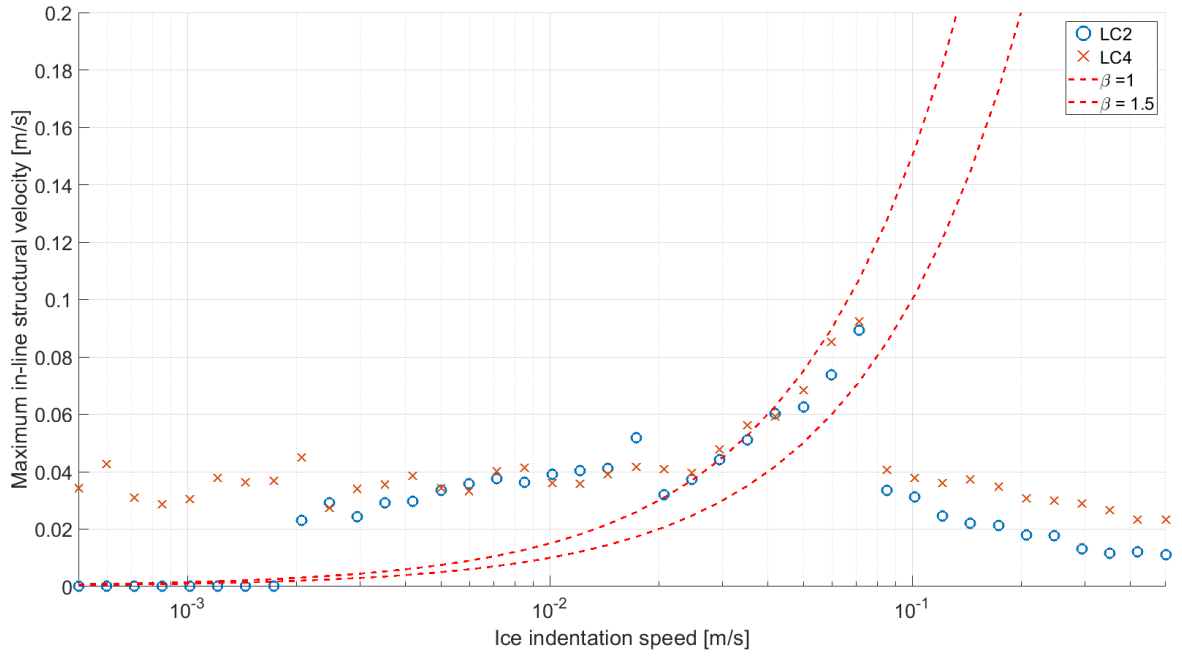

Figure 7.5: β-values, both for a 2D idling turbine (LC2) and a 2D turbine experiencing superposed wind loads (LC4)

All four ice indentation regimes are simulated. However, the boundaries of the ice indentation regimes differ between load cases. Since the transitions between the four interaction regimes are most clearly observable for the idling turbine of load case 2, they are described here as an example. By applying the hereafter discussed regime identification criteria, one can identify the exact regime transitions for each load case. Moreover, Table 7.2 lists the observed regime transitions for each load case. For the idling turbine of load case 2, from ice indentation speeds of 0.5 [mm/s] to

1.7 [mm/s] creep deformation occurs. This transition is well recognisable by the absent ice load standard deviation in Figure 7.2.

Then from 1.7 [mm/s] to roughly 7 [mm/s] intermittent crushing occurs, this regime is recognisable in Figure 7.4 by the frequencies building up to the 1st bending mode modal frequency. The observed differences between load cases in this regime will be discussed at length in Section 7.3. Subsequently, from 7 [mm/s] to roughly 14 [mm/s] a special ice-structure interaction regime occurs that has not been discussed earlier in this thesis. In this interaction regime, ice and structure synchronisation occurs. Yet, it can neither be identified as intermittent crushing nor as frequency lock-in. This ice-structure interaction regime will be discussed in more detail in Section 7.4.

For even higher ice indentation speeds, from roughly 20 [mm/s] to 80 [mm/s], frequency-lock in occurs, as is well observable by the β-ratios of Figure 7.5 in this regime, which lie between 1.0 [-] and 1.5 [-]. When observing Figure 7.4, it becomes clear that frequency lock-in occurs solely in the 2nd bending mode. This observation holds for all analysed load cases. Nevertheless, remarkable differences between load cases for this ice structure interaction regime are observed. They are discussed in Section 7.5.

Ultimately, for even higher ice-indentation speeds, continuous brittle crushing occurs, which is not further analysed in this work. Still, one notable finding during continuous brittle crushing is the simulated cross-drift vibrations in the 3rd bending mode. Possibly, these 3rd bending mode cross-drift vibrations occur because of the low damping in the 3rd bending mode as discussed in Chapter 6, making it excitable by ice loads despite having a smaller modal amplitude at the waterline than the 2nd bending mode.

Table 7.2: Overview of the observed ranges of ice indentation speeds of the ice-structure interaction regimes for all 6 load cases, where the accuracy of these values is subject to the local simulation resolution. Abbreviations: IC is intermittent crushing, 1st BM is the identified special ice-structure interaction regime in the 1st bending mode, FLI is frequency lock-in and CBC is continuous brittle crushing

Load case	Creep	IC	1st BM	FLI	CBC	[Unit]
1	≤ 1.7	1.7-7	7-9	20-85	≥ 85	[mm/s]
2	≤ 1.7	1.7-7	7-12	20-70	≥ 70	[mm/s]
3	Non-existent	≤ 20	Semi develops 7-11	20-85	≥ 85	[mm/s]
4	Non-existent	≤ 20	Semi develops 7-13	20-70	≥ 70	[mm/s]
5	Non-existent	≤ 3	3-14	20-70	≥ 85	[mm/s]
6	Non-existent	≤ 20	Semi develops 7-14	20-70	≥ 85	[mm/s]

7.3. Reduced global ice loads for two-dimensional ice

The first specific finding of this coupled analysis that needs to be discussed is the reduced global ice loads for two-dimensional ice, as this effect contributes to some of the later findings discussed in this analysis. These reduced global ice loads for two-dimensional ice are the only of the notable findings that were hypothesised prior to running simulations, as described in Section 5.2. The reasoning for this difference is as follows. For two-dimensional ice, cross-drift structural vibrations affect the ice floe whereas, for one-dimensional ice, they do not. Then, for cross-drift structural vibrations in two-dimensional ice, ice elements positioned at the sides of the structure locally encounter in-line ice indentation, causing ice elements to fail in crushing at the sides of the structure. Thus, these ice elements crush for two-dimensional ice but do not crush for one-dimensional ice. As crushed ice elements do not build-up load on the structure, the global loads for two-dimensional ice in the in-line direction must be lower than those for one-dimensional ice. This difference man-

ifests across all ice-indentation speeds. However, it is best observable in the lower ice-indentation regimes, such as intermittent crushing, where the load build-up in ice elements is most crucial. In Figure 7.6, these 2% larger loads are observable in the highlighted differences between maximum simulated in-line loads for one- and two-dimensional ice during idling.

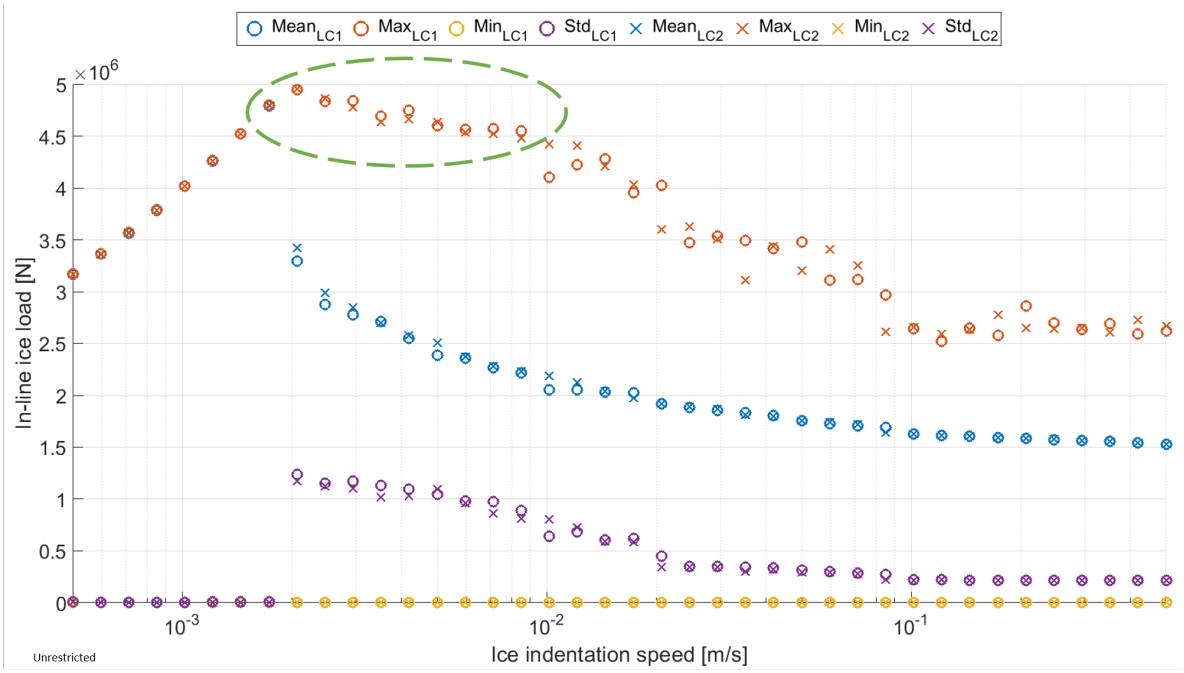

Figure 7.6: Statistical representation of in-line ice loads during idling, both for an in-line restricted turbine (LC1) and a 2D turbine (LC2). The highlighted difference shows the higher simulated maximum loads for the in-line restricted turbine

Furthermore, as this difference between one- and two-dimensional ice is caused by cross-drift vibrations, the effect of these cross drift vibrations must be especially observable for load case 5, where the wind is applied in the cross-drift direction, supposedly causing heavy cross-drift vibrations. Therefore, in Figure 7.7 load cases 2 (idling) and 5 (cross-drift wind) are compared. Indeed, one can observe larger mean loads in the intermittent crushing regime for the idling case, as underlined by the highlighted section.

Still, these statistical representations of in-line loads do not give detailed insight into the differences between intermittent crushing events for these load cases. Therefore, in Figure 7.8, three time series are presented during a typical intermittent crushing simulation at an ice indentation speed of 2.5 [mm/s]. More specifically, Figure 7.8a displays the load time series of this simulation, Figure 7.8b presents the time series of the ice-structure contact line and Figure 7.8c gives the time series of the displacement at waterline during this particular simulation.

When observing Figure 7.8b, the hypothesised reasoning is confirmed. Indeed, the maximum contact line reached during each simulation's loading phase is longest for load case 1 (idling 1D), followed by load case 2 (idling 2D) and then followed by load case 5 (cross-drift wind). Interestingly, when observing Figure 7.8a, the maximum global force reached before the extrusion phase is initiated, during each intermittent crushing cycle, is relatively similar for the different load cases. However, the maximum structural deflection at that point is somewhat different, where again, load case 1 deflects the most and load case 5 deflects the least. The author hypothesises that this apparent incompatibility is caused by the different mean loads and durations of each loading cycle for the different load cases. Since the ultimately reached displacement at the end of the loading phase follows

from the load during the full loading phase, the maximum load prior to crushing does not solely determine the structural displacement. On average, during each intermittent crushing load cycle, the maximum deflection of load case 1 (idling 1D) is roughly 5% larger than the maximum deflection of load case 2 (idling 2D). In turn, the maximum structural deflection of load case 5 (cross-drift wind) trails that of load case 2 by roughly 10% on average. These are notable differences, as intermittent crushing is one of the more critical ice load cases. If true, from a design perspective, the conclusion reached here indicates that the maximum structural displacement during intermittent crushing is slightly overpredicted with the current one-dimensional ice models.

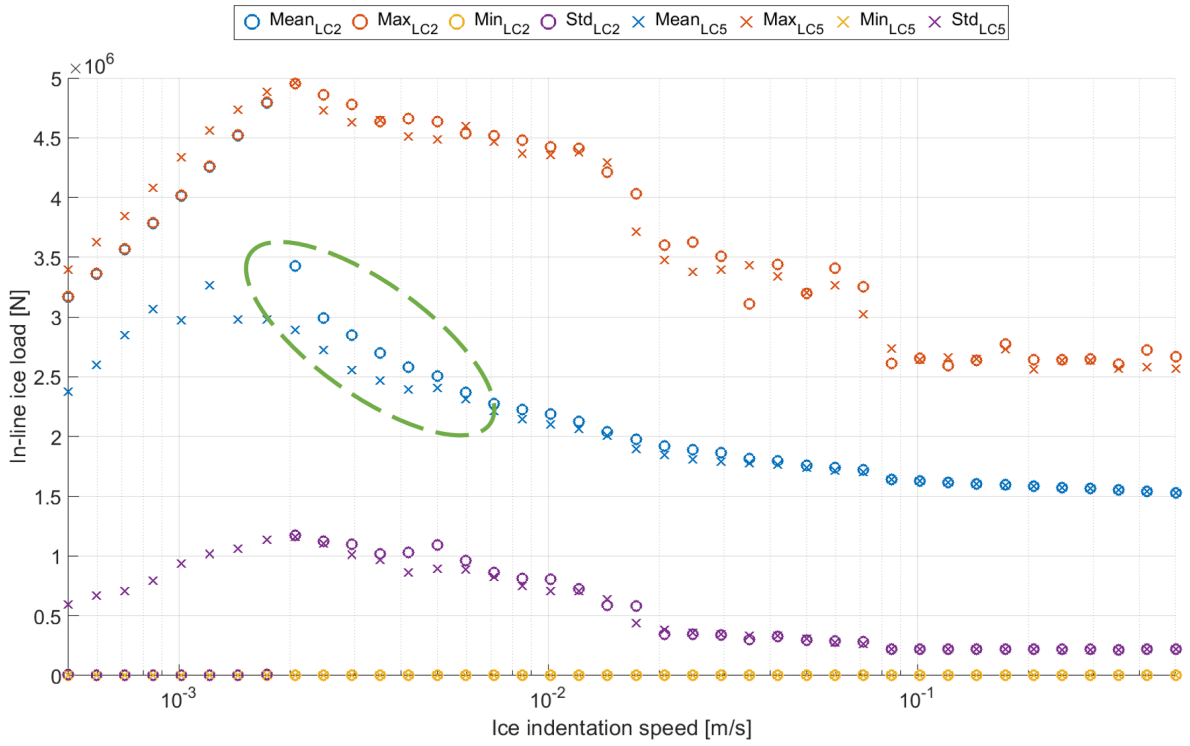

Figure 7.7: Statistical representation of in-line ice loads, both for a 2D idling turbine (LC2) and a 2D turbine experiencing cross-drift wind loads (LC5). The highlighted difference shows the significantly smaller in-line ice loads for LC5

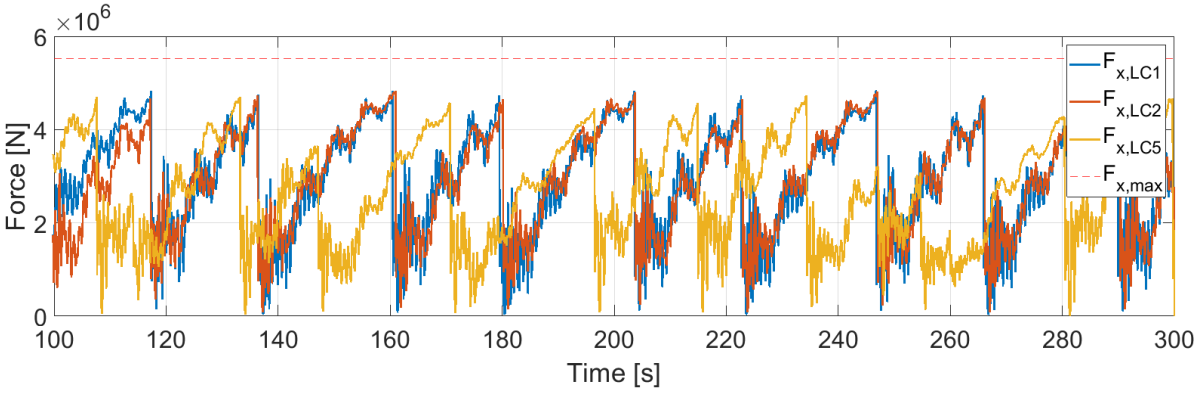

(a) In-line ice load

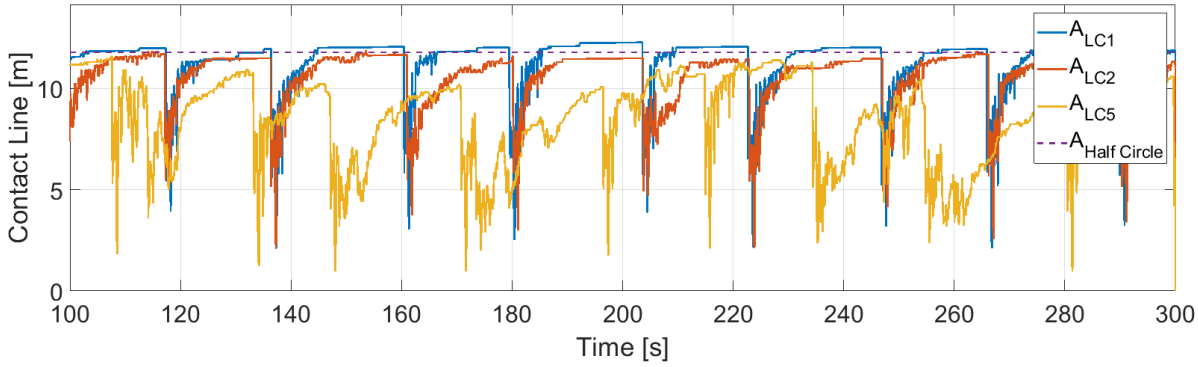

(b) Contact line

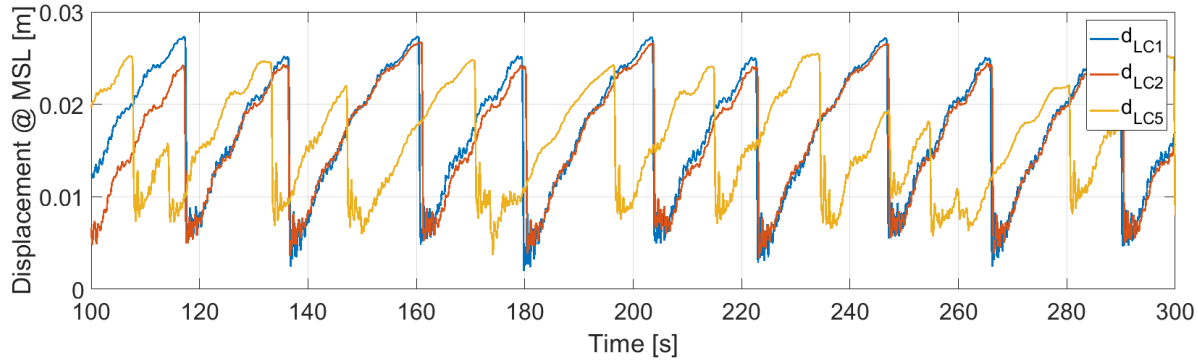

(c) In-line displacements @ MSL

Figure 7.8: Time series at an ice indentation speed of 25 [mm/s] for three load cases; 1D idling (LC1), 2D idling (LC2) and 2D with cross-drift wind (LC5)

7.4. The 1st bending mode ice-structure interaction regime

The next important part of analysis in these coupled simulations concerns the 1st bending mode ice-structure interaction regime. In contrast to the conventional ice structure interaction regimes of intermittent crushing, frequency lock-in and continuous brittle crushing, this interaction regime has not been discussed in Chapter 2 and thus requires a separate introduction.

The 1st bending mode ice-structure interaction regime is best described as a combination of intermittent crushing and frequency lock-in. When observing the time series of Figure 7.9b, the displacement at the waterline in this ice-structure interaction regime resembles the saw-tooth pattern typical for intermittent crushing. However, this saw-tooth pattern occurs at such a high frequency, that the displacement at hub height follows a near harmonic-vibration, as observable in Figure 7.9c.

Furthermore, when observing Figure 7.13, clearly in this ice-structure interaction regime, the vibration frequency of the structure is locked into a structural mode, which is typical for frequency lock-in. However, when the β-relation of Toyama et al. (1983) is applied, this ice-structure interaction regime does not identify as frequency lock-in, as the β-factors lie well above 1.5 [-]. Due to the incompatibility with either of those phenomena, the 1st bending mode synchronisation must be concerned as a separate ice-structure interaction regime.

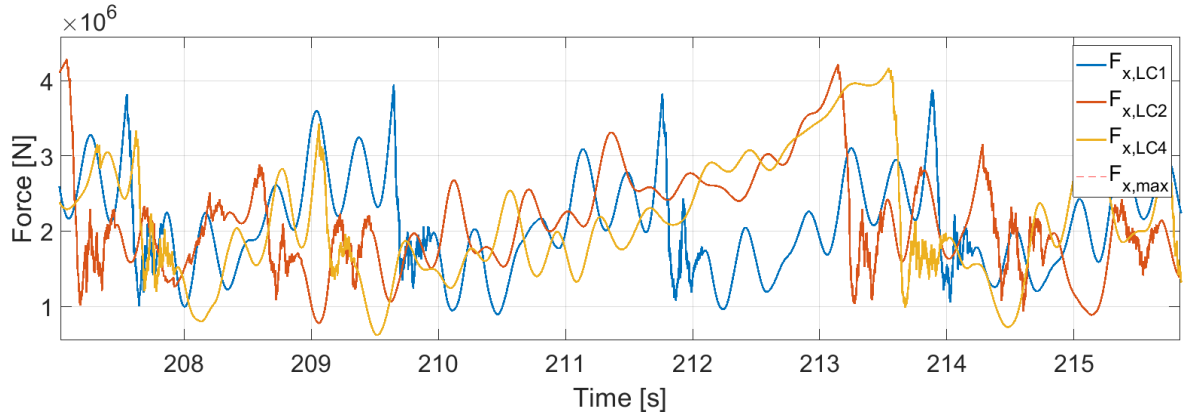

(a) In-line ice load

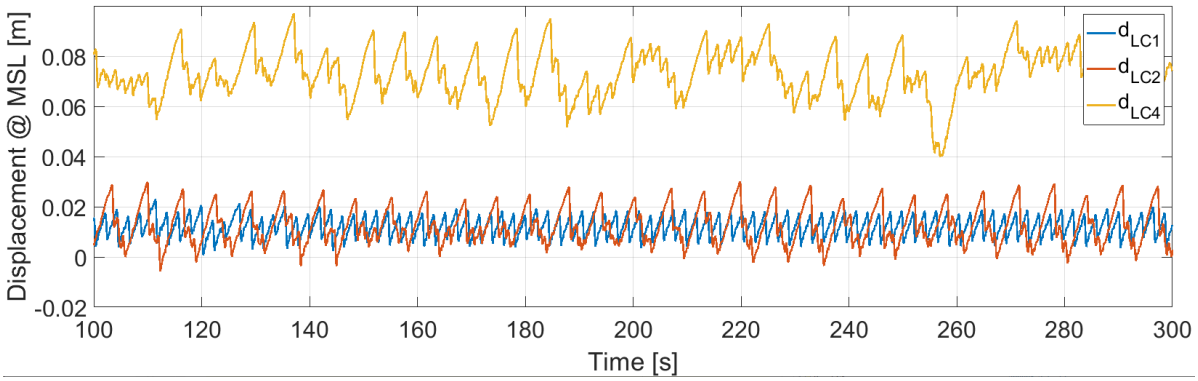

(b) In-line displacements @ MSL

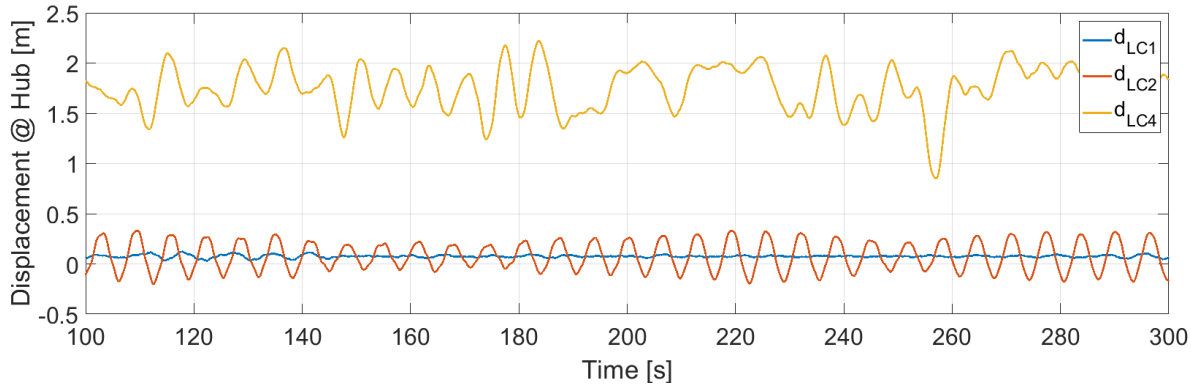

(c) In-line displacements @ Hub

Figure 7.9: Time series at an ice indentation speed of 10 [mm/s] for three load cases; 1D idling (LC1), 2D idling (LC2) and 2D with aligned wind (LC5)

To the author's knowledge, this 1st bending mode synchronisation phenomenon has neither been observed in full scale nor model tests. Nevertheless, its existence was simulated earlier in Willems and Hendrikse (2019). According to Willems and Hendrikse (2019), this regime occurs for specific

structures where frequency lock-in occurs in the 2nd bending mode only. Indeed, in order for frequency lock-in to occur in the 2nd bending mode, the vibration frequency must undergo a build-up, crossing the 1st bending mode, to the 2nd bending mode. Then, it seems rather unlikely that no synchronisation would occur when the vibration frequency approaches and crosses the 1st bending mode. This expected synchronisations likely constitutes the simulated 1st bending mode ice-structure interaction regime simulated. Also, this reasoning makes the existence of this 1st bending mode ice-structure interaction subject to frequency lock-in occurring in the 2nd (or higher) bending mode. As no 2nd bending mode frequency lock-in has been observed, it is sensible that the 1st bending mode ice-structure interaction regime has neither been observed. However, when accepting that this ice-structure interaction regime does occur, it immediately poses a critical load case, as was also concluded in Willems and Hendrikse (2019). Then, broadening the view to the different load cases once again, the effect of applying two-dimensional ice and misaligned wind on the development of this 1st bending mode synchronisation phenomenon is crucial.

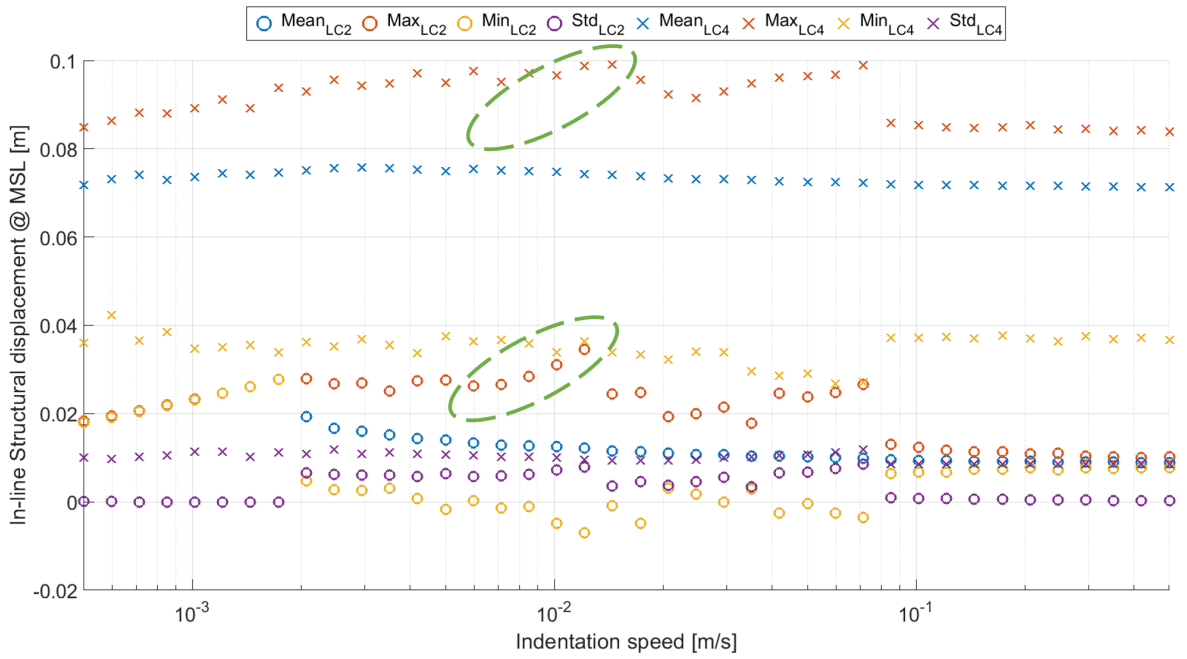

Figure 7.10: Statistical representation of in-line structural displacements at MSL during 2D idling (LC2) and 2D aligned wind (LC4). The highlighted difference shows how the maximum structural displacement increases with ice indentation speed during this newly identified dynamic ice-structure interaction regime

To that end, firstly, the effect of aligned wind loads on the development of this 1st bending mode synchronisation phenomenon is assessed. The highlighted sections of Figure 7.10 show the increased maximum displacement with increased ice indentation speed typical for ice-structure synchronisation, for both an idling turbine (load case 2) and a turbine with aligned ice and wind (load case 4). However, for the idling turbine, this phenomenon manifests more purely. The following two causes are expected to cause the suppression of the 1st bending mode synchronisation phenomenon for the aligned wind load case (load case 4):

1. The development is disturbed by high irregular wind loads.
2. The development is suppressed by aerodynamic damping, which' effect is especially noteworthy in the 1st bending mode

Indeed, when observing the structural velocities at hub height of Figure 7.11 - where the 1st bending mode is most pronounced - the 1st bending mode synchronisation phenomenon manifests more clearly in for the idling turbine (load case 2). Towards the upper ice indentation range of the highlighted 1st bending mode synchronisation region, the simulated standard deviation of the structural velocity at hub height for the idling turbine even reaches higher values than that of the aligned wind load, indicating a highly dynamic turbine.

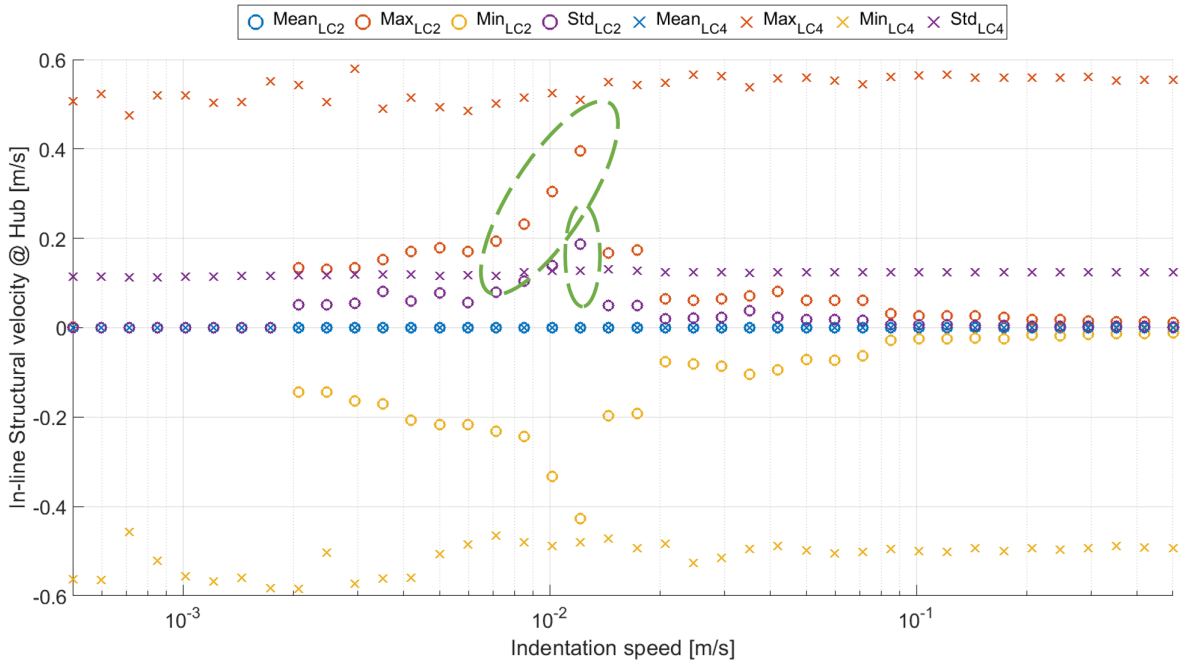

Figure 7.11: Statistical representation of in-line structural displacements at hub height during 2D idling (LC2) and 2D with aligned wind (LC4). The highlighted difference shows how the maximum structural displacement increases with ice indentation speed during this newly identified dynamic ice-structure interaction regime and the fact that the maximum structural velocities at hub heights are reached in this regime

Thus, the 1st bending mode phenomenon is relevant for both idling turbines for which it develops to a more considerable extent, and turbines in power production, where it develops to a lesser extent but the superposed wind loads cause similarly dynamic turbine behaviour. Regarding the extent to which this 1st bending mode phenomenon develops for both one-dimensional and two-dimensional ice, the displacements at waterline for idling load cases 1 (one-dimensional) and 2 (two-dimensional) are compared in Figure 7.12, yielding an interesting finding. Namely, as observable by the highlighted range in which 1st bending mode synchronisation occurs, the 1st bending mode synchronisation region appears to be terminated at lower ice indentation speeds for the one-dimensional ice. Therefore, the maximum simulated displacements at MSL grows roughly 25 % larger for two-dimensional ice than for one-dimensional ice, which results in up to 80 % higher maximum structural displacements and velocities at hub height for two-dimensional ice than for one-dimensional ice during idling. When observing the highlighted range of Figure 7.13, the cause of the abrupt termination of the 1st bending mode synchronisation regime for one-dimensional ice can be deducted. Apparently, for one-dimensional ice, several higher modes are excited before reaching the 2nd bending mode for frequency lock-in, terminating the 1st bending mode synchronisation. These bending modes are not excited for the two-dimensional configuration, raising the question of why this crucial difference manifests. To that end, the frequency spectra of structural vibrations for load cases 1 (idling 1D), 2 (idling 2D) and 4 (aligned wind) are shown jointly in Figure 7.14. These load cases are shown at an ice indentation speed of 10 [mm/s], at which 1st bending

mode synchronisation still occurs for load case 2 but has been terminated for load case 1. Clearly, for all three load cases, both the 1st bending mode and a higher global mode are excited to some extent. However, in case of load case 1, this higher global mode is excited to a more considerable extent such that this mode becomes dominant.

Suppose these higher-order bending mode excitations also occur for the certified one-dimensional ice-structure interaction models such as the Hendrikse (2017) model. In that case, these models might underestimate the dynamic behaviour of idling wind turbines during 1st bending mode synchronisation. This is noteworthy, as it is the only finding for which two-dimensional ice leads to a more critical load case. Still, it should be noted that these maximum structural displacements during idling remain significantly larger for the aligned wind case, making it questionable whether they will ultimately result in critical load cases at all.

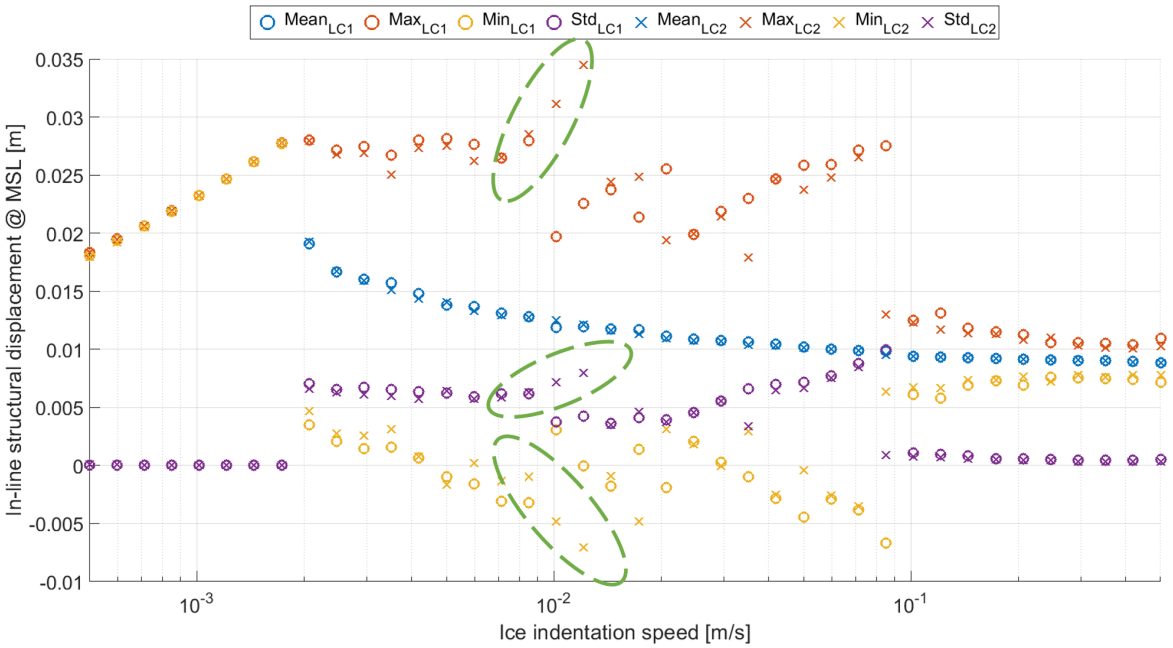

Figure 7.12: Statistical representation of in-line structural displacements at MSL during idling for the 1D restricted turbine (LC1) and a 2D turbine (LC2). The highlighted difference shows how the 1st bending mode interaction develops more significantly for LC2

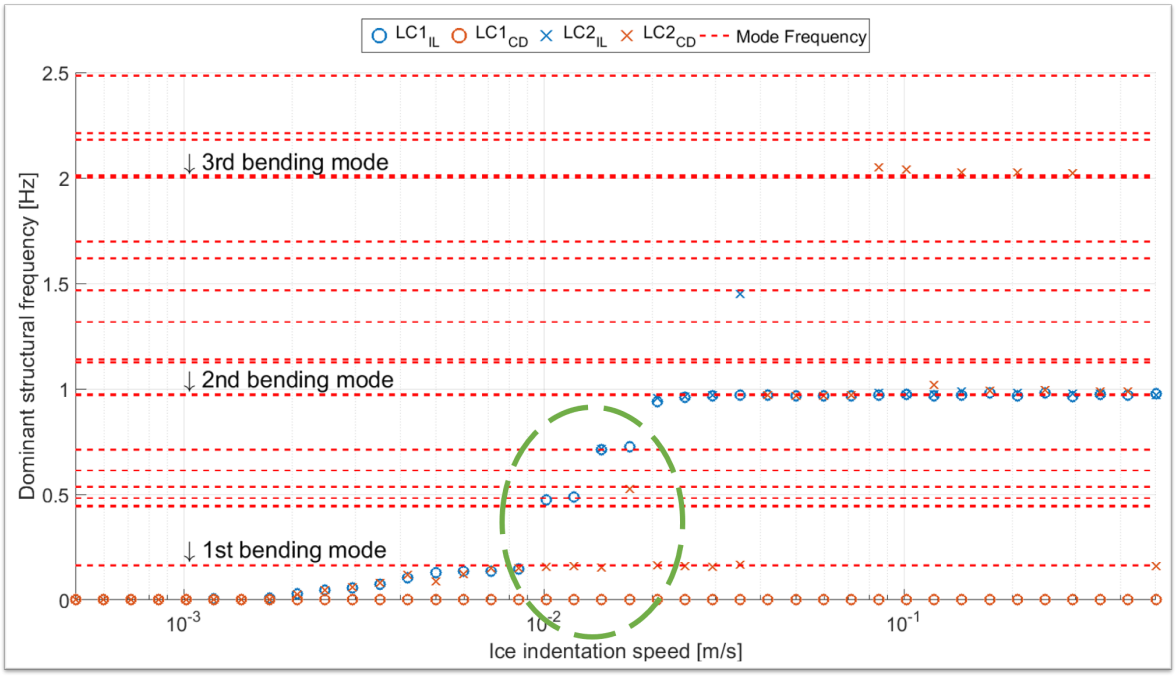

Figure 7.13: Statistical representation of dominant structural frequencies for the 1D restricted turbine (LC1) and a 2D turbine (LC2). The highlighted difference shows how for (LC1), non-bending modes are excited

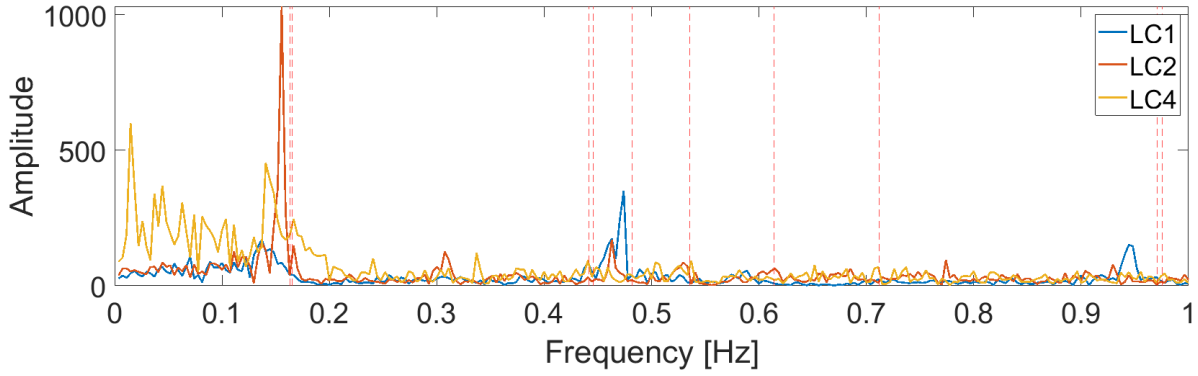

Figure 7.14: Frequency spectra at an ice indentation speed of 100 [mm/s] for three load cases; 1D idling (LC1), 2D idling (LC2) and 2D with aligned wind (LC4)

7.5. Reduced frequency lock-in range in a two-dimensional environment

One of the better observable differences between the one-dimensional load cases (load cases 1 and 3) and their two-dimensional counterparts (load cases 2 and 4) is the lower transition ice indentation speed from frequency lock-in to continuous brittle crushing. As argued in Chapter 2, this transition speed is best determinable by evaluating the β-factors. Therefore, the ice indentation speeds at which transition from frequency lock-in to continuous brittle crushing occurs are highlighted by the drop in β-factors for idling and aligned-wind turbines in Figure 7.15 and Figure 7.16 respectively. This lower transition speed is a significant finding, as around the upper bound of the frequency lock-in regime, the most dynamic structural behaviour occurs. Note that the term 'most dynamic structural behaviour' is used in general terms here. Naturally, the phenomenon at which the most dynamic behaviour occurs depends on which location along the height of the turbine is evaluated.

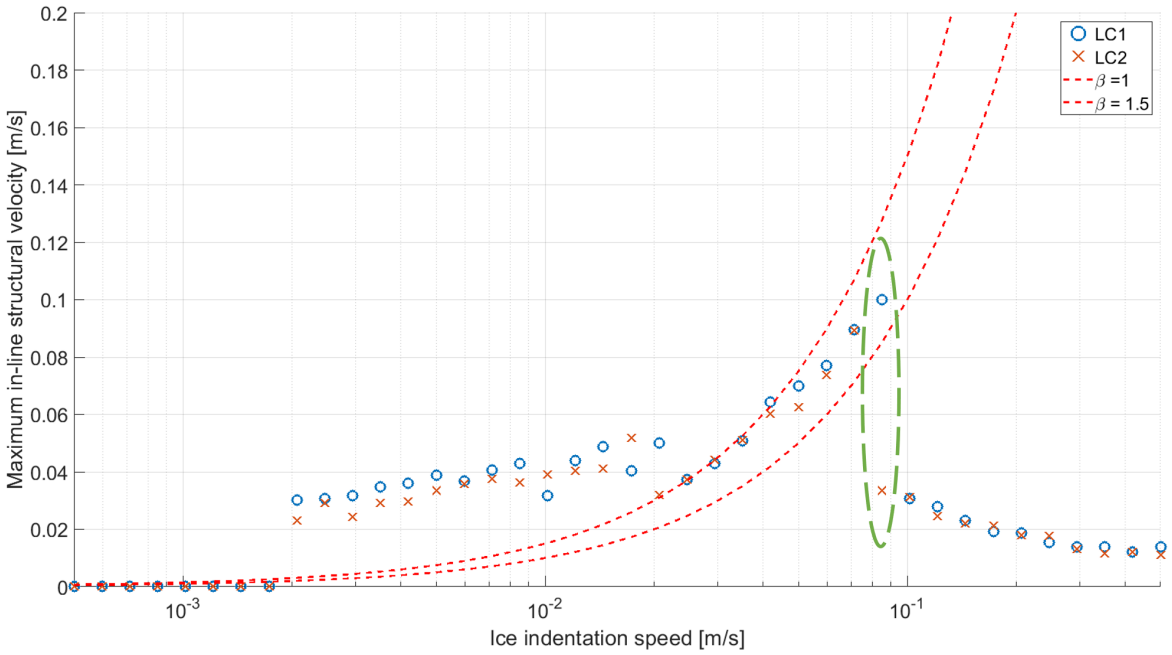

Figure 7.15: β-ratios during idling, both for an in-line restricted turbine (LC1) and a 2D turbine (LC2). The highlighted difference shows that frequency lock-in is terminated at a lower ice indentation speed for LC2 than for LC1

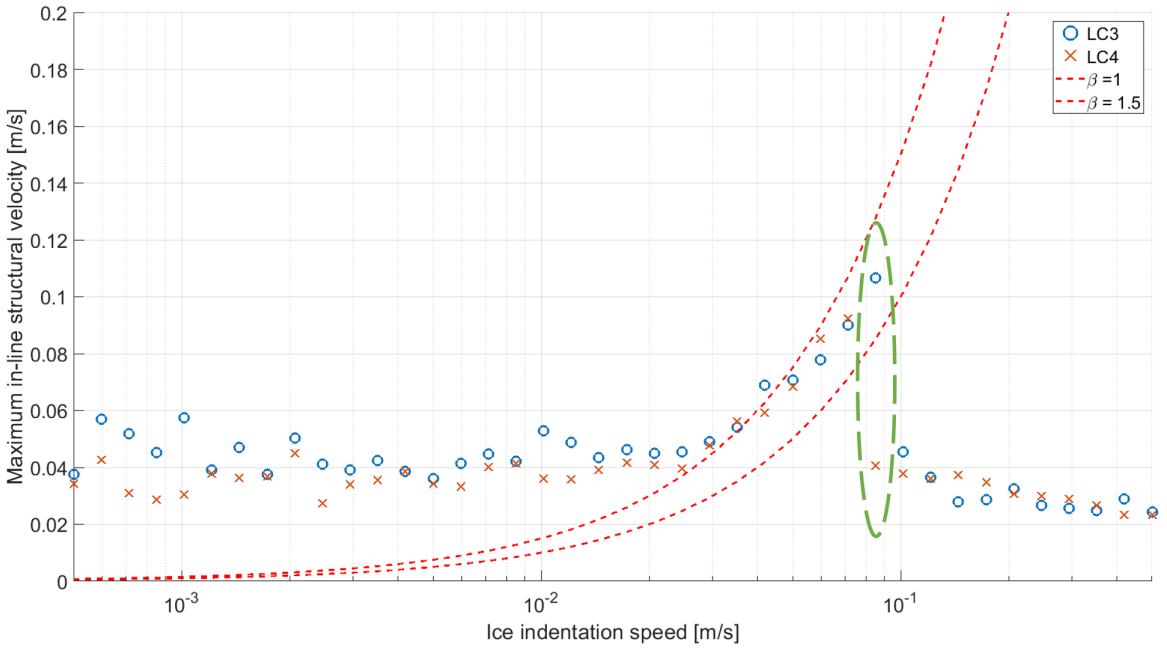

Figure 7.16: β-ratios during production, both for an in-line restricted turbine (LC1) and a 2D turbine (LC2). The highlighted difference shows that frequency lock-in is terminated at a lower ice indentation speed for LC2 than for LC1

Unfortunately, deducing why this transition ice indentation speed lies higher for one-dimensional ice than for two-dimensional ice is somewhat more difficult to comprehend than the earlier discussed findings of Section 7.3 and Section 7.4. Since in Section 7.3, the observed differences occurred within a single phenomenon thus allowing for a detailed evaluation through comparing the time series and in Section 7.4, the observed differences manifested in a shift of dominant natural

frequency, thus allowing for deducing the observed difference to a difference in dominant vibration frequency. Unfortunately, in this case, comparing time series in this around the transition speed is not useful as that would yield a comparison between frequency lock-in time series and continuous brittle crushing time series. Also, as the in-line structural frequency does not shift from frequency lock-in to continuous brittle crushing, frequency analysis will not yield any insight towards these different transition speeds. Therefore, at this stage, declaring why the transition from frequency lock-in to continuous brittle crushing occurs at higher ice-indentation speeds for the 1D case remains speculative. Nevertheless, the following two main explanations are proposed:

1. As shown in Section 7.3, the global ice loads are higher for one-dimensional ice than for two-dimensional ice. Thus, for one-dimensional ice, more energy is transferred from the ice to the structure, possibly making frequency lock-in occur up to higher ice indentation speeds. Additionally, the frequency lock-in prediction criteria of Equation 2.1 indicates that for thicker and stronger ice floes, frequency lock-in is more likely to develop, which is analogous to stating that for higher ice forces, frequency lock-in is more likely to develop.

2. Forcing the structure to move solely into one direction channels the energy transferred from the ice to the structure in the in-line direction, possibly resulting in frequency lock-in developing for higher ice-indentation speeds. Also, for a two-dimensional structure, energy dissipates in the cross-drift direction, which does not occur for the one-dimensionally constrained turbine.

If the former of these two explanations applies, one-dimensional ice overpredicts the range at which frequency lock-in occurs. However, if the latter of these explanations applies, the observed difference might be caused entirely by the application of a one-dimensionally restrained structure.

Finally, the transition speed result observed here cannot be seen in isolation from the transition speed discussion of Subsection 4.3.3. Interestingly, in that result, the transition from frequency lock-in to continuous brittle crushing was simulated to occur at higher ice indentation speeds for the two-dimensional case. However, despite its appearances, this is not necessarily a contradiction with the result simulated here, as in Subsection 4.3.3, the observed higher transition speeds for the two-dimensional case were attributed entirely to the shape effect. Then, as the one-dimensional ice discussed here includes the two-dimensional shape effect, this difference should not manifest for these coupled simulations. If anything, the findings here further underline the conclusion reached in Subsection 4.3.3 that the there observed higher transition speeds for ZAMBONI must be due to the shape effect.

7.6. The effect of misaligned wind on ice-structure interactions

The final area of analysis which is discussed in further detail does not concern a difference between load cases but instead concerns a high degree of similarity between the misaligned and aligned wind cases. This similarity is noteworthy as smaller global loads were hypothesised in Section 7.1, which in turn were hypothesised to lead to differences in simulation results.

For the cross drift load case (load case 5), such differences are indeed observable. As argued in detail in Section 7.3, cross-drift wind loads lead to ice crushing at the side of the structure, causing reduced in-line ice loads. In turn, these smaller loads lead to some interesting observations for load case 5, such as the relatively long-lasting 1st bending mode synchronisation phenomenon.

However, load case 5 represents a mostly theoretical loading scenario that is expected to seldom occur (Koreman, 2019). In contrast, load case 6, with an ice wind misalignment of 20 [°] represents the

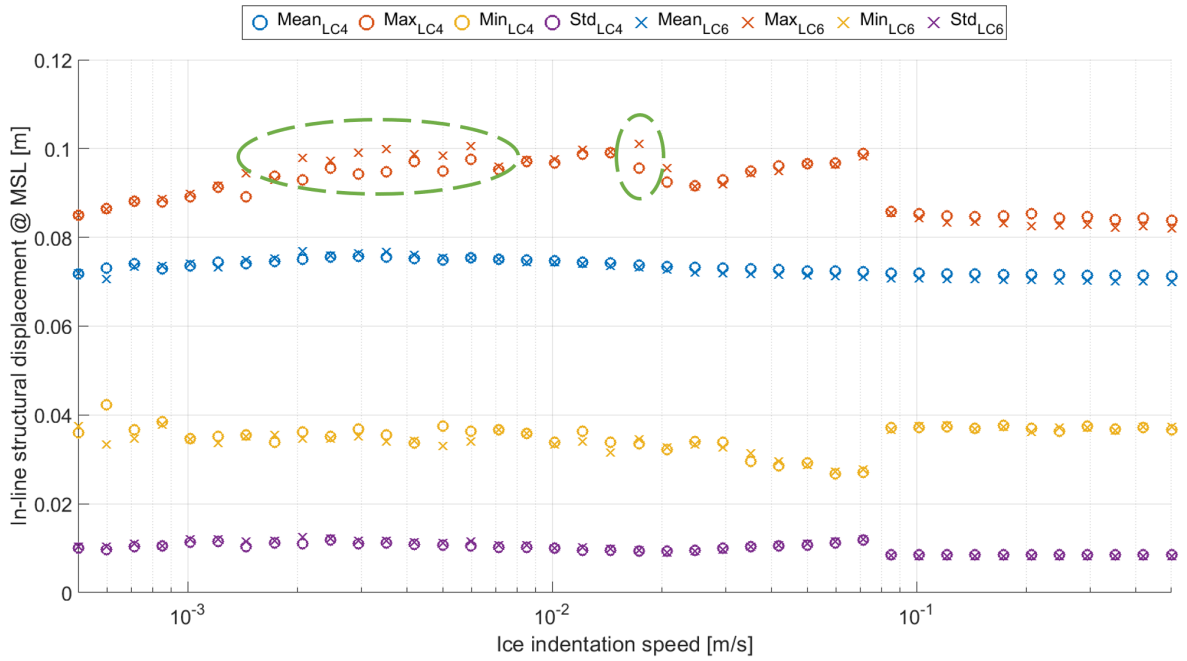

Figure 7.17: Statistical representation of the in-line structural displacements at MSL for 2D aligned wind loads (LC4) and 2D 20 [°] misaligned wind loads (LC6), the highlighted sections show the consistently higher maximum displacement in the intermittent crushing range for load case 6 and the higher ice indentation speed at which the 1st bending mode regime is terminated for misaligned winds

most frequently occurring relative directions of ice and wind loads. In fact, according to the analysis in Koreman (2019), a 20 [°] misalignment is even more common than aligned ice and wind loads. However, as observable by all figure in Appendix E, hardly any differences are observable between load cases 4 (aligned wind) and 6 (20 [°] misaligned wind). Still, one remarkable finding is shown in Figure 7.17, where the highlighted ranges show larger in-line displacements consistently for the misaligned load case and a higher termination speed for the 1st bending mode synchronisation regime for the misaligned load case.

The larger in-line displacements during intermittent crushing are remarkable, as by the theory argued in Section 7.3, the in-line ice loads and structural displacements during intermittent crushing should be smaller for misaligned winds due to ice crushing at the sides of the structure. It is expected that these larger structural displacements are due to the non-symmetric turbine model discussed in Chapter 6. In Section 6.3, it was shown that upon applying an in-line wind force, the turbine vibrates slightly in the cross-drift direction as well. Therefore, applying a slightly misaligned wind as in load case 6 might cause the ice load to be exerted more aligned to the turbine's vibration direction instead of less aligned. In turn, this would lead to larger maximum displacements during intermittent crushing.

In part, the higher ice indentation speed at which the 1st bending mode synchronisation regime is terminated might also be explained by this unsymmetrical effect. In Section 7.4, it was shown that aligned wind causes a less pronounced 1st bending mode synchronisation but simultaneously appears to cause the 1st bending mode synchronisation regime to last up to higher ice indentation speeds. Additionally, it should be noted that for the 90 [°] misalignment of load case 5, the 1st bending synchronisation phenomenon is simulated to manifest up to even higher ice indentation speeds. This indicates that perhaps misaligned ice and wind cause the 1st bending mode synchronisation phenomenon to last up to higher ice indentation speeds. However, in order to draw any definitive conclusions in this field, simulations should be performed at additional ice and wind misalignment

conditions.

Finally, if these findings are accurate, the slightly misaligned load case of load case 6 might be more critical than the fully aligned load case of load case 4. If so, this might cause the current one-dimensional ice-structure interaction models to underestimate the most critical load cases slightly. Therefore, this observation is the second and final observation, where ZAMBONI predicts a possibly more critical load case.

7.7. Recommendations towards further coupled analysis

Thus, in this chapter, in total, 240 simulations were performed. These consist of 40 distinct ice indentation speeds for 6 different load cases. Although these simulations allowed for the analyses discussed in Section 7.2 to Section 7.6, for several analyses, additional simulations might yield additional insight. Furthermore, in several of the analyses, uncertainty was introduced by how ZAMBONI was applied. Therefore, for further analyses of coupled simulations in ZAMBONI, the following five recommendations are given.

1. For the performed simulations, 40 ice indentations speeds were distributed logarithmically from 0.5 [mm/s] to 500 [m/s]. Although this gives a useful broad scope, this method results in a lack of data point resolution near the most relevant areas. Most notably, the different ice indentation speeds at which regimes terminate as discussed in Section 7.4 and Section 7.5, were deducted from different phenomena occurring at only one ice indentation speed. For example frequency lock-in occurred with one-dimensional ice up to 85 [mm/s] whereas for two-dimensional ice, at 85 [mm/s] continuous brittle crushing was already occurring. However, it is unclear at which point from 70 [mm/s] to 85 [mm/s] FLI transitions to continuous brittle crushing for two-dimensional ice. In turn, it is unclear at which point between 85 [mm/s] and 100 [mm/s] one-dimensional ice transitions from frequency lock-in to continuous brittle crushing. Therefore, the currently registered differences between one- and two-dimensional ice can still result from large termination speed differences such as 72 [mm/s] and 98 [mm/s], but might just as well result from a small termination speed difference such as 84 [mm/s] and 86 [mm/s]. Therefore, it is recommended to add more simulations when required locally. Specifically, around the termination of the 1st bending mode synchronisation regime and the frequency lock-in regime, such additional points would increase the accuracy of the drawn conclusions

2. Similarly, as argued in Section 4.4, the ice solver of ZAMBONI is applied on a time-step basis rather than integrating it in the ODE solver used to solve the turbine motions structurally. Although the verification procedure of Chapter 4 has shown this method to be acceptable, it does, by definition, introduce small inaccuracies, especially in the more dynamic regimes. Therefore, it is recommended to integrate the ice solver of ZAMBONI in its ODE environment to eliminate these uncertainties.

3. As outlined in Section 7.1, one-dimensional ice load cases have been mimicked in these analyses by restraining the turbine in the in-line ice-drift direction. Therefore, some of the differences between one- and two-dimensional ice are not simulated, as argued in Section 7.1. Additionally, in Section 7.4, suspicion was raised on the validity of such a restrained turbine as only for the one-dimensionalised turbines, in-line vibration frequencies exciting non-bending modes were observed. In order to overcome this uncertainty, one can attempt to compare ZAMBONI's coupled simulations with the VANILLA simulations of Willems and Hendrikse (2019). In that case, the incompatibility of ZAMBONI and the Hendrikse (2017) model through assumed rectangular versus cylindrical structures has to be overcome. To that end,

for ZAMBONI, ice parameters have to be derived that correspond to a rectangular structure, as discussed in Section 4.4.

4. Aside from adding simulations at more ice-indentation speeds, it can also be insightful to add simulations for various ice wind misalignment directions. When varying the wind direction, the most critical combination of ice and wind loads can be determined. As hinted in Section 7.6, that critical combination does not necessarily occur for aligned ice and wind conditions. In order not to perform impractically many simulations, one can consider performing simulations at a specific ice indentation speed. Possibly, an intermittent crushing ice indentation speed such as 3 [mm/s] is suitable for this analysis. That way, the misalignment direction at which maximum deflection during intermittent crushing occurs can be identified

5. Finally, the statistical representations of the performed simulations all make use of the minimum and maximum values. However, as each simulation covers an ice indentation event lasting hundreds of seconds, these minimum and maximum values are easily corrupted by one outlier. An example of this effect is the maximum ice load during intermittent crushing for idling and aligned wind. As observable in Figure 7.2, the maximum ice loads are near identical. However, for the idling case, that maximum ice load is reached during each loading phase, whereas for the aligned wind case, that maximum ice load is only reached sporadically. As an initially recommended improvement, one can consider displaying the mean of the ten highest peaks instead.

8

Conclusion

The main goal of this work is to develop a model capable of simulating ice-structure interactions in a two-dimensional model. A second goal is to identify the differences when simulating ice one-dimensionally or two-dimensionally by making use of that model. Finally, a third goal is to analyse the effect of misaligned ice and wind loads, which represents a newly simulable load case.

To this end, first, the 'Zero-friction contact Area variation Model By Omnidirectional Numerical Ice' (ZAMBONI) is outlined through its five fundamental principles. ZAMBONI fundamentally is an extension of the Hendrikse (2017) model in a two-dimensional environment. These five fundamental principles are, in ZAMBONI:

1. The location of each ice point is given by its 2D Cartesian coordinates, which jointly represent the frontal edge of the indenting ice floe in a finite area surrounding the structure
2. The ice-structure interface is assumed to be frictionless
3. The ice parameter N, representing a constant number of elements is replaced with an average ice element resolution R
4. Ice elements are added and deleted when required
5. For global force computations, the frontal spring of each ice element K_2, representing the linear elastic stiffness of the ice floe, act as one distributed spring $\bar{K}_2$ rather than an integer number of individual springs

Thereafter, to assess the correctness of ZAMBONI, it is verified and validated. Both of these areas pose their individual challenge. Firstly, for the verification procedure, ZAMBONI can only be verified in the in-line direction, as no suitable ice-structure interaction model simulating the cross-drift direction exists to verify with. However, the in-line verification procedure of ZAMBONI is considered largely successful, as the deviations between the Hendrikse (2017) model and ZAMBONI found are all well explained by the two-dimensionality of ice. Specifically, the following noteworthy findings are deduced from the verification procedure:

1. Ice loads in the creep and intermittent crushing regime are larger for the Hendrikse (2017) model than for ZAMBONI. This finding is shown to be a shape effect between rectangular and cylindrical structures.
2. Within the frequency lock-in regime, no differences in structural velocities, structural displacements, structural frequencies or beta values are observed. This finding is attributed to

the observation that the structural response in the frequency lock-in is governed by the natural frequency in which lock-in occurs and the ice indentation speed.
3. The frequency lock-in terminates at higher ice indentation speeds for ZAMBONI than for the Hendrikse (2017) model. This finding is again attributed to the shape effect between rectangular and cylindrical structures.

Secondly, the possibilities of validating ZAMBONI are limited by the scarcity of ice-structure interaction data, especially regarding cross-drift measurements. However, it is vital to validate ZAMBONI in the cross-drift direction, since this direction was not included in the verification. Generally, the validation procedure is considered successful, with simulated cross-drift loads validated to be in the same order-of-magnitude as the measured ice loads.

This concludes the first aim of this thesis. In order to fulfil the second and third aim, ZAMBONI is coupled to a full-scale wind turbine in the modal domain, including aerodynamic damping. Thereafter, coupled ice and wind loads are performed. Specifically, the following six load cases have been simulated, all for a wide range of ice indentation speeds:

1. Idling wind turbine with a one-dimensional structure
2. Idling wind turbine with a two-dimensional structure
3. Aligned power-producing wind turbine with a one-dimensional structure
4. Aligned power-producing wind turbine with a two-dimensional structure
5. 90 [°] misaligned power-producing turbine with a two-dimensional structure
6. 20 [°] misaligned power-producing turbine with a two-dimensional structure

Then, upon comparing the simulation results, several notable findings were deduced. The most important findings are listed below:

- For the two-dimensional load cases, smaller global ice loads were observed, especially during creep and intermittent crushing.
- A special 1st bending mode synchronisation load case was observed, especially for idling turbines. This ice-structure interaction regime occurs up to higher ice indentation speeds for two-dimensional ice. Furthermore, misaligned ice and wind loads appear to extend further the upper ice indentation speed limit of this regime
- For the two-dimensional load cases, the frequency lock-in regime was terminated at lower ice indentation speeds.
- A slightly misaligned wind appears to have a limited effect on ice-structure interactions. However, for the 20 [°] misaligned load cases, the most critical structure displacements during intermittent crushing are observed

Mostly, these findings conclude an overprediction of loads and displacement for one-dimensional ice. However, for two particular cases, the two-dimensional analyses appear to trigger more critical load cases than the one-dimensional analyses. These are the second and fourth of the notable finding listed above. Most of these findings are explainable and along with expectations. However, in order to create more insight in the extent to which these different findings apply, it is recommended to perform additional simulations around the ice indentation speeds and load cases that best describe the findings listed above. Ultimately, the three most vital next steps regarding ZAMBONI are:

- Coupling of ZAMBONI to mode shapes rather than to modal amplitudes

- A simulation campaign where ZAMBONI is compared to VANILLA (Willems and Hendrikse, 2019), to assert whether the simulated differences between one- and two-dimensional ice found in the coupled analysis indeed apply
- A detailed validation campaign to assert whether these simulations hold in an unstable ice environment.

If the findings of the coupled simulations indeed prove accurate, wind turbine design for ice-structure interactions can be optimised significantly.

Bibliography

Arapogianni, A., Moccia, J., and European Wind Energy Association. Wind in our sails - The coming of Europe's offshore wind energy industry. Technical Report November, European Wind Energy Association (2011).

Bjork, B. Ice-induced vibration of fixed offshore structures. part 2: Experience with Baltic lighthouses. Technical report, Ship Research Institute of Norway, Information Department (1981).

Blenkarn, K. A. Measurement and analysis of ice forces on cook inlet structures. In *Proceedings of the Annual Offshore Technology Conference*, volume 1970-April. Offshore Technology Conference (1970). ISBN 9781555637095. doi: 10.4043/1261-ms.

Dempsey, J. P. (2000). Research trends in ice mechanics. *International Journal of Solids and Structures*, 37(1-2):131–153. ISSN 00207683. doi: 10.1016/S0020-7683(99)00084-0.

Engelbrektson, A. Observations of a resonance vibrating lighthouse structure in moving ice. In *7th International Conference on Port and Ocean Engineering in Arctic Conditions (POAC)*, pages 895–964, Helsinki, Finland (1983).

Hendrikse, H. *Ice-induced vibrations of vertically sided offshore structures*. PhD thesis, Delft University of Technology (TU Delft) (2017).

Hendrikse, H. Model for simulation of dynamic ice-structure interaction for verically sided offshore structures - SDOF MATLAB implementation (2018). URL `https://doi.org/10.17632/582m8565dj`.

Hendrikse, H., Ziemer, G., and Owen, C. C. (7 2018). Experimental validation of a model for prediction of dynamic ice-structure interaction. *Cold Regions Science and Technology*, 151:345–358. ISSN 0165232X. doi: 10.1016/j.coldregions.2018.04.003.

Hendrikse, H. and Metrikine, A. (12 2015). Interpretation and prediction of ice induced vibrations based on contact area variation. *International Journal of Solids and Structures*, 75-76:336–348. ISSN 00207683. doi: 10.1016/j.ijsolstr.2015.08.023.

Hendrikse, H. and Nord, T. S. (5 2019). Dynamic response of an offshore structure interacting with an ice floe failing in crushing. *Marine Structures*, 65:271–290. ISSN 09518339. doi: 10.1016/j.marstruc.2019.01.012.

HSVA. Ivos Final Report. Technical report, HSVA, Hamburg (2020). URL `file:///C:/Users/osrrao02/Documents/forskning/Sensemaking_Final_Report.pdf`.

Huang, G. and Liu, P. (2 2009). A dynamic model for ice-induced vibration of structures. *Journal of Offshore Mechanics and Arctic Engineering*, 131(1):1–6. ISSN 08927219. doi: 10.1115/1.2979795.

Huang, Y., Shi, Q., and Song, A. (8 2007). Model test study of the interaction between ice and a compliant vertical narrow structure. *Cold Regions Science and Technology*, 49(2):151–160. ISSN 0165232X. doi: 10.1016/j.coldregions.2007.01.004.

ISO 19906. Petroleum and natural gas industries - Arctic offshore structures. Technical report, The International Organisation for Standardisation (2019).

Izumiyama, K. and Uto, S. Ice loading on a compliant indentor. In *Proceedings of the 16th International Conference on Offshore Mechanics and Arctic Engineering*, pages 431–436, Yokohama, Japan (1997).

Izumiyama, K., Irani, M., and Timco, G. Influence of compliance of structure on ice load. In *Proceedings of the 12th IAHR International Symposium on Ice*, pages 431–436, Trondheim, Norway (1994).

Jefferies, M. and Wright, W. Dynamic response of 'Molikpaq' to ice-structure interaction. In *Seventh International Conference on Offshore Mechanics and Arctic Engineering*, pages 201–220, Houston, Texas (1988).

Jordaan, I. J. (10 2001). Mechanics of ice-structure interaction. *Engineering Fracture Mechanics*, 68 (17-18):1923–1960. ISSN 00137944. doi: 10.1016/S0013-7944(01)00032-7.

Kärnä, T. and Jochmann, P. Field observations on ice failure modes. In *POAC*, number January 2003 (2003). URL http://virtual.vtt.fi/virtual/proj6/arki/julkaisut/strice/ObservedFailureModes_POAC03.pdf.

Koreman, D. Review of ice actions and ice-structure interactions for monopile supported offshore wind turbines. Technical report, Norwegian University of Science and Technology (2019).

Korzhavin, K. (1962), *Actions of ice on engineering structures*. Publishing House of Siberian Branch of USSR Acadery of Sciences.

Løset, S., Shkhinek, K. N., Gudmestad, O. T., and Høyland, K. V. (2006), *Actions from ice on Arctic offshore and coastal structures*. LAN. ISBN 5811407033.

Määttänen, M. Ten years of ice-induced vibrations in lighthouses. In *6th International Conference on Offshore Mechanics and Arctic Engineering (OMAE)*, pages 261–266, Houston, Texas (1987).

Muhonen, A. *Evaluation of three ice-structure interaction models*. PhD thesis, Helsinki University of Technology (1996).

Nordlund, O., Kärnä, T., and Järvinen, E. Measurements of ice-induced vibrations on Channel markers. In *9th IAHR Ice Symposium*, pages 537–539, Sapporo, Japan (1988).

Peyton, H. (1968). Sea Ice Strength. *Conference on Ice pressure against structures*.

Sodhi, D. S. (10 2001). Crushing failure during ice-structure interaction. *Engineering Fracture Mechanics*, 68(17-18):1889–1921. ISSN 00137944. doi: 10.1016/S0013-7944(01)00038-8.

Sodhi, D. S. (1 1995). An Ice-Structure Interaction Model. *Studies in Applied Mechanics*, 42(C):57–75. ISSN 09225382. doi: 10.1016/S0922-5382(06)80006-1.

Sodhi, D. S. and Haehnel, R. B. (12 2003). Crushing Ice Forces on Structures. *Journal of Cold Regions Engineering*, 17(4):153–170. ISSN 0887-381X. doi: 10.1061/(ASCE)0887-381X(2003)17:4(153). URL http://ascelibrary.org/doi/10.1061/%28ASCE%290887-381X%282003%2917%3A4%28153%29.

The International Energy Agency. World Energy Outlook. Technical report, The International Energy Agency (2019). URL https://www.iea.org/weo/.

Timco, G. W. and Weeks, W. F. A review of the engineering properties of sea ice (2 2010). ISSN 0165232X.

Timco, G. W., Irani, M. B., Tseng, J., Liu, L. K., and Zheng, C. B. (10 1992). Model tests of dynamic ice loading on the Chinese JZ-20-2 jacket platform. *Canadian Journal of Civil Engineering*, 19(5): 819–832. ISSN 0315-1468. doi: 10.1139/l92-093. URL `http://www.nrcresearchpress.com/doi/10.1139/l92-093`.

Toyama, Y., Sensu, T., Minami, M., and Yashima, N. Model tests on ice-induced self-excited vibration of cylindrical structures. In *Proceedings of the 7th International Conference on Port and Ocean Engineering under Arctic Conditions*, pages 834–844, Helsinki, Finland (1983).

Tsuchiya, M., Kanie, S., Ikejiri, K., Yoshida, A., and Saeki, H. An experimental study on ice-structure interaction. In *Proceedings of the Annual Offshore Technology Conference*, volume 1985-May, pages 321–327. Offshore Technology Conference (1985). ISBN 9781613990780. doi: 10.4043/5055-ms.

Willems, T. and Hendrikse, H. (2019). Coupled simulation of ice-structure interaction of offshore wind turbines in bhawc using vanilla. *Proceedings of the International Conference on Port and Ocean Engineering under Arctic Conditions, POAC*, 2019-June(June). ISSN 20777841.

Yue, Q. and Li, L. (2003). Ice problems in Bohai Sea oil exploitation. *Proceedings of the 17th International Conference on Port and Ocean Engineering under Arctic Conditions (POAC'03)*, 1(1993): 151–164.

List of Tables

List of Figures

A

All simulation results for the comparison of load cases 1 and 2

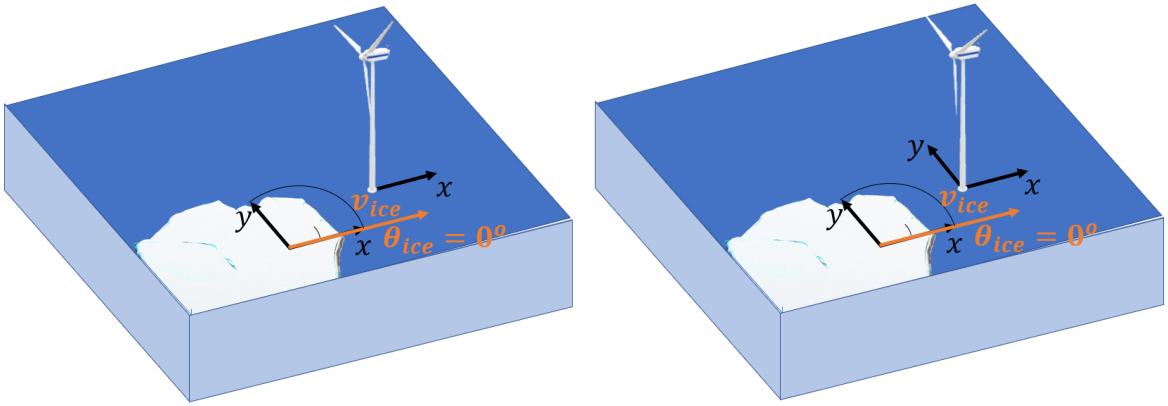

(a) Load case 1

(b) Load case 2

Figure A.1: Overview of the applied loads and structural degrees of freedom in load cases 1 and 2

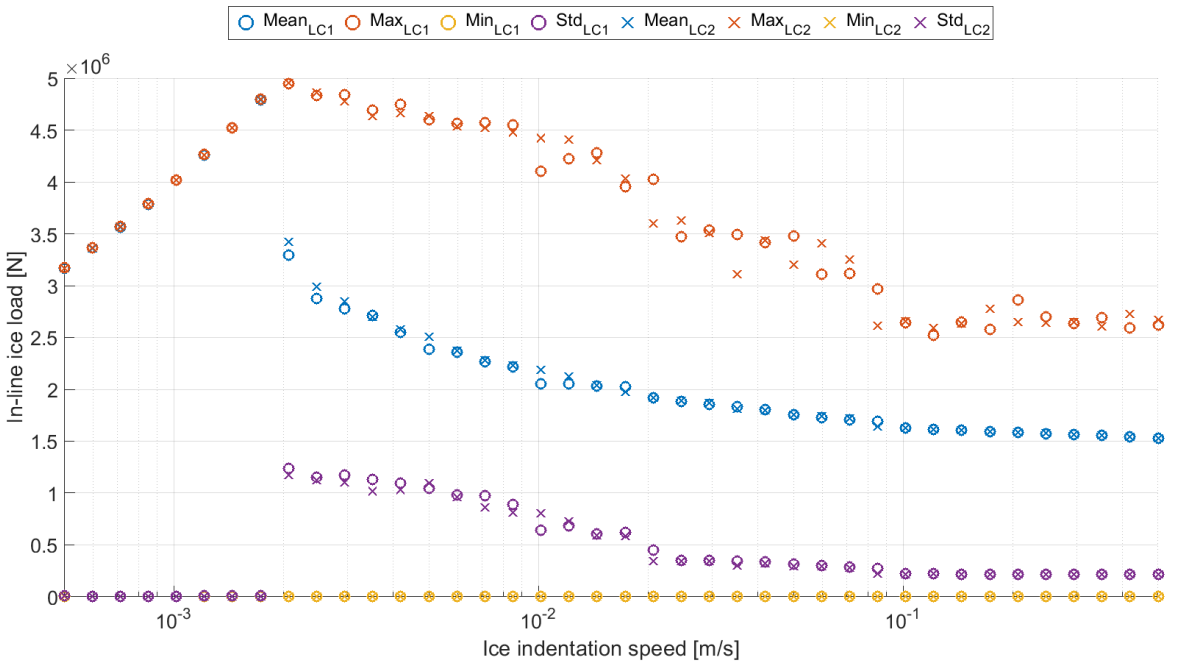

Figure A.2: Statistical characteristics of the in-line force exerted by an indenting ice floe on a cylindrical structure for varying ice indentation speeds and ice and structure characteristics as listed in Table 7.1. Results are shown for load cases 1 and 2, according to the load case overview of Section 7.1 and Figure A.1

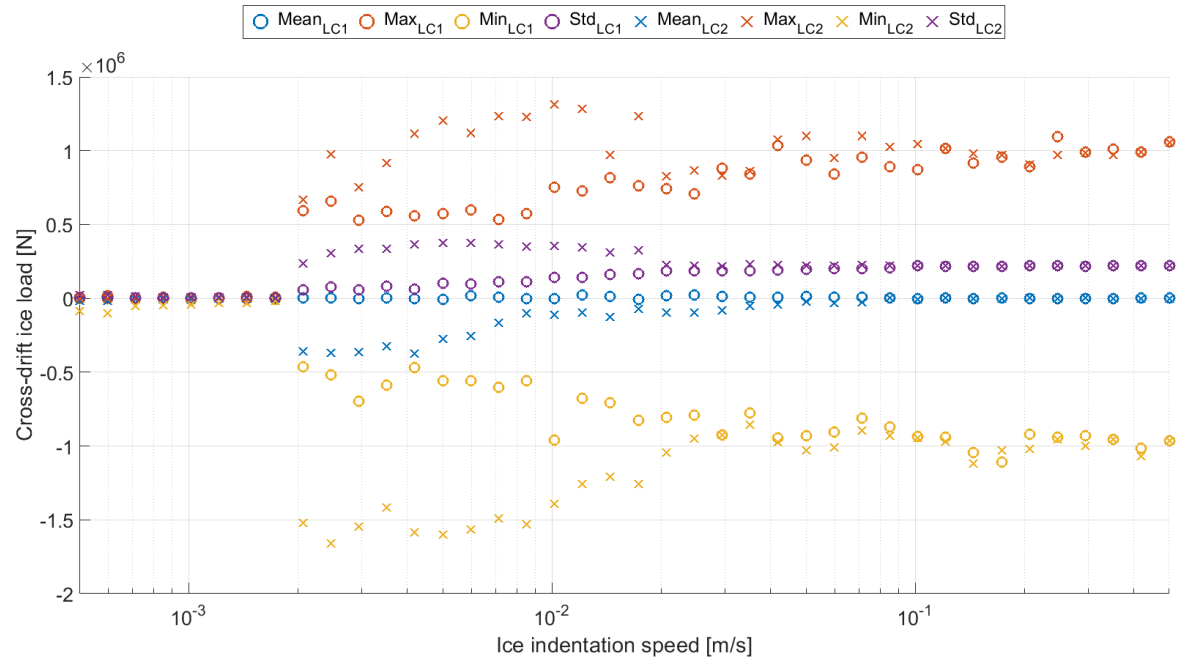

Figure A.3: Statistical characteristics of the cross-drift force exerted by an indenting ice floe on a cylindrical structure for varying ice indentation speeds and ice and structure characteristics as listed in Table 7.1. Results are shown for load cases 1 and 2, according to the load case overview of Section 7.1 and Figure A.1

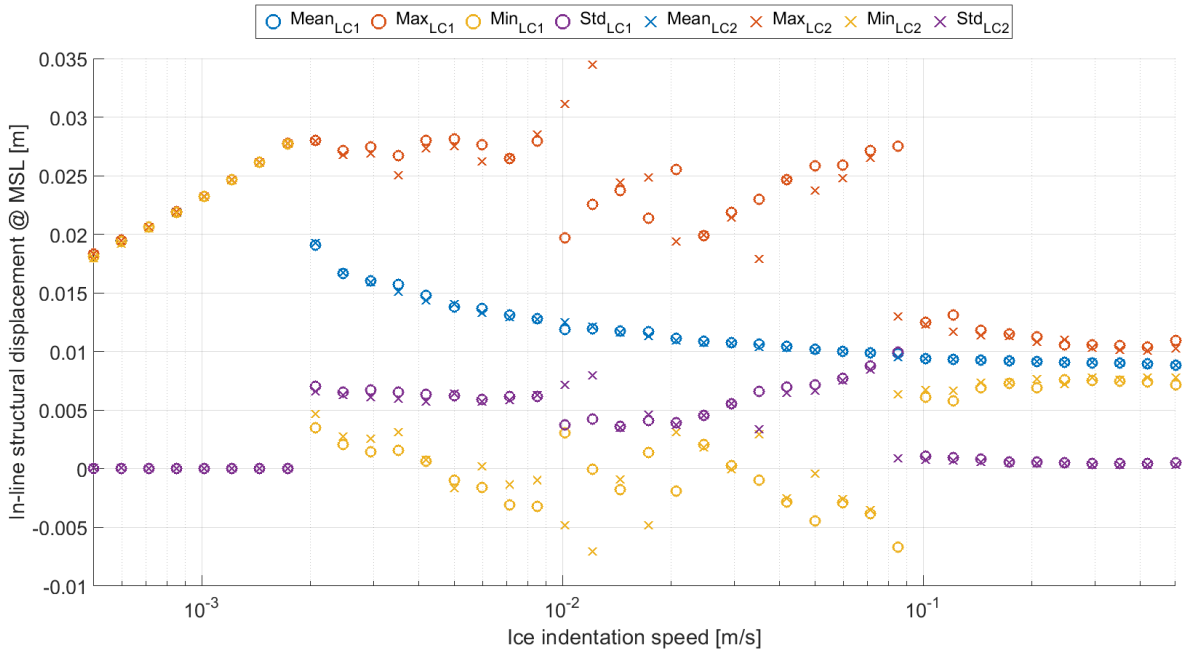

Figure A.4: Statistical characteristics of the in-line structural displacement at MSL caused by an indenting ice floe on a cylindrical structure for varying ice indentation speeds and ice and structure characteristics as listed in Table 7.1. Results are shown for load cases 1 and 2, according to the load case overview of Section 7.1 and Figure A.1

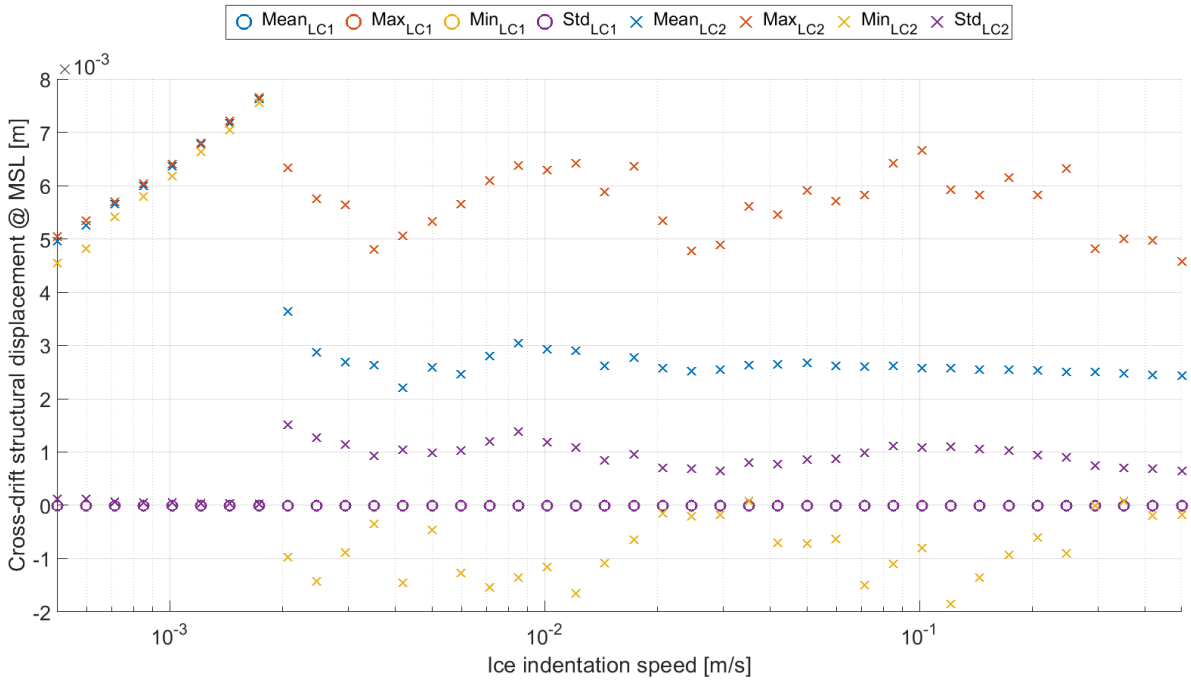

Figure A.5: Statistical characteristics of the cross-drift structural displacement at MSL caused by an indenting ice floe on a cylindrical structure for varying ice indentation speeds and ice and structure characteristics as listed in Table 7.1. Results are shown for load cases 1 and 2, according to the load case overview of Section 7.1 and Figure A.1

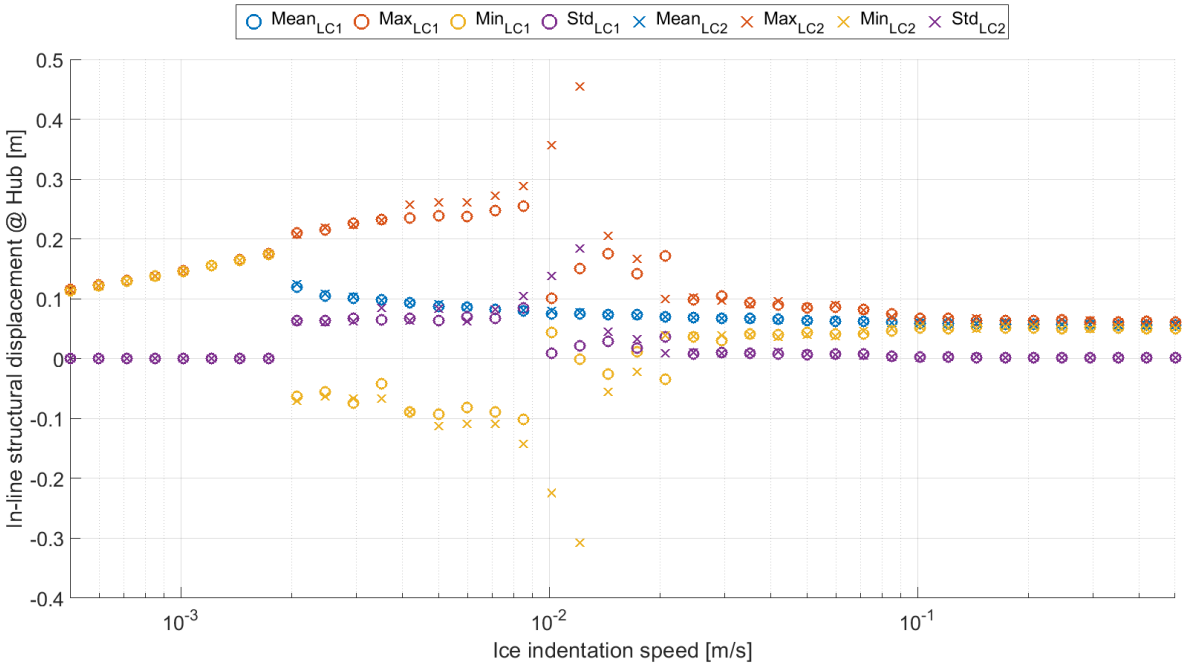

Figure A.6: Statistical characteristics of the in-line structural displacement at hub height caused by an indenting ice floe on a cylindrical structure for varying ice indentation speeds and ice and structure characteristics as listed in Table 7.1. Results are shown for load cases 1 and 2, according to the load case overview of Section 7.1 and Figure A.1

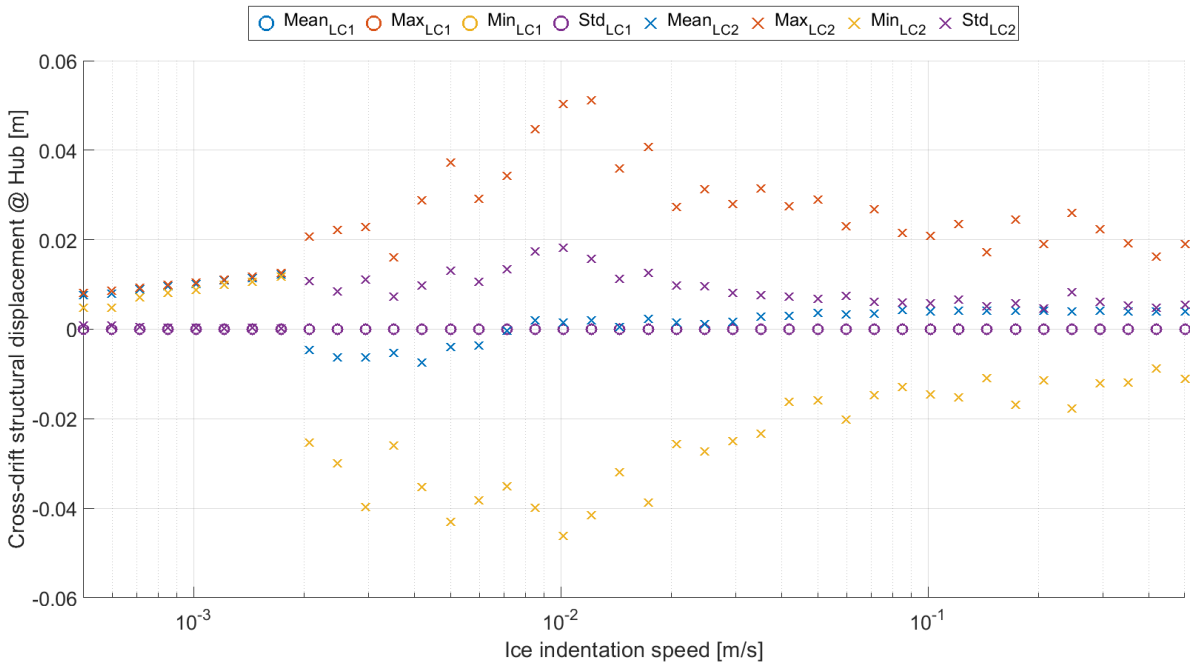

Figure A.7: Statistical characteristics of the cross-drift structural displacement at hub height caused by an indenting ice floe on a cylindrical structure for varying ice indentation speeds and ice and structure characteristics as listed in Table 7.1. Results are shown for load cases 1 and 2, according to the load case overview of Section 7.1 and Figure A.1

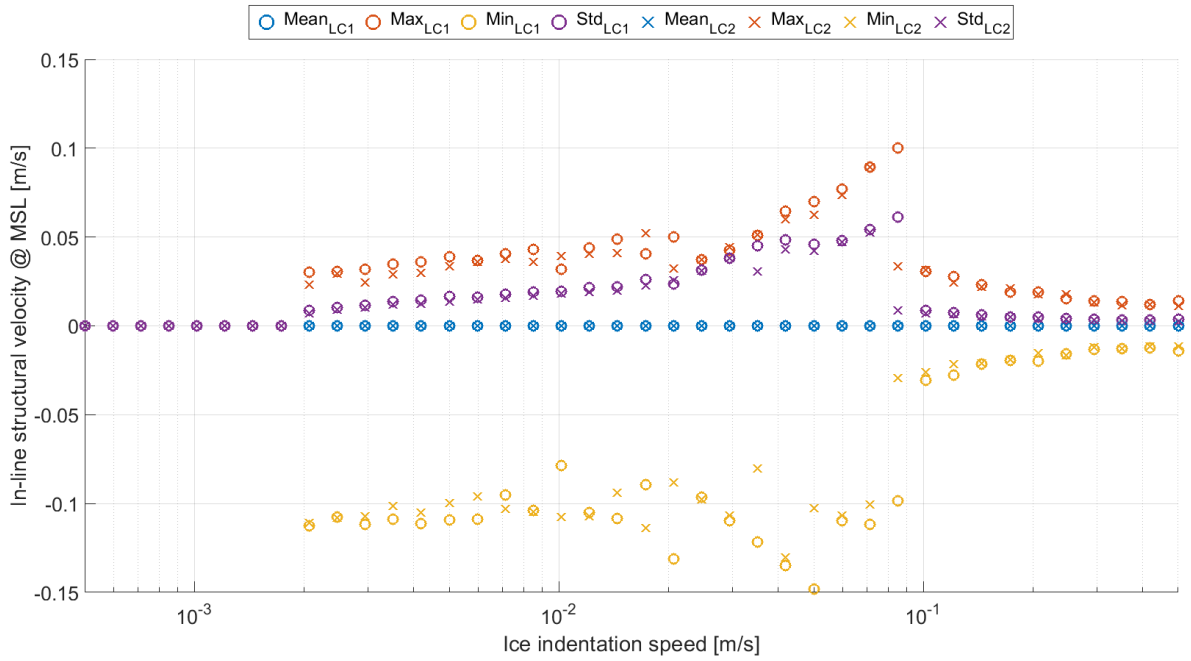

Figure A.8: Statistical characteristics of the in-line structural velocity at MSL caused by an indenting ice floe on a cylindrical structure for varying ice indentation speeds and ice and structure characteristics as listed in Table 7.1. Results are shown for load cases 1 and 2, according to the load case overview of Section 7.1 and Figure A.1

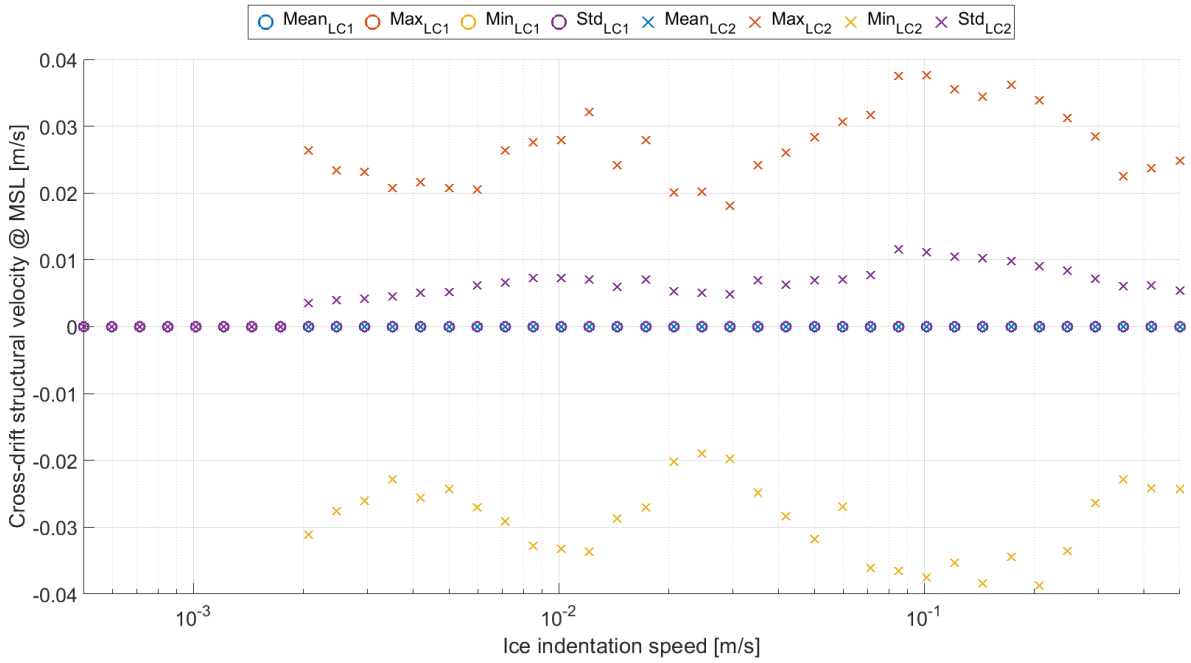

Figure A.9: Statistical characteristics of the cross-drift structural velocity at MSL caused by an indenting ice floe on a cylindrical structure for varying ice indentation speeds and ice and structure characteristics as listed in Table 7.1. Results are shown for load cases 1 and 2, according to the load case overview of Section 7.1 and Figure A.1

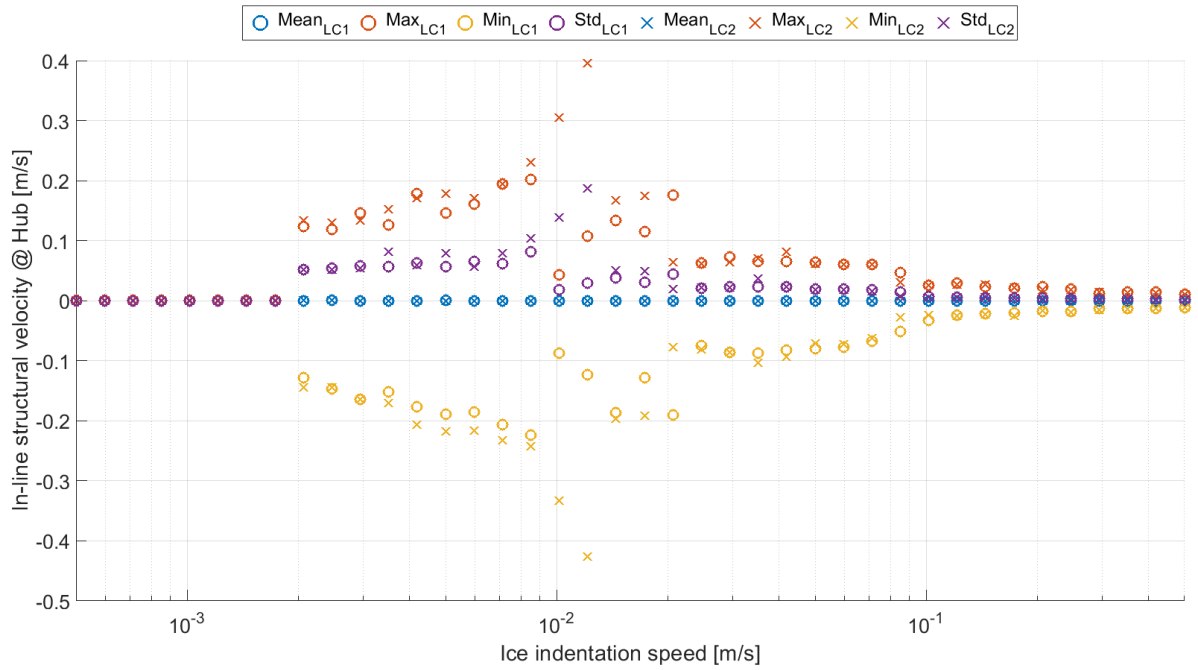

Figure A.10: Statistical characteristics of the in-line structural velocity at hub height caused by an indenting ice floe on a cylindrical structure for varying ice indentation speeds and ice and structure characteristics as listed in Table 7.1. Results are shown for load cases 1 and 2, according to the load case overview of Section 7.1 and Figure A.1

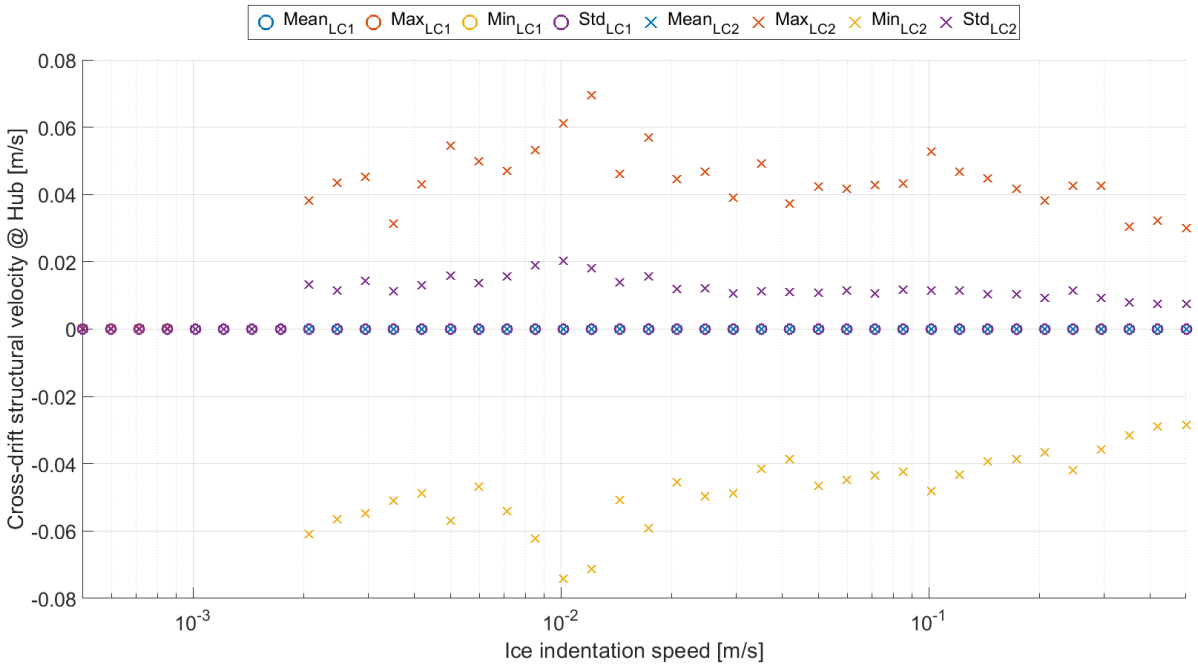

Figure A.11: Statistical characteristics of the cross-drift structural velocity at hub height caused by an indenting ice floe on a cylindrical structure for varying ice indentation speeds and ice and structure characteristics as listed in Table 7.1. Results are shown for load cases 1 and 2, according to the load case overview of Section 7.1 and Figure A.1

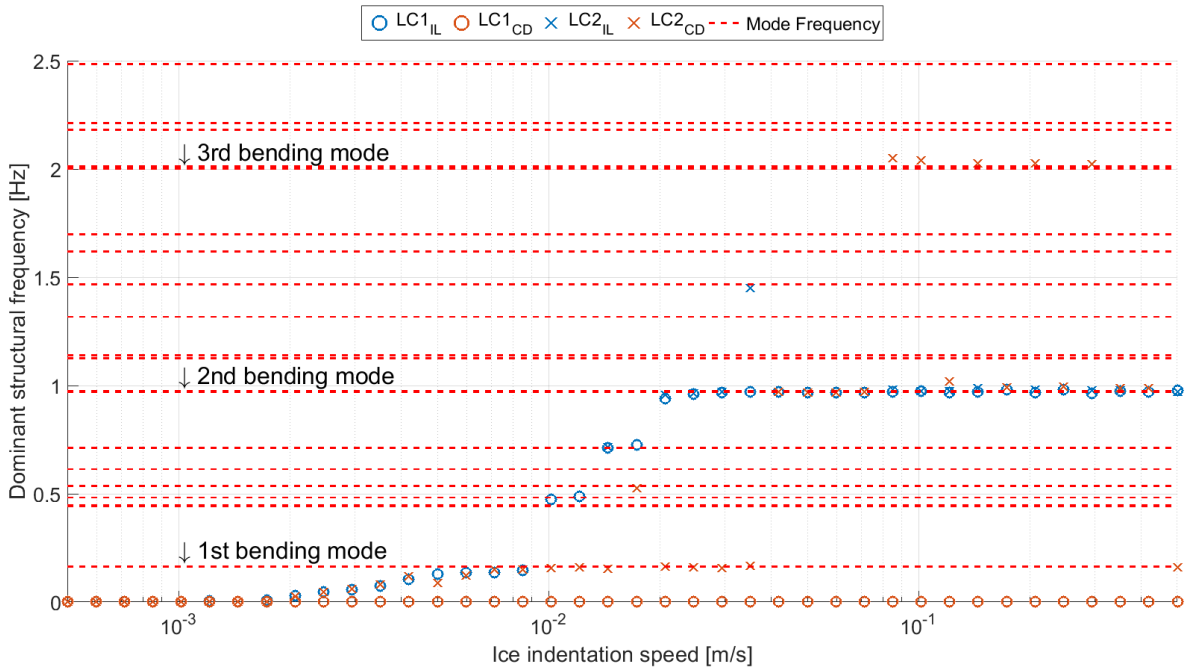

Figure A.12: Dominant structural frequencies for both the in-line and cross-drift direction for varying ice indentation speeds and ice and structure characteristics as listed in Table 7.1. Results are shown for load cases 1 and 2, according to the load case overview of Section 7.1 and Figure A.1

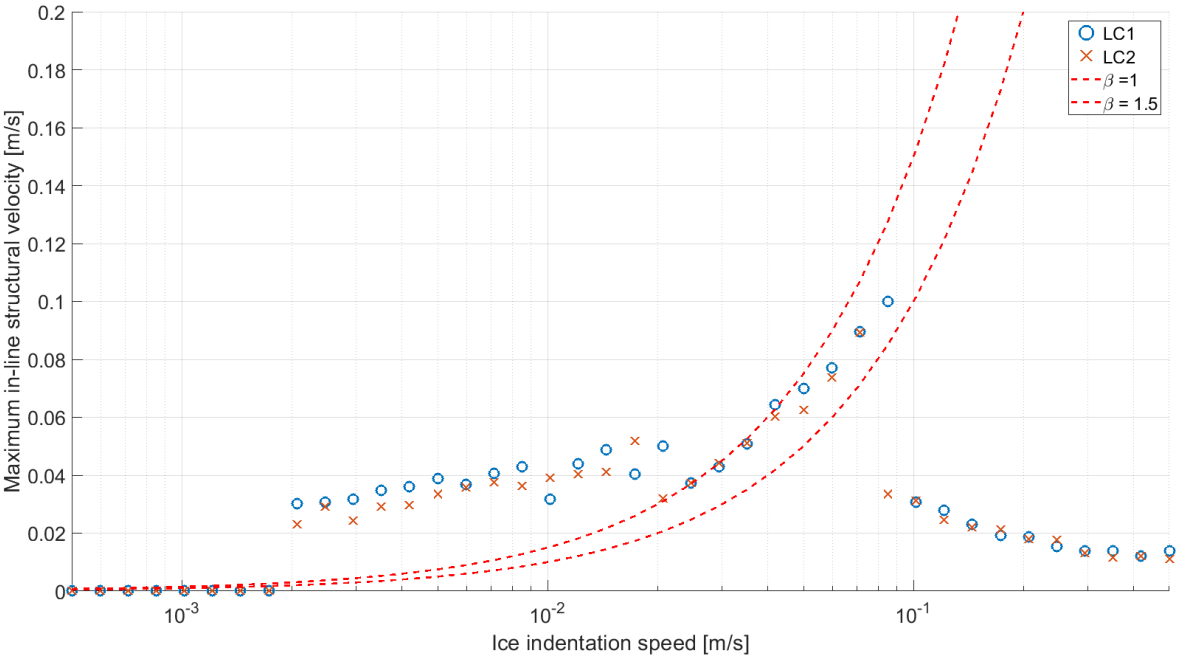

Figure A.13: β-values for varying ice indentation speeds and ice and structure characteristics as listed in Table 7.1. Results are shown for load cases 1 and 2, according to the load case overview of Section 7.1 and Figure A.1

B

All simulation results for the comparison of load cases 3 and 4

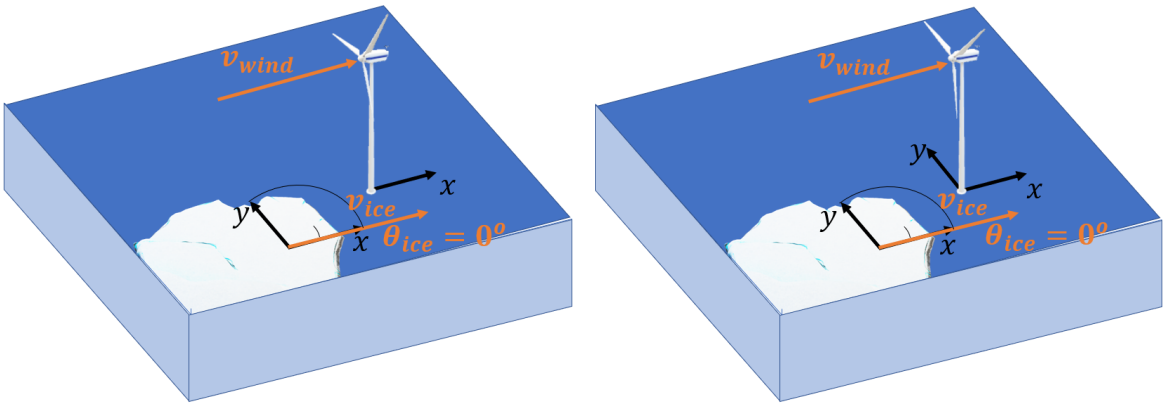

(a) Load case 3

(b) Load case 4

Figure B.1: Overview of the applied loads and structural degrees of freedom in load cases 3 and 4

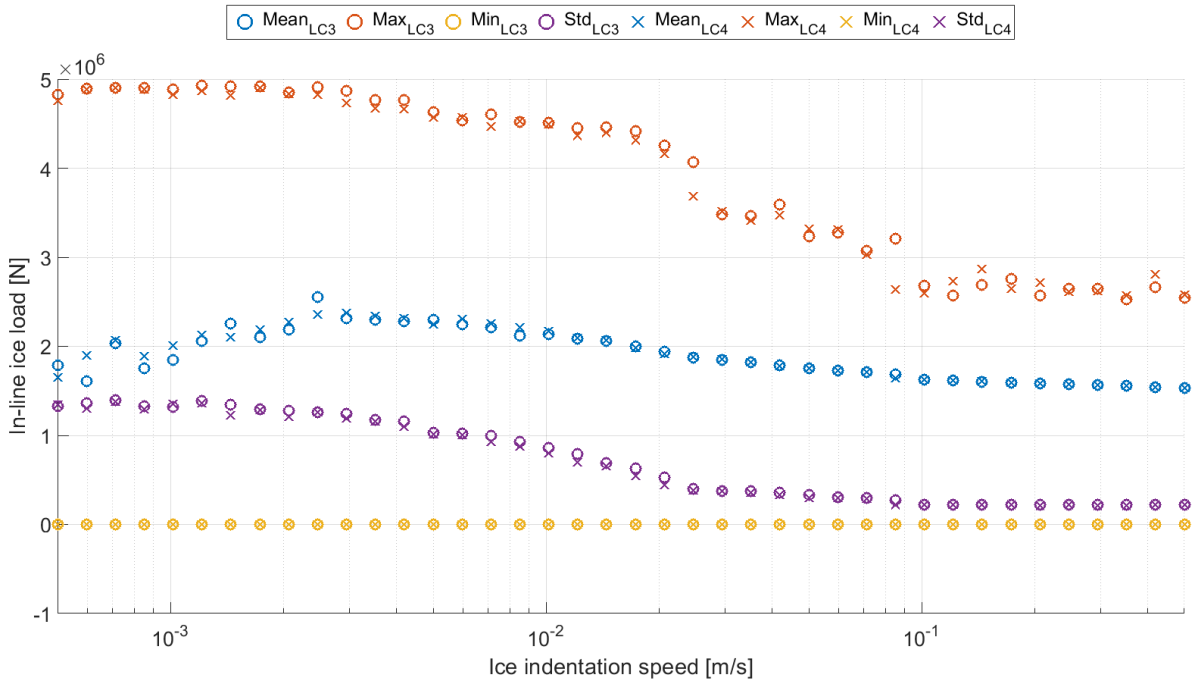

Figure B.2: Statistical characteristics of the in-line force exerted by an indenting ice floe on a cylindrical structure for varying ice indentation speeds and ice and structure characteristics as listed in Table 7.1. Results are shown for load cases 3 and 4, according to the load case overview of Section 7.1 and Figure B.1

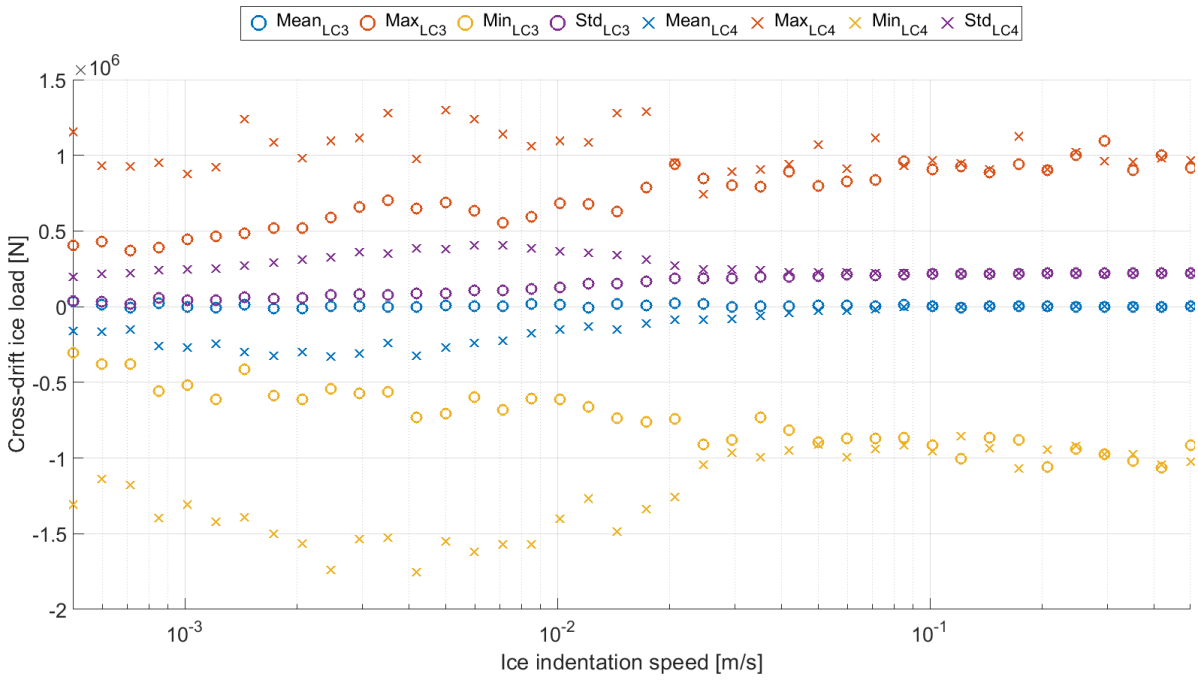

Figure B.3: Statistical characteristics of the cross-drift force exerted by an indenting ice floe on a cylindrical structure for varying ice indentation speeds and ice and structure characteristics as listed in Table 7.1. Results are shown for load cases 3 and 4, according to the load case overview of Section 7.1 and Figure B.1

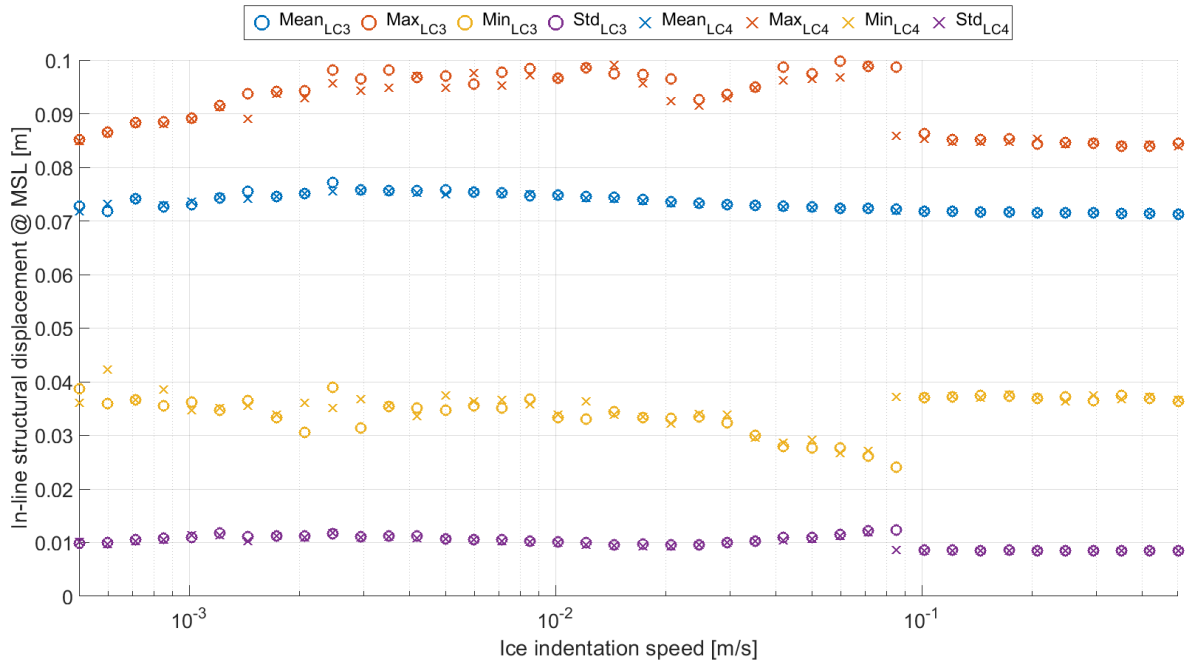

Figure B.4: Statistical characteristics of the in-line structural displacement at MSL caused by an indenting ice floe on a cylindrical structure for varying ice indentation speeds and ice and structure characteristics as listed in Table 7.1. Results are shown for load cases 3 and 4, according to the load case overview of Section 7.1 and Figure B.1

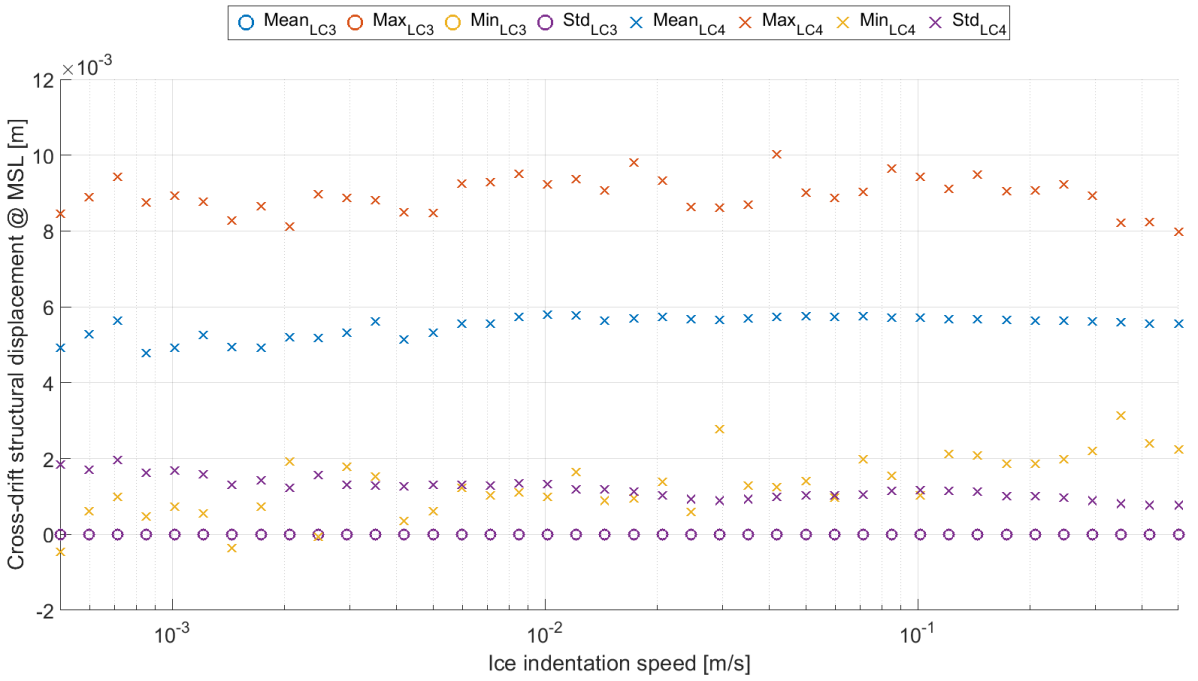

Figure B.5: Statistical characteristics of the cross-drift structural displacement at MSL caused by an indenting ice floe on a cylindrical structure for varying ice indentation speeds and ice and structure characteristics as listed in Table 7.1. Results are shown for load cases 3 and 4, according to the load case overview of Section 7.1 and Figure B.1

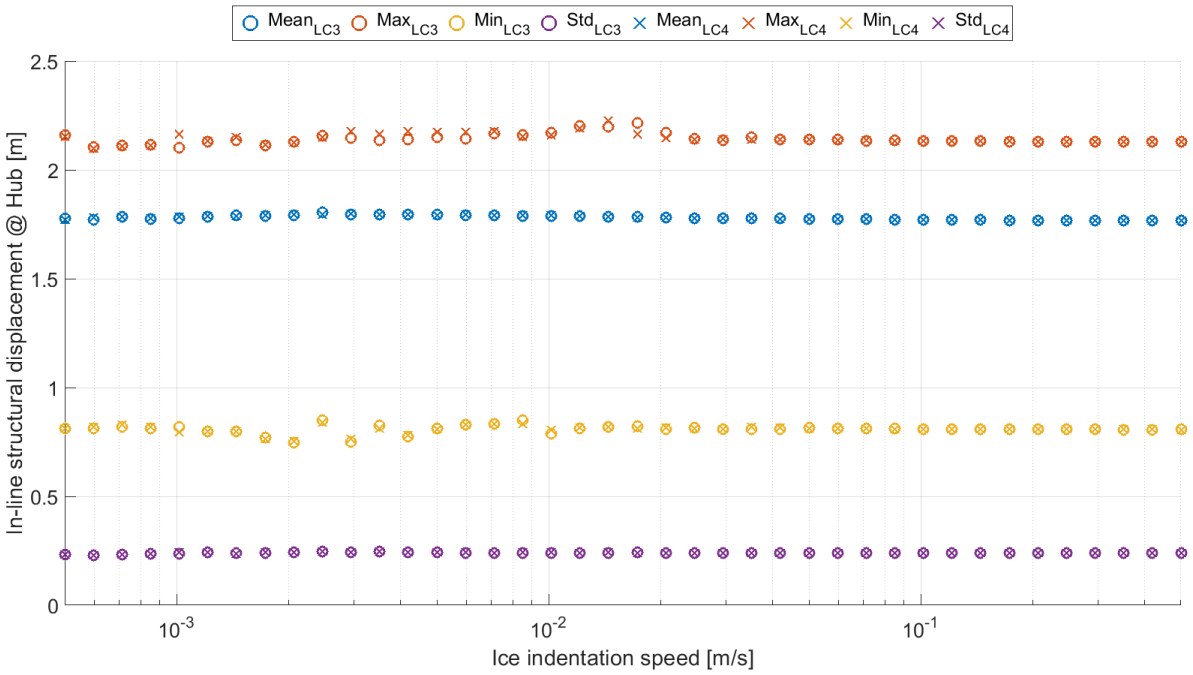

Figure B.6: Statistical characteristics of the in-line structural displacement at hub height caused by an indenting ice floe on a cylindrical structure for varying ice indentation speeds and ice and structure characteristics as listed in Table 7.1. Results are shown for load cases 3 and 4, according to the load case overview of Section 7.1 and Figure B.1

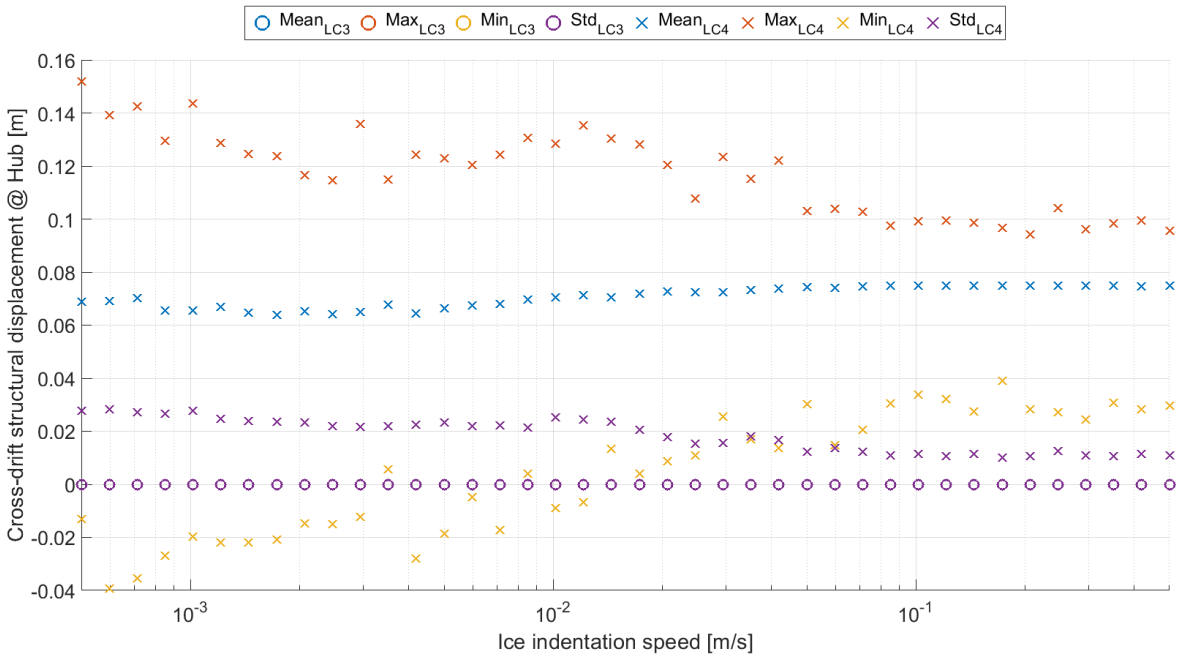

Figure B.7: Statistical characteristics of the cross-drift structural displacement at hub height caused by an indenting ice floe on a cylindrical structure for varying ice indentation speeds and ice and structure characteristics as listed in Table 7.1. Results are shown for load cases 3 and 4, according to the load case overview of Section 7.1 and Figure B.1

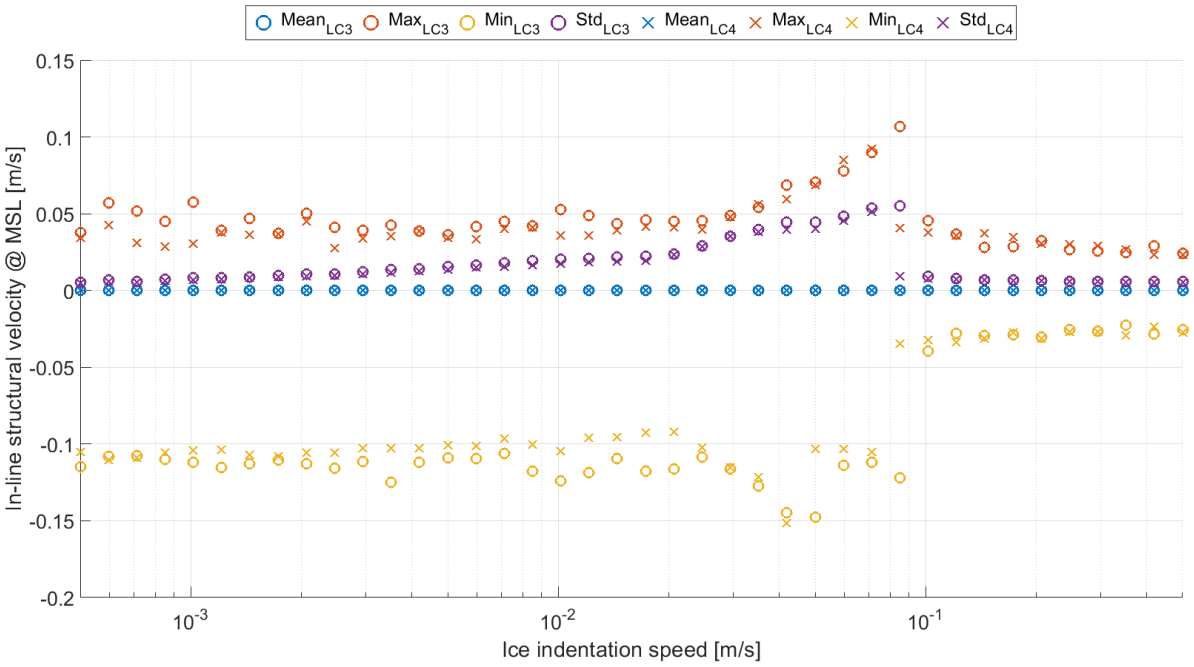

Figure B.8: Statistical characteristics of the in-line structural velocity at MSL caused by an indenting ice floe on a cylindrical structure for varying ice indentation speeds and ice and structure characteristics as listed in Table 7.1. Results are shown for load cases 3 and 4, according to the load case overview of Section 7.1 and Figure B.1

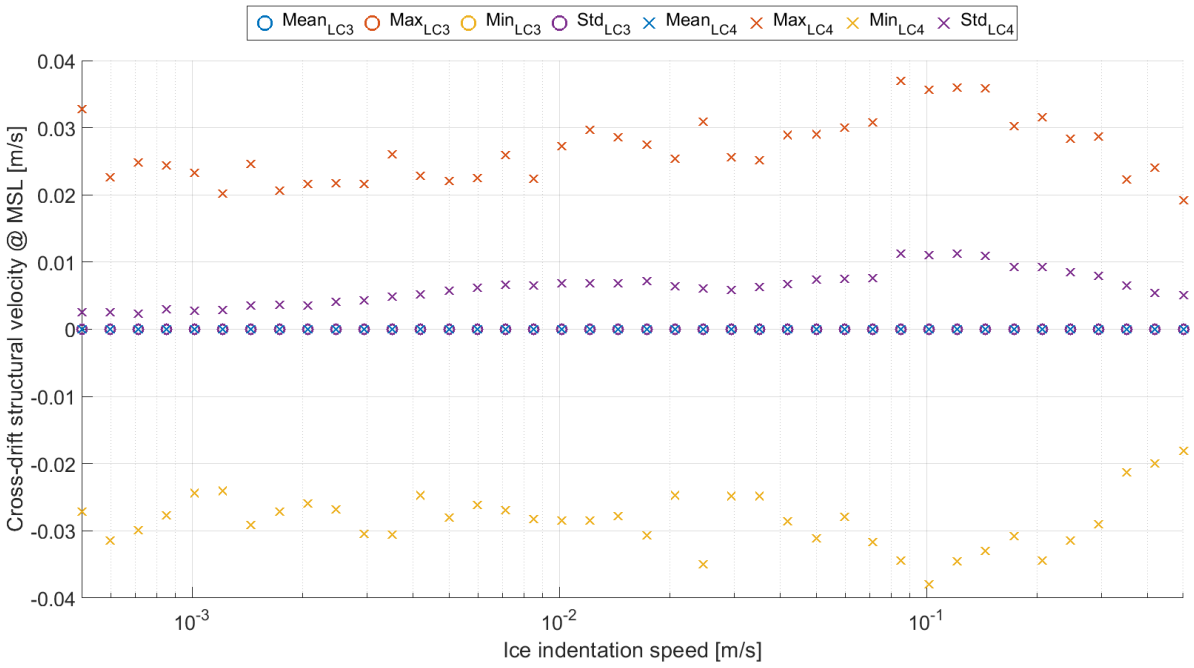

Figure B.9: Statistical characteristics of the cross-drift structural velocity at MSL caused by an indenting ice floe on a cylindrical structure for varying ice indentation speeds and ice and structure characteristics as listed in Table 7.1. Results are shown for load cases 3 and 4, according to the load case overview of Section 7.1 and Figure B.1

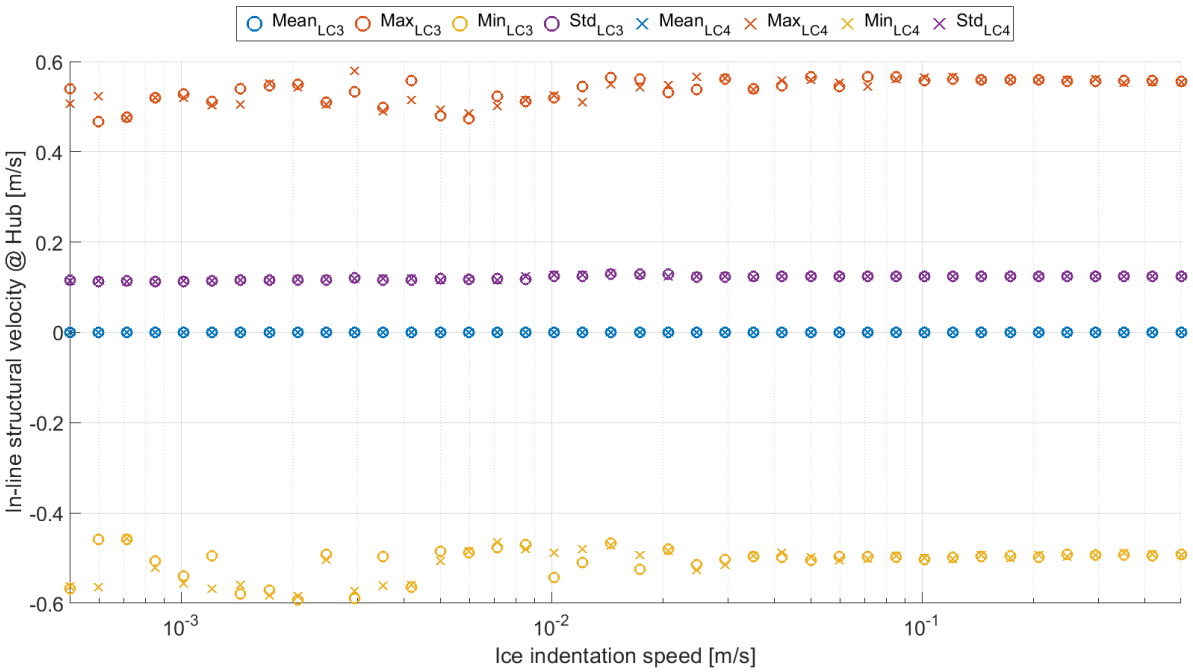

Figure B.10: Statistical characteristics of the in-line structural velocity at hub height caused by an indenting ice floe on a cylindrical structure for varying ice indentation speeds and ice and structure characteristics as listed in Table 7.1. Results are shown for load cases 3 and 4, according to the load case overview of Section 7.1 and Figure B.1

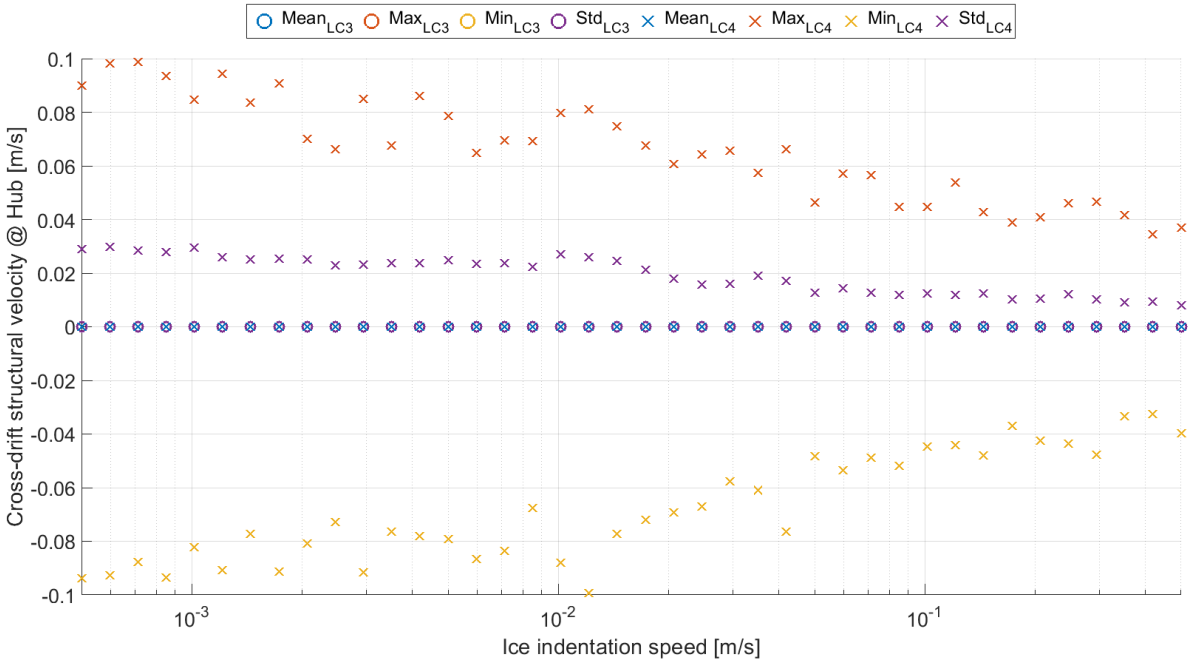

Figure B.11: Statistical characteristics of the cross-drift structural velocity at hub height caused by an indenting ice floe on a cylindrical structure for varying ice indentation speeds and ice and structure characteristics as listed in Table 7.1. Results are shown for load cases 3 and 4, according to the load case overview of Section 7.1 and Figure B.1

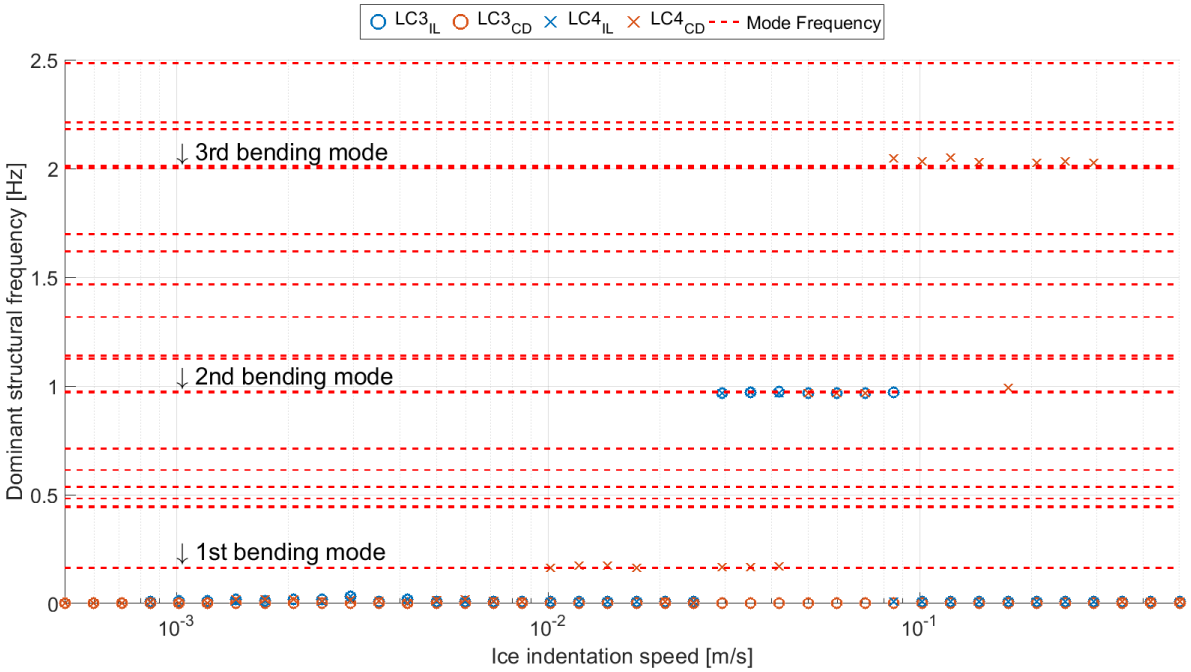

Figure B.12: Dominant structural frequencies for both the in-line and cross-drift direction for varying ice indentation speeds and ice and structure characteristics as listed in Table 7.1. Results are shown for load cases 3 and 4, according to the load case overview of Section 7.1 and Figure B.1

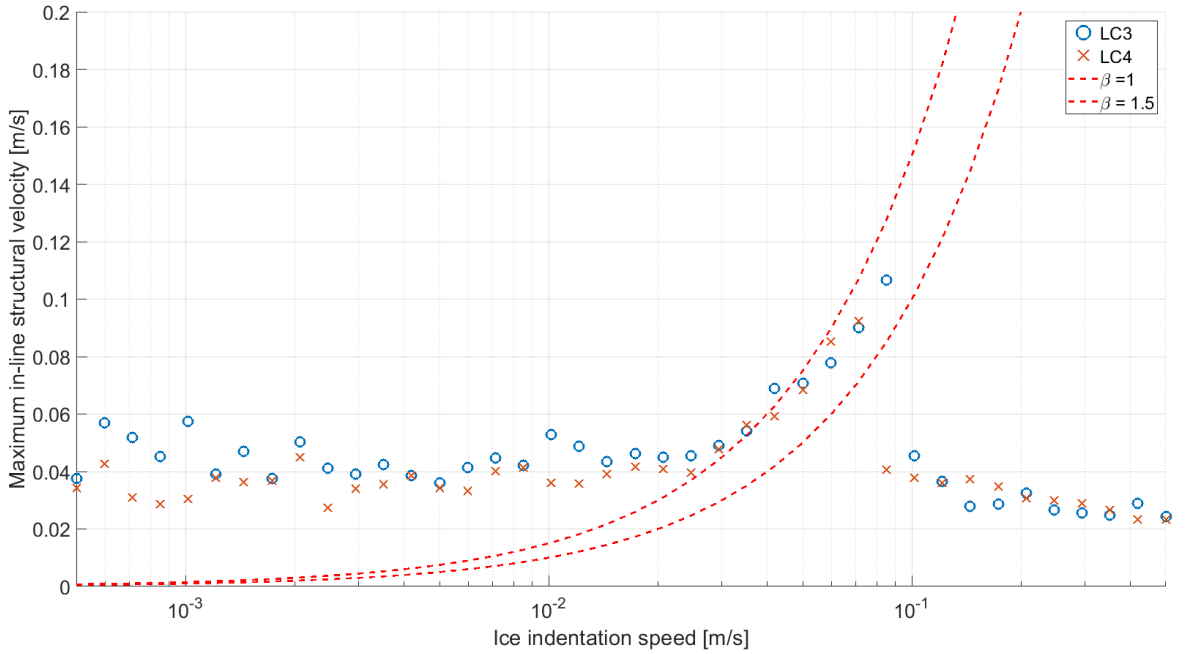

Figure B.13: β-values for varying ice indentation speeds and ice and structure characteristics as listed in Table 7.1. Results are shown for load cases 3 and 4, according to the load case overview of Section 7.1 and Figure B.1

C

All simulation results for the comparison of load cases 2 and 4

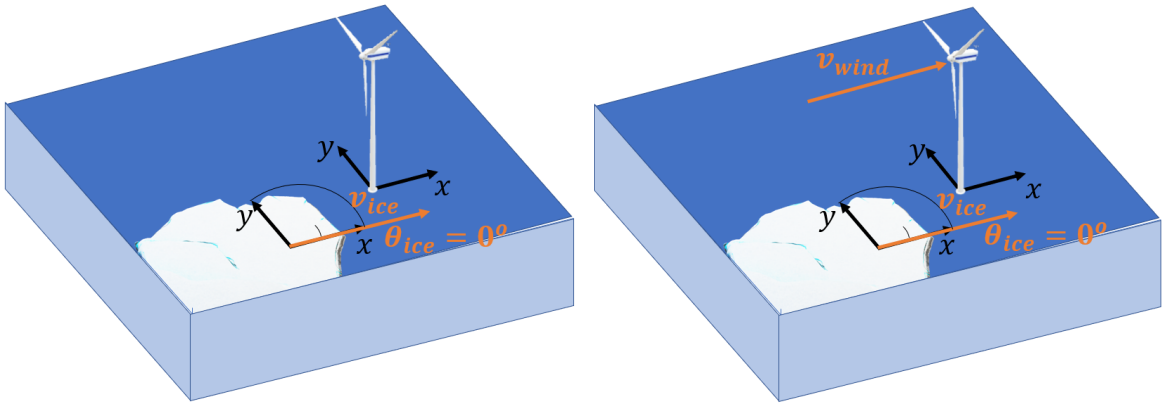

(a) Load case 2

(b) Load case 3

Figure C.1: Overview of the applied loads and structural degrees of freedom in load cases 2 and 4

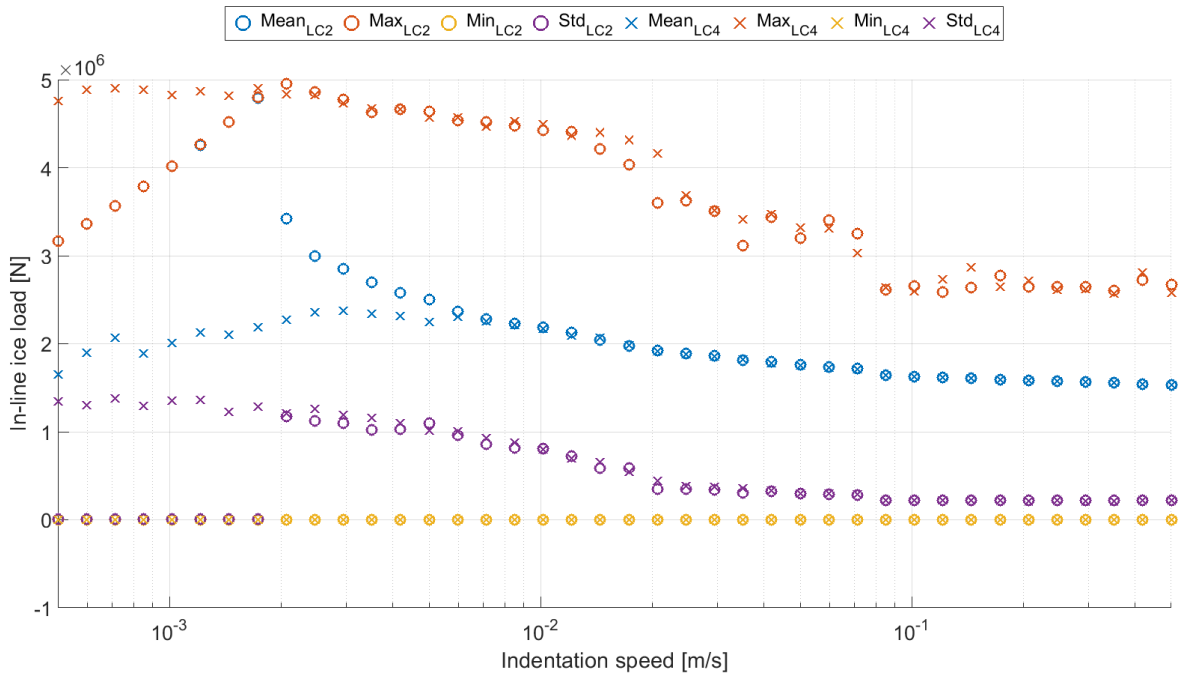

Figure C.2: Statistical characteristics of the X-force exerted by a combination of wind loads and an indenting ice floe on a cylindrical structure for varying ice indentation speeds and ice and structure characteristics as listed in Table 7.1. Results are shown for load cases 2 and 4, according to the load case overview of Section 7.1 and Figure C.1

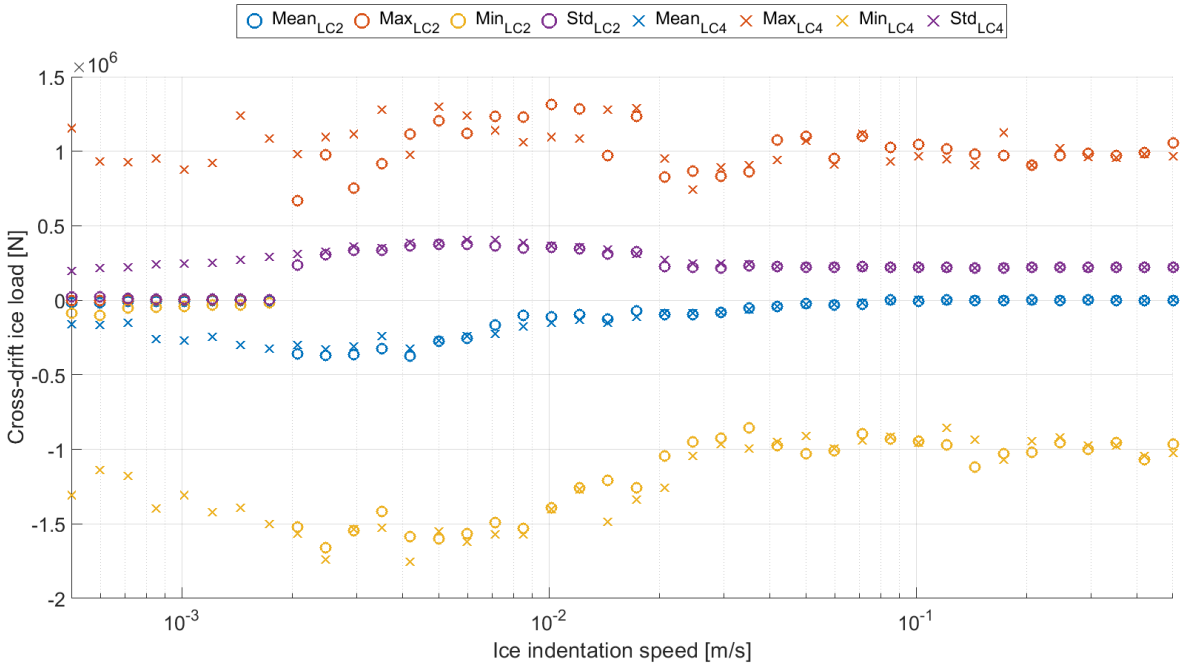

Figure C.3: Statistical characteristics of the Y-force exerted by a combination of wind loads and an indenting ice floe on a cylindrical structure for varying ice indentation speeds and ice and structure characteristics as listed in Table 7.1. Results are shown for load cases 2 and 4, according to the load case overview of Section 7.1 and Figure C.1

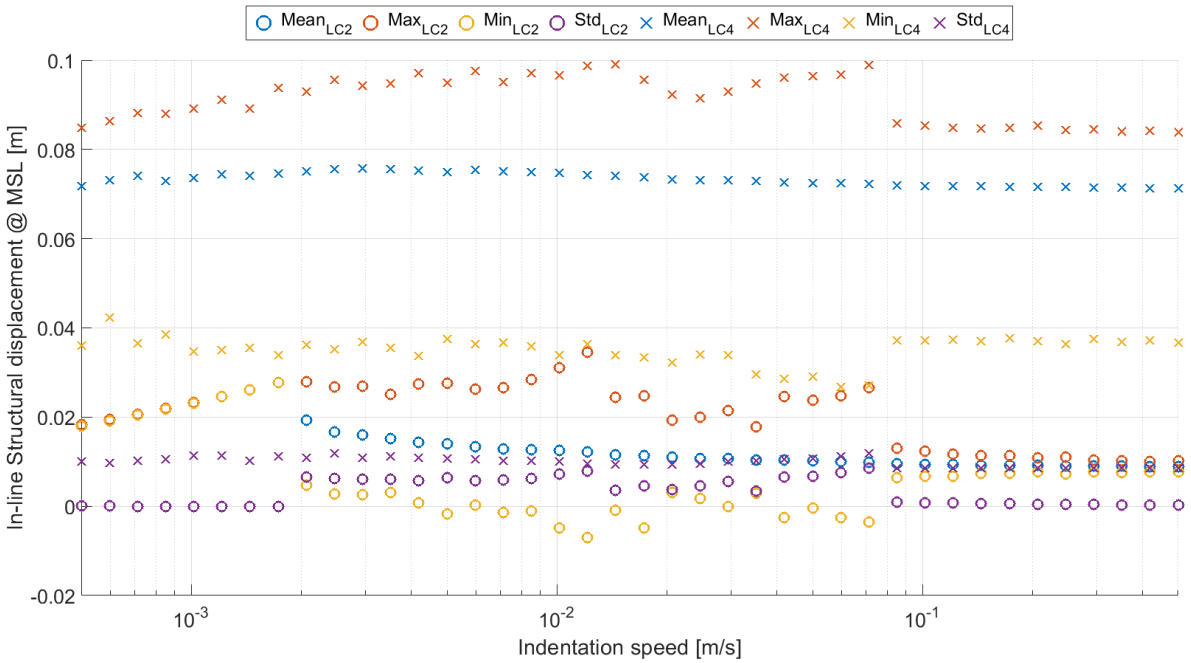

Figure C.4: Statistical characteristics of the structural X-displacement at MSL caused by a combination of wind load and an indenting ice floe on a cylindrical structure for varying ice indentation speeds and ice and structure characteristics as listed in Table 7.1. Results are shown for load cases 2 and 4, according to the load case overview of Section 7.1 and Figure C.1

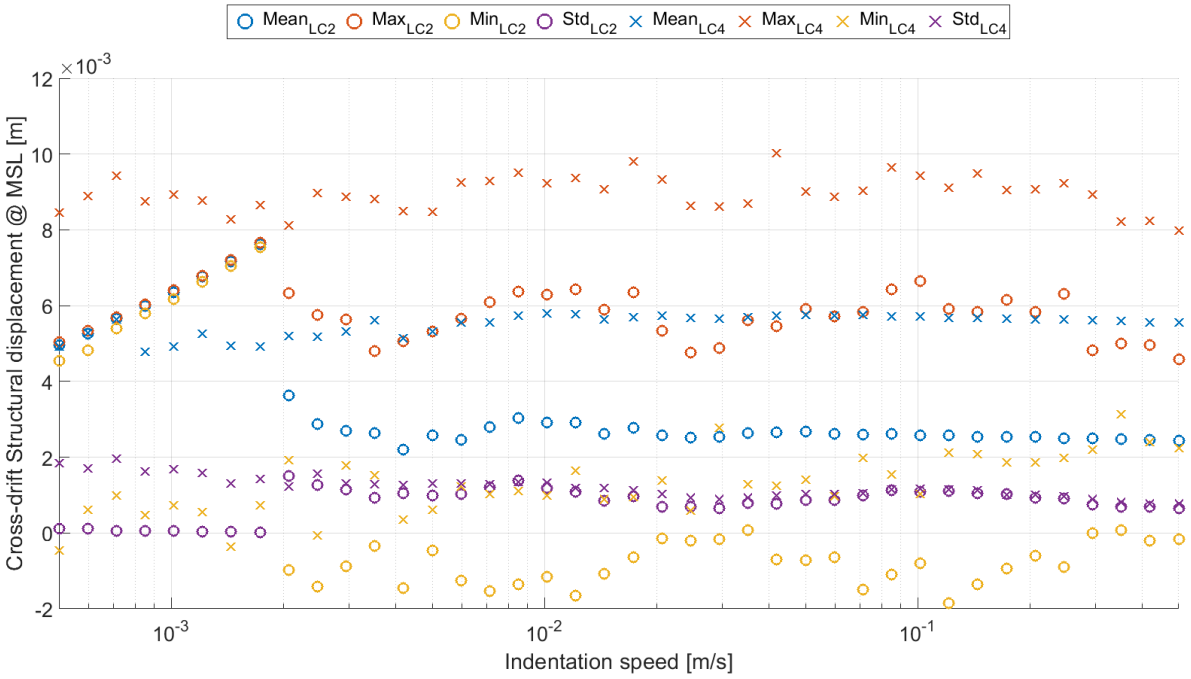

Figure C.5: Statistical characteristics of the structural Y-displacement at MSL caused by a combination of wind load and an indenting ice floe on a cylindrical structure for varying ice indentation speeds and ice and structure characteristics as listed in Table 7.1. Results are shown for load cases 2 and 4, according to the load case overview of Section 7.1 and Figure C.1

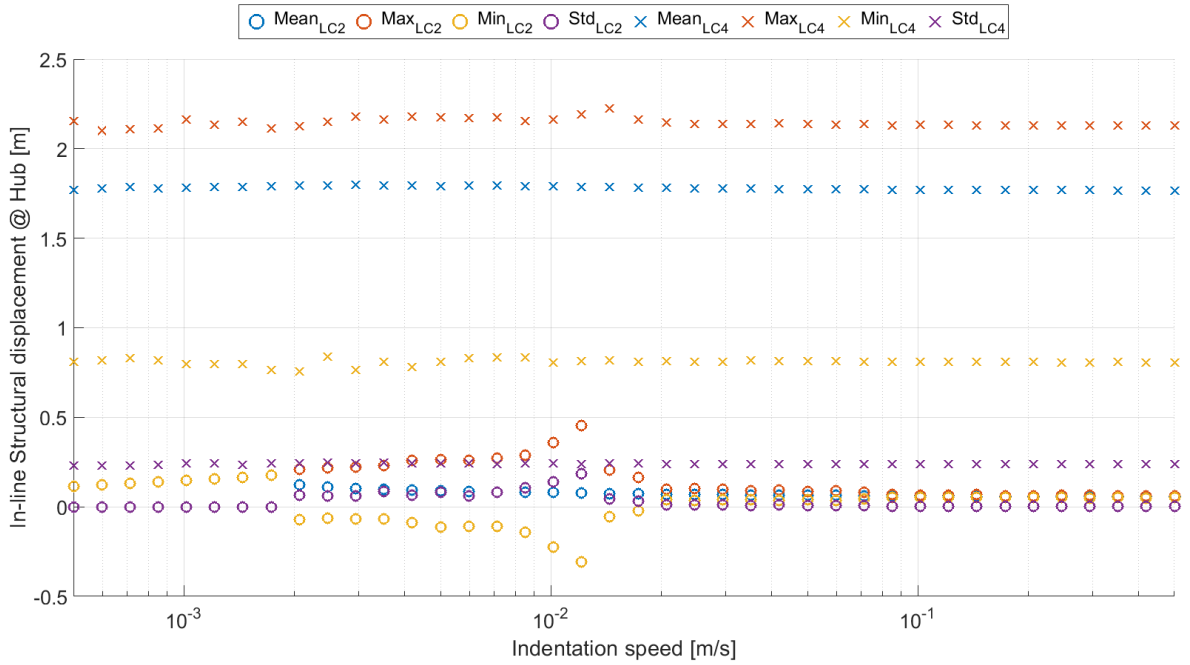

Figure C.6: Statistical characteristics of the structural X-displacement at hub heigth caused by a combination of wind load and an indenting ice floe on a cylindrical structure for varying ice indentation speeds and ice and structure characteristics as listed in Table 7.1. Results are shown for load cases 2 and 4, according to the load case overview of Section 7.1 and Figure C.1

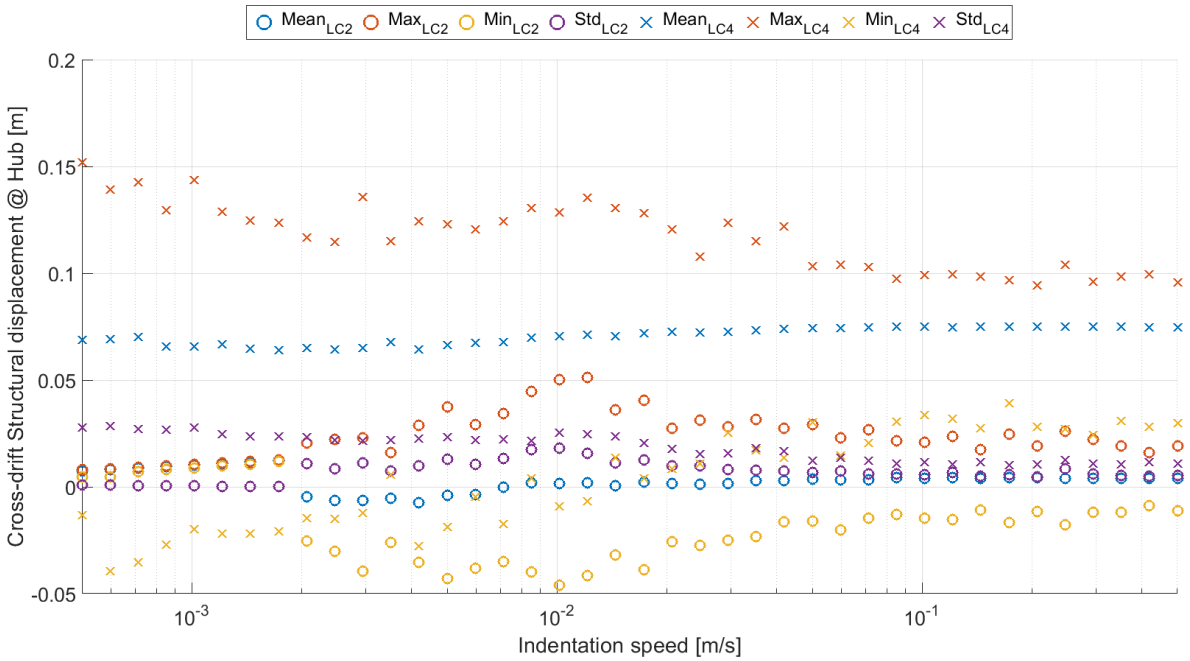

Figure C.7: Statistical characteristics of the structural Y-displacement at hub height caused by a combination of wind load and an indenting ice floe on a cylindrical structure for varying ice indentation speeds and ice and structure characteristics as listed in Table 7.1. Results are shown for load cases 2 and 4, according to the load case overview of Section 7.1 and Figure C.1

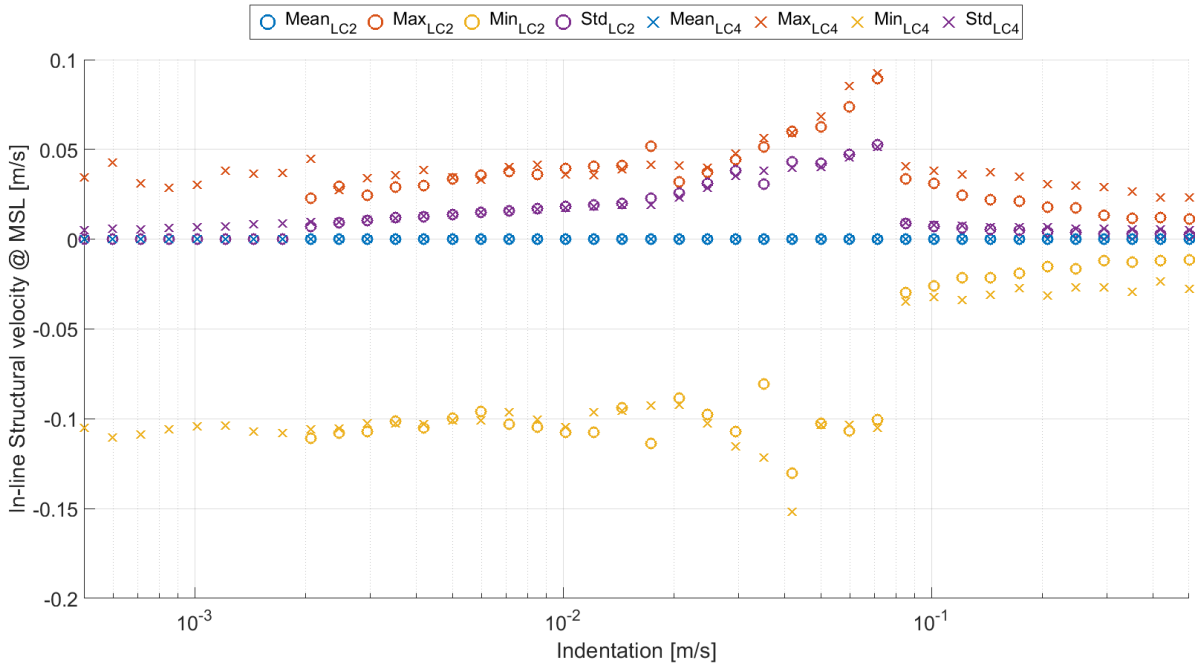

Figure C.8: Statistical characteristics of the structural X-velocity at MSL caused by a combination of wind load and an indenting ice floe on a cylindrical structure for varying ice indentation speeds and ice and structure characteristics as listed in Table 7.1. Results are shown for load cases 2 and 4, according to the load case overview of Section 7.1 and Figure C.1

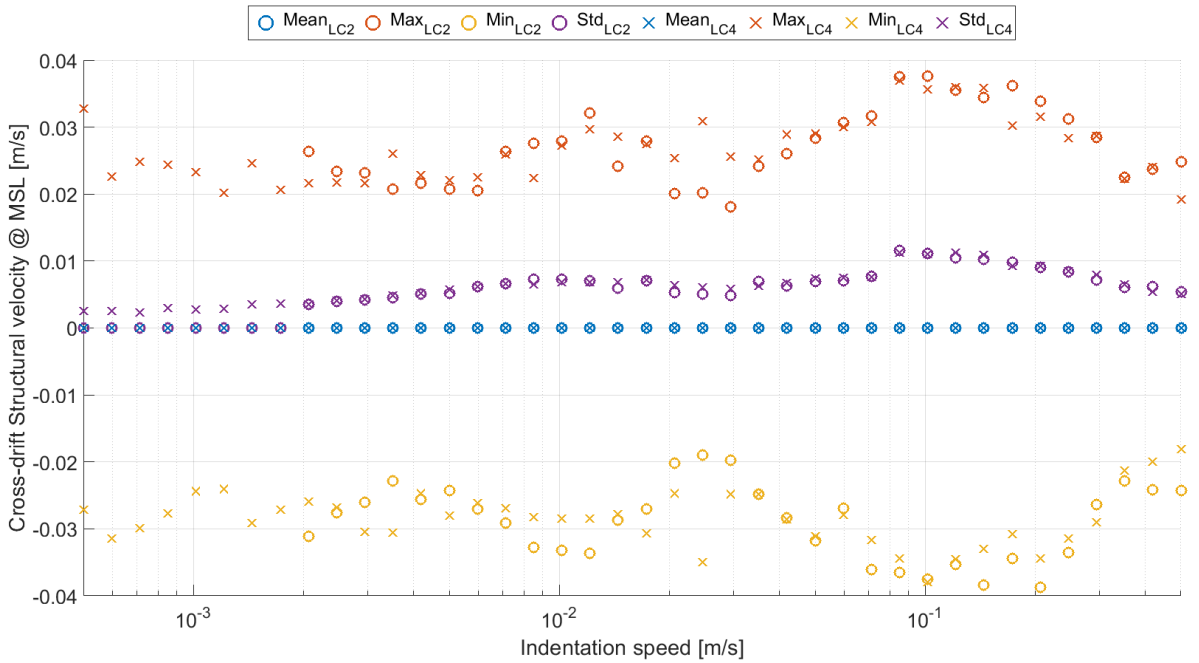

Figure C.9: Statistical characteristics of the structural Y-velocity at MSL caused by a combination of wind load and an indenting ice floe on a cylindrical structure for varying ice indentation speeds and ice and structure characteristics as listed in Table 7.1. Results are shown for load cases 2 and 4, according to the load case overview of Section 7.1 and Figure C.1

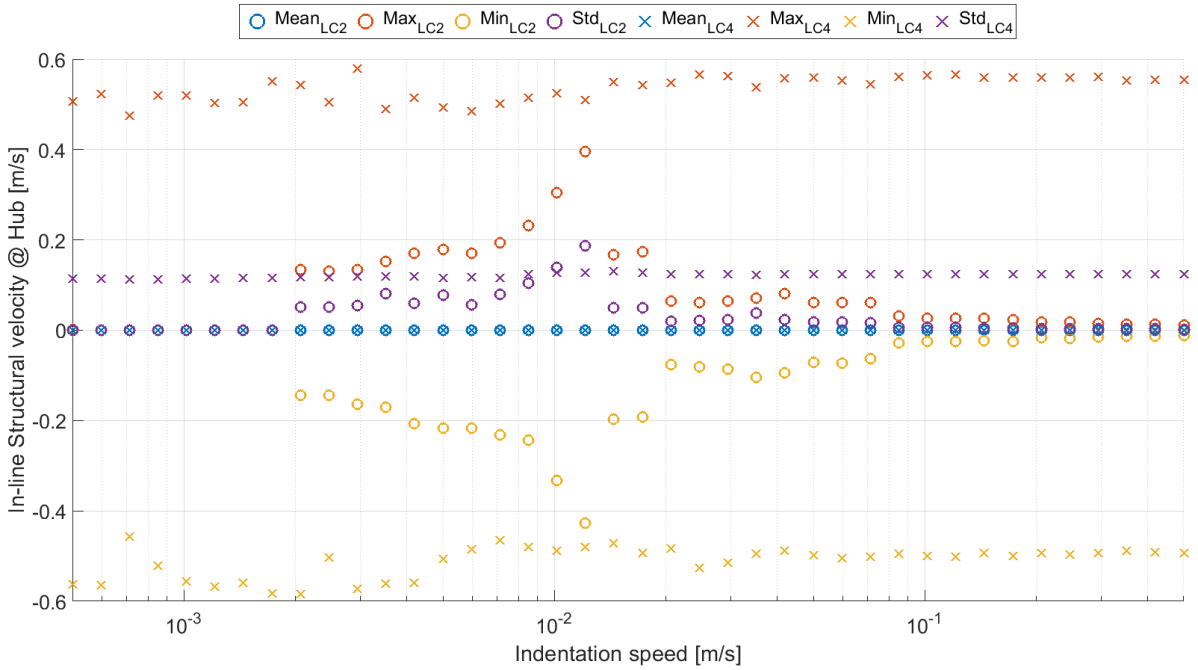

Figure C.10: Statistical characteristics of the structural X-velocity at hub heigth caused by a combination of wind load and an indenting ice floe on a cylindrical structure for varying ice indentation speeds and ice and structure characteristics as listed in Table 7.1. Results are shown for load cases 2 and 4, according to the load case overview of Section 7.1 and Figure C.1

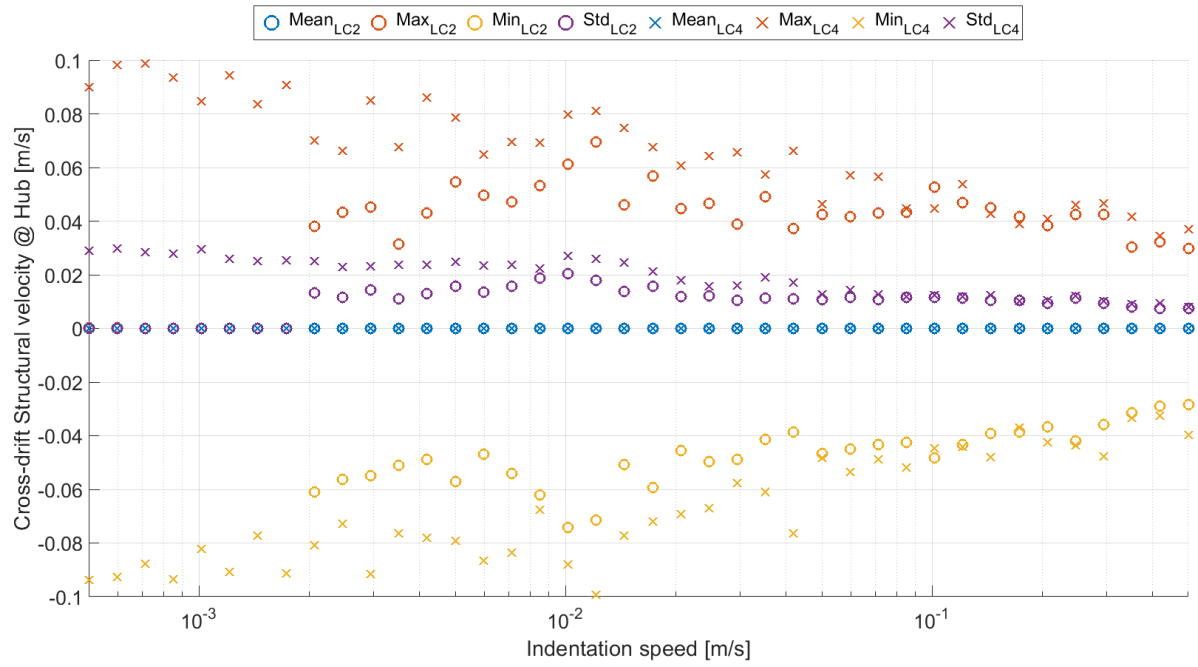

Figure C.11: Statistical characteristics of the structural Y-velocity at hub height caused by a combination of wind load and an indenting ice floe on a cylindrical structure for varying ice indentation speeds and ice and structure characteristics as listed in Table 7.1. Results are shown for load cases 2 and 4, according to the load case overview of Section 7.1 and Figure C.1

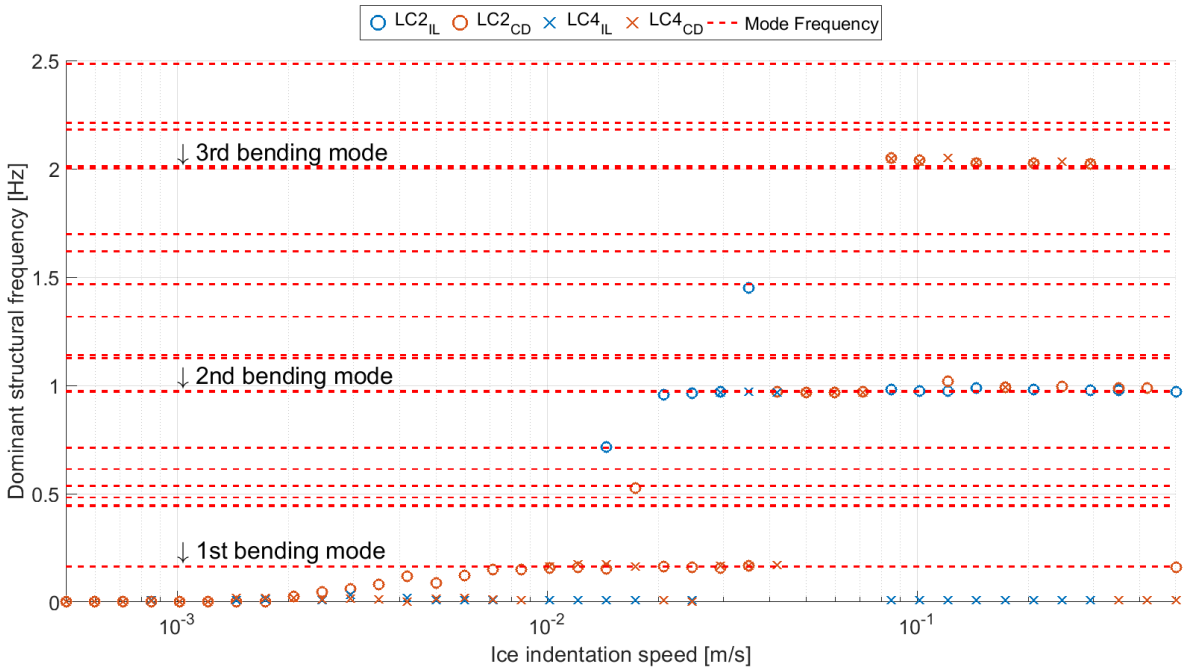

Figure C.12: Dominant structural frequencies for both the X- and Y-directions caused by a comination of wind load and an indenting ice floe on a cylindrical structure for varying ice indentation speeds and ice and structure characteristics as listed in Table 7.1. Results are shown for load cases 2 and 4, according to the load case overview of Section 7.1 and Figure C.1

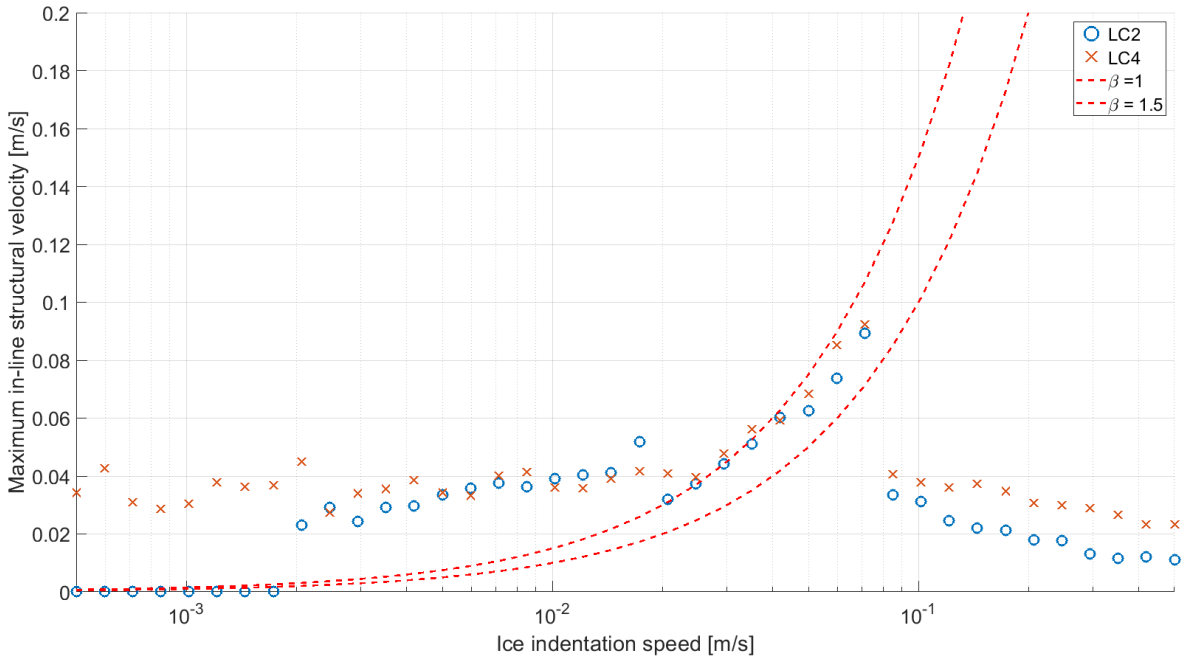

Figure C.13: β-values caused by a combination of wind load and an indenting ice floe on a cylindrical structure for varying ice indentation speeds and ice and structure characteristics as listed in Table 7.1. Results are shown for load cases 2 and 4, according to the load case overview of Section 7.1 and Figure C.1

D

All simulation results for the comparison of load cases 4 and 5

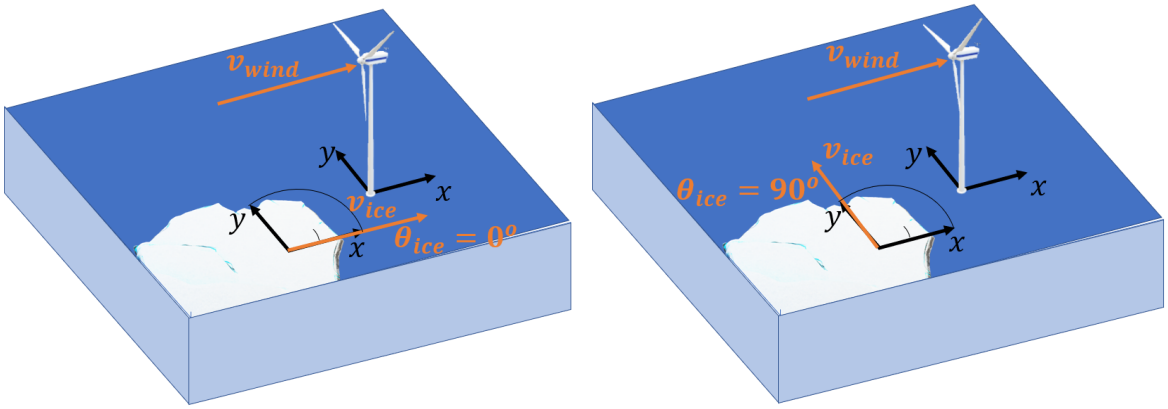

(a) Load case 4

(b) Load case 5

Figure D.1: Overview of the applied loads and structural degrees of freedom in load cases 4 and 5

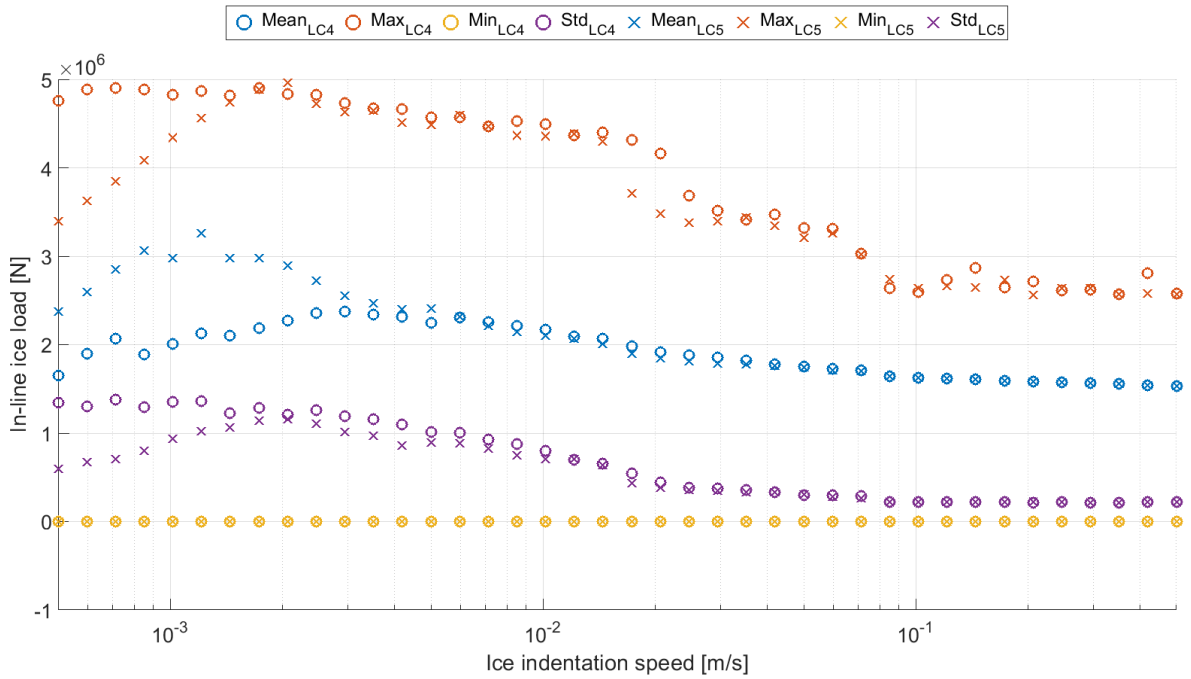

Figure D.2: Statistical characteristics of the X-force exerted by a combination of wind loads and an indenting ice floe on a cylindrical structure for varying ice indentation speeds and ice and structure characteristics as listed in Table 7.1. Results are shown for load cases 4 and 5, according to the load case overview of Section 7.1 and Figure D.1

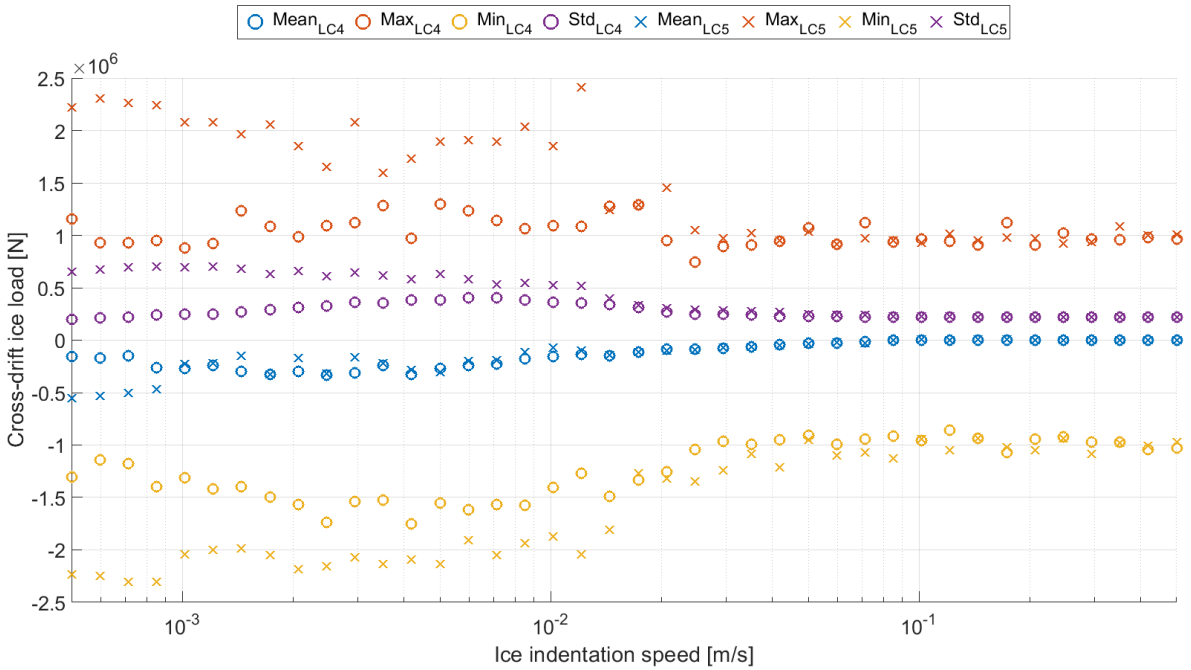

Figure D.3: Statistical characteristics of the Y-force exerted by a combination of wind loads and an indenting ice floe on a cylindrical structure for varying ice indentation speeds and ice and structure characteristics as listed in Table 7.1. Results are shown for load cases 4 and 5, according to the load case overview of Section 7.1 and Figure D.1

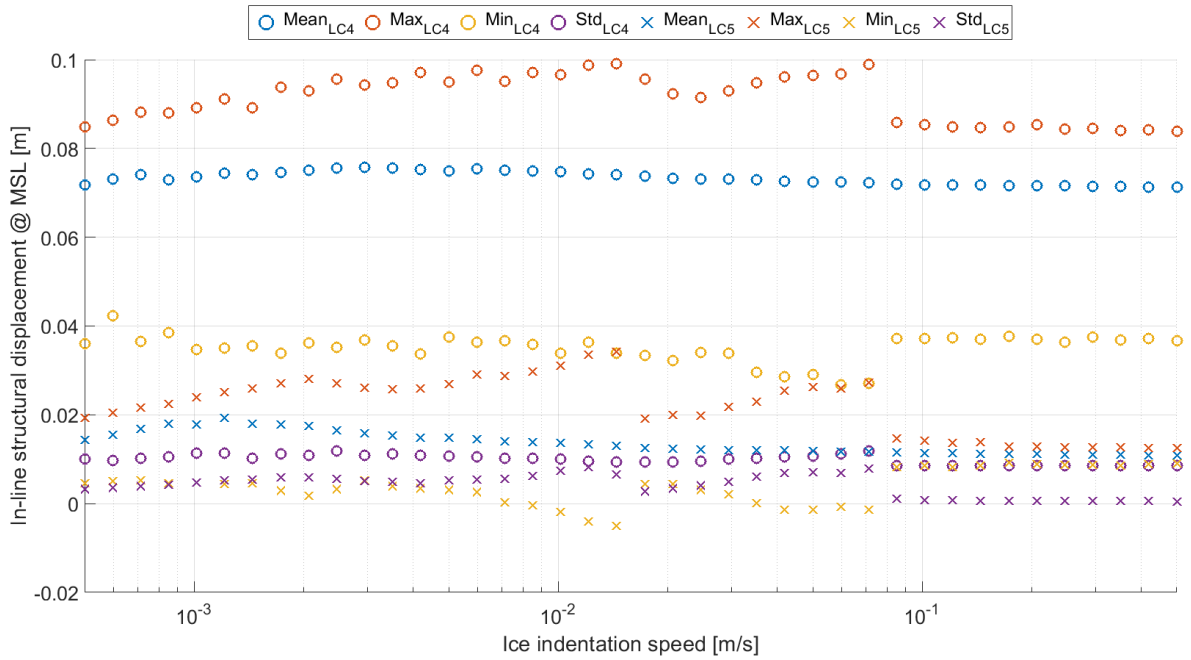

Figure D.4: Statistical characteristics of the structural X-displacement at MSL caused by a combination of wind load and an indenting ice floe on a cylindrical structure for varying ice indentation speeds and ice and structure characteristics as listed in Table 7.1. Results are shown for load cases 4 and 5, according to the load case overview of Section 7.1 and Figure D.1

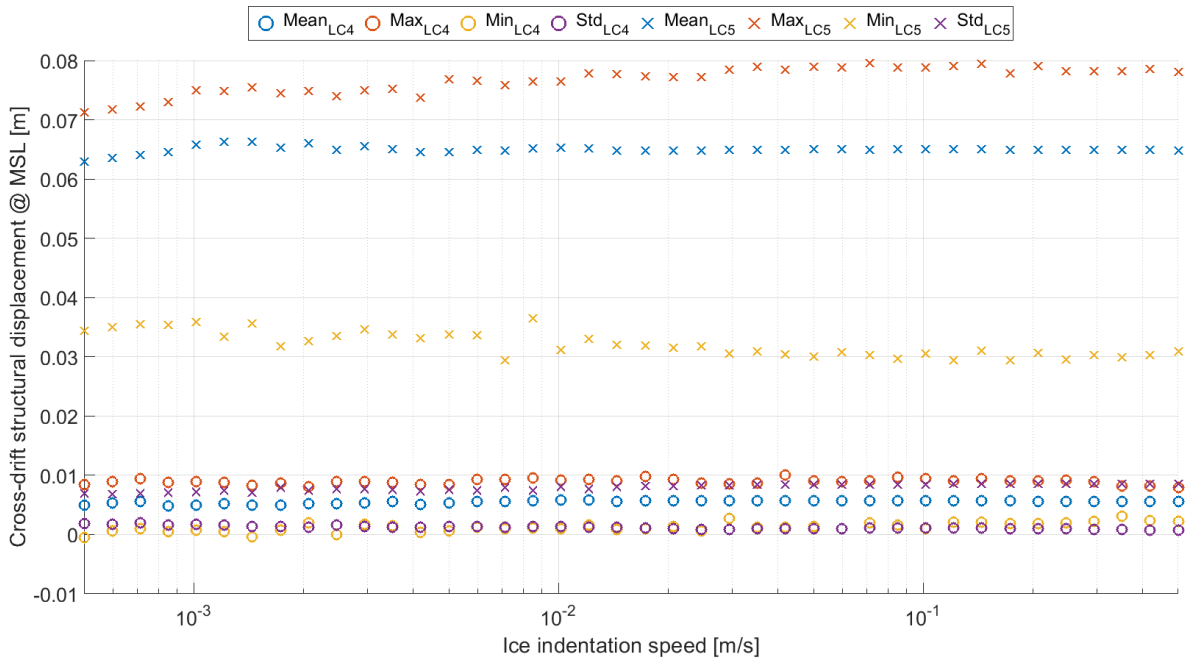

Figure D.5: Statistical characteristics of the structural Y-displacement at MSL caused by a combination of wind load and an indenting ice floe on a cylindrical structure for varying ice indentation speeds and ice and structure characteristics as listed in Table 7.1. Results are shown for load cases 4 and 5, according to the load case overview of Section 7.1 and Figure D.1

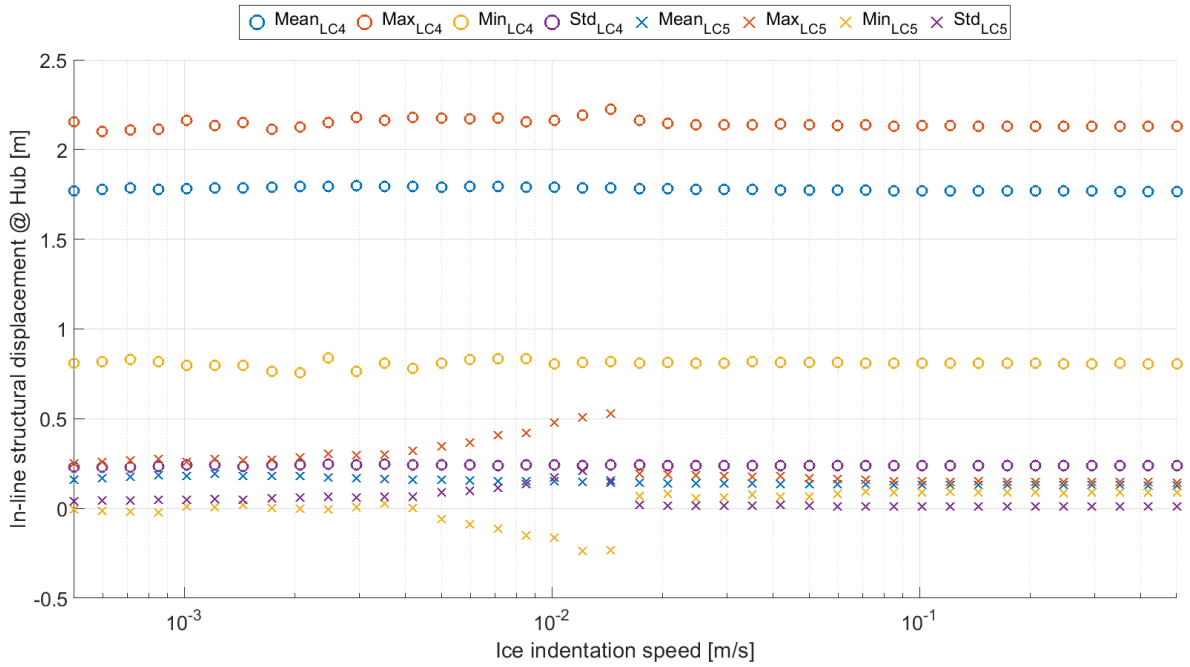

Figure D.6: Statistical characteristics of the structural X-displacement at hub heigth caused by a combination of wind load and an indenting ice floe on a cylindrical structure for varying ice indentation speeds and ice and structure characteristics as listed in Table 7.1. Results are shown for load cases 4 and 5, according to the load case overview of Section 7.1 and Figure D.1

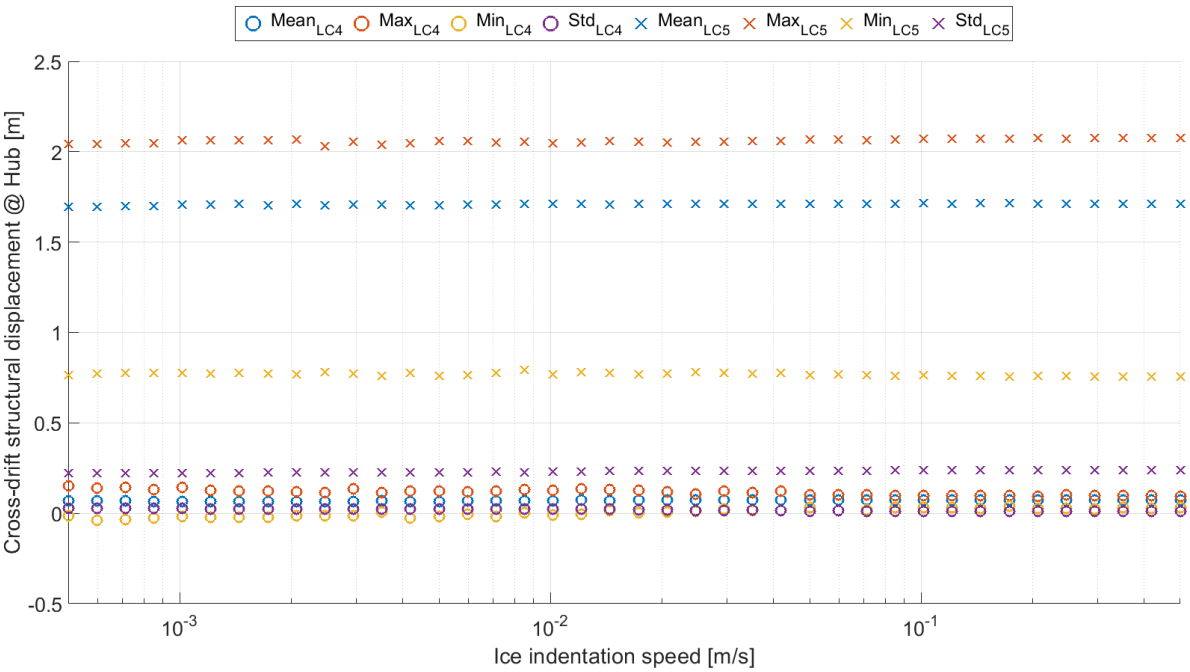

Figure D.7: Statistical characteristics of the structural Y-displacement at hub height caused by a combination of wind load and an indenting ice floe on a cylindrical structure for varying ice indentation speeds and ice and structure characteristics as listed in Table 7.1. Results are shown for load cases 4 and 5, according to the load case overview of Section 7.1 and Figure D.1

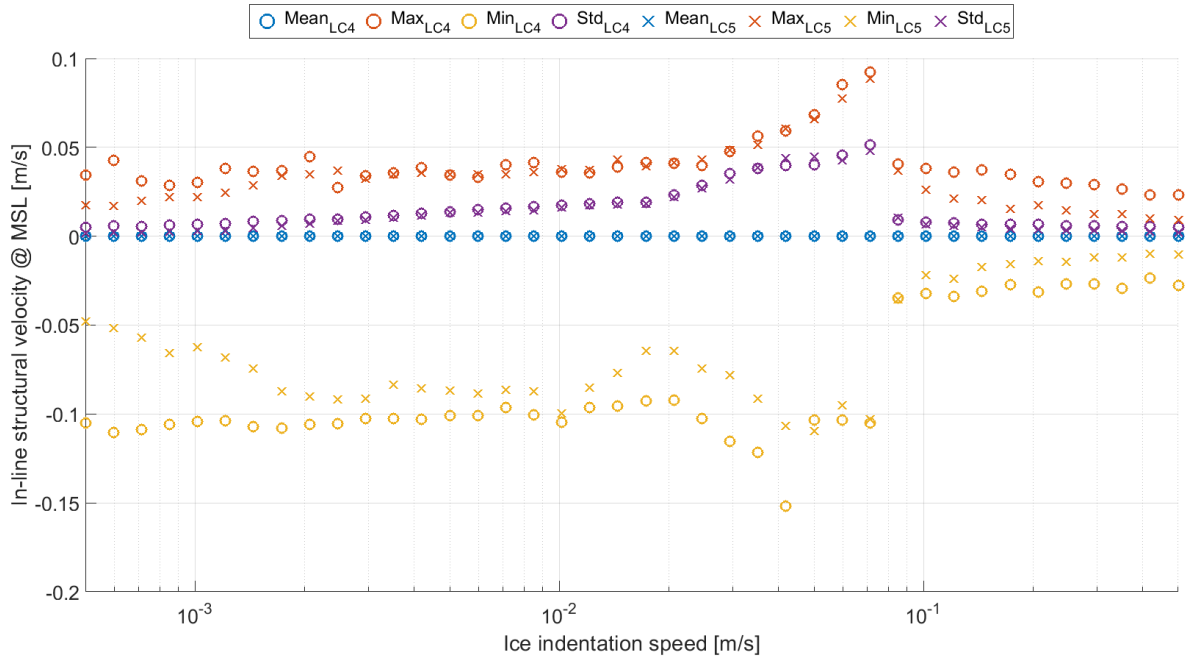

Figure D.8: Statistical characteristics of the structural X-velocity at MSL caused by a combination of wind load and an indenting ice floe on a cylindrical structure for varying ice indentation speeds and ice and structure characteristics as listed in Table 7.1. Results are shown for load cases 4 and 5, according to the load case overview of Section 7.1 and Figure D.1

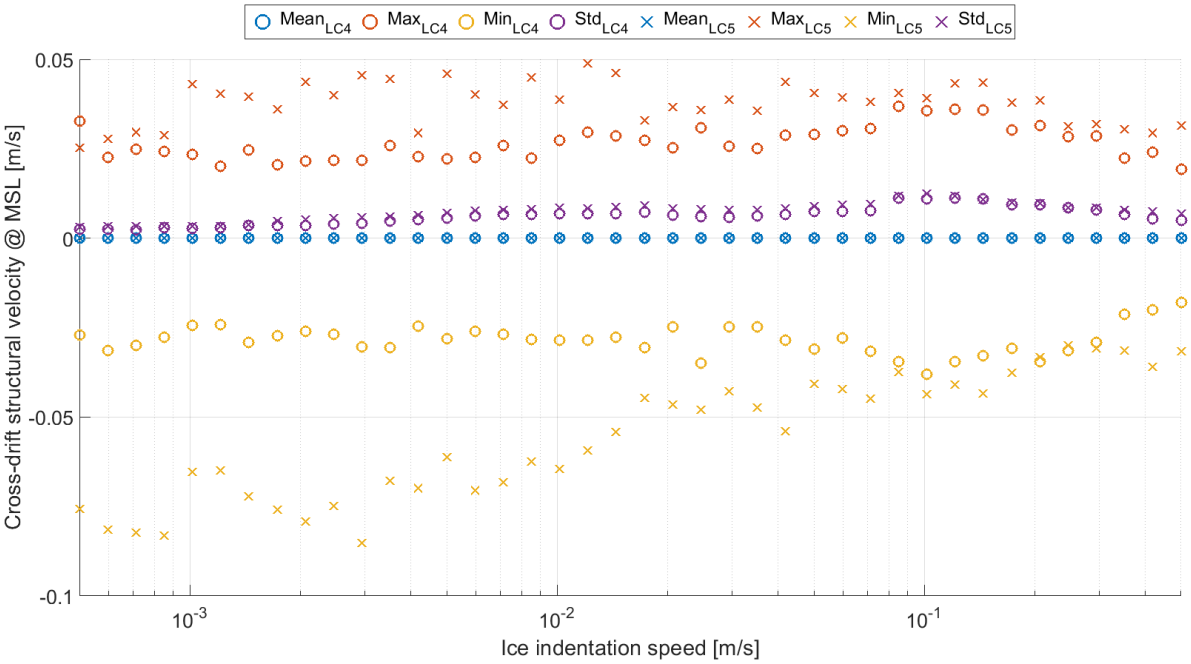

Figure D.9: Statistical characteristics of the structural Y-velocity at MSL caused by a combination of wind load and an indenting ice floe on a cylindrical structure for varying ice indentation speeds and ice and structure characteristics as listed in Table 7.1. Results are shown for load cases 4 and 5, according to the load case overview of Section 7.1 and Figure D.1

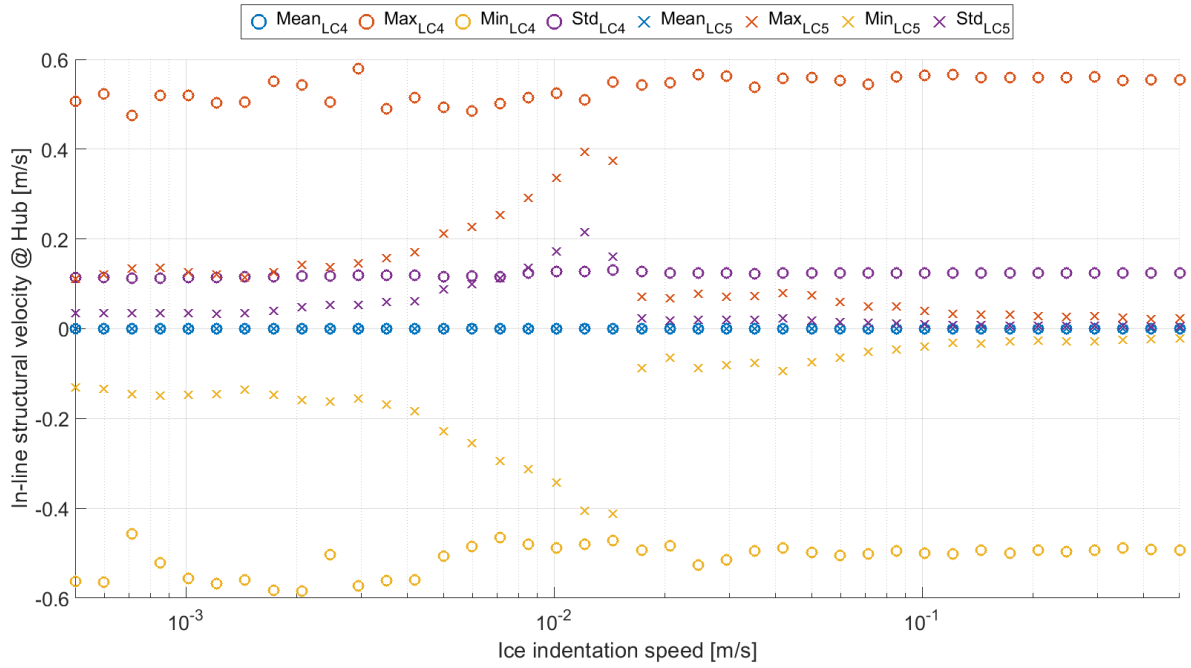

Figure D.10: Statistical characteristics of the structural X-velocity at hub heigth caused by a combination of wind load and an indenting ice floe on a cylindrical structure for varying ice indentation speeds and ice and structure characteristics as listed in Table 7.1. Results are shown for load cases 4 and 5, according to the load case overview of Section 7.1 and Figure D.1

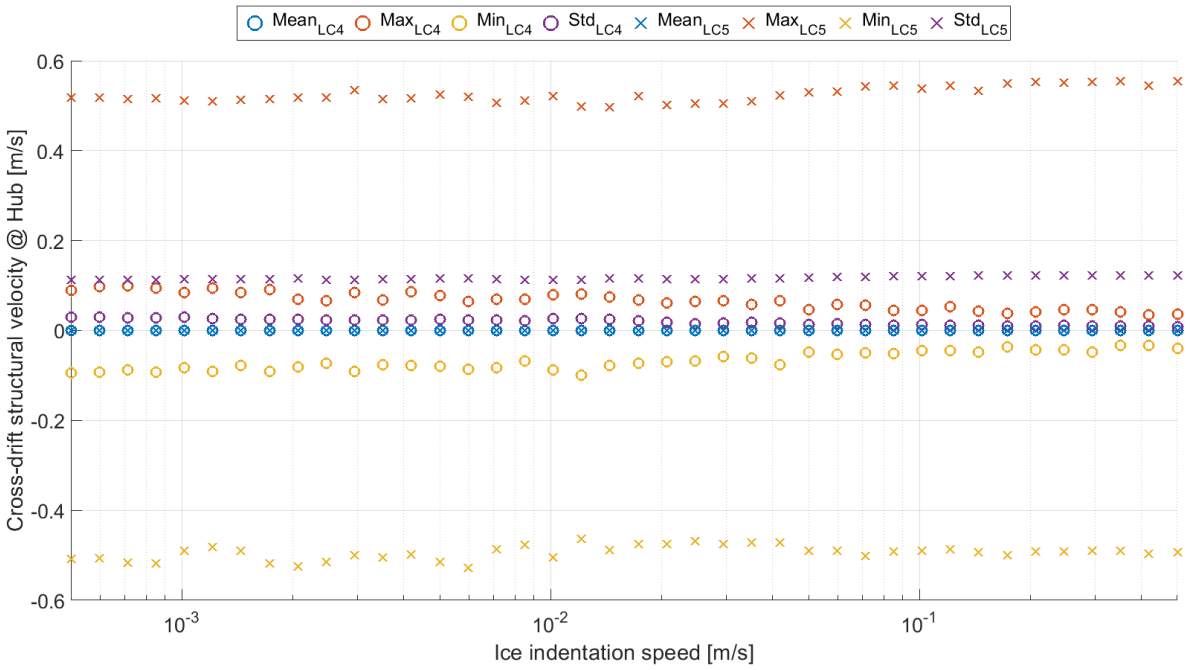

Figure D.11: Statistical characteristics of the structural Y-velocity at hub height caused by a combination of wind load and an indenting ice floe on a cylindrical structure for varying ice indentation speeds and ice and structure characteristics as listed in Table 7.1. Results are shown for load cases 4 and 5, according to the load case overview of Section 7.1 and Figure D.1

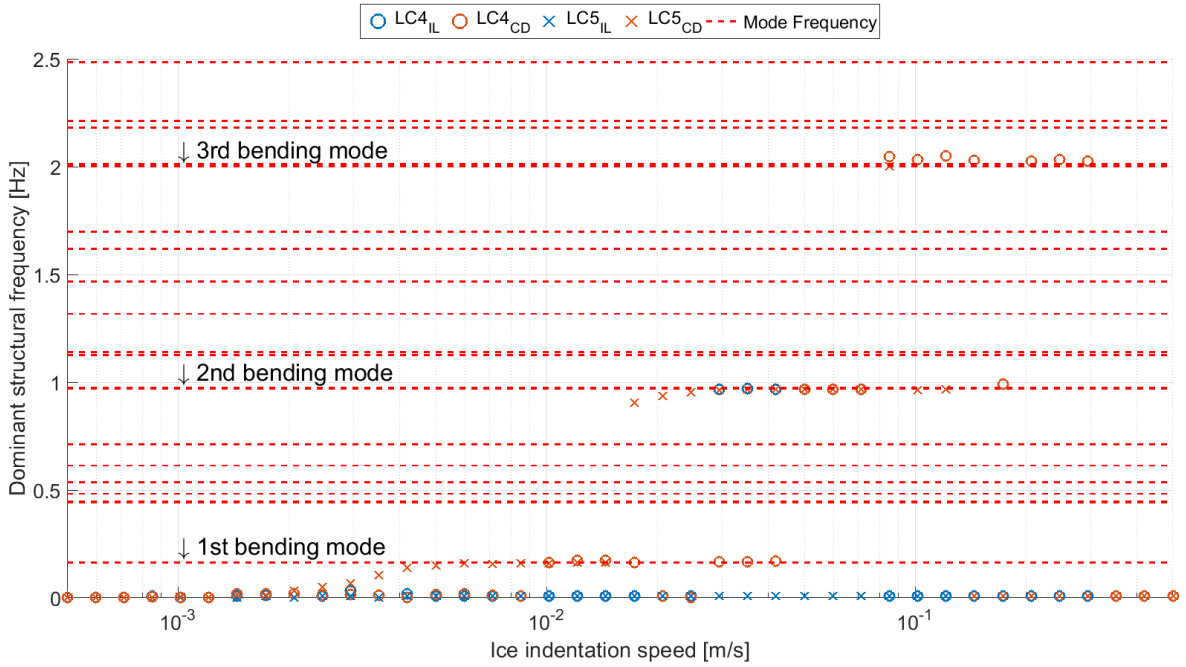

Figure D.12: Dominant structural frequencies for both the X- and Y-directions caused by a comination of wind load and an indenting ice floe on a cylindrical structure for varying ice indentation speeds and ice and structure characteristics as listed in Table 7.1. Results are shown for load cases 4 and 5, according to the load case overview of Section 7.1 and Figure D.1

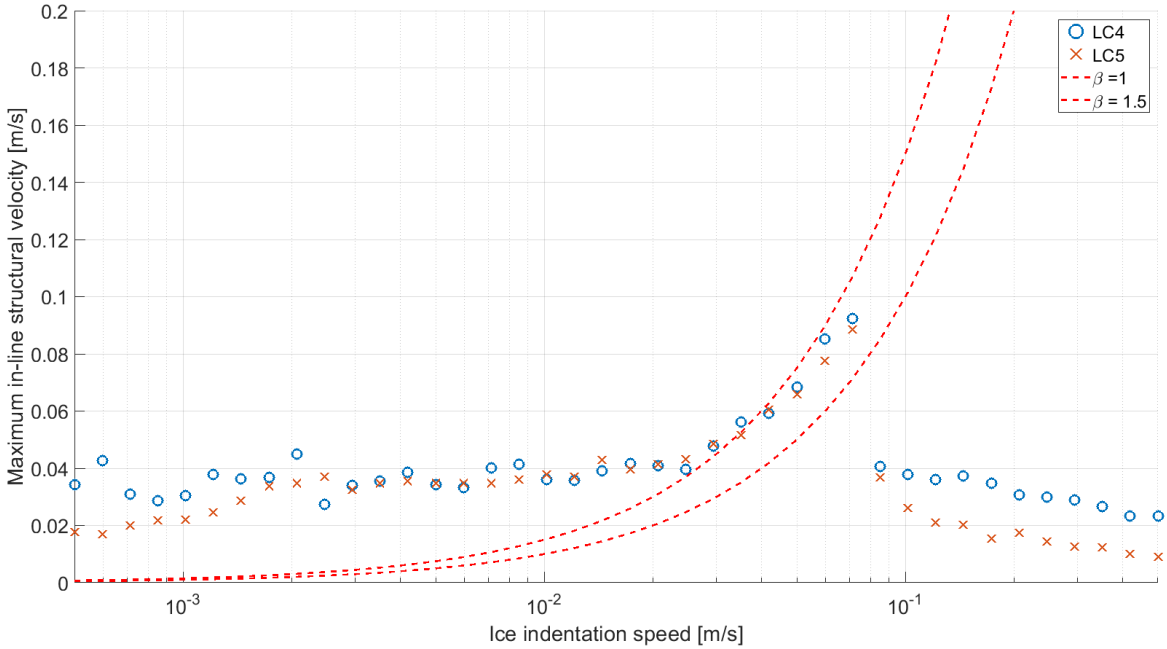

Figure D.13: β-values caused by a combination of wind load and an indenting ice floe on a cylindrical structure for varying ice indentation speeds and ice and structure characteristics as listed in Table 7.1. Results are shown for load cases 4 and 5, according to the load case overview of Section 7.1 and Figure D.1

E

All simulation results for the comparison of load cases 4 and 6

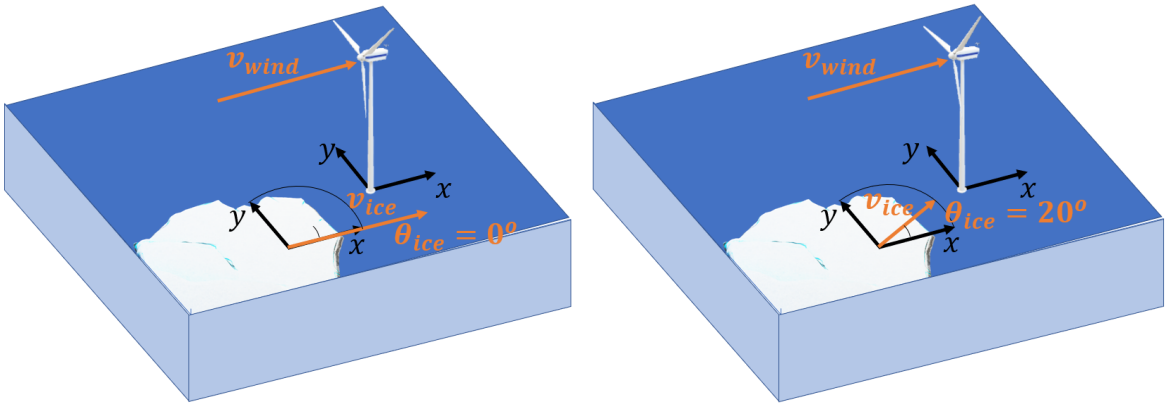

(a) Load case 4

(b) Load case 6

Figure E.1: Overview of the applied loads and structural degrees of freedom in load cases 4 and 6

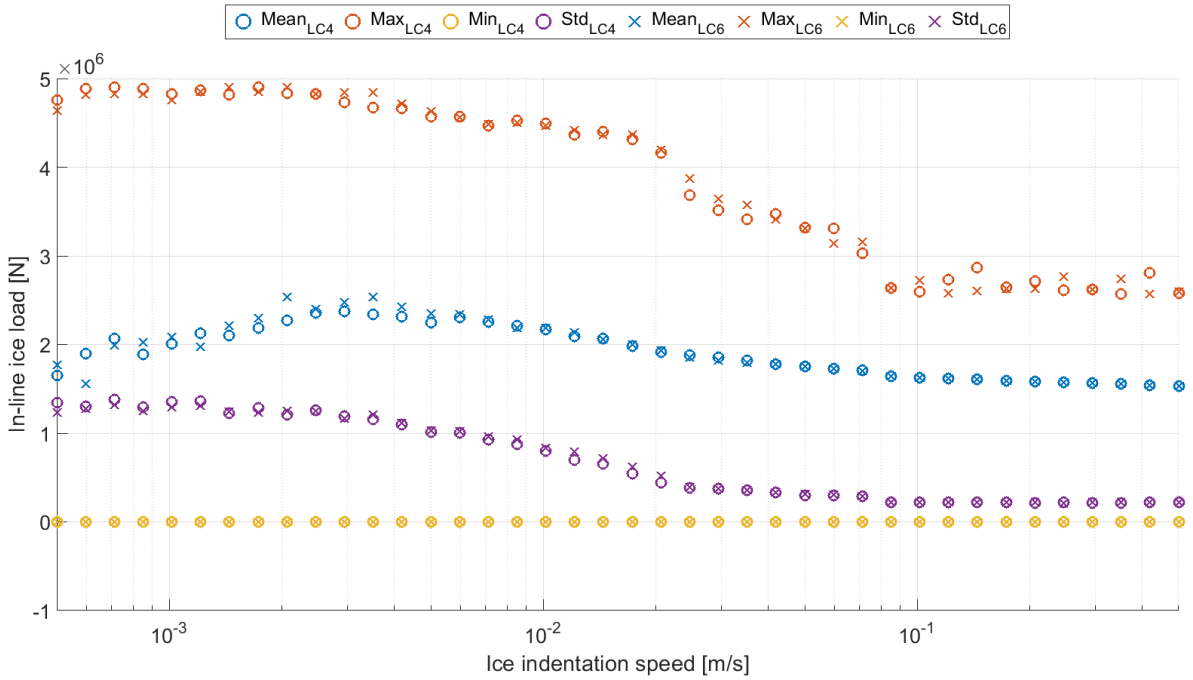

Figure E.2: Statistical characteristics of the X-force exerted by a combination of wind loads and an indenting ice floe on a cylindrical structure for varying ice indentation speeds and ice and structure characteristics as listed in Table 7.1. Results are shown for load cases 4 and 6, according to the load case overview of Section 7.1 and Figure E.1

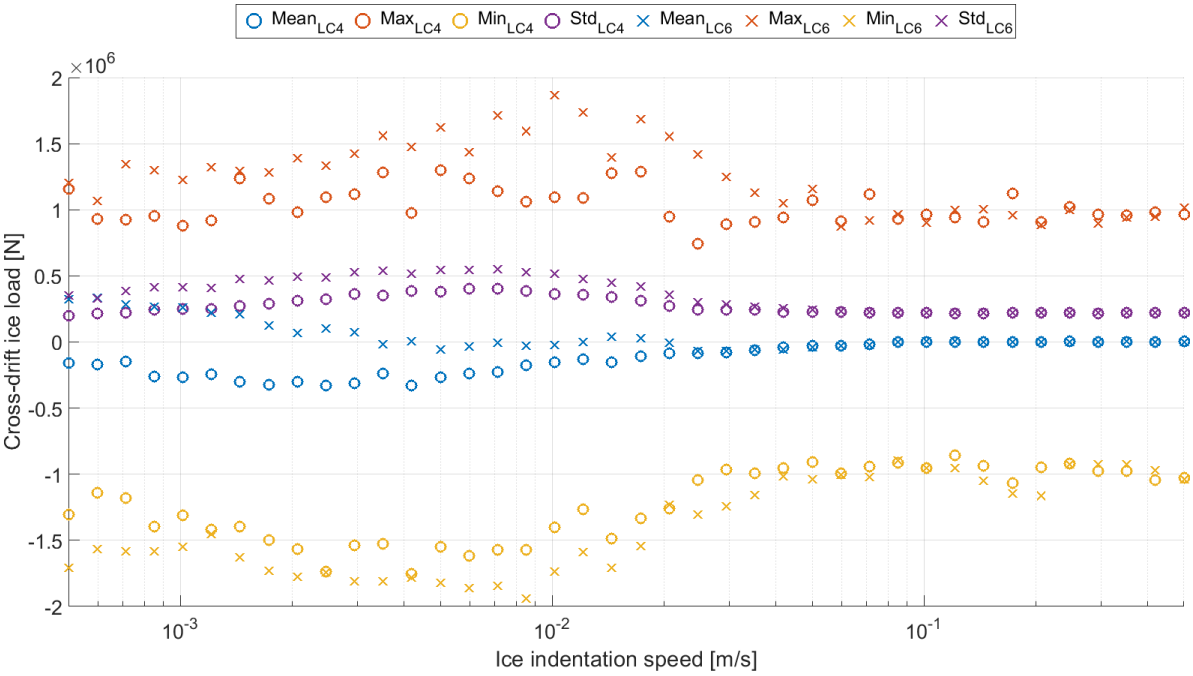

Figure E.3: Statistical characteristics of the Y-force exerted by a combination of wind loads and an indenting ice floe on a cylindrical structure for varying ice indentation speeds and ice and structure characteristics as listed in Table 7.1. Results are shown for load cases 4 and 6, according to the load case overview of Section 7.1 and Figure E.1

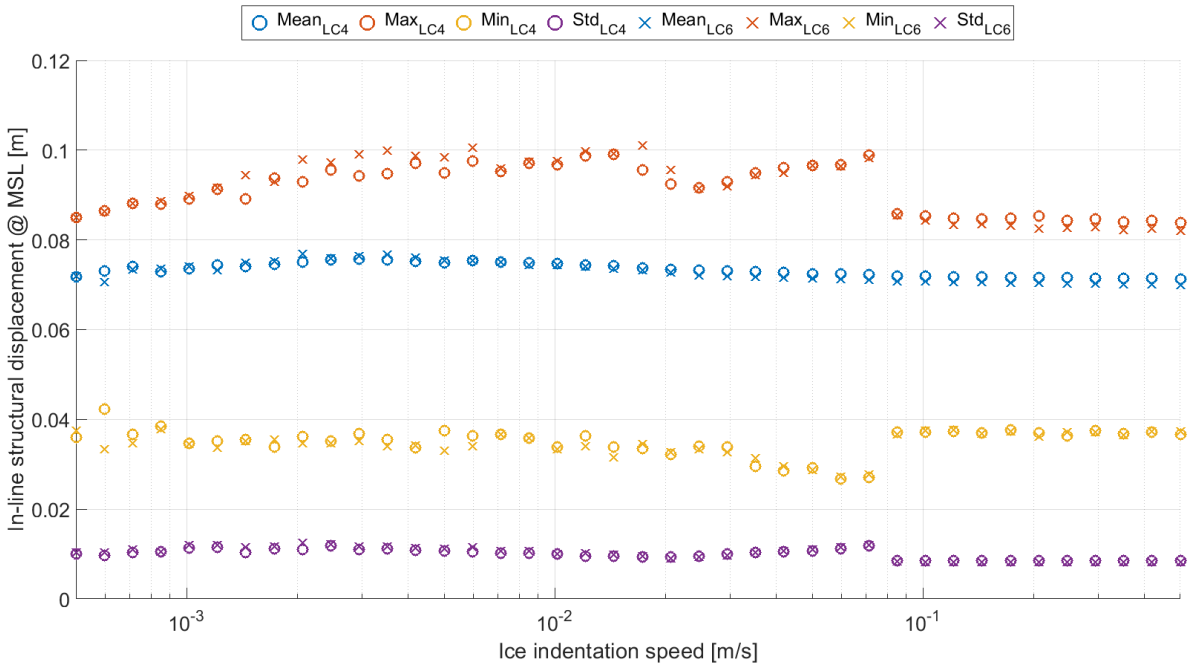

Figure E.4: Statistical characteristics of the structural X-displacement at MSL caused by a combination of wind load and an indenting ice floe on a cylindrical structure for varying ice indentation speeds and ice and structure characteristics as listed in Table 7.1. Results are shown for load cases 4 and 6, according to the load case overview of Section 7.1 and Figure E.1

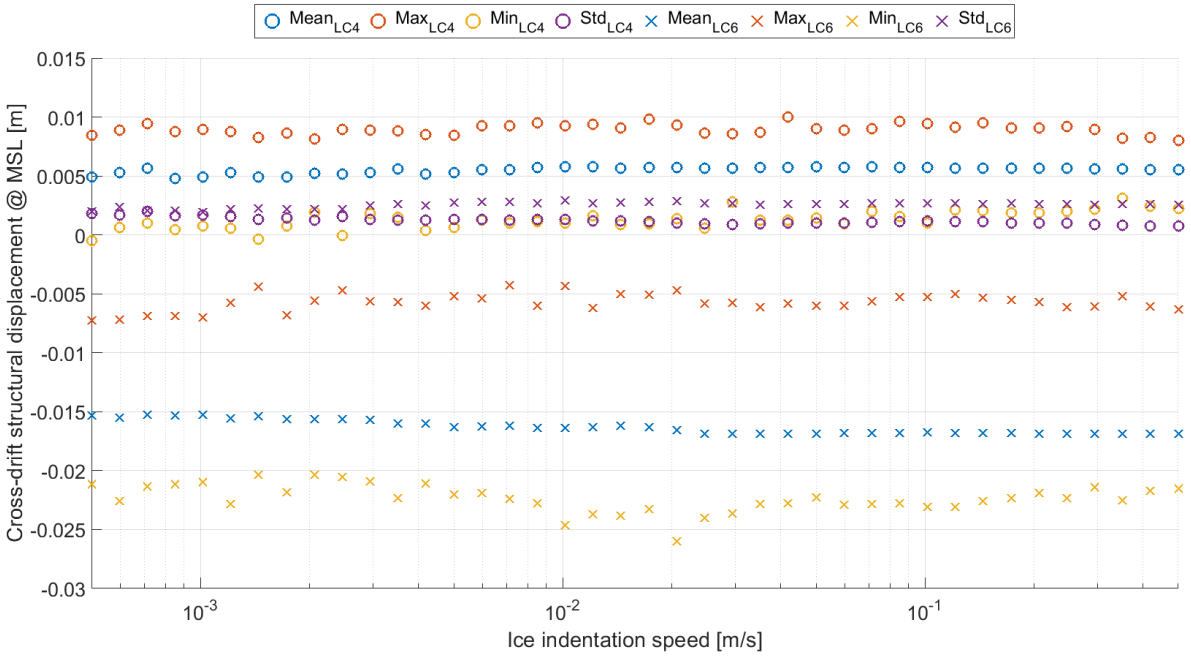

Figure E.5: Statistical characteristics of the structural Y-displacement at MSL caused by a combination of wind load and an indenting ice floe on a cylindrical structure for varying ice indentation speeds and ice and structure characteristics as listed in Table 7.1. Results are shown for load cases 4 and 6, according to the load case overview of Section 7.1 and Figure E.1

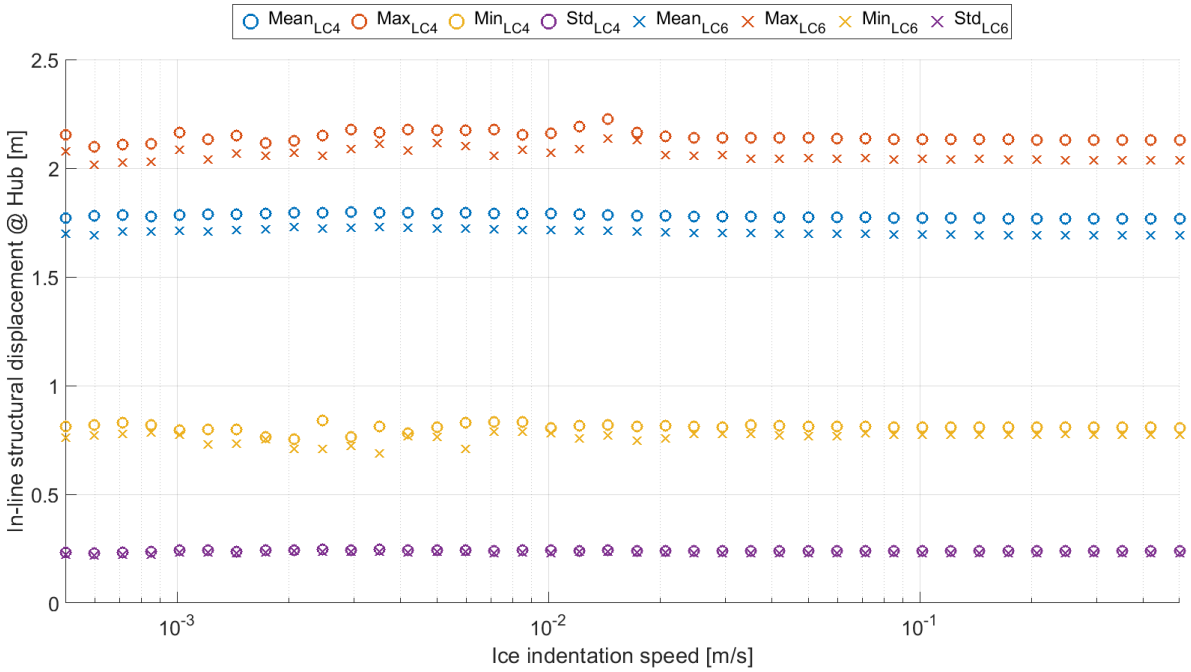

Figure E.6: Statistical characteristics of the structural X-displacement at hub heigth caused by a combination of wind load and an indenting ice floe on a cylindrical structure for varying ice indentation speeds and ice and structure characteristics as listed in Table 7.1. Results are shown for load cases 4 and 6, according to the load case overview of Section 7.1 and Figure E.1

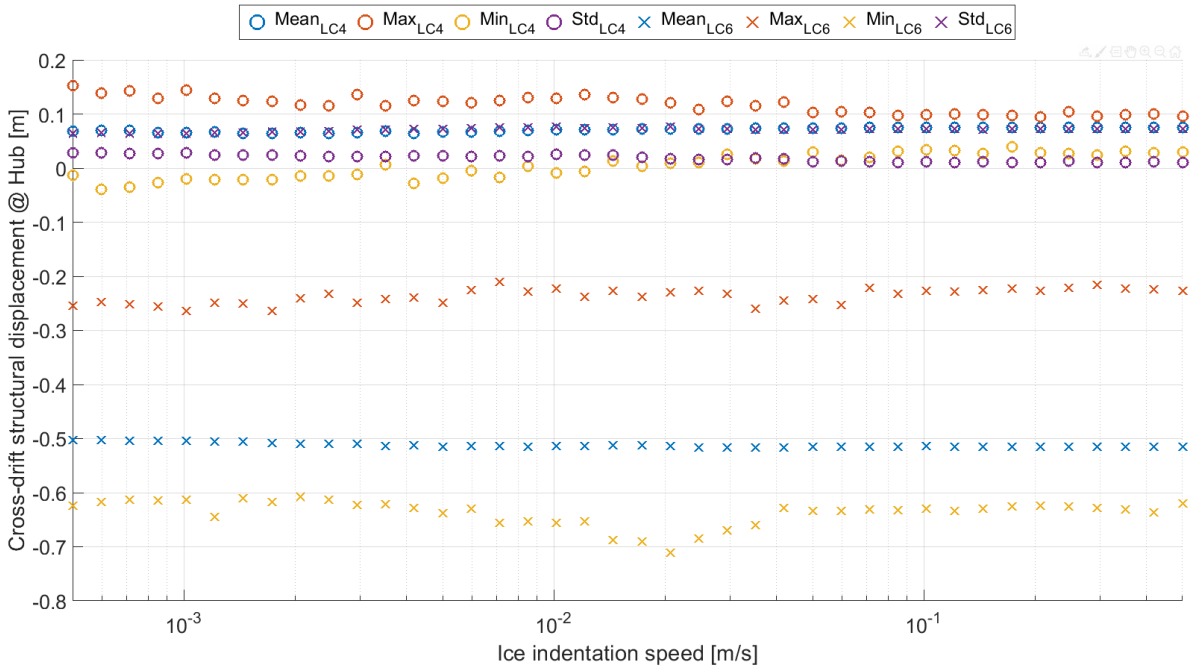

Figure E.7: Statistical characteristics of the structural Y-displacement at hub height caused by a combination of wind load and an indenting ice floe on a cylindrical structure for varying ice indentation speeds and ice and structure characteristics as listed in Table 7.1. Results are shown for load cases 4 and 6, according to the load case overview of Section 7.1 and Figure E.1

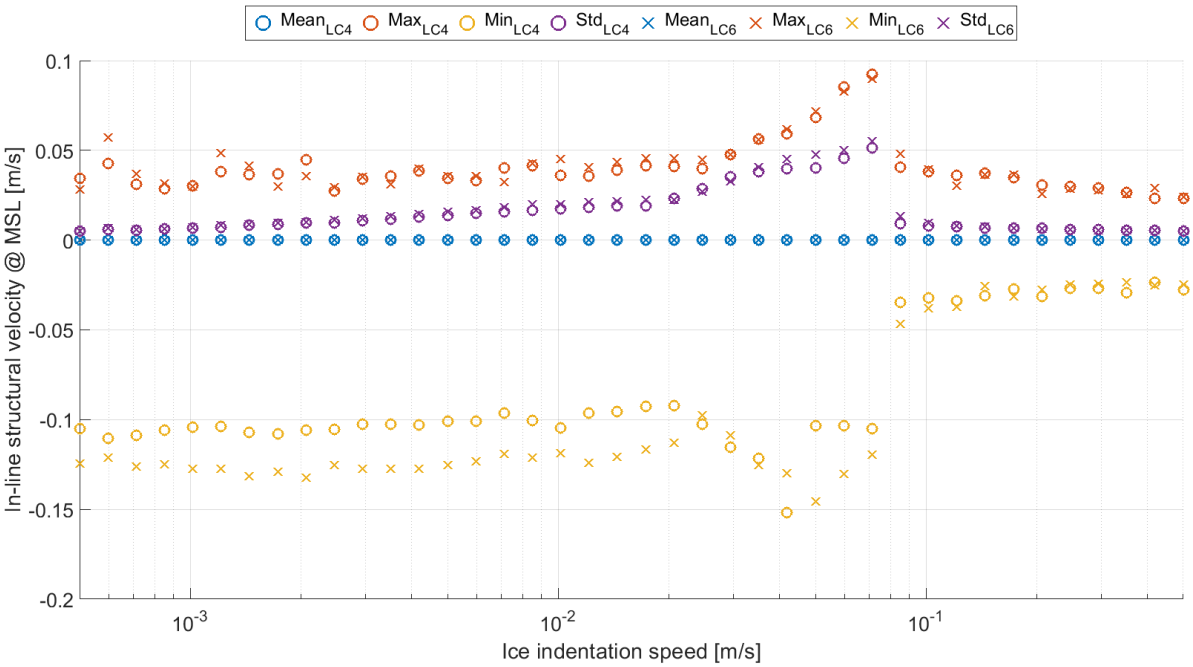

Figure E.8: Statistical characteristics of the structural X-velocity at MSL caused by a combination of wind load and an indenting ice floe on a cylindrical structure for varying ice indentation speeds and ice and structure characteristics as listed in Table 7.1. Results are shown for load cases 4 and 6, according to the load case overview of Section 7.1 and Figure E.1

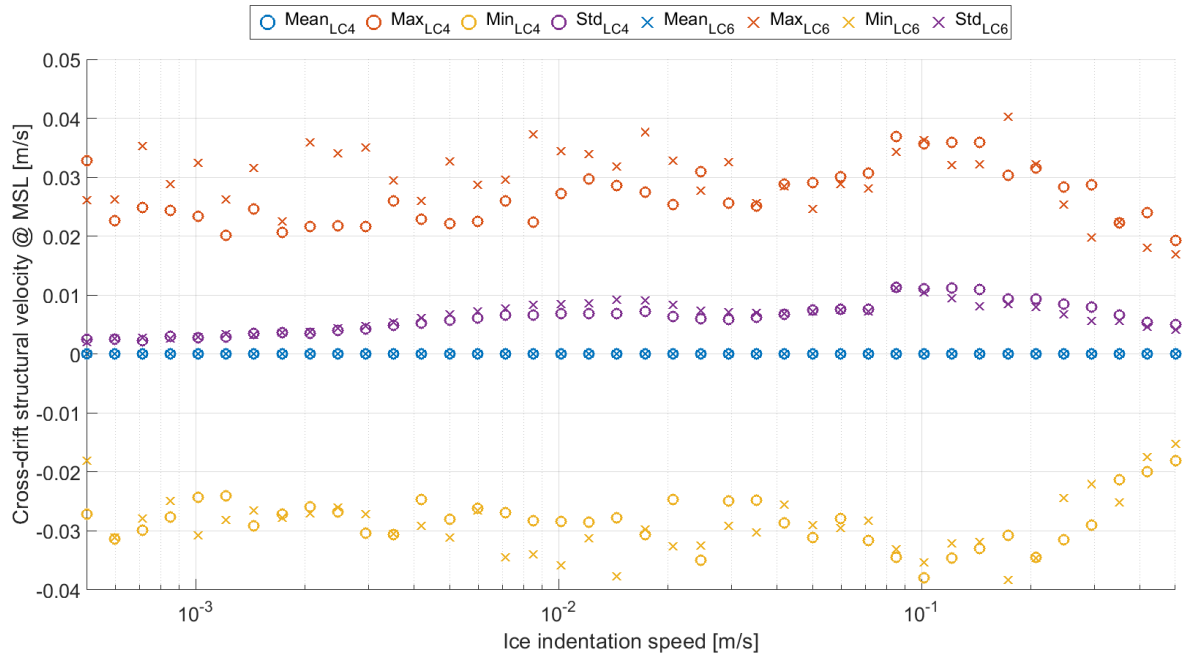

Figure E.9: Statistical characteristics of the structural Y-velocity at MSL caused by a combination of wind load and an indenting ice floe on a cylindrical structure for varying ice indentation speeds and ice and structure characteristics as listed in Table 7.1. Results are shown for load cases 4 and 6, according to the load case overview of Section 7.1 and Figure E.1

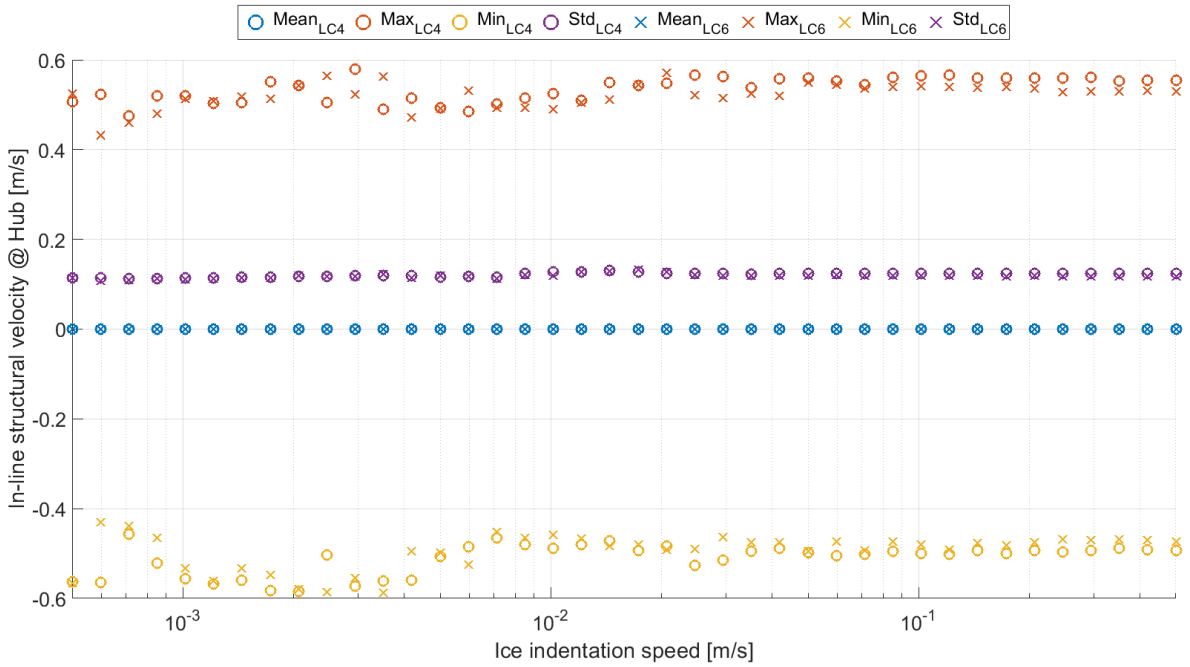

Figure E.10: Statistical characteristics of the structural X-velocity at hub heigth caused by a combination of wind load and an indenting ice floe on a cylindrical structure for varying ice indentation speeds and ice and structure characteristics as listed in Table 7.1. Results are shown for load cases 4 and 6, according to the load case overview of Section 7.1 and Figure E.1

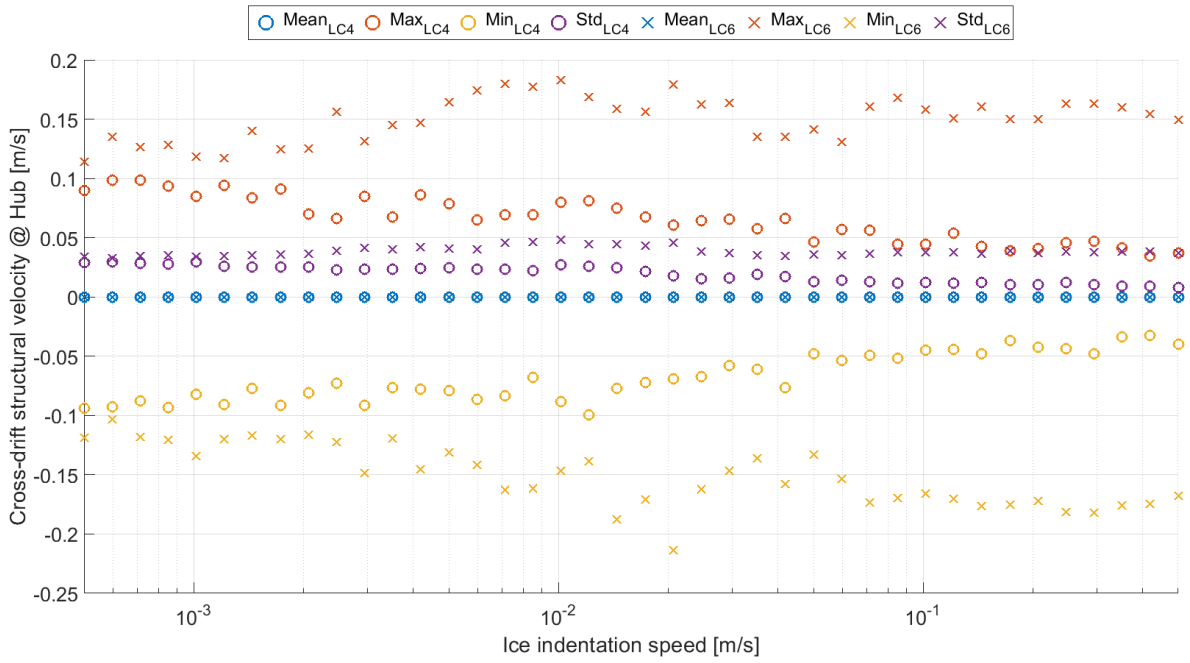

Figure E.11: Statistical characteristics of the structural Y-velocity at hub height caused by a combination of wind load and an indenting ice floe on a cylindrical structure for varying ice indentation speeds and ice and structure characteristics as listed in Table 7.1. Results are shown for load cases 4 and 6, according to the load case overview of Section 7.1 and Figure E.1

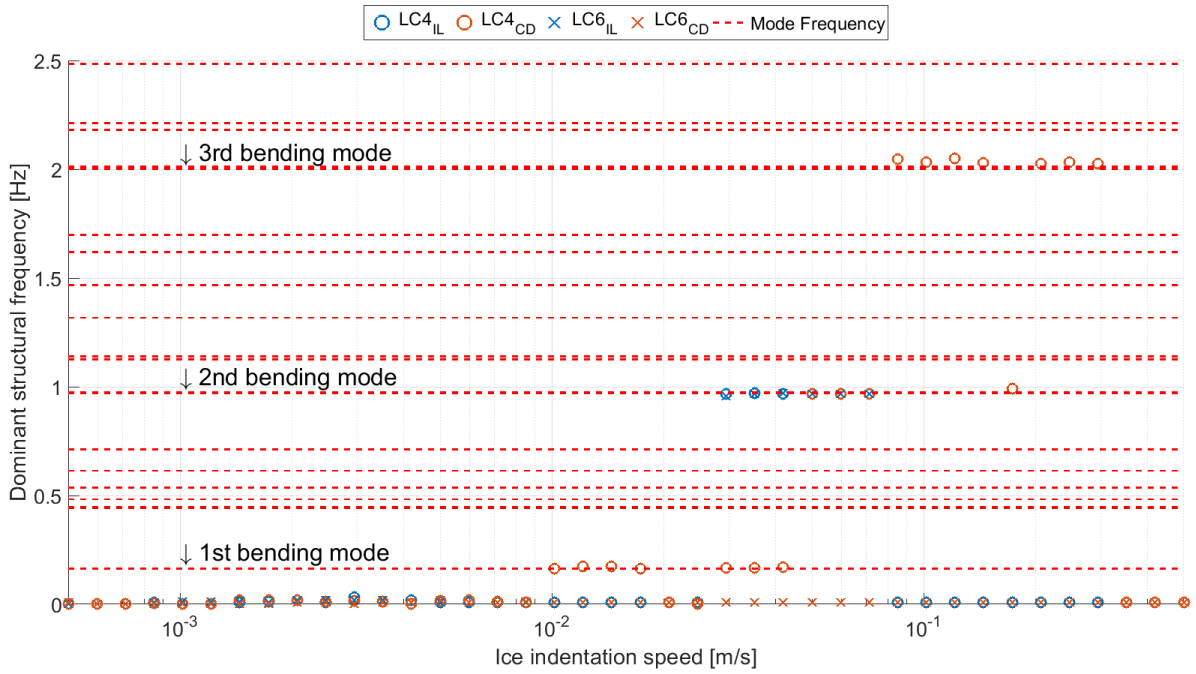

Figure E.12: Dominant structural frequencies for both the X- and Y-directions caused by a comination of wind load and an indenting ice floe on a cylindrical structure for varying ice indentation speeds and ice and structure characteristics as listed in Table 7.1. Results are shown for load cases 4 and 6, according to the load case overview of Section 7.1 and Figure E.1

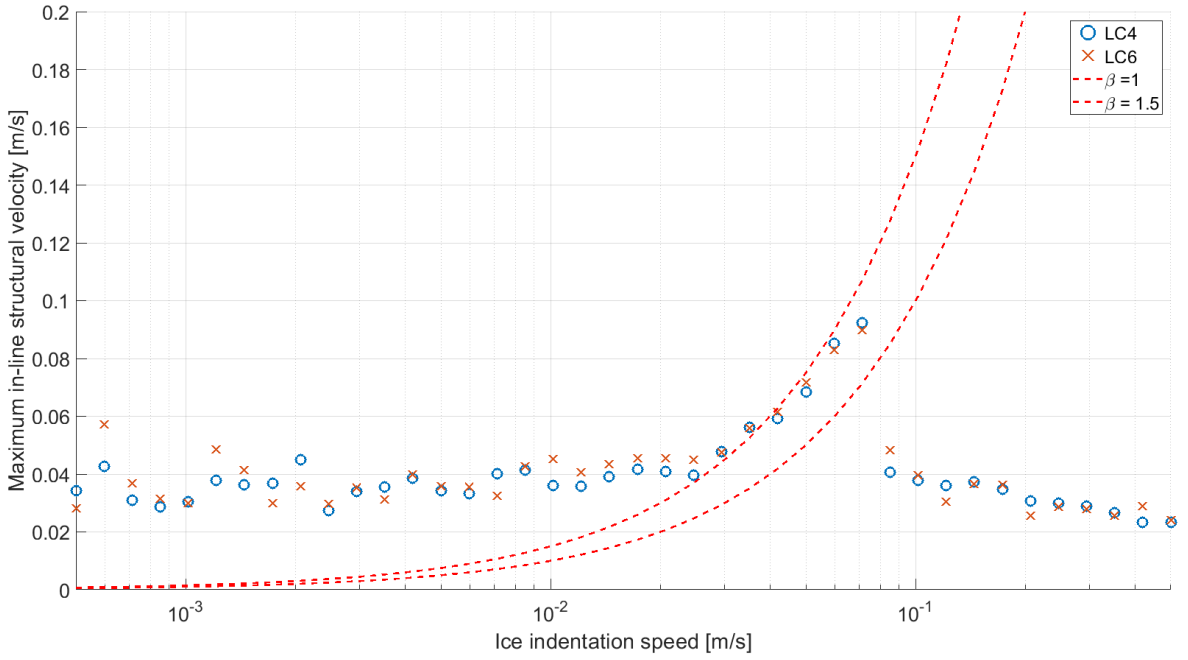

Figure E.13: β-values caused by a combination of wind load and an indenting ice floe on a cylindrical structure for varying ice indentation speeds and ice and structure characteristics as listed in Table 7.1. Results are shown for load cases 4 and 6, according to the load case overview of Section 7.1 and Figure E.1